Theses and Dissertations                                    Student Graduate Works

9-13-2012

# Ground Vehicle Navigation Using Magnetic Field Variation

Jeremiah A. Shockley

Follow this and additional works at: https://scholar.afit.edu/etd

Part of the Electromagnetics and Photonics Commons

Recommended Citation

Shockley, Jeremiah A., "Ground Vehicle Navigation Using Magnetic Field Variation" (2012). *Theses and Dissertations*. 1156.
https://scholar.afit.edu/etd/1156

GROUND VEHICLE NAVIGATION
USING MAGNETIC FIELD VARIATION

DISSERTATION

Jeremiah A. Shockley, Major, USAF

AFIT/DEE/ENG/12-17

**DEPARTMENT OF THE AIR FORCE**
**AIR UNIVERSITY**

# AIR FORCE INSTITUTE OF TECHNOLOGY

**Wright-Patterson Air Force Base, Ohio**

# Ground Vehicle Navigation
# Using Magnetic Field Variation

DISSERTATION

Presented to the Faculty

Graduate School of Engineering and Management

Air Force Institute of Technology

Air University

Air Education and Training Command

In Partial Fulfillment of the Requirements for the

Degree of Doctor of Philosophy
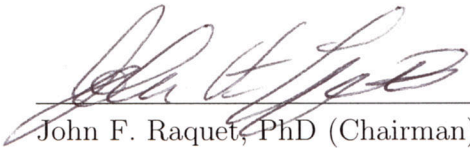
Jeremiah A. Shockley, BS, MS

Major, USAF

September 2012

AFIT/DEE/ENG/12-17
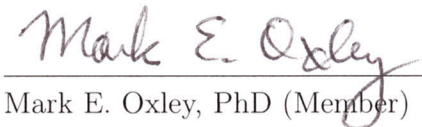
GROUND VEHICLE NAVIGATION
USING MAGNETIC FIELD VARIATION

Jeremiah A. Shockley, BS, MS

Major, USAF

Approved:

_____          _____
John F. Raquet, PhD (Chairman)            21 AUG 2012
                                          Date

_____          _____
Mark E. Oxley, PhD (Member)               21 Aug 2012
                                          Date

_____          _____
LtCol Kenneth A. Fisher, PhD (Member)     21 Aug 2012
                                          Date

Accepted:

_____          _____
M. U. THOMAS                              3 Sep 2012
Dean, Graduate School of Engineering      Date
   and Management

AFIT/DEE/ENG/12-17

## *Abstract*

The Earth's magnetic field has been the bedrock of navigation for centuries. The latest research highlights the uniqueness of magnetic field measurements based on position due to large scale variations as well as localized perturbations. These observable changes in the Earth's magnetic field as a function of position provide distinct information which can be used for navigation. This dissertation describes ground vehicle navigation exploiting variation in Earth's magnetic field using a self-contained navigation system consisting of only a magnetometer and magnetic field maps. In order to achieve navigation, effective calibration enables repeatable magnetic field measurements from different vehicles and facilitates mapping of the observable magnetic field as a function of position. A new modified ellipsoid calibration technique for strapdown magnetometers in large vehicles is described, as well as analysis of position measurement generation comparing a multitude of measurement compositions using existing and newly developed likelihood techniques. Finally, navigation solutions are presented using both a position measurement and direct incorporation of the magnetometer measurements via a particle filter to demonstrate road navigation in three different environments. Emphatically, the results affirm that navigation using magnetic field variation in ground vehicles is viable and achieves adequate performance for road level navigation.

## Acknowledgements

## Table of Contents

## List of Figures

x

xiii

# List of Tables

# Ground Vehicle Navigation
# Using Magnetic Field Variation

## I. Introduction

THIS dissertation details research focused on the exclusive utilization of three-dimensional magnetic field information for self-contained, passive navigation in ground vehicles. The motivation stems from the requirement for navigation in all environments where navigation sources such as the Global Positioning System (GPS) are not available. The goal for this research is the ability to use only three-axis magnetometer measurements and a magnetic field map to provide road-level navigation in different vehicle types and various environments.

Successful navigation has been a focus of mankind for centuries. From the early explorers of the Earth to the current exploration of Earth and space, the need for navigation accuracy and precision increases daily. Even in the present day era of multiple Global Navigation Satellite Systems (GNSS) proclaiming millimeter accuracy, there exists a large focus on self-contained navigation systems especially for environments where external signals such as GNSS cannot be obtained. These systems are termed self-contained because they do not rely on receiving a signal from an external man-made system in order to navigate. Rather, they use information from the environment coupled with pre-existing information to determine position. Examples include terrain navigation, celestial navigation (astronavigation), inertial navigation, magnetic navigation and other forms of deduced reckoning. Historically, self-contained navigation systems have dominated navigation due to robustness and stability, while recent decades have seen the ascension of GNSS with the seduction of increased accuracy and precision. Presently, self-contained navigation systems have

been relegated to the subservient role of aiding GNSS when signal strength is weak or unavailable for short periods of time. However, some conditions offer no opportunity to receive GNSS or other signal-based navigation systems. This research will expand the capability of a self-contained magnetometer-based navigation system.

Indoor, urban, and canyon environments present challenges for GNSS in terms of limited or poor signal reception. Luckily, these locations often provide feature rich conditions for self-contained navigation systems and merit exploration to improve navigation capability. While the use of the Earth's magnetic field for navigation is certainly not new, the ability to accurately determine position based on the three-dimensional magnetic field information is an application showing great merit.

This research addresses specific issues related to magnetic field measurements and provides a framework for determining measurement utility and composition prior to navigation. The navigation solution is then analyzed to relate the expected navigation performance to the measurement composition. Finally, the specific contributions of this research and possible future work are discussed.

## 1.1   Related Work

In the last few decades, the improvement in inexpensive magnetometers has led to greater use in navigation, from simple compassing systems to attitude determination aiding. The focus for many of these groups is the aiding of another navigation device for course correction and heading determination in varying environments. Examining previous work using magnetic fields for navigation provides a bounty of knowledge to build upon as well as determine the state of the art. The following articles provide related work which is either a building block or a different vein of research than what will be proposed in this document.

### 1.1.1   Wilson, Kline-Schoder, Kenton, Sorensen, and Clavier.   Wilson et al., proposed using magnetic field variations over a large area to navigate in an aircraft using US Geological Survey magnetic field maps. The algorithm uses the

magnetic field information combined with "an aircraft dead-reckoning navigation system" to determine the aircraft position [48].

The magnetic field map contains sources and associated strengths of magnetic field anomalies so that the magnetic field at a particular location is computed based on the position relative to the sources and strengths, within a precomputed distance. This information is combined with other sensors to produce a navigation solution. Flight test results compare the dead-reckoning solution with the magnetically-aided navigation solution to demonstrate the advantage of using the magnetic field information. The use of the magnetic field information did improve the navigation solution significantly, but overall maintained a typical error of 2.5 kilometers.

*1.1.2 Goldenberg.* Taking the idea of aerial mapping a bit further, Goldenberg [18] compares magnetic field measurements taken in the air with mathematically interpreted magnetic field measurements on the ground. Additionally, the concept of a worldwide magnetic anomaly map conveys the importance of magnetic field mapping.

Comparison of the aircraft magnetic field mapping with interpreted ground observations requires solving a Laplace equation using a Poisson integral for a plane [18]. The resulting calculated magnetic field map measurements agree with aerial mapping up to approximately 30 kilometers. The magnetic field map is then used in an integrated navigation system along with an inertial measurement unit, an altimeter, and two microprocessors. Unfortunately, Goldenberg does not provide results of the comparison or performance of the integrated navigation system.

The World Digital Magnetic Anomaly Map (WDMAM) [18] project attempts to create a coherent global map of magnetic field anomalies. While Goldenberg only eludes to the project in the article published in 2006, in 2011 the WDMAM created a global 3-arc-minute resolution grid of magnetic field intensities at an altitude of five kilometers above mean sea level.

*1.1.3  Storms.*     Storms adeptly applied a terrain navigation algorithm to the indoor magnetic field environment to aid an inertial navigation system (INS) and achieved sub-meter positioning results [42]. An overview of the two methods used by Storms provides insight into how such accuracy is achieved.

The first method captures three-axis magnetic field measurements traveling down a hallway at a constant height to generate an equally spaced grid. The grid is interpolated to generate a higher resolution magnetic field map [42]. The map is then used during navigation to provide a position estimate based on the likelihood that a magnetic field measurement is located on the map. This position estimate serves as the measurement estimate in an extended Kalman filter, which also uses INS measurements to determine two-dimensional position and velocity. Using real measurements the maximum error was 0.6 meters.

The second method uses a leader-follower methodology in which a more highly equipped lead vehicle traverses an area and sends magnetic field map information to a less equipped follower vehicle [42]. The follower vehicle uses the map information combined with an additional sensor to navigate the path established by the lead vehicle. The cross-track errors were less than 0.4 meters between the lead and follower vehicles.

These methods established the use of unique three-axis magnetic field measurements as navigable features and demonstrated effective use of the information. This fundamental work opens the door for further exploration using three-axis magnetic field measurements for navigation.

While Storms innovative work exposed the ability to navigate using three-axis magnetometer measurements, it also warrants further exploration. For instance, there is no mention of calibration which is crucial in the assumption that the three magnetometers used to generate the map report consistent measurements. Furthermore, without calibration Storms could not ensure that the magnetometer used during navigation would yield measurements consistent with those contained in the

magnetic field map. Additionally, Storms' observation of "dead areas" in the magnetic field map indicate insufficient changes in the magnetometer measurements for navigation. An analysis of measurement utility in different environments is needed to determine areas where navigation can occur and at what level of accuracy.

*1.1.4 The Position, Location, and Navigation Group at the University of Calgary.* Lachapelle, Renaudin, and Afzal are currently using a sensor suite of 12 magnetometers specifically for indoor navigation. The focus is to determine the true heading by successfully detecting large magnetic perturbations and mitigating them without causing course deviation [41]. A critical component of their work relies on successful calibration of all magnetometers while mounted on the collection platform and while exposed to the Earth's magnetic field.

The multi-magnetometer platform uses 12 magnetometers in a geometric circle to locate and mitigate magnetic field anomalies and provide correct heading estimation. The arrangement of the magnetometers allows the mitigation of the perturbation when the magnetic field measurements are resolved with the body axis, highlighting magnetic field measurements from magnetometers which do not agree with the rest. The results showed that a single magnetometer experiencing a perturbation possessed a heading deviation of 16°, compared to 4° for the multi-magnetometer platform.

The calibration sequence applies an ellipsoid fitting technique developed by Li and Griffiths [29] to magnetometers in an open environment. Since the magnitude of the observed magnetic field should be the same regardless of the magnetometer orientation, the calibration attempts to resolve the errors and biases by fitting the observations to a sphere of radius equal to the magnitude of the Earth's magnetic field at the location of calibration. The method hinges on the ability to rotate the entire collection platform in multiple axes in order to obtain enough points on the sphere to resolve the calibration parameters. This approach is nearly identical to

Vasconcelos [44]. Additionally, the composition of the multi-magnetometer platform is non-ferrous (i.e., plastic, wood, aluminum, etc.) such that the platform interferes with the calibration as little as possible.

*1.1.5   Three-axis Magnetometer Calibration.*   Vasconcelos et al., addressed three-dimensional ellipsoid calibration techniques for magnetometers and other sensors, with minor variations [2, 7, 9, 14, 16, 19, 25, 34, 41, 44]. The foundation for these methods lies in the ability to rotate the sensor about all three axes while maintaining a relatively stable position. The methods are also predicated on knowledge of an unchanging magnetic field at the location so that the relationship between the observed measurements and the known field can be resolved via determination of the bias, scale-factors, and distortions.

*1.1.6   Pedestrian Navigation.*   Many researchers are currently working with magnetometers in pedestrian navigation for both indoor and outdoor environments to aid other sensors by estimating heading. While the implementation is similar, the obstacles and results concerning the use of magnetic fields is very different.

The most straightforward case is the use of a single magnetometer for heading while outdoors. Ladetto et al. [27] compare the integration of a digital magnetic compass into a pedestrian navigation system versus the ability to determine heading using gyroscopes. Typical issues of using the Earth's magnetic field outdoors included declination and perturbations due to the environment.

Increasing the level of difficulty, Ascher et al. combine a magnetometer with a pair of inertial measurement units, a barometer, and a laser for precise indoor navigation [4]. Since the indoor environment contains many more error sources for the magnetometer, obtaining the correct heading from a magnetometer requires significantly more mitigation of errors.

Judd and Vu tackle the indoor pedestrian navigation problem similarly, but note interesting correlation in three-axis magnetometer measurements in the indoor environment [24]. While attempting to correct heading estimation indoors, the magnetic field along the route shows distinct "fingerprints" at unique locations along the route [24]. The resulting fingerprints allow correlation of previous magnetic field data with measurements during a new route to determine if a specific location is reached. The issues of the strength of perturbation necessary to be labeled a fingerprint as well as the possibility of traveling the route in reverse are highlighted, but not completely resolved.

Finally, Kemppi et al. investigate the use of pre-stationed magnetic field emitters in doorways of a building to determine position for pedestrian navigation [26]. Each emitter is unique and identifies a particular location in the building, as well as having greater strength than the Earth's magnetic field or magnetic field perturbations due to the environment. This method provides precise positioning at times when passing near an emitter and relies on other deduced reckoning methods during periods between doorways. Overall the method provides sub-meter positioning and allows improved step length estimation during pedestrian navigation.

Most recently, a company called Indoor Atlas advertised indoor location technology using a smartphone with a built-in magnetometer and 20 centimeter positioning. Haverinen, a lead researcher for the company and the University of Oulu in Finland, has produced publications covering indoor and underground magnetic field navigation [20, 21] with solutions on the order of 1.5 meters. The solutions still require extensive mapping and minimal interference from the collection platform.

Building upon these works, this research concentrates on magnetic field measurements as the sole measurement for navigation, while also determining the utility of the magnetic field environments.

The focus of this research is the exploitation of three-axis magnetometer measurements for navigation of ground vehicles. For this to occur, the magnetometer measurements must be relevant and useful, an analysis that had not been accomplished to great extent. Furthermore, the navigation solution must deliver an acceptable level of performance, based on the measurement quality. This dissertation demonstrates this fundamental feat has been accomplished, as well as increasing the overall body of knowledge. To this end, the following contributions are claimed as a result of this work.

*Calibration.* In order for the magnetometer measurements to be relevant and useful across different platforms, the calibration must provide some level of repeatability at a given position. The modified ellipsoid calibration for strapdown three-axis magnetometers developed in this research reduced the variation of magnetometer measurements across multiple platforms. The background for the method is covered in Chapter II, while the details of the modification are in Chapter III.

*Position Measurement Generation.* Once the measurements are repeatable, an analysis on composition of the magnetometer measurements was performed. The composition of the magnetometer measurements provides a framework for utilizing the measurements based on environment and system limitations. In addition to a basic maximum likelihood method, two additional methods to determine a position solution from likelihood values are also proposed. The ability to properly match the magnetometer measurement to the magnetic field map, including advantages and disadvantages of different likelihood methods, is included in Chapter IV.

*Filter-Based Solutions.* The ability to navigate exclusively using three-axis magnetometer measurements was achieved through application of a particle filter. The analysis of the navigation solution characteristics provides insight on the level of expected navigation performance, dependent upon the environment and magnetometer measurements, as detailed in Chapter V.

This dissertation is organized as follows. Chapter II provides the required background, knowledge, and tools concerning the Earth's magnetic field, magnetometer measurements, and navigation. Chapter III illustrates the new calibration method including simulated and real data results. Chapter IV demonstrates the multitude of methods for magnetometer measurement composition and presents a framework for utility. Chapter V presents the navigation performance characteristics based on different measurement compositions and environments. Chapter VI provides the conclusion as well as potential areas for future exploration.

## II. Background

$T$HE Earth's magnetic field has been used for navigation since the dawn of time in the animal kingdom. Nature provides several examples of animals that skillfully find their way to mating areas and migration locations using only the Earth's magnetic field [30]. In the case of many birds, loggerhead turtles, and lobsters, the ability is part of their anatomy. In humans however, the ability is not innate and has been learned and refined over centuries.

Navigation using magnetic fields requires knowledge in several disciplines. A succinct understanding of the magnetic field enveloping the Earth provides the foundation of the sensor measurement environment. A focused characterization of magnetic sensors and the multitude of errors involved provides the necessary information to comprehend how magnetic fields might be used for navigation. Once the information is obtained via the magnetic sensor, several tools transform the raw measurements into useful information for navigation. These tools include calibration, coordinate transformations, and filtering. But before elaborating on the tools, the foundation must be established.

### 2.1  Earth's Magnetic Field

The different layers of the Earth and the surrounding magnetic field is depicted in Figure 2.1, which shows that the magnetic field can be observed from anywhere on the Earth. The magnetic field encompassing the Earth is modeled as a large dipole magnet, describing the two opposing poles routinely referenced as the north and south pole. Although not actually a dipole magnet, the magnetic current loop generated by the outer-core region of the Earth, which is composed of a hot and dense liquid of highly conducting nickel-iron, and the Earth's spin and shape form characteristics similar to a dipole magnet [8]. Therefore the magnetic field can also be modeled as vector components where the magnetic field vector $\mathbf{B}$ is composed of the
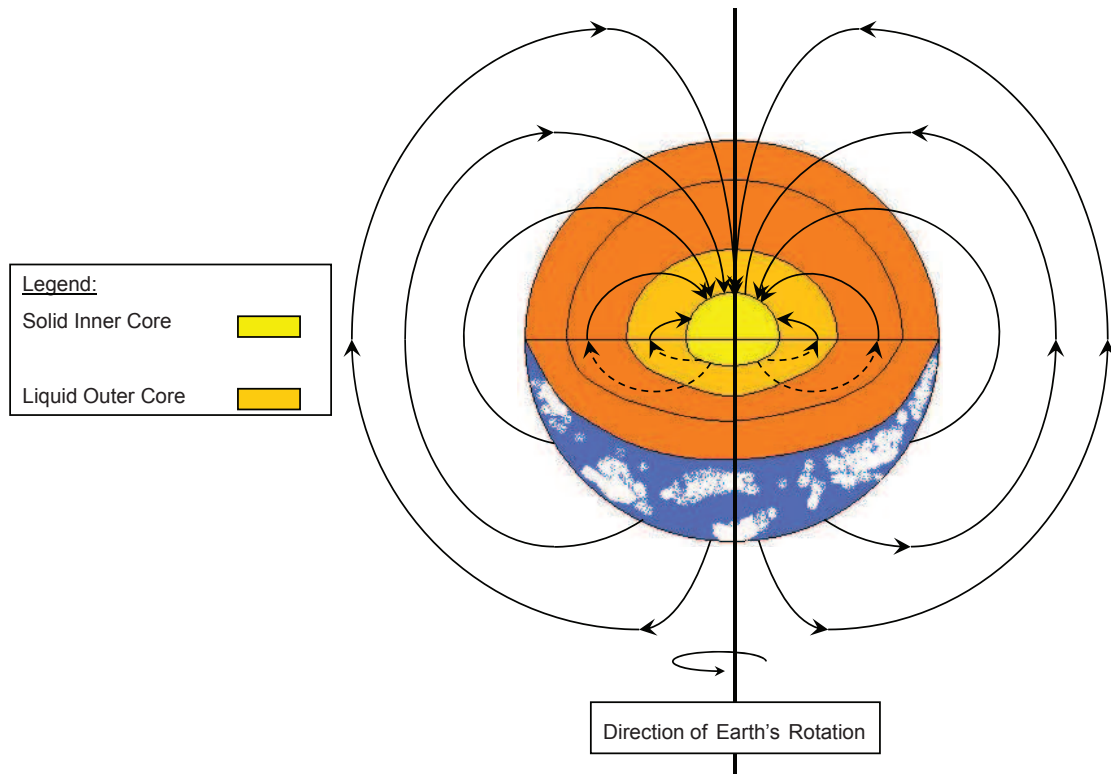
Figure 2.1:    Example of the Earth's magnetic field. The Earth's rotation and liquid outer core are believed to be the source of the dipole-like magnetic field [8].

individual components $B_x, B_y$, and $B_z$ (north/south, east/west, and perpendicular to the surface of the Earth). The total field strength or magnitude is represented as a scalar value, $\|\mathbf{B}\|$. Similarly, the horizontal magnitude is expressed as $\|\mathbf{B_h}\|$. Changes in the Earth's magnetic field can be thought of in terms of variations and perturbations. Variations are often large-scale and change slowly over time or due to external factors while perturbations cause specific changes in the local magnetic field and vary greatly in intensity, direction, and duration.

  *2.1.1   Magnetic Field Variations.*    Overall, the Earth's magnetic field is fairly constant [8]. For instance, a typical magnetic compass points to magnetic north which is offset from the geographic north pole (true north) by approximately 12° in latitude [8,43]. This is known as magnetic declination. Over time (2000-3000 years) the magnetic pole location rotates around the geographic pole due to the

11

nature of the Earth's magnetic field. Other variations such as a change in the Earth's electrical conductivity can be caused by significant events such as volcano eruptions or groundwater content due to "deep subsurface fractures" [8]. Volcanoes and even man-made occurrences such as filling a large reservoir after a dam is completed can affect the magnetic field by changing the "magnetic domain boundaries of rocks" [8]. While these changes have global implications, local variations exist as well.

Deposits in the Earth's crust, both large and small, change the locally observable magnetic field. The size and composition of the deposit determines the relative change in the magnetic field and the distance at which it may be observable. For example, a large deposit of a ferrous material can be observed to cause a magnetic deviation for several miles, both on the ground and in the air. This is often considered when flying or navigating near mountainous terrain using a traditional compass or magnetic instruments. As altitude increases, the intensity of the magnetic field has less variation due to these deposits in the crust [38, 48]. Smaller deposits in the Earth may only cause perturbations at or near ground level, such as archaeological artifacts. Archaeologists detect perturbations near the ground to find small deposits or even map out deposits over a large area before performing an excavation [23].

Other factors contributing to variations in the magnetic field include magnetic storms or changes in the ionosphere. These events often occur due to external factors such as solar activity. Depending on the scale of the magnetic storm, the impact can be quite severe. Boteler [5] discusses the impact of magnetic storms with documented events starting as early as 1844, although observances such as auroras have been viewed for thousands of years. While these variations often possess large-scale implications, the overall change to the Earth's magnetic field is generally minimal and in most cases predictable [43].

For decades the Earth's magnetic field has been modeled and variations known well enough that the differences between areas were reported and mapped. Figure 2.2 depicts the magnetic declination for various locations on the globe so that magnetic
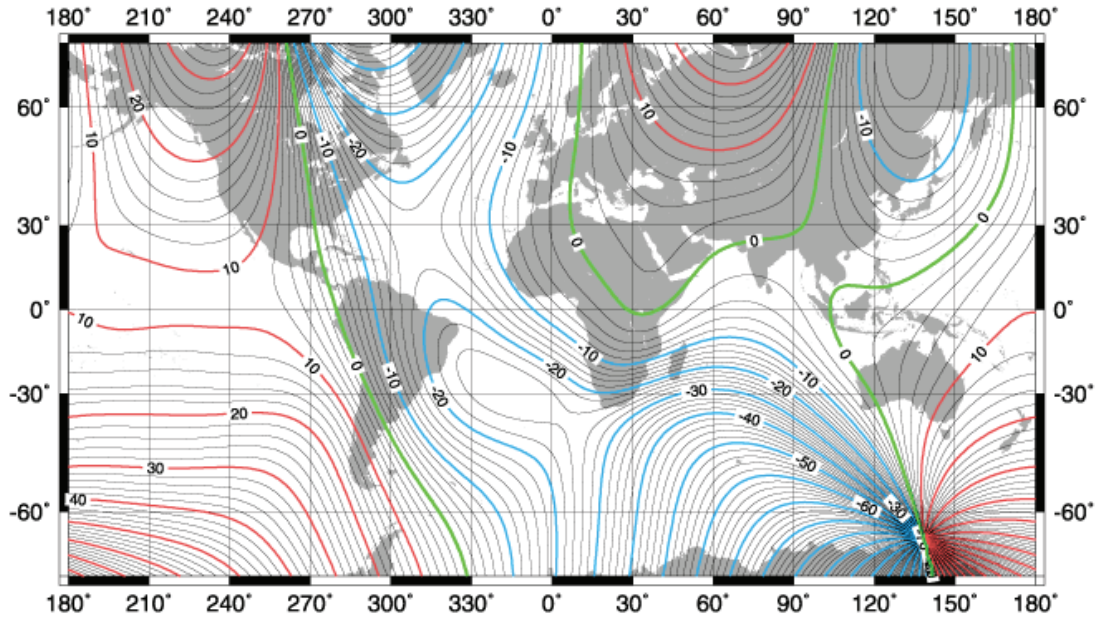
Figure 2.2: Magnetic declination lines in degrees overlaid on a map of the globe. The declination combined with observed magnetic north readings provides the direction to true north. Courtesy of NOAA as of 2000.

navigators can correct the difference between magnetic north observances and true north, courtesy of the National Oceanic and Atmospheric Administration (NOAA).

The magnetic field also varies each 24 hour period, known as the diurnal cycle [8]. The plots shown on the left in Figure 2.3 represent the vector components of the magnetic field from the magnetic observatory located at Fredericksburg, Virginia (observatory identifier FRD). Similar plots on the right side show observations taken over the same time period while inside the AFIT Advanced Navigation and Technology (ANT) Center. While the measurements are not identical due to geolocation, different sensor qualities, and misalignments, the comparison does show the ability to detect the changes due to the diurnal cycle and therefore account for them in some fashion. Typical diurnal variation in $B_x$ at FRD is $\pm0.45$ milliGauss (mG) or $\pm45$ nanoTesla (nT), and also typical of data observed at AFIT. However, diurnal variation depends greatly on the proximity to the poles. Figure 2.4 depicts the much larger variations from the observatory at Pt. Barrow, Alaska. Thus, magnetic
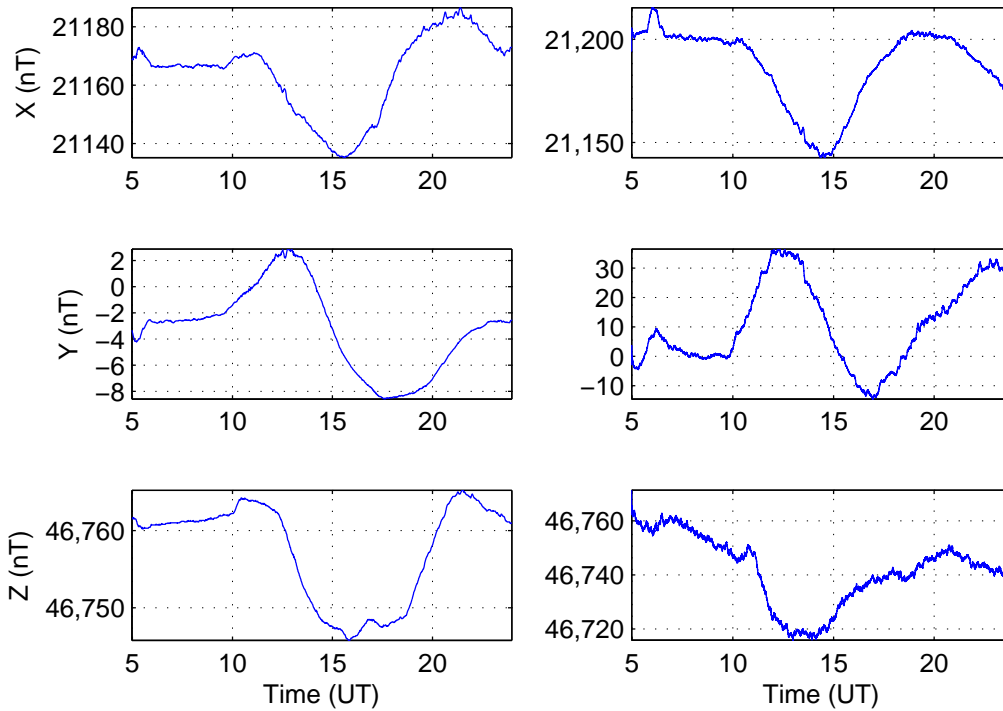
Figure 2.3:    Magnetic field diurnal comparison as measured at Fredericksburg, VA observatory and indoor AFIT environment over the same time period on 1 May 2010. The units for this figure are in nT for consistency with Figure 2.4 which was generated by INTERMAGNET.

noise strength varies by location, more specifically by latitude. Also of note, in both Figures 2.3 and 2.4 magnetic events were present which were not part of the diurnal cycle but due to some other magnetic event, such as a magnetic storm. These events also differ greatly in scale and may be smaller in magnitude than the diurnal cycle or significantly larger.

More recently, computer modeling of the Earth's magnetic field has allowed comparison with magnetic observatories to provide well-defined magnetic obser-vances as well as predicted magnetic field data. The International Geomagnetic Ref-erence Field (IGRF) by the International Association of Geomagnetism and Aeron-omy and used by NOAA delivers software modeling of the magnetic field and is a
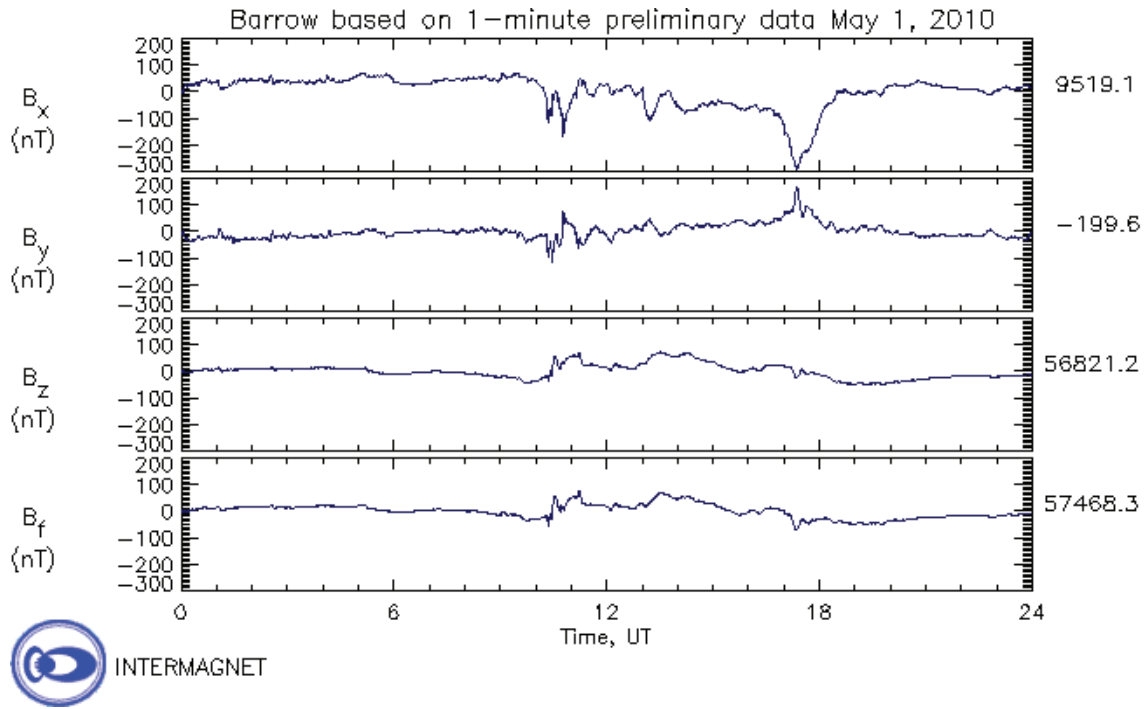
Figure 2.4: Magnetic field observed at Pt. Barrow, Alaska on 1 May 2010. The changes in the magnetic field due to the diurnal cycle vary by location. Courtesy of INTERMAGNET.

collaborative product between magnetic field modelers and data collection observatories around the world. Additionally, the World Magnetic Model (WMM) covers five year periods, and is generally referenced as WMM-2010 to describe the predictive model from 2010 through 2015. Maus [31] describes the difference succinctly, stating "While the WMM is a purely predictive model, the IGRF is adjusted retrospectively to provide more accurate 'definitive' models for past epochs." Both models capture the slowly varying changes in the Earth's magnetic field which happen over time, but the choice of model data depends on the purpose. Engineering applications often prefer the WMM for prediction, while the scientific community prefers the IGRF for studying past effects.

Focusing on the changes over time, NOAA records an annual change in the magnitude of the magnetic field at FRD of -1.227mG (-122.7nT) per year for the last 10 years. This equates to a change of about -0.1mG (-10nT) per month. The

15

WMM-2010 model also predicts the magnetic field change up to 2015 including the vector components $(B_x, B_y, B_z)$ and shows the trend will continue. Interestingly, at FRD the strength increases slightly in $B_x$ and $B_y$ but decreases substantially in $B_z$ causing the overall decrease in $\|\mathbf{B}\|$. Conversely, Pt. Barrow's magnitude increases slightly each year, with the major contribution stemming from a negative change in $B_y$. Location matters significantly when observing the magnetic field. While variations affect large portions of the Earth's magnetic field, perturbations provide more localized effects.

*2.1.2  Perturbations.*   Artificial disturbances that perturb the Earth's magnetic field include magnetic fields generated by electrical currents, buildings and other structures, or any type of activity using ferrous materials such as steel or rebar. Therefore the local magnetic field near or inside a structure may vary wildly from the Earth's magnetic field observed outdoors away from such perturbations. The direction and intensity of these perturbations are often determined by the size and distance from the source. Static items such as buildings simply cause small deviations in the existing magnetic field such that a compass heading might not be affected, but the vector components $(B_x, B_y, B_z)$ may have changed significantly. Moving objects such as cars will provide similar deviations. However, even smaller objects such as chairs or archaeological artifacts perturb the magnetic field enough that most sensors can easily detect the change when placed within a few feet [23].

Electrical currents on the other hand, create magnetic fields orthogonal to the direction of the electric field and can induce significant local deviations in the Earth's magnetic field. Therefore magnetic field measurements indoors or in close proximity to electrical devices require special attention. If these fields are transient in nature (i.e., varying strength or switching on or off) the measurements may not be repeatable over time.

*2.2   Magnetic Sensors*

From the early days of the compass to the current ability to measure the magnetic field from space, magnetic sensors have been used in numerous fields with many applications. While early sensors focused on using the magnetic field for heading determination, more sophisticated sensors focused on sensing the magnetic field vector components $(B_x, B_y, B_z)$ [18]. Specifically, magnetometers measure the intensity of magnetic fields and are used in many scientific and engineering measurement devices. While scalar magnetometers sense the magnetic field in a single direction, vector magnetometers sense the magnetic field in multiple axes. These vector magnetometers are actually composed of a pair or triad of scalar magnetometers set orthogonally to observe the vector components of the magnetic field. Sensors used only for heading typically consist of a pair of scalar magnetometers , such that when the magnetometer is level (orthogonal to $B_z$) magnetic heading can be computed.

Sensors measuring all three axis components consist of a triad or multiple triads depending on the application. A typical three-axis magnetometer consisting of a triad of sensors will have errors caused by fabrication and misalignments. For a single sensor, these must be resolved via calibration to provide consistent measurements. When multiple sensors are combined the individual and inter sensor errors must be accounted for to obtain repeatable measurements.

*2.2.1   Honeywell HMR2300.*    The Honeywell HMR2300 depicted in Figure 2.5 is a triad magnetometer which senses the magnetic field in the $x$, $y$, and $z$ axes via three magneto-resistive sensors oriented orthogonally [22]. The HMR2300 outputs the strength of each axis in *counts*. A single count is equal to 0.067mG or 6.7nT. This level of sensitivity easily detects changes in the magnetic field encountered in the indoor or outdoor environment. The measurement range is $\pm2$ Gauss, which allows for much stronger readings than the typical Earth's magnetic field which is near 0.5 Gauss in magnitude in most areas. For example, if a perfect

Figure 2.5:    Honeywell HMR2300 digital magnetometer.

magnetometer were aligned such that the vector components were perfectly aligned with the magnetic field vector (i.e., $x=B_x$, $y=B_y$ and $z=B_z$) the measurements would yield the true magnetic vector for that location. The HMR2300 receives power and communicates through the 9-pin serial connection on the body housing as shown in Figure 2.5.

The HMR2300 is also able to sample the magnetic field environment at selectable rates, ranging from 1 Hz to 154 Hz, which allows investigation of magnetic fields produced by electrical currents. The HMR2300 was chosen for measurement sensitivity in the field of interest while remaining fairly inexpensive with a small sensor size. However, the HMR2300 is not error free, and errors must be resolved in order to deliver repeatable measurements from day to day and from sensor to sensor.

## 2.3  Measurement Error Sources

Magnetometers are corrupted by a plethora of errors. The errors associated with the magnetometer include bias (offset), scale factor, non-orthogonality and misalignments as well as setup errors. The interfering magnetic fields, known as environment errors, consist of hard iron biases and soft iron biases specific to the location of the magnetometer. These would include any ferromagnetic material in the

vicinity of the magnetometer, especially the structure the magnetometer is mounted on or in.

2.3.1 *Setup errors.* The Honeywell HMR2300 error resolution process begins with the installation. If the magnetometer body is not secured tightly, slight movements will manifest as completely different measurements. Additionally, the serial connector may contain ferrous components, resulting in inconsistent measurements if the connector is not secured at approximately the same tightness each time. The use of serial connectors formed entirely from plastic along with ribbon cable greatly reduced this type of error.

2.3.2 *Test environment errors.* The next source of errors are from the test environment. The magnetometer power supplies, laptop, electric cabling, and battery packs change the magnetic field in the vicinity of the magnetometers. Great care must be taken when attempting to characterize the magnetometers and error sources since the scientist may inadvertently change the test environment. Additionally, most indoor environments are not well suited to characterize the magnetometer. Moving the magnetometer outside or in a large open environment significantly reduces perturbations in the sensed magnetic field.

2.3.3 *Fixed environment errors.* Some materials generate their own magnetic fields. These hard iron biases stem from "slowly time-varying fields generated by primarily ferromagnetic structural materials" [17]. These generally typify immovable objects in an area. The hard iron biases result in a fixed magnetic deviation and can be modeled as a true bias (offset)

$$\mathbf{b^{hi}} = [b_x^{hi} \ b_y^{hi} \ b_z^{hi}]^{\mathbf{T}} \tag{2.1}$$

and would remain constant for a given area.

19

The second type of bias consists of soft iron deviations due to induced magnetization caused by the permeability of ferromagnetic material interacting with an external magnetic field [41]. For example, the metal body of a car distorts the Earth's magnetic field even when the car is not running. These soft iron effects are modeled by a symmetric matrix

$$\mathbf{C^{si}} = \begin{bmatrix} c_{11} & c_{12} & c_{13} \\ c_{12} & c_{22} & c_{23} \\ c_{13} & c_{23} & c_{33} \end{bmatrix} \tag{2.2}$$

and these would be dependent on the location as well as other instrumentation near the magnetometer.

*2.3.4 Internal Magnetometer Errors.* The magnetometer bias, or offset, requires a fixed correction represented by

$$\mathbf{b^{so}} = [b_x^{so} \ b_y^{so} \ b_z^{so}]^{\mathbf{T}} \tag{2.3}$$

where the measurements from magnetometer A will be different from magnetometer B simply due to fabrication issues, even if all other errors were removed.

The magnetometer also suffers from scale-factor errors. For example, a measurement of 100mG in the magnetometer $x$ axis may represent the true magnetic field value of 110mG, while a measurement of 10mG represents a true value of 11mG. The resulting scale factor for that magnetometer axis would be 1.1. Scale factor errors represent the uncertainty in the constant of proportionality and are modeled by a diagonal matrix

$$\mathbf{C^{sf}} = \begin{bmatrix} sf_x & 0 & 0 \\ 0 & sf_y & 0 \\ 0 & 0 & sf_z \end{bmatrix} \tag{2.4}$$

In a perfect magnetometer, all measurements would be orthogonal. However, due to fabrication issues this is not the case and small misalignments are introduced. The correction for these errors can be modeled as

$$\mathbf{C^m} = \begin{bmatrix} 1 & \epsilon_{xy} & \epsilon_{xz} \\ \epsilon_{xy} & 1 & \epsilon_{yz} \\ \epsilon_{xz} & \epsilon_{yz} & 1 \end{bmatrix}^{-1} \tag{2.5}$$

where $\epsilon_x, \epsilon_y, \epsilon_z$ are the misalignments.

The magnetometer measurements are also corrupted by noise, as seen in Figure 2.6. For typical measurements the HMR2300 datasheet provides sensor noise characteristics of 0.01% of field strength (FS) and a maximum of 0.52% when the magnetic field is less than 1 Gauss [22]. Table 2.1 provides the statistics for the three magnetometers during this period when changes in the Earth's magnetic field were not greatly affected by the diurnal cycle. The magnetometers are identified by their serial number (i.e., SN237 is magnetometer with serial number ending in 237).

The noise characterization from Table 2.1 shows noise strengths slightly larger than typical. This was expected since the indoor environment, even in a quiet environment from midnight to 2 A.M. on a weekend contains perturbations such as electrical lines and equipment even though they are a significant distance from the magnetometers.

Table 2.1:   Magnetometer noise characteristics in milliGauss (mG).

| Magnetometer | $\bar{x}$ | $\sigma_x^2$ | $\bar{y}$ | $\sigma_y^2$ | $\bar{z}$ | $\sigma_z^2$ |
|---|---|---|---|---|---|---|
| SN237 | -195.3290 | 0.0070 | -54.6442 | 0.0035 | -414.4118 | 0.0171 |
| SN241 | -201.2587 | 0.0146 | -68.4668 | 0.0106 | -442.9471 | 0.0222 |
| SN242 | -205.9915 | 0.0177 | -60.9721 | 0.0159 | -440.1646 | 0.0154 |
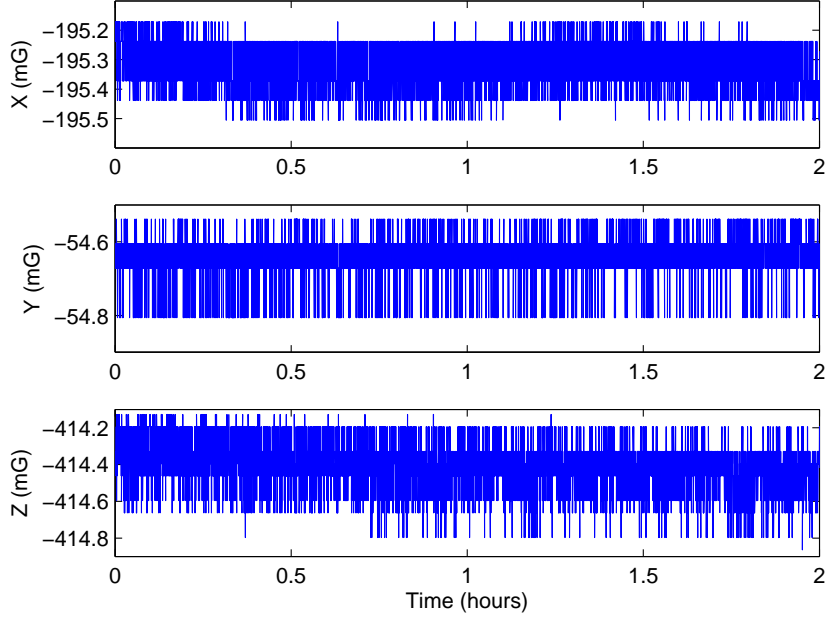
Figure 2.6: HMR2300 measurements taken in a quiet indoor environment from midnight to 2 A.M., representative of observations from three separate magnetometers.

The identification of these errors allow the construction of the full measurement model as developed in Renaudin [41] where

$$\hat{\mathbf{B}} = \mathbf{C^{sf}}\mathbf{C^{m}}(\mathbf{C^{si}}\mathbf{B} + \mathbf{b^{hi}}) + \mathbf{b^{so}} + \mathbf{v} = \mathbf{CB} + \mathbf{b} + \mathbf{v} \qquad (2.6)$$

such that $\hat{\mathbf{B}}$ is the $3x1$ vector of measurements from the sensor and $\mathbf{B}$ is the $3x1$ vector representing the true magnetic field. The matrix $\mathbf{C}$ is the $3x3$ matrix of scale factors, distortions (misalignments and soft iron disturbances) and the $3x1$ vector $\mathbf{b}$ is the combined bias. Finally, the $3x1$ vector $\mathbf{v}$ is the measurement noise modeled as a zero-mean additive white Gaussian noise process with

$$E[\mathbf{v}_k\mathbf{v}_j^{\mathbf{T}}] = \mathbf{R}\delta_{kj} \qquad (2.7)$$

22

where $E[\cdot]$ is the expected value operator, $\mathbf{R}$ is the measurement covariance matrix, and $\delta_{kj}$ is the Kronecker delta. The subscripts $k$ and $j$ denote discrete time indices. The strength of $\mathbf{v}_j$ is determined from the sensor noise and the diurnal cycle. Although the noise from the diurnal cycle is highly time correlated, modeling as zero-mean additive white Gaussian noise allows compensation for magnetic events without specific knowledge of time of occurrence.

Temperature, hysteresis, vibration and even the power supply also provide sources of error, however, significantly smaller in scale. To account for the multitude of errors present in measurements, several methods exist for calibration depending on the type of magnetometer and environment.

## 2.4   Calibration methods

Many magnetometer calibration methods exist depending on the type of magnetometer and application required. Knowledge of the Earth's magnetic field is often available to some degree and differing calibration techniques benefit in differing ways. An overview of the methods typically used to calibrate magnetometers in the presence of Earth's magnetic field are presented in the sections that follow.

Magnetometer calibration generally requires 12 parameters: three biases (or offsets), three scale-factors, three non-orthogonal angles (or distortions) and three Euler angles (if calibrating to an absolute reference frame). Since the vehicle body frame is the only frame available in this research, only the first nine parameters will be discussed.

*2.4.1   Swinging methods.*   For the purposes of this dissertation, swinging will describe existing methods which rotate exclusively around the vertical axis either by spinning around the axis in place or by traversing a circle. Swinging methods utilize straightforward techniques for heading correction as well as bias and scale-factor estimation. Depending on the purpose of the swinging calibration, true heading or

knowledge of the Earth's magnetic field may be used to determine the calibration parameters. The main detractor of swinging methods is the inability to determine the distortion terms between the axes. For example, if the sensor is tilted slightly upwards a misalignment calibration term is needed to correct for the vertical component present in the horizontal measurements.

*2.4.1.1 Compass swinging.* Often used in 2D heading applications, compass swinging is prevalent in vehicle platforms such as airplanes and ships [1]. Gebre-Egziabher also provided a thorough overview of compass swinging before proceeding with three-axis magnetometer calibration [17]. A standard compass or a two-axis magnetometer is leveled and exposed to known headings either via rotation about the vertical axis or by traveling in a circle. The differences between the observed heading and the known heading are recorded in order to create a table of heading corrections. For two-axis magnetometers the compass swinging method calculates the heading $\psi$ via the principle arctangent function

$$\psi = -tan^{-1}\left(\frac{\hat{B}_y}{\hat{B}_x}\right) \tag{2.8}$$

where $\hat{B}_x$ and $\hat{B}_y$ are the observed magnetic field measurements in the horizontal axes. The ˆ symbol specifically denotes observed measurements from a sensor. For simple applications such as personal vehicles, Equation (2.8) is often used to simply determine the heading without specific knowledge of the Earth's magnetic field and the value of zero degrees is set to true north.

*2.4.1.2 Bias and scale-factor estimation without knowledge of the Earth's magnetic field.* Estimation of the biases and scale-factors uses measurements collected during the magnetometer rotation about the vertical axis (or circle traversal) [10, 11, 28, 37]. The method proposed by Caruso [10] estimates the scale-factors

and biases in each axis as

$$sf_x = Max\left(1, \frac{\hat{B}_y^{Max} - \hat{B}_y^{Min}}{\hat{B}_x^{Max} - \hat{B}_x^{Min}}\right)$$

$$sf_y = Max\left(1, \frac{\hat{B}_x^{Max} - \hat{B}_x^{Min}}{\hat{B}_y^{Max} - \hat{B}_y^{Min}}\right) \tag{2.9}$$

and biases

$$b_x = \frac{\hat{B}_x^{Max} - \hat{B}_x^{Min}}{2} - \hat{B}_x^{Max}$$

$$b_y = \frac{\hat{B}_y^{Max} - \hat{B}_y^{Min}}{2} - \hat{B}_y^{Max} \tag{2.10}$$

where $\hat{B}_x^{Max}$, $\hat{B}_y^{Max}$, $\hat{B}_x^{Min}$, and $\hat{B}_y^{Min}$ are the maximum and minimum of the measurement observations along the $x$ and $y$ axes, respectively. A more accurate heading estimate can be obtained,

$$\psi = -tan^{-1}\left(\frac{sf_y(\hat{B}_y + b_y)}{sf_x(\hat{B}_x + b_x)}\right) \tag{2.11}$$

as presented in [37]. Again, if the heading is known, Equation (2.11) can be used to create a more accurate set of heading corrections by comparing the calculated heading with the known heading. If the true heading is unknown, Equation (2.11) is viewed as the best estimate [37]. If the sensor is freely rotated through all three axes, the same methods can be used to find $sf_z$ and $b_z$.

*2.4.1.3 Bias and scale-factor when the components of the Earth's magnetic field are known.* If the individual components of the Earth's magnetic field $\mathbf{B} = [B_x \ B_y \ B_z]$ are known from a model such as the IGRF, an extension of the equations derived by [10] yields better estimates of the scale-factors and an estimate for $b_z$ is

$$b_z = \frac{\hat{B}_z^{Max} + \hat{B}_z^{Min}}{2} - B_z \tag{2.12}$$

25

for the vertical axis. The scale-factors for each axis are

$$
\begin{aligned}
sf_x &= \frac{B_x}{\hat{B}_x^{Max} - b_x} \\
sf_y &= \frac{B_x}{\hat{B}_y^{Max} - b_y} \\
sf_z &= \frac{B_z}{\sqrt{\left\| \hat{\mathbf{B}} \right\|^2 - \left\| \hat{\mathbf{B}}_{\mathbf{h}} \right\|^2}}
\end{aligned}
\tag{2.13}
$$

where $\left\| \hat{\mathbf{B}} \right\|$ and $\left\| \hat{\mathbf{B}}_{\mathbf{h}} \right\|$ are the total magnitude and horizontal magnitude of the observed magnetic field, respectively. At first glance, the equation for $sf_y$ appears to have the incorrect value of $B_x$ as the numerator. However, when the magnetometer is rotated in the horizontal plane, $\hat{B}_y^{Max}$ is a function of $B_x$ since the $y$ axis is exposed to the maximum true value of $B_x$.

2.4.1.4 *Additional improvements for calibration.* Even in these cases, measurements are often skewed by tilt in each axis. To correct these errors Caruso [10] proposed exploiting liquid filled tilt sensors. Similarly, measurements from an inertial measurement unit mounted in the same frame as the magnetometer could be used. The common component missing in all of these methods is the ability to determine the relationship between the axes due to misalignments.

2.4.2 *Sensor matching.* A high-quality and very sensitive magnetometer such as a nuclear magnetometer or cryogenic superconducting quantum interference devices (SQUID) magnetometer provide the most accurate magnetic field measurements available and can be used to provide comparison data in order to determine calibration parameters for a lower quality sensor [35]. However these magnetometers have significant requirements and in most cases are cost prohibitive if the only purpose is to provide calibration parameters.

26

*2.4.3  Known magnetic field .*    Magnetic induction coils can provide a magnetic field of known magnitude and direction of greater strength than the Earth's magnetic field. In an environment with low hard and soft iron biases the magnetometer is exposed to the coil or set of coils and then rotated orthogonally to produce a set of calibration parameters [6].

*2.4.4  Filtering.*    Kalman filtering implementations model the error parameters and utilize a measurement model with a dynamic model of movement to find the optimal estimate of the calibration parameters. This technique is often used when the platform has a well-defined motion model. The benefits of Kalman filtering are greatest when combining multiple magnetometer measurements or measurements from different types of sensors. However, the optimality is reduced as the magnetometer measurements become nonlinear, and this technique relies heavily on the quality of the underlying measurement and dynamic models for proper estimation. Additionally, initial estimates of the error parameters must be fairly accurate to prevent filter divergence. Gebre-Egziabher [15] used that technique by estimating the initial error parameters and then implemented a Kalman filter using measurement data from magnetometers and gyros to determine attitude. Additionally, batch linear least squares, an extended Kalman filter (EKF), and an unscented Kalman filter (UKF) approach are compared by Crassidis [13] for use in real-time on orbit calibration of a magnetometer in a space environment. The use of neural networks has also been explored in separate research by Wang [47] and Moafipoor [37]. However, these methods require extensive training sets and focus on heading correction rather than the actual calibration of magnetometer measurements in each axis.

*2.4.5  Ellipsoid fitting.*    When possible, some variant of ellipsoid fitting is the method of choice for calibration in the Earth's magnetic field [2, 7, 9, 14, 16, 19, 25, 34, 41, 44]. Ellipsoid fitting can determine nine of the possible 12 calibration parameters, the remaining three parameters required for absolute orientation cannot

be resolved from comparison with the Earth's magnetic field. The reasons to use ellipsoid fitting are understandable. No extra equipment is required, the routine is simple, and knowledge of the Earth's magnetic field is easily obtained via the IGRF given a latitude, longitude, and height.

A straightforward model for measurements of the Earth's magnetic field is

$$\hat{\mathbf{B}} = \mathbf{C}\mathbf{B} + \mathbf{b} + \mathbf{v} \tag{2.14}$$

where $\hat{\mathbf{B}}$ is a $3x1$ vector of measurements from the sensor and $\mathbf{B}$ is the $3x1$ vector representing the true magnetic field. The $3x3$ matrix $\mathbf{C}$ is composed of the scale factors and distortions while the $3x1$ vector $\mathbf{b}$ is the combined hard iron and soft iron biases. The hard and soft iron biases as well as the soft iron disturbances are external to the magnetometer and a product of the local environment caused by ferrous materials near the magnetometer and large ferrous deposits in the Earth. Finally, the $3x1$ vector $\mathbf{v}$ is the measurement noise typical of the sensor. Ellipsoid fitting relies on magnetometer measurements in an environment where, regardless of sensor rotation, the magnitude of the magnetic field $\|\mathbf{B}\|$ would be the same. This is true when the calibrated magnetometer is placed away from ferrous materials completely, or when the relative position of the ferrous materials is fixed with respect to the magnetometer. In this case, measurements obtained by rotating the sensor through all three axes at varying inclinations should be points on a sphere with radius equal to the magnitude of the magnetic field. However, the measurements are generally not perfect and create an ellipsoid. Fitting the ellipsoid of measurements to the sphere of known magnitude via a least-squares technique results in the bias vector $\mathbf{b}$ and transformation matrix, $\mathbf{A} = \mathbf{C}^{-1}$, needed to calibrate the original measurements. The following development in three dimensions illustrates the core technique which is common to $[2, 7, 9, 14, 16, 34, 41]$.

The ellipsoid fitting method seeks the best correction matrix $\mathbf{A} = \mathbf{C}^{-1}$ and bias vector $\mathbf{b}$ such that the best estimate of the true magnetic field $\mathbf{B}$ is obtained. The equation to solve is

$$\|\mathbf{B}\|^2 = \|\mathbf{A}(\mathbf{x}_i - \mathbf{b})\|^2 \qquad \text{for } i = 1 \ldots N \tag{2.15}$$

where $\mathbf{A}$ is a $3x3$ matrix representative of the scale-factors and distortions, $\mathbf{x}_i$ is the $i^{\text{th}}$ $3x1$ magnetic field measurement vector with $N$ measurements taken, and $\mathbf{b}$ is the $3x1$ bias vector. $\|\mathbf{B}\|$ is the total field magnitude of the Earth's magnetic field. The right side of Equation 2.15 can be expanded, allowing

$$\|\mathbf{B}\|^2 = (\mathbf{x} - \mathbf{b})^{\mathbf{T}}\mathbf{A}^{\mathbf{T}}\mathbf{A}(\mathbf{x} - \mathbf{b})$$

$$= \mathbf{x}^{\mathbf{T}}\mathbf{A}^{\mathbf{T}}\mathbf{A}\mathbf{x} - \mathbf{b}^{\mathbf{T}}\mathbf{A}^{\mathbf{T}}\mathbf{A}\mathbf{x} - \mathbf{x}^{\mathbf{T}}\mathbf{A}^{\mathbf{T}}\mathbf{A}\mathbf{b} + \mathbf{b}^{\mathbf{T}}\mathbf{A}^{\mathbf{T}}\mathbf{A}\mathbf{b}$$

$$= \mathbf{x}^{\mathbf{T}}\mathbf{Q}\mathbf{x} - 2\mathbf{b}^{\mathbf{T}}\mathbf{Q}\mathbf{x} + k$$

$$\|\mathbf{B}\|^2 - k = \mathbf{x}^{\mathbf{T}}\mathbf{Q}\mathbf{x} - 2\mathbf{b}^{\mathbf{T}}\mathbf{Q}\mathbf{x} \tag{2.16}$$

where $\mathbf{Q} = \mathbf{A}^{\mathbf{T}}\mathbf{A}$ is a $3x3$ symmetric matrix and $k = \mathbf{b}^{\mathbf{T}}\mathbf{A}^{\mathbf{T}}\mathbf{A}\mathbf{b} = \mathbf{b}^{\mathbf{T}}\mathbf{Q}\mathbf{b}$ is simply a constant, the difference between $\left\|\hat{\mathbf{B}}\right\|^2$, the total field magnitude squared measured by the magnetometer, and $\|\mathbf{B}\|^2$, the true total field magnitude squared. Additionally, the subscripts on $\mathbf{x}$ are suppressed. Now, expanding the elements of $\mathbf{x}^{\mathbf{T}}\mathbf{Q}\mathbf{x}$ yields

$$\mathbf{x}^{\mathbf{T}}\mathbf{Q}\mathbf{x} = \begin{bmatrix} x & y & z \end{bmatrix} \begin{bmatrix} q_{11} & q_{12} & q_{13} \\ q_{12} & q_{22} & q_{23} \\ q_{13} & q_{23} & q_{33} \end{bmatrix} \begin{bmatrix} x \\ y \\ z \end{bmatrix}$$

$$= q_{11}x^2 + q_{22}y^2 + q_{33}z^2 + 2q_{12}xy + 2q_{13}xz + 2q_{23}yz \tag{2.17}$$

and similarly

$$-2\mathbf{b^TQx} = -2[b_x \quad b_y \quad b_z] \begin{bmatrix} q_{11} & q_{12} & q_{13} \\ q_{12} & q_{22} & q_{23} \\ q_{13} & q_{23} & q_{33} \end{bmatrix} \begin{bmatrix} x \\ y \\ z \end{bmatrix}$$

$$= -2(q_{11}b_x + q_{12}b_y + q_{13}b_z)x$$
$$\quad -2(q_{12}b_x + q_{22}b_y + q_{23}b_z)y$$
$$\quad -2(q_{13}b_x + q_{23}b_y + q_{33}b_z)z \tag{2.18}$$
$$= -2(p_7 x + p_8 y + p_9 z)$$

where $p$ simply represents a variable in the parameter matrix. Setting $k = 0$ on the left side of Equation (2.16) and using IGRF model data for $\mathbf{B}$, the left side becomes an $Nx1$ vector of $\|\mathbf{B}\|^2$ terms. The right side of Equation 2.16 becomes

$$\|\mathbf{B}\|^2_{Nx1} = \mathbf{Dp} \tag{2.19}$$

where

$$\mathbf{p} = \begin{bmatrix} q_{11} & q_{22} & q_{33} & q_{12} & q_{13} & q_{23} & p_7 & p_8 & p_9 \end{bmatrix}^{\mathbf{T}}$$

$$\mathbf{D} =$$

$$\begin{bmatrix} x_1^2 & y_1^2 & z_1^2 & 2x_1y_1 & 2x_1z_1 & 2y_1z_1 & -2x_1 & -2y_1 & -2z_1 \\ x_2^2 & y_2^2 & z_2^2 & 2x_2y_2 & 2x_2z_2 & 2y_2z_2 & -2x_2 & -2y_2 & -2z_2 \\ \vdots & \vdots & \vdots & \vdots & \vdots & \vdots & \vdots & \vdots & \vdots \\ x_N^2 & y_N^2 & z_N^2 & 2x_Ny_N & 2x_Nz_N & 2y_Nz_N & -2x_N & -2y_N & -2z_N \end{bmatrix}_{Nx9}$$

the $Nx9$ design matrix and the $9x1$ parameter vector.

The overdetermined system of equations can be solved by least squares where

$$\mathbf{D^T}\|\mathbf{B}\|^2_{Nx1} = \mathbf{D^T}\mathbf{D}\mathbf{p}$$

$$(\mathbf{D^T}\mathbf{D})^{-1}\mathbf{D^T}\|\mathbf{B}\|^2_{Nx1} = \mathbf{p} \qquad (2.20)$$

assuming $\mathbf{D^T}\mathbf{D})^{-1}\mathbf{D^T}$ exists. This results in the $9x1$ parameter vector $\mathbf{p}$ of which the first six parameters are the components of $\mathbf{Q}$ as shown in Equations (2.13) and (2.18). The symmetric, positive definite matrix $\mathbf{Q} = \mathbf{Q^T}$ will be invertible, provided a sufficient number of data points $(N)$ have been captured. The last three components of $\mathbf{p}$ are the solutions to Equation (2.18), which provide the information needed to find the bias vector

$$(\mathbf{b^T}\mathbf{Q})^{\mathbf{T}} = \mathbf{Q}\mathbf{b} = \mathbf{p}_{7,8,9}$$

$$\begin{bmatrix} q_{11} & q_{12} & q_{13} \\ q_{12} & q_{22} & q_{23} \\ q_{13} & q_{23} & q_{33} \end{bmatrix} \begin{bmatrix} b_x \\ b_y \\ b_z \end{bmatrix} = \begin{bmatrix} p_7 \\ p_8 \\ p_9 \end{bmatrix}$$

$$\mathbf{b} = \mathbf{Q^{-1}}\mathbf{p}_{7,8,9} \qquad (2.21)$$

and resolve the bias in each axis. Remembering that $\mathbf{Q}$ is actually $\mathbf{A^T}\mathbf{A}$ requires finding the symmetric square root of $\mathbf{Q}$, which is found by performing a singular value decomposition such that $\mathbf{Q} = \mathbf{U}\mathbf{\Sigma}\mathbf{U^T}$, the product of two orthogonal matrices and a diagonal matrix. Taking the square root of the diagonal terms in $\mathbf{\Sigma}$ such that $\mathbf{U}\sqrt{\mathbf{\Sigma}}\mathbf{U^T} = \mathbf{A} = \mathbf{C}^{-1}$, where $\mathbf{C}^{-1}$ is the matrix containing the best estimate of the scale-factors and distortions. In terms of Equation (2.14), the best estimate of the

true magnetic field can be found by

$$\mathbf{CB} + \mathbf{b} + \mathbf{v} = \hat{\mathbf{B}}_i \qquad \text{for } i = 1 \ldots N$$

$$\mathbf{CB} + \mathbf{v} = \hat{\mathbf{B}}_i - \mathbf{b}$$

$$\mathbf{B} = \mathbf{C}^{-1}(\hat{\mathbf{B}}_i - \mathbf{b} - \mathbf{v})$$

$$\mathbf{B} = \mathbf{A}(\hat{\mathbf{B}}_i - \mathbf{b} - \mathbf{v}) \tag{2.22}$$

which yields calibrated measurements for each sensor. However, full observability in each axis is not always attainable due to restrictions in movement. For example, rotation about the horizontal axes (roll and pitch) is not possible in most large vehicles. Subsequently, attempting the ellipsoid calibration method with measurement observations that do not represent the 3D magnetic field will result in very poor estimates of the error terms.

*2.4.5.1    The strictly two-dimensional ellipse method.*    If the $B_z$ component were completely ignored and only $B_x$ and $B_y$ were assumed to be present in the measurements, a strict ellipse method would provide corrections in two dimensions only. Beginning with the two-dimensional versions of Equations (2.17 - 2.21) the strict ellipse method would be

$$\mathbf{x^T Q x} = [x \quad y] \begin{bmatrix} q_{11} & q_{12} \\ q_{12} & q_{22} \end{bmatrix} \begin{bmatrix} x \\ y \end{bmatrix}$$

$$= q_{11}x^2 + q_{22}y^2 + 2q_{12}xy \tag{2.23}$$

$$-\mathbf{2b^T Q x} = -2[b_x \quad b_y] \begin{bmatrix} q_{11} & q_{12} \\ q_{12} & q_{22} \end{bmatrix} \begin{bmatrix} x \\ y \end{bmatrix}$$

$$= -2(q_{11}b_x + q_{12}b_y)x - 2(q_{12}b_x + q_{22}b_y)y$$

$$= -2(p_4 x + p_5 y) \tag{2.24}$$

$$\|\mathbf{B_h}\|_{Nx1}^2 = \mathbf{Dp} \tag{2.25}$$

$$\begin{bmatrix} \|\mathbf{B_h}\|^2 \\ \vdots \\ \vdots \\ \vdots \\ \|\mathbf{B_h}\|^2 \end{bmatrix} = \begin{bmatrix} x_1^2 & y_1^2 & 2x_1y_1 & -2x_1 & -2y_1 \\ x_2^2 & y_2^2 & 2x_2y_2 & -2x_2 & -2y_2 \\ x_3^2 & y_3^2 & 2x_3y_3 & -2x_3 & -2y_3 \\ \vdots & \vdots & \vdots & \vdots & \vdots \\ x_N^2 & y_N^2 & 2x_Ny_N & -2x_N & -2y_N \end{bmatrix} \begin{bmatrix} q_{11} \\ q_{22} \\ q_{12} \\ p_4 \\ p_5 \end{bmatrix}$$

$$\mathbf{D^T}\|\mathbf{B_h}\|_{Nx1}^2 = \mathbf{D^T D p}$$

$$(\mathbf{D^T D})^{-1}\mathbf{D^T}\|\mathbf{B_h}\|_{Nx1}^2 = \mathbf{p} \tag{2.26}$$

$$(\mathbf{b^T Q})^\mathbf{T} = \mathbf{Qb} = \mathbf{p}_{4,5}$$

$$\begin{bmatrix} q_{11} & q_{12} \\ q_{12} & q_{22} \end{bmatrix} \begin{bmatrix} b_x \\ b_y \end{bmatrix} = \begin{bmatrix} p_4 \\ p_5 \end{bmatrix}$$

$$\mathbf{b} = \mathbf{Q^{-1}p}_{4,5} \tag{2.27}$$

and strictly pertains to the horizontal axes. Relating Equation (2.15) to the two-dimensional equivalent to focus on the horizontal portion $\left\|\mathbf{\hat{B}_h}\right\|$ of the magnetic field yields

$$\|\mathbf{B_h}\|^2 = \left\|\mathbf{A_h}(\mathbf{\hat{B}_h} - \mathbf{b_h})\right\|^2 \tag{2.28}$$

where $\mathbf{A_h} = \mathbf{C_h}^{-1}$ is a 2x2 matrix containing the scale-factor and distortion corrections, $\mathbf{\hat{B}_h}$ is the 2x1 magnetic field measurement vector in two axes with $N$ measurements observed, and $\mathbf{b_h}$ is the 2x1 bias vector. $\|\mathbf{B_h}\|$ is the horizontal magnitude of the Earth's magnetic field for the location of measurement observations from a model such as the IGRF. Equations (2.23 - 2.27) for the two-dimensional case yield the scale-factor and distortion correction matrix $\mathbf{A_h}$ and biases $\mathbf{b_h}$ for the horizontal axes, as long as the measurement observations only include components from the horizontal axes.

33

Many reference frames exist which relate the position of a particular object to a frame of reference to determine location. In navigation systems, the measurement sensors are often not aligned with the body of the vehicle they are helping to navigate. Additionally, the moving vehicle generally requires a relationship with the Earth to determine position and heading. In order to make all of this information useful, a relationship between the reference frames must be established.

The direction cosine matrix (DCM) is one way of relating reference frames. The DCM uses geometry and vector math to rotate between reference frames. The DCM is is represented as $\mathbf{C}_s^b$, where the DCM converts from the sensor frame $s$ to the body frame $b$. The use of $\mathbf{C}$ as the $3x3$ matrix defined as the inner products of the unit basis vectors is simply standard notation, not to be confused with the scale-factor and misalignments matrix in Section 2.4. Similarly, the DCM $\mathbf{C}_b^n$ converts from the body frame $b$ to the navigation frame $n$. The angles used to determine the DCM are provided by the sensor mount in the navigation system. The DCM can be combined with a vector to change the origin of the coordinate system as well. A vector expressed in the body frame $b$ ($\mathbf{x}^b$) can be rotated into the navigation frame $n$ ($\mathbf{x}^n$) and undergo a change of origin using

$$\mathbf{x}^n = \mathbf{C}_b^n \mathbf{x}^b + \mathbf{r}_b^n \tag{2.29}$$

The transformation now conveys a rotation as well as a change in origin between the coordinate frames, such as changing from WGS-84 coordinates to a local level frame like east, north, and up (ENU).

## 2.6 Kalman Filtering

A linear Kalman filter is "an optimal, recursive data processing algorithm" that is used to generate an estimate of the states based on current measurement values

and all previous measurements [32]. However, the Kalman filter does not require specific knowledge of previous measurements. The generalized system model used in a Kalman filter is comprised of a dynamics matrix, $\mathbf{F}$, a matrix that describes how the noises affect the system model, $\mathbf{G}$, and a matrix that describes how control inputs affect the outcome of the system, $\mathbf{B}$. The stochastic differential equation is

$$\dot{\mathbf{x}}(t) = \mathbf{F}(t)\mathbf{x}(t) + \mathbf{B}(t)\mathbf{u}(t) + \mathbf{G}(t)\mathbf{w}(t) \tag{2.30}$$

where $\mathbf{w}(t)$ represents the white, Gaussian, driving noises on the system [32]. The matrix $\mathbf{Q}$ is defined as

$$E[\mathbf{w}(t)\mathbf{w}^{\mathbf{T}}(t + \tau)] = \mathbf{Q}(t)\delta(\tau) \tag{2.31}$$

where $\delta(\tau)$ is the Dirac delta function. In order to combine the state estimate with the discrete measurements, Equation 2.30 must be discretized, which results in a stochastic difference equation. The equivalent stochastic difference equation for Equation 2.30 which is developed in Maybeck [32], becomes,

$$\mathbf{x}(t_{k+1}) = \mathbf{\Phi}(t_{k+1}, t_k)\mathbf{x}(t_k) + \mathbf{B_d}(t_k)\mathbf{u}(t_k) + \mathbf{G_d}(t_k)\mathbf{w_d}(t_k) \tag{2.32}$$

where

$$\Delta t = t_{k+1} - t_k$$
$$\mathbf{\Phi}(t_{k+1}, t_k) = e^{\mathbf{F}(t_k)\Delta t}$$
$$\mathbf{B_d} = \int_{t_k}^{t_{k+1}} \mathbf{\Phi}(t_{k+1}, \tau)\mathbf{B}(\tau)d\tau \tag{2.33}$$
$$E[\mathbf{w_d}(t_k)\mathbf{w_d}^{\mathbf{T}}(t_k)] = \mathbf{Q_d}(t_k) = \int_{t_k}^{t_{k+1}} \mathbf{\Phi}(t_{k+1}, \tau)\mathbf{G}(\tau)\mathbf{Q}(\tau)\mathbf{G^T}(\tau)\mathbf{\Phi^T}(t_{k+1}, \tau)d\tau$$

The time difference, denoted by $\Delta t$, may or may not be uniformly spaced. The state transition matrix $\mathbf{\Phi}$ describes the change in the states over time. $\mathbf{B_d}$ is the discrete-time input matrix, and $\mathbf{w_d}$ is the discrete-time process noise.

The discrete measurements are modeled as

$$\mathbf{z}(t_k) = \mathbf{H}(t_k)\mathbf{x}(t_k) + \mathbf{v}(t_k) \tag{2.34}$$

where $\mathbf{H}(t_k)$ is the observation matrix, and $\mathbf{v}(t_k)$ is the measurement corruption noise.

*2.6.1 Propagation and Measurement Updates.* Using the system model as defined above, the first step in the Kalman filtering process is to propagate the current information forward in time. This step is a prediction of how the states will change over a specific time interval, $\Delta t$. The system dynamics matrix, $\mathbf{F}$, contains the behavior information of the system. The Kalman filter advances the state estimates based on the system model. The propagated state and covariance are represented by

$$\hat{\mathbf{x}}(t_{k+1}^-) = \boldsymbol{\Phi}(t_{k+1}, t_k)\hat{\mathbf{x}}(t_k^+) + \mathbf{B_d}\mathbf{u}(t_k) + \mathbf{G_d}(t_k)\mathbf{w_d}(t_k) \tag{2.35}$$

$$\mathbf{P}(t_{k+1}^-) = \boldsymbol{\Phi}(t_{k+1}, t_k)\mathbf{P}(t_k^+)\boldsymbol{\Phi}^{\mathbf{T}}(t_{k+1}, t_k) + \mathbf{Q_d}(t_k). \tag{2.36}$$

where $\hat{\mathbf{x}}(t_k^+)$ is the post-measurement update state estimate at time $t_k$, $\hat{\mathbf{x}}(t_{k+1}^-)$ is the propagated (pre-measurement) state estimate at time $t_{k+1}$, $\mathbf{P}(t_k^+)$ is the post measurement filter covariance, and $\mathbf{P}(t_{k+1}^-)$ is the propagated filter covariance.

With the state estimates propagated, the next step combines the measurement data, when it is available, with the propagated state estimate. This is done using

$$\mathbf{K}(t_k) = \mathbf{P}(t_k^-)\mathbf{H^T}(t_k)[\mathbf{H}(t_k)\mathbf{P}(t_k^-)\mathbf{H^T}(t_k) + \mathbf{R}(t_k)]^{-1} \tag{2.37}$$

$$\hat{\mathbf{x}}(t_k^+) = \hat{\mathbf{x}}(t_k^-) + \mathbf{K}(t_k)[\mathbf{z}(t_k) - \mathbf{H}(t_k)\hat{\mathbf{x}}(t_k^-)] \tag{2.38}$$

$$\mathbf{P}(t_k^+) = \mathbf{P}(t_k^-) - \mathbf{K}(t_k)\mathbf{H}(t_k)\mathbf{P}(t_k^-) \tag{2.39}$$

where the matrix $\mathbf{K}(t_k)$ is the Kalman gain.

*2.6.2 Nonlinear estimation.* Many systems cannot be described by linear stochastic models and require an extension to the model of the linear Kalman filter for use in nonlinear filtering. The nonlinear system model is defined as the following stochastic differential equation driven by white Gaussian noise:

$$\dot{\mathbf{x}}(\mathbf{t}) = \mathbf{f}[\mathbf{x}(t), \mathbf{u}(t), t] + \mathbf{G}(t)\mathbf{w}(t) \tag{2.40}$$

The noise corrupted discrete measurements are modeled as

$$\mathbf{z}(t_k) = \mathbf{h}[\mathbf{x}(t_k), t_k] + \mathbf{v}(t_k) \tag{2.41}$$

The full derivation as well as applications such as the extended Kalman filter can be found in [33].

## 2.7 Particle filtering

Unlike a linear Kalman filter, a particle filter addresses the problem of non-linearities through propagation of the non-Gaussian probability density function (PDF). As Arulampalam [3] states, "it is a technique for implementing a recursive Bayesian filter by Monte-Carlo simulations." The particle filter contains similar components to a Kalman filter such as the overall system model as well as propagation and update cycles. This section develops a generalized particle filter.

*2.7.1 Particles.* The particle filter method maps PDFs of interest to a collection of discrete, weighted particles [46]. Arulampalam [3] provided a guide for several possible filters, including the grid-based filter and development of the particle filter. Additionally, Rekleitis [40] offered a tutorial on the overall particle filter as well as choices in resampling methods.

Each particle in the particle filter represents an individual state estimate $\mathbf{x}_k$ at time $k$, independent of the other particles. The state estimate $\mathbf{x}_k$ is represented as

a vector since the state estimate often contains several values and has size $NS$. For example, a three dimensional navigation state estimate normally includes nine states representing position, velocity, and acceleration in each axis $(NS{=}9)$ . $\mathbf{X}$ represents the collection of particles such that

$$\mathbf{X} = \left[ \begin{array}{cccc} \mathbf{x_1} & \mathbf{x_2} & \ldots & \mathbf{x}_{NP} \end{array} \right]^{\mathbf{T}} \qquad NP = \text{number of particles} \qquad (2.42)$$

with corresponding weights

$$\mathbf{W} = \left[ \begin{array}{cccc} w_1 & w_2 & \ldots & w_{NP} \end{array} \right]^{\mathbf{T}} \qquad NP = \text{number of particles} \qquad (2.43)$$

and

$$\sum_{i=1}^{NP} w_i = 1 \qquad (2.44)$$

such that a single particle $(\mathbf{x_i})$ with corresponding weight $(w_i)$ represents a discrete sample of the PDF [3]. The collection of particles and weights now represent the entire discrete PDF. Now the entire state estimate and underlying PDF can be expressed in terms of the collection of particles $\mathbf{X}(t_k)$ and the corresponding weights $\mathbf{W}(t_k)$ at time $t_k$. Initial weights are constructed such that the initial prior PDF is simply 1/NP for all values of $\mathbf{W}(t_0)$ which conveys a flat PDF that sums to one. The initial particles for $\mathbf{X}(t_0)$ are based on the estimate of the states at initialization. However, if the process is well known at initialization, the particles and weights can be initialized to accurately represent the PDF.

It is also useful to define a few statistics which will be used throughout the particle filter. The weighted mean of the particles at time $t_k$ can now be expressed as

$$\bar{\mathbf{X}}(t_k) = E[\mathbf{X}(t_k)] = \sum_{i=1}^{NP} w_i(t_k)\mathbf{x}_i(t_k) \qquad \text{at time } t_k \qquad (2.45)$$

38

and the weighted covariance is

$$\mathbf{P}(t_k) = E\left[(\mathbf{x}_i(t_k) - \bar{\mathbf{X}}(t_k))(\mathbf{x}_i(t_k) - \bar{\mathbf{X}}(t_k))^{\mathbf{T}}\right] \tag{2.46}$$

$$= \sum_{i=1}^{NP} w_i(t_k)\left[\mathbf{x}_i(t_k) - \bar{\mathbf{X}}(t_k)\right]\left[\mathbf{x}_i(t_k) - \bar{\mathbf{X}}(t_k)\right]^{\mathbf{T}}$$

Additionally, Bayes' rule is defined as

$$P\left[B|A\right] = \frac{P\left[A \cap B\right]}{P\left[A\right]} = P\left[B|A\right] = \frac{P\left[A|B\right]P\left[B\right]}{P\left[A\right]}. \tag{2.47}$$

where $P[A|B]$ is the probability of $A$ given all values of $B$.

The goal of the particle filter is to estimate the posterior PDF based on the prior PDF, likelihood, and the evidence. The algorithm is

$$p\left(\mathbf{x}(t_{k-1})|\mathbf{Z}(t_{k-1})\right) \stackrel{propagation}{\rightarrow} p\left(\mathbf{x}(t_k)|\mathbf{Z}(t_{k-1})\right) \stackrel{update}{\rightarrow} p\left(\mathbf{x}(t_k)|\mathbf{Z}(t_k)\right)$$

where $p\left(\mathbf{x}(t_{k-1})|\mathbf{Z}(t_{k-1})\right)$ represents the PDF of the previous estimate conditioned on the measurement history, $p\left(\mathbf{x}(t_k)|\mathbf{Z}(t_{k-1})\right)$ is the prior PDF of the current esti-mate after propagation, and $p\left(\mathbf{x}(t_k)|\mathbf{Z}(t_k)\right)$ is the posterior PDF after the update is applied. The posterior PDF is found by

$$p\left(\mathbf{x}(t_k)|\mathbf{Z}(t_k)\right) = \frac{\overbrace{p\left(\mathbf{z}(t_k)|\mathbf{x}(t_k)\right)}^{likelihood}\overbrace{p\left(\mathbf{x}(t_k)|\mathbf{Z}(t_{k-1})\right)}^{prior}}{\underbrace{p\left(\mathbf{z}(t_k)|\mathbf{Z}(t_{k-1})\right)}_{evidence}} \tag{2.48}$$

which is composed of the likelihood $p\left(\mathbf{z}(t_k)|\mathbf{x}(t_k)\right)$, the prior PDF $p\left(\mathbf{x}(t_k)|\mathbf{Z}(t_{k-1})\right)$, and the evidence $p\left(\mathbf{z}(t_k)|\mathbf{Z}(t_{k-1})\right)$. To obtain the prior PDF, propagation must occur via the dynamics model.

*2.7.1.1 Propagation.* The previous state estimate $\mathbf{x}^+(t_{k-1})$ is propa-gated forward based on a dynamics model to generate $\mathbf{x}^-(t_k)$. The superscript "$-$"

indicates the propagated estimate prior to a measurement being received and an update applied. Now the collection of independently propagated state estimates $\mathbf{x}_i^-(t_k)$ at time $t_k$ form the propagated particle filter estimate $\mathbf{X}^-(t_k)$. $\mathbf{W}^-(t_k)$ has not changed yet. $\bar{\mathbf{X}}^-(t_k)$ and $\mathbf{P}^-(t_k)$ can now be calculated using Equations 2.45-2.46.

*2.7.1.2  Likelihood.*    The likelihood function provides how well the incoming measurement $\mathbf{z}(t_k)$ correlates to the estimated measurement based on each $\mathbf{h}[\mathbf{x}_i^-(t_k)]$ in $\mathbf{X}^-(t_k)$. The generalized multivariate Gaussian likelihood function from Maybeck [33] is

$$L\left(\mathbf{x}_i^-(t_k)|\mathbf{z}(t_k),\mathbf{P}^-(t_k)\right) = \beta \exp\left\{-\frac{1}{2}\left[\mathbf{z}(t_k) - \hat{\mathbf{z}}_i(t_k)\right]\mathbf{P}^-(t_k)^{-1}\left[\mathbf{z}(t_k) - \hat{\mathbf{z}}_i(t_k)\right]^{\mathbf{T}}\right\}$$

$$(2.49)$$

where

$$\beta = \frac{1}{\sqrt{(2\pi)^N\,|\mathbf{P}^-(t_k)|}} \tag{2.50}$$

$$i = 1, 2...NP$$

$$\sigma = \text{measurement parameter noise characteristics}$$

$$\mathbf{P}^-(t_k) = \text{measurement covariance matrix}$$

$$N = \text{number of measurements contained in } \mathbf{z}(t_k)$$

$$\hat{\mathbf{z}}_i = \mathbf{h}[\mathbf{x}_i^-(t_k)]$$

and provides a scalar likelihood value for each $\mathbf{x}_i^-(t_k)$ in $\mathbf{X}^-(t_k)$. If the measurement variance is the same in each axis and the measurements are independent, the equation is reduced to

$$L\left(\mathbf{x}_i^-(t_k)|\mathbf{z}(t_k),\sigma_z^2\right) = \beta \exp\left\{-\frac{1}{2\sigma_z^2}\left[\mathbf{z}(t_k) - \hat{\mathbf{z}}_i(t_k)\right]\left[\mathbf{z}(t_k) - \hat{\mathbf{z}}_i(t_k)\right]^{\mathbf{T}}\right\} \qquad (2.51)$$

where

$$\beta = \frac{1}{\sqrt{(2\pi\sigma_z^2)^N}} \tag{2.52}$$

$$\sigma_z^2 = \text{measurement noise variance}$$

The $\beta$ term outside the exponential represents a scaling factor conditioned on $\sigma_{\mathbf{z}}$, which can lead to a condition known as $\beta$ dominance if all the likelihoods are approximately equal [12]. The information contained in the likelihood function lies in the measurement residual $[\mathbf{z}(t_k) - \hat{\mathbf{z}}_i(t_k)]$. The incoming measurements $\mathbf{z}(t_k)$ provide the most recent measurement available, while $\mathbf{h}[\mathbf{x}_i^-(t_k)]$ is the estimated measurement based on the propagated state estimate $\mathbf{x}_i^-(t_k)$ and the function $\mathbf{h}$ based on the measurement model (i.e., the relationship between the measurements and the states). With the likelihood and prior PDF knowledge, the evidence serves as a normalizing factor such that the posterior PDF will sum to one.

    *2.7.1.3 Posterior PDF.* In the particle filter, creating the posterior PDF starts by combining $\mathbf{W}^-(t_k)$ with the likelihood from Equation 2.51 via Bayes rule. This information now represents the fusion of the independently propagated state estimates for each particle $\mathbf{x}^-(t_k)$ with the likelihood based on the most recent measurement. In order for this information to represent the posterior PDF, the $\beta$ term outside the exponential from the likelihood function in Equation 2.51 and the evidence from Equation 2.48 serve as normalizing constants and are not required

explicitly. Instead

$$\mathbf{W}^+(t_k) = [\ w_1^+ \quad w_2^+ \quad \ldots \quad w_{NP}^+ \ ]^T \tag{2.53}$$

$$w_i^+(t_k) = \frac{L(\mathbf{x}_i^-(t_k)|\mathbf{z}(t_k), \sigma_z^2)w_i^-(t_k)}{\sum_{i=1}^{NP}\left(L(\mathbf{x}_i^-(t_k))w_i^-(t_k)\right)}$$

$$\sum_{i=1}^{NP} w_i^+(t_k) = 1$$

such that the normalizing constants are equivalent to the sum of the likelihood and prior PDF to cause the new particle weights $\mathbf{W}^+(t_k)$ to sum to one. With the posterior PDF calculated, the state and covariance estimates can be updated after particle resampling occurs.

*2.7.1.4 Particle resampling.* In the particle filter, a condition known as particle starvation can occur when the preponderance of particles possess near zero weight and only a few particles contain the bulk of the probability. This can reduce accuracy and even cause filter instability. To overcome this problem, particle resampling eliminates particles with low likelihood and increases the number of particles in high likelihood areas without changing the PDF. This is completed via sequential importance resampling. Particles with the greatest weight, above some threshold, are kept while the rest are eliminated. The resulting particles still represent the underlying PDF, and the weights become constant values of $1/NP$ [40].

*2.7.1.5 Update.* $\bar{\mathbf{X}}^+(t_k)$ and $\mathbf{P}^+(t_k)$ can now be calculated using Equations 2.45-2.46. These values are provided as the output of the particle filter and serve as the estimated states for comparison with a meaningful reference.

*2.8 Summary*

This chapter outlines the background theory required to conduct research in magnetic field navigation. The investigation of the error sources and stability of

the Earth's magnetic field convey the utility of the measurements while highlighting potential pitfalls in measurement quality. The application of the calibration technique will allow comparison of measurements from different platforms. Finally, the particle filter provides an estimation method to begin using the measurements in a meaningful fashion.

## III. A Modified Ellipsoid Calibration for Strapdown Three-Axis Magnetometers

IN order to consider magnetic field information as a potential source for navigation in multiple platforms, the measurements must be repeatable with respect to position. Effective calibration of the magnetometer mounted in the platform allows comparison with respect to position, and ultimately insight for the estimated measurement noise variance $\sigma_\mathbf{z}$. While several calibration methods were outlined in Section 2.4, most did not correctly calibrate the measurements in each axis. Those that did correctly calibrate the measurements in each axis required rotation about multiple axes. Therefore a new calibration method was developed for large vehicles limited to rotation about a single axis.

Recalling Equations 2.23- 2.27 for the two-dimensional case spotlight the scale-factor and distortion correction matrix $\mathbf{A_h}$ and biases $\mathbf{b_h}$ for the horizontal axes, as long as the measurement observations only include components from the horizontal axes. If a strict ellipse implementation were the goal, the method would stop here. However, small misalignments and non-horizontal sensor orientation during collection will map the vertical component of the magnetic field into the horizontal measurements. Without tilt angle sensors or inertial measurement unit data, these factors often remain unresolved. Therefore $\mathbf{A_h}$ contains the relationship for the two-dimensional scale-factors and distortions, but does not account for the vertical component $B_z$ included in the measurements due to tilt and/or misalignment. The next section describes how the modified ellipsoid method accounts for this mapping.

### 3.1 Modified ellipsoid method

Since existing 2D or 3D calibration methods do not fit the problem of a strapdown magnetometer in a large vehicle, a new method was sought to provide the best calibration possible. Utilizing the information from the strict ellipse derivation, a

modification accounts for the $z$ component mapping into the $x - y$ plane. If the $B_z$ component is present in the horizontal axes, the two-dimensional $\mathbf{A_h}$ can be scaled and combined with $sf_z$ to create the full three-dimensional $\mathbf{A}$ correction matrix using the approach described below.

Applying $\mathbf{A_h}$ and $\mathbf{b_h}$ to the measurement observations yields

$$\left\|\tilde{\mathbf{B}}_\mathbf{h}\right\|^2 = \left\|\mathbf{A_h}(\hat{\mathbf{B}}_\mathbf{h} - \mathbf{b_h})\right\|^2 \tag{3.1}$$

where $\left\|\tilde{\mathbf{B}}_\mathbf{h}\right\|$ represents the horizontal magnitude of the measurement observations after applying $\mathbf{A_h}$ and $\mathbf{b_h}$, but $\left\|\tilde{\mathbf{B}}_\mathbf{h}\right\| \neq \|\mathbf{B_h}\|$ if any portion of $\hat{B}_z$ is present in the $\hat{B}_x$ and $\hat{B}_y$ measurement observations. To obtain $\left\|\tilde{\mathbf{B}}_\mathbf{h}\right\| = \|\mathbf{B_h}\|$, the scaling term $\alpha$ must be calculated where

$$\alpha = \frac{\|\mathbf{B_h}\|^2}{\left\|\tilde{\mathbf{B}}_\mathbf{h}\right\|^2} \tag{3.2}$$

While it is easily discernible that $\alpha$ is a scalar, it must also be a constant, for the reasons described in the following. The measurements associated with the Earth's magnetic field were defined to be a sphere with radius $\|\mathbf{B}\|$ and origin at the position on the Earth the measurements were taken. The resulting sphere equation is

$$\|\mathbf{B}\|^2 = B_x^2 + B_y^2 + B_z^2 \ \forall \ B_x, B_y, B_z \in \mathbb{R} \tag{3.3}$$

and strictly adheres to the relationship of the magnetic field measurements defined by the models used for the IGRF and WMM. Since $\mathbf{B_h}$ represents only the horizontal components of this sphere, the horizontal measurements form a circle whereby

$$\|\mathbf{B_h}\|^2 = B_x^2 + B_y^2 \ \forall \ B_x, B_y \in \mathbb{R} \tag{3.4}$$

From Equation (3.1), $\tilde{\mathbf{B}}_\mathbf{h}$ also represents a circle since the original elliptical measurement observations were transformed to a circle centered at the origin via the

correction matrix $\mathbf{A_h}$ and bias $\mathbf{b_h}$. Now $\mathbf{B_h}$ and $\tilde{\mathbf{B}}_\mathbf{h}$ represent two circles of different sizes centered at the same origin. Any two circles centered at the same origin differ only by a constant scaling factor, which in this case is defined as $\alpha$.

Now the full 3x3 correction matrix $\mathbf{A}$ and the 3x1 bias matrix $\mathbf{b}$ can be formed by applying $\alpha$ to $\mathbf{A_h}$ to preserve the relationship identified during the strict two-dimensional ellipse method, but properly scaled such that $\left\|\tilde{\mathbf{B}}_\mathbf{h}\right\|=\|\mathbf{B_h}\|$ for corrected measurements. The resulting matrix contains scale-factor and distortion corrections for the horizontal axes, but only a scale-factor correction for the vertical axis, shown as

$$\mathbf{A}_\alpha = \begin{bmatrix} \alpha\mathbf{A_h} & \vdots & 0 \\ \dots & \dots & \dots \\ 0 & \vdots & sf_z \end{bmatrix} \tag{3.5}$$

$$\mathbf{b} = [b_x \ b_y \ b_z]^\mathbf{T} \tag{3.6}$$

where $b_z$ and $sf_z$ are calculated as in Equations (2.12) and (2.13) respectively. The modified ellipsoid equations are

$$\mathbf{B_{h}}_{calibrated} = \alpha\mathbf{A_h}(\hat{\mathbf{B}}_\mathbf{h} - \mathbf{b_h}) \tag{3.7}$$

$$\mathbf{B}_{calibrated} = \mathbf{A}_\alpha(\hat{\mathbf{B}} - \mathbf{b}) \tag{3.8}$$

where $\mathbf{B_{h}}_{calibrated}$ represents the $N$x2 calibrated measurement observations in the horizontal axes and $\|\mathbf{B_{h}}_{calibrated}\| = \|\mathbf{B_h}\|$. $\mathbf{B}_{calibrated}$ represents the resulting $N$x3 calibrated measurement observations and $\|\mathbf{B}_{calibrated}\| \approx \|\mathbf{B}\|$. Due to the lack of observability in the $z$ axis, $\|\mathbf{B}_{calibrated}\|$ is approximately the value of $\|\mathbf{B}\|$, but contains any unresolved errors relating to the $z$ axis.

Equation 3.8 delivers properly calibrated measurements in each axis, as will be shown in the forthcoming results. Significant improvement in the horizontal axes is due to the inclusion of the distortion terms. Although the improvement in the vertical

46

axis is not significant, the limitation of only rotating about the $z$ axis precludes using a full 3D calibration algorithm. Under these conditions, the calibration of the $z$ axis measurements is the best available.

## 3.2  Results

This section describes results of applying the modified ellipsoid method to both simulated and real data. A 1000 run Monte-Carlo analysis was conducted using simulated data to determine performance of the modified ellipsoid calibration method. The strict ellipse method is not commonly used in practice, but is shown to highlight the need for the scaling parameter $\alpha$. The simulated measurements were reflective of a two-dimensional collection platform such as a vehicle collecting the measurements while driving in a circular pattern for three revolutions (a widely practiced technique). To corroborate the findings in simulation, the same calibration procedure was performed with real data from three different vehicles to verify the modified ellipsoid method under normal conditions. The results from using both simulated and real data with the modified ellipsoid method were compared with the uncalibrated measurements and a swinging method based on [10]. The swinging method results utilized knowledge of the Earth's magnetic field and calculated biases using Equations (2.10) and (2.12) and scale-factors from Equation (2.13). Since the vehicle only rotated about the vertical axis, magnetometer measurements could not sufficiently describe an ellipsoid to yield a solution from a 3D algorithm.

*3.2.1  Simulation Results.*  For the simulation, the parameters that were varied included the scale-factors, biases, distortions, and noise. Measurement noise was modeled as additive white-Gaussian noise with a standard deviation of 2 milli-Gauss (mG), representative of the noise for a Honeywell HMR2300 magneto-resistive sensor in the presence of Earth's magnetic field in a vehicle platform. The Earth's magnetic field $\mathbf{B} = [B_x\ B_y\ B_z] = [200\ -21\ 493]$ in milliGauss (mG) was representative of the area near AFIT, although values from any location could have

been used. Figure 3.1 depicts an example result highlighting the comparison of uncalibrated measurements, calibration using the swinging method, a strict ellipse calibration, and calibrated measurements using the modified ellipsoid method.

The simulated truth was generated by projecting the 3D magnetic field of the Earth onto the horizontal plane. This created a vector of $\mathbf{B}_x$ and $\mathbf{B}_y$ simulated measurements with magnitude $\|\mathbf{B_h}\|$. When plotted, the simulated truth depicts a circle with radius $\|\mathbf{B_h}\|$. The uncalibrated measurements reflect the scale-factor and distortions creating the ellipse in Figure 3.1. The distance from the center of the ellipse to the origin (0,0) represents the biases, and the small perturbations about the edges are reflective of the sensor noise. Using the swinging method the biases are easily resolved, and the scale-factors well estimated. However, the inability to estimate the distortions results in no correction of the ellipse shape. Conversely, the strictly two-dimensional ellipse method corrects for the shape of the ellipsoid, but improperly estimates the scale-factors and distortions. The addition of the scaling term $\alpha$ from the modified ellipsoid method corrects the scale-factor and distortion terms for the best estimate in the horizontal plane. This effect on the measurements is highlighted in Figures 3.2 - 3.5.

In Figure 3.2 the horizontal magnitude $\|\mathbf{B_h}\|$ shows that the scale-factors and biases are clearly resolved, especially when compared to the uncalibrated or swinging calibrated measurements.The calibrated measurements do not form a perfect match with the simulated truth due to noise. The strict ellipse calibration was not shown in the remaining simulation results since the method is not used in practice and only shown in Figure 3.1 to highlight the effectiveness of the $\alpha$ parameter. After examining the horizontal axis, checking the overall magnitude $\|\mathbf{B}\|$ is in order.

Figure 3.3 shows the calibration effect on the overall magnetic field magnitude $\|\mathbf{B}\|$ is improved, but not nearly as well as the horizontal case from Figure 3.2. This is a direct result of the inability to resolve the errors in the $z$ axis, which becomes the dominant error in the overall magnitude. The modified ellipsoid calibration
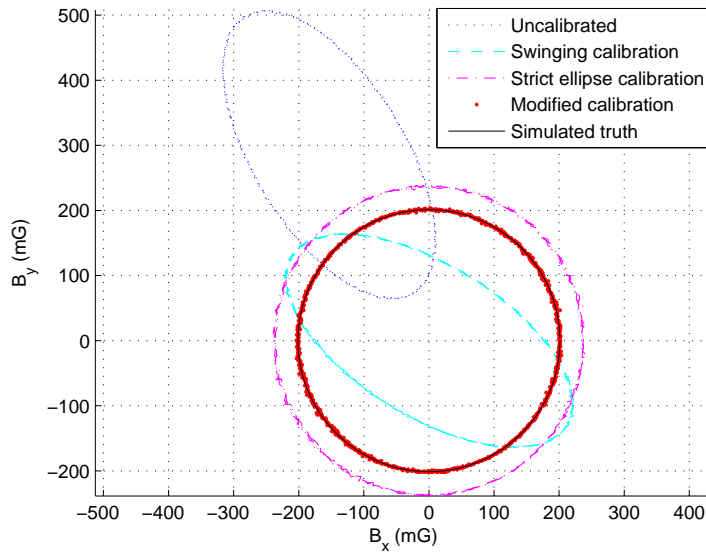
Figure 3.1: Single run sample comparison of simulated measurements in two dimensions. Note the weakness of a strictly two-dimensional ellipse method.
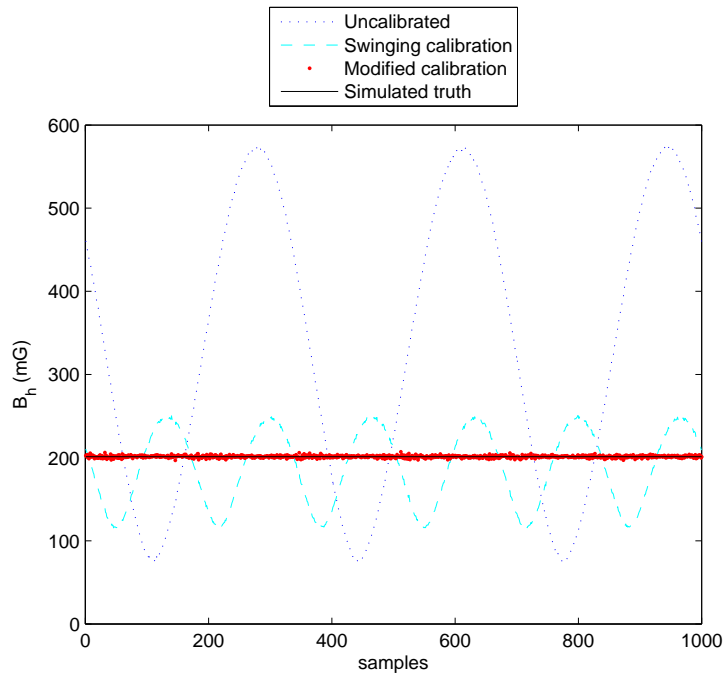


Figure 3.2: Sample comparison of the horizontal magnitude $\|\mathbf{B_h}\|$ of simulated measurements.
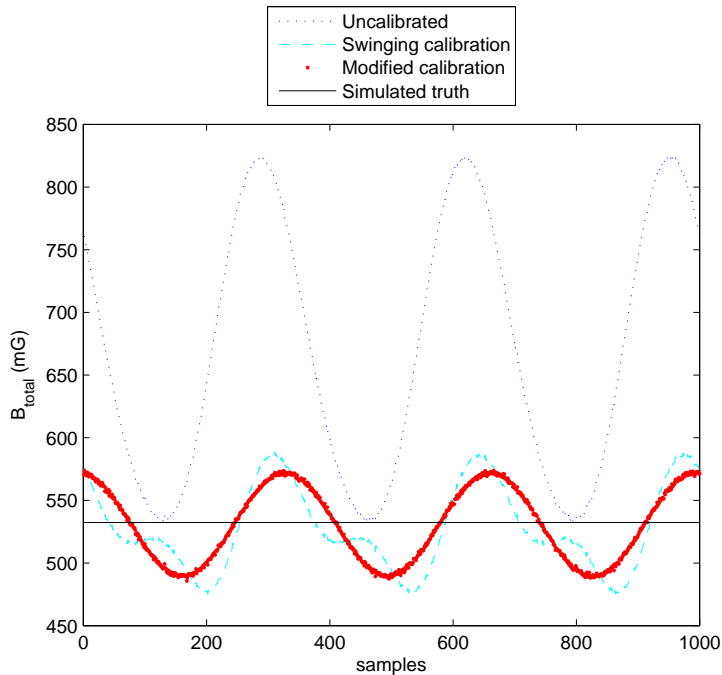
Figure 3.3:    Sample comparison of the 3D magnitude $\|\mathbf{B}\|$ of simulated measurements.

retains the relationship of the measurements, while the swinging method skews the magnitude. This is a result of determining the bias and scale-factors in each axis without regard to the effects in another axis. Also, the lack of distortion terms does not allow a full transformation in all three axes. Investigating the individual axes $B_x$, $B_y$, and $B_z$ yields additional gains.

Studying Figure 3.4 underscores the improved quality in each axis. The $B_x$ and $B_y$ measurements show good agreement between calibrated measurements and the simulated truth. For applications such as two-dimensional magnetic fingerprinting, calibration of the individual $B_x$ and $B_y$ measurements is crucial [24]. Conversely, the $B_z$ measurements show that there was no difference in performance for the calibration methods, as expected.

50
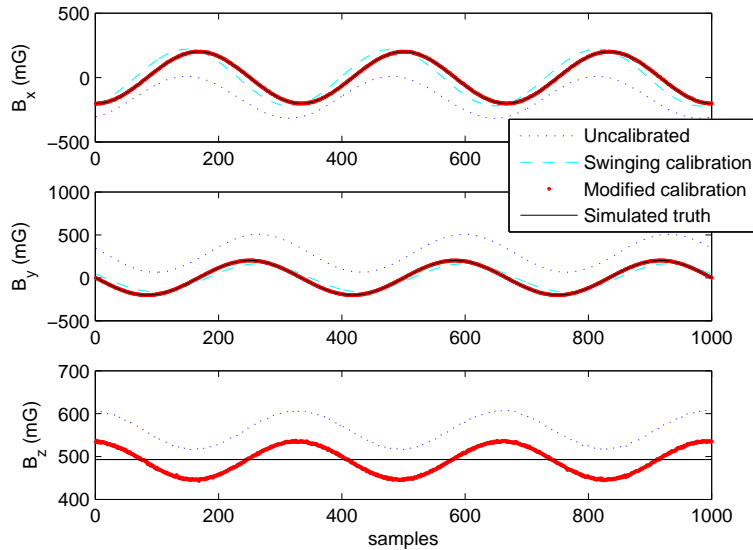
Figure 3.4:    Sample comparison of simulated measurements in each axis $B_x$, $B_y$, and $B_z$.

Many applications of magnetometers involve calculation of heading. Figure 3.5 shows a sample heading comparison as the simulated truth completes three revolutions of a circle, beginning at 180 degrees and going through the transition from 359 degrees to 0 degrees. The headings were calculated using Equation 2.11. The improvement in heading versus both the uncalibrated and swinging calibrated measurements is discernible from the figure. In relation to the simulated truth, the modified ellipsoid calibration had a mean error of 0.0234 degrees with a standard deviation of 2.1145 degrees over the entire Monte-Carlo simulation.

3.2.1.1   *Mean errors from simulation.*    The Monte-Carlo simulation varied the following parameters: scale-factors, biases, distortions and noise. Measurement noise was modeled as additive white-Gaussian noise with a variance of 2 milliGauss (mG), representative of the noise for a magneto-resistive sensor in a vehicle platform.

Statistics for the biases, scale-factors, and distortions were calculated to compare each method with the true values used to generate the simulated measurements.

51
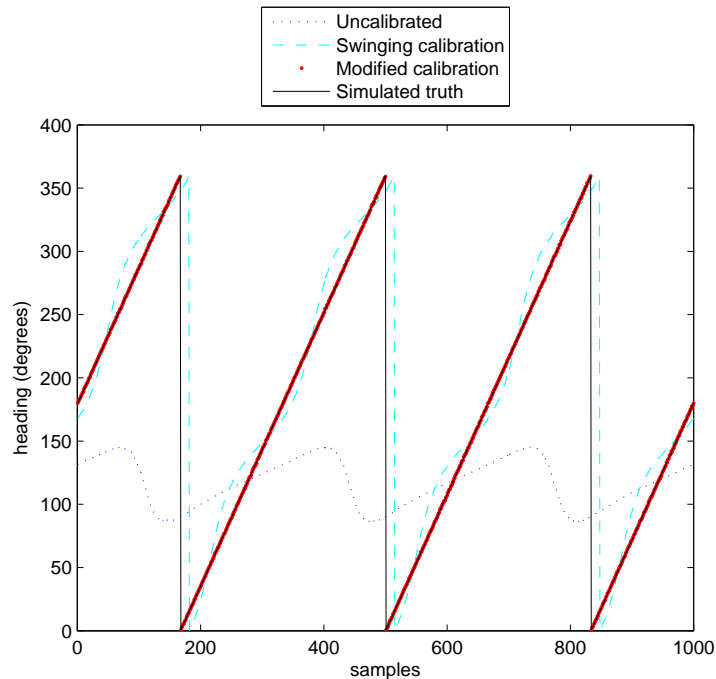
Figure 3.5:    Sample comparison of the heading of simulated measurements.

Table 3.1 shows the mean error results while Table 3.2 provides the error standard deviations. The swinging method provides excellent bias estimation and good scale-factor estimation. Since the bias is calculated directly and is only slightly affected by noise, the mean and standard deviation for the bias terms is extremely small. The strict ellipse method delivers good bias estimation, but the scale-factor errors are significantly higher. Finally, the modified ellipsoid method yields good bias information, and improved scale-factor and distortion over the other methods. The bias errors for the strict ellipse and modified ellipsoid method are the same since $\alpha$ does not affect the bias terms. Note that the $z$ axis is not included since the values were the same for all methods. Table 3.2 provides the error standard deviations to complement the mean error statistics. The standard deviation emphasizes the consistency in the error, and again shows that the modified ellipsoid method offers improvement over the swinging method.

52

Table 3.1:     Mean errors for entire Monte-Carlo simulation.

| Mean error | Swinging method | Strict ellipse method | Modified ellipsoid method |
|---|---|---|---|
| $x$ scale-factor | -0.0771 | 0.3929 | 0.0139 |
| $y$ scale-factor | -0.0761 | 0.3890 | 0.0137 |
| $xy$ distortion | N/A | 0.0278 | -0.0106 |
| $x$ bias | 0.0000 | 0.0863 | 0.0863 |
| $y$ bias | 0.0000 | 0.1682 | 0.1682 |

Table 3.2:     Error standard deviations for entire Monte-Carlo simulation.

| Error 1-$\sigma$ | Swinging method | Strict ellipse method | Modified ellipsoid method |
|---|---|---|---|
| $x$ scale-factor | 0.0276 | 0.7357 | 0.0243 |
| $y$ scale-factor | 0.0275 | 0.7221 | 0.0241 |
| $xy$ distortion | N/A | 0.0660 | 0.0285 |
| $x$ bias | 0.0000 | 3.6898 | 3.6898 |
| $y$ bias | 0.0000 | 4.1115 | 4.1115 |

*3.2.1.2   Simulated extreme noise, bias, scale-factor, and distortion.*
While the Monte-Carlo simulation provided results for typical data for a given area, the true test of an algorithm is under extreme conditions. Figures 3.6 - 3.7 depict sample results when the parameters of variation are increased to levels higher than a typical magnetometer would report in most conditions.

The uncalibrated measurements suffer from severe bias, scale-factor, distortion, and noise. Although the swinging method does a good job of resolving the bias, it cannot overcome the large distortions and scale-factors. The modified ellipsoid method however resolves all of the errors with the exception of noise. Although the noise is dampened, it will continue to be the dominant error source in the calibration. Even under these extreme conditions, the heading (calculated via Equation 2.11) improvement seen in Figure 3.7 is easily discernible. For the uncalibrated measurements the heading is essentially unusable. The swinging method also suffers significantly and would disrupt most dead reckoning navigation efforts. Yet the modified ellipsoid method continues to perform well despite the adverse conditions.
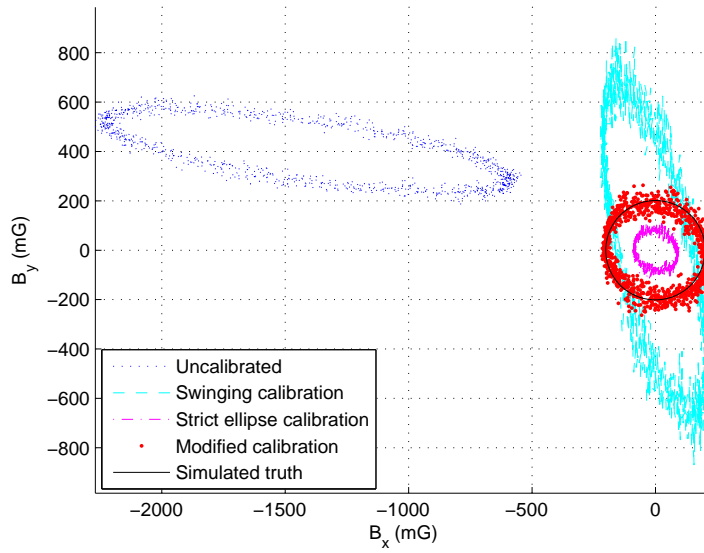
Figure 3.6:    Sample calibration comparison of simulated measurements when variation parameters are taken to the extreme.
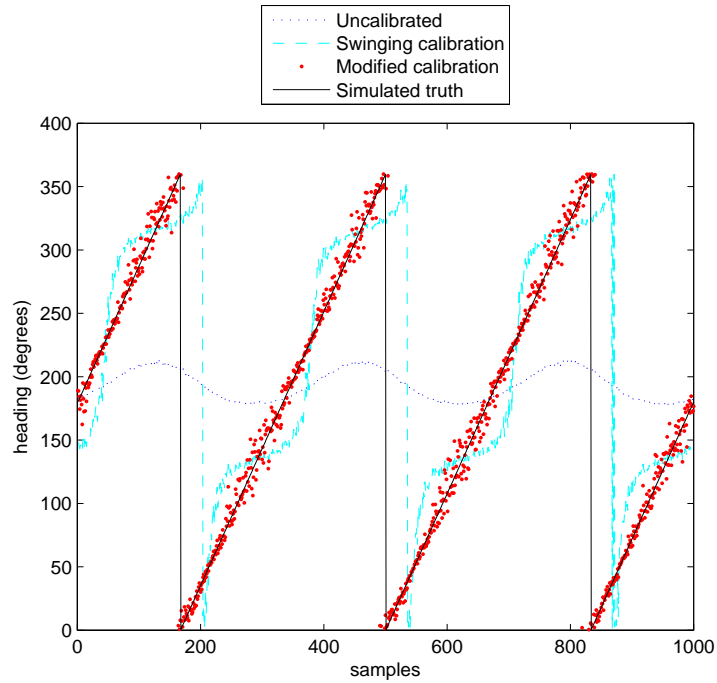


Figure 3.7:    Sample heading comparison of simulated measurements when variation parameters are taken to the extreme.

These simulation results show that the proposed modified ellipsoid method works well in a simulation environment. The next section will show results when using real measurements.

*3.2.2  Real Data Results.*    A 2004 Chevrolet Avalanche truck, a 2003 Pontiac Aztek sports utility vehicle (SUV), and a 2005 Nissan Altima car were chosen as typical vehicles. Each platform represented a different vehicle type in order to demonstrate portability of the calibrated measurements. A Honeywell HMR2300 magnetometer was mounted in each vehicle on a level surface and aligned with the body frame as much as possible [22]. Care was taken during placement to avoid known emitters of magnetic fields to mitigate electromagnetic interference (EMI). However, the magnetometer along with the Synchronized Position Attitude Navigation (SPAN) system was mounted inside the cargo or passenger areas of the vehicle with no special extensions to distance the magnetometer from the vehicle. Examples of installation are shown in Figures 3.8 and 3.9. Therefore EMI from the engine, turn indicators, and other sources was present under typical operating conditions.

The SPAN system consisting of a Novatel Global Positioning System (GPS) receiver integrated with a Honeywell HG1700 inertial navigation system (IMU) collects position, heading, roll, tilt, and pitch information [39].

Calibration data was collected at 50 Hertz in a level parking lot with a surface similar to local roadways, as far as possible from buildings or other vehicles. No underground piping or structures were observable. Each vehicle began the calibration routine facing north and was driven in a tight counterclockwise circle. The counterclockwise direction was chosen to reduce the magnetometer observation radius as much as possible, since the magnetometer was mounted on the left side of the vehicle, as seen in Figure 3.8. The vehicle speed was nominally 5 miles/hour ($\approx$ 8 kilometers/hour) during each revolution. The SPAN information was used to illustrate the position and provide comparison data.
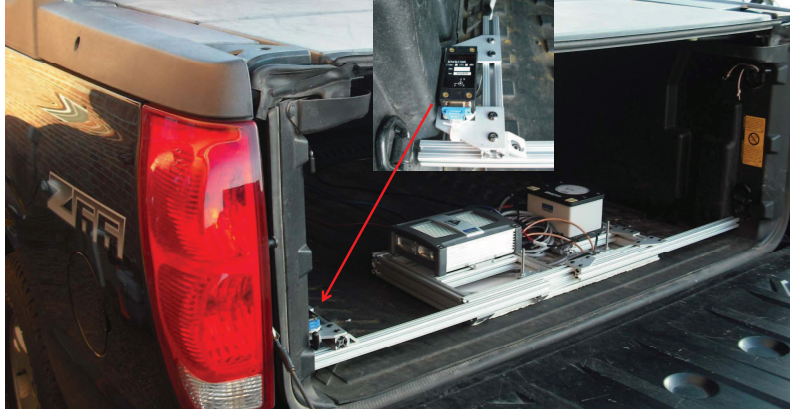
Figure 3.8: The HMR2300 magnetometer and SPAN mounted at the rear of the truck cargo compartment.
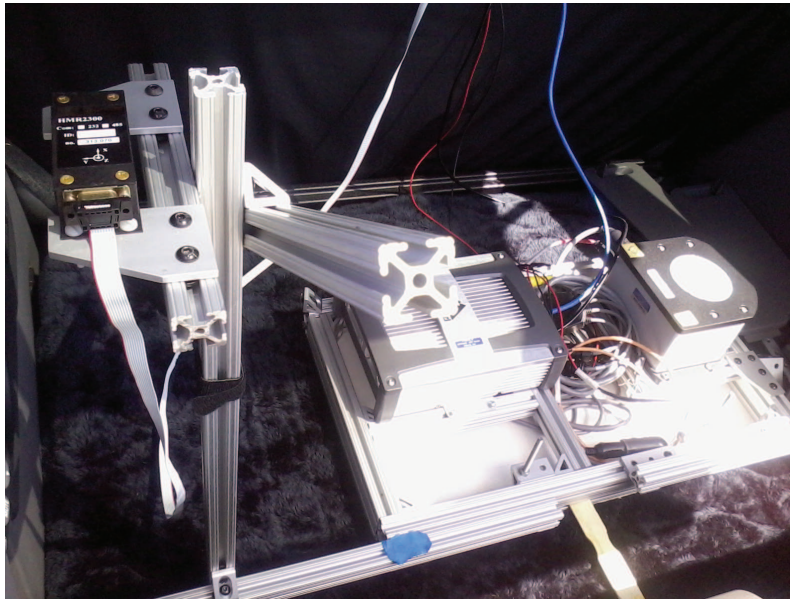


Figure 3.9: HMR2300 and SPAN mounted in the SUV cargo compartment. The HMR2300 was elevated to mitigate electromagnetic interference from the turn indicators.

*3.2.2.1  Calibration results for the horizontal axes.*     The uncalibrated and calibrated measurements of the truck are shown in Figure 3.10. The results are quite similar to those found in simulation. The main differences stem from the fact that the revolutions are not identical due to the slight variations of vehicle speed and tire slip. While the calibrated magnetometer measurements appear slightly noisier than in simulation, this is expected due to the unmodeled magnetic errors from the vehicle and the environment. The tight calibration in the horizontal axes promotes the utility and portability of magnetic field measurements across platforms and for applications other than heading.

The SUV calibration results in Figure 3.11 show much less elliptical shaping indicating less interference due to the vehicle. Since many of the installation issues
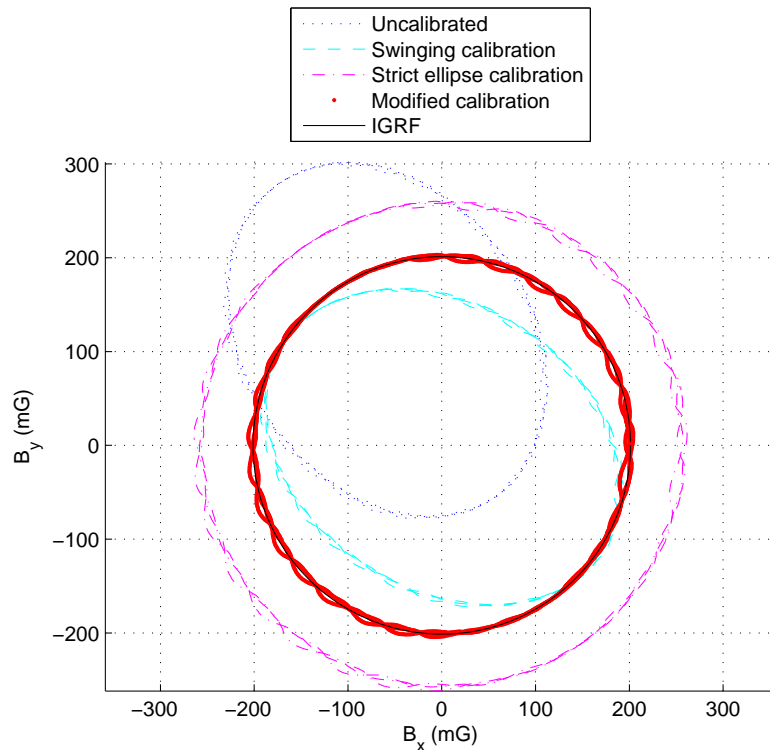


Figure 3.10:    Truck calibration collection measurements and calibrated results. The solid black line is the calculated truth based on the IGRF data for 11 Aug 2011.
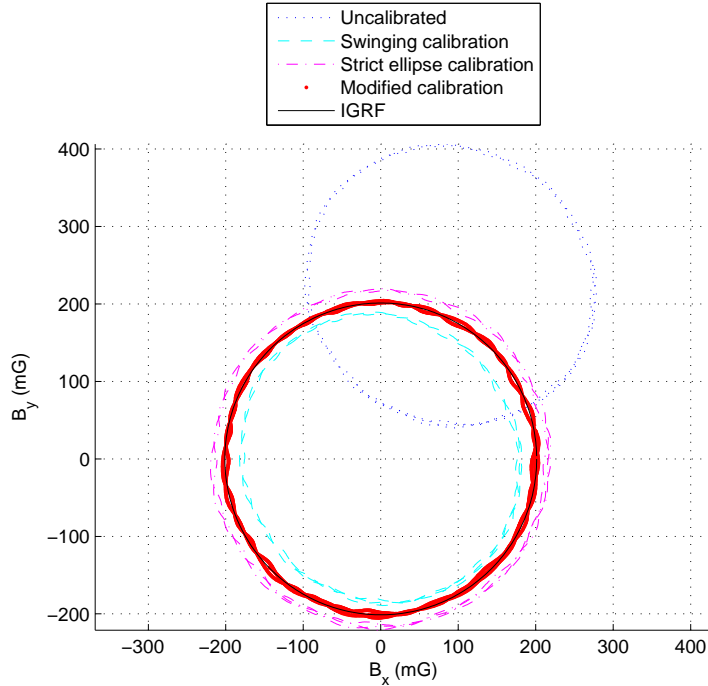
Figure 3.11:    SUV calibration collection measurements and calibrated results. The solid black line is the calculated truth based on the IGRF data for 16 Aug 2011.

were resolved during collection in the truck, this setup benefits from the experience previously gained. Additionally, the SUV environment is quite different, with more windows and less metal near the magnetometer. The modified ellipsoid method continues to calibrate the measurements in line with the IGRF model representation.

For the car, the magnetometer was placed in the rear passenger compartment along with the SPAN. Initial attempts for placement in the trunk proved futile due to the extremely high (60 mG) turn indicator interference. The rear seat of the passenger compartment proved adequate and yielded similar results to the SUV in terms of reduced scale-factor and distortion issues, shown in Figure 3.12.

*3.2.2.2   Calibration results pertaining to the horizontal magnitude.*
The horizontal magnitude $\|\mathbf{B_h}\|$ in Figure 3.13 allows a slightly different perspective
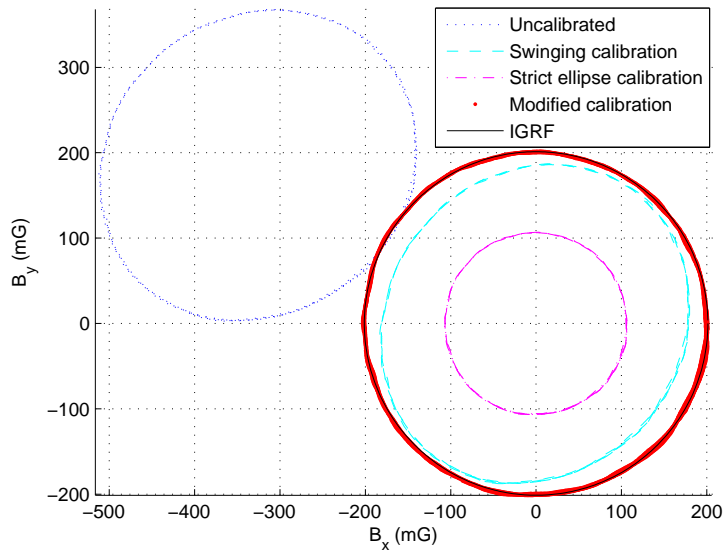
Figure 3.12: Car calibration collection measurements and calibrated results. The solid black line is the calculated truth based on the IGRF data for 15 Aug 2011.

of the results as presented in Figure 3.12. The comparison of the uncalibrated, the swinging calibration, and the modified ellipsoid calibration highlights the significance of the improvement. Although not shown, the SUV and car had nearly identical results.

3.2.3 *Calibration results pertaining to heading.* Figure 3.14 depicts the field derived magnetic heading of the truck compared with the SPAN heading while completing three revolutions of a circle. The magnetic headings were calculated using Equation 2.11 and then decreased by 5.93 degrees, the magnetic declination for AFIT. Although the swinging method does fairly well, the modified ellipsoid calibration method provided superior performance to the other methods. Again, the car and SUV heading yielded similar results.

3.2.4 *Comparison of calibrated measurements via position.* In order to compare calibrated magnetometer measurements from each vehicle under typical road conditions, all three vehicles were driven on roadways surrounding the AFIT
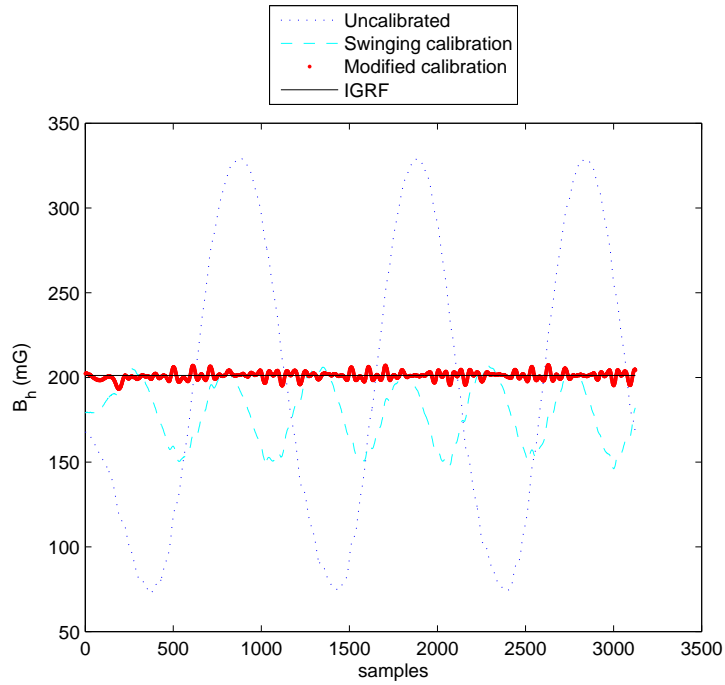
Figure 3.13:   Truck uncalibrated and calibrated measurements depicting the horizontal magnitude $\|\mathbf{B_h}\|$.
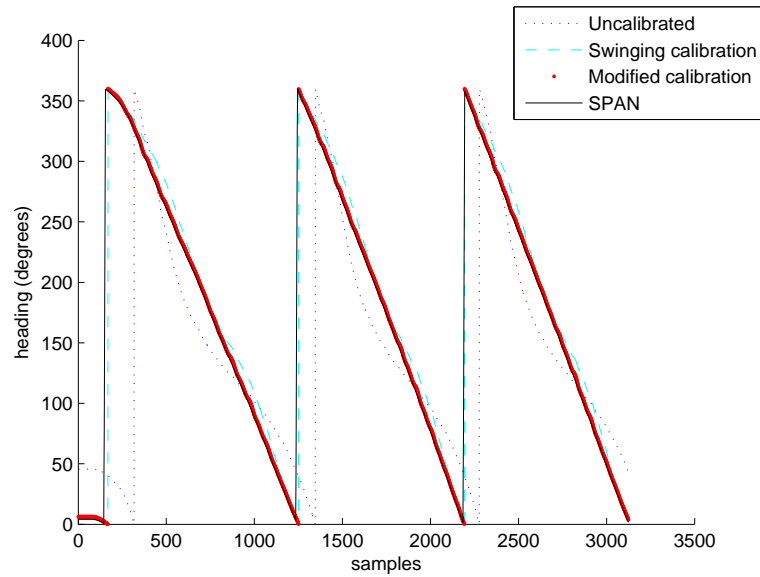


Figure 3.14:   Truck heading during calibration collection.

60

building. This allowed a relative comparison of the calibrated magnetometer measurements as a function of position. The segments used in this part of the analysis did not include the position used for calibration, which provided an opportunity to analyze performance in an environment different from where calibration occurred. Additionally, the true magnetic field is not known at any of the locations. While the IGRF provides the Earth's magnetic field values based on position, and even corrects past data based on magnetic field observatory information, the information is for the overall field and does not account for local disturbances. The perturbed magnetic field due to buildings, roadways, ferrous deposits in the Earth, etc. is what the magnetometer mounted in the vehicle observes.

Each vehicle was driven along a roadway to collect magnetic field measurements for comparison. Representative samples were chosen where the recorded SPAN positions of all three vehicles were as close as possible. This allowed a reasonable comparison while reducing the variability due to the position of the vehicle, which would in turn cause more variability in the magnetic field measurements. Figure 3.15 is a sample of the measurements as the vehicles were traveling south resulting in very little change in longitude, but change in latitude as expected. The measurements reflect the calibrated measurements at a particular latitude but shown simply as a function of distance in meters from the first measurement. The uncalibrated measurements were not shown since the scale required would impair discernment between the calibrated sets of measurements. The vehicles did not collect this data at the same time or day, and the path of each vehicle differs slightly (approximately one meter) due to normal driving variation. The sample data from each vehicle was calibrated by both the swinging method (dotted lines) and the modified ellipsoid method (solid lines). For the three vehicles, if the calibrations and SPAN positions were perfect, and the vehicles were in the exact same orientation when the magnetometer measurement was taken, then the calibrated measurements should be identical (other than noise). While not a perfect indicator, the extent to which the

61
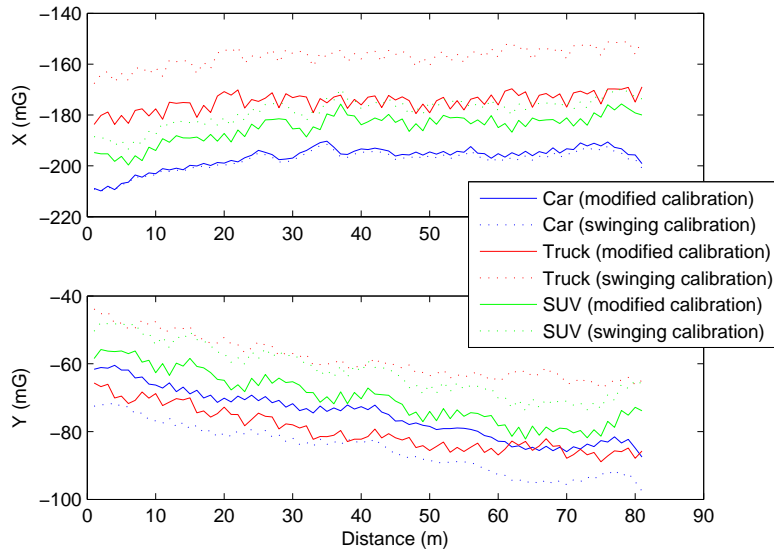
Figure 3.15: Comparison of road measurements from each vehicle based on distance in meters in the $x$ and $y$ axes. The dotted lines represent measurements calibrated using the swinging method. The solid lines depict the calibrated measurements using the modified ellipsoid method.

calibrated magnetometer measurements agree between vehicles is a good indication of the quality of the calibration.

Focusing on the measurements calibrated with the modified ellipsoid method (solid lines), the measurements along these positions are all within approximately 25mG for the $x$ axis, as opposed to 40mG using the swinging method (dotted lines). Similarly, in the $y$ axis measurements calibrated using the modified ellipsoid method fall within 11mG, as opposed to 30mG for the swinging method. The ability of the modified ellipsoid method to improve the calibration of magnetic field measurements under these conditions highlights the utility when considering multiple platforms of differing types.

While Figure 3.15 provides a sample of the improved performance for one particular section, the same analysis was performed on several sections of roadway to provide an indication of overall performance. Four sections of roadway were chosen where the SPAN positions were similar, as seen in Figure 3.16. These sections
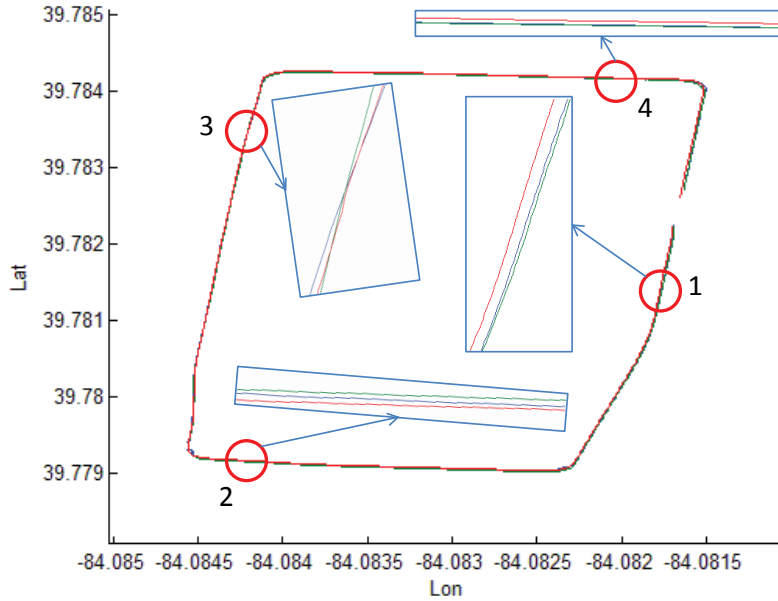
Figure 3.16:    Entire clockwise position track with the four sample sections high-lighted.

were chosen due to the consistency of position over the multiple runs to reduce the variability in the magnetometer measurements due to variation in the position of the vehicle.

Table 3.3 shows the average spread (maximum minus minimum value, averaged over time) over the four sample sections of road where the SPAN positions were similar. For each calibration method, the value of the magnetic field in each axis at a particular position was compared with the magnetic field value at the nearest position from the other vehicles. The relative direction of travel is merely to show variation in the direction of sampling.

Table 3.3:    Comparison of average spread (in mG).

| Sample | $x$ axis | | $y$ axis | | Direction |
|---|---|---|---|---|---|
| number | Swinging | Modified | Swinging | Modified | of travel |
| 1 | 39.39 | 21.17 | 29.76 | 4.69 | South |
| 2 | 63.23 | 27.24 | 11.14 | 11.01 | West |
| 3 | 14.27 | 9.74 | 23.28 | 16.41 | North |
| 4 | 33.56 | 20.17 | 7.86 | 7.36 | East |

The visual example in Figure 3.15 and the information in Table 3.3 clearly shows the modified ellipsoid method reduces the spread in magnetic field measurements from different vehicles. Again, the uncalibrated measurements were not included because the severe bias and scale-factor errors would simply show an egregious error, irrelevant for comparison.

The modified ellipsoid method promotes the utility of using magnetic field measurements across vehicle platforms with consistency. This improves efforts such as heading, but also lends itself to more advanced applications such as magnetic fingerprinting [24], navigation using magnetic fields [42] or identification of unique magnetic features.

# IV.  Magnetic Field Measurement Analysis

MAGNETOMETER measurement analysis requires collection, calibration, and mapping in preparation for using the magnetometer measurements for position estimation or navigation. The purpose for this measurement analysis is to explore the possible ways to use the magnetometer measurements to relate position based solely on magnetometer measurements and a magnetic field map. This will include different measurement compositions such as time or distance, as well as the effects of combining multiple measurements.

## 4.1  Assumptions

In order to advance the concept of using only magnetometer measurements for navigation, efforts were limited in a few areas. The subject Earth's magnetic field could provide enumerable explorations in how changes affect magnetometer measurements. Additionally, the frame of reference for the sensor as well as the effects of tilt, roll, pitch, or misalignment could be investigated ad nauseum. This section details the assumptions and recognizes these conditions also present opportunities for future work, discussed later.

### 4.1.1  Measurements only in the Body Frame.
The magnetometer was mounted in a strapdown configuration aligned with the body frame along with the SPAN (although only a GPS could have been used). Since the focus is using solely magnetometer measurements without gimballing or conversion to an absolute reference frame, no aides such as tilt sensors or the roll and pitch information from the SPAN were used to correct the magnetometer measurements. Therefore, any collected magnetometer measurement is in the body frame. Comparison assumes the magnetometer measurement platform and the magnetic field map platform are in similar orientations and directions of travel, which is reasonable, since the comparison is limited to roadways.

*4.1.2 Changes in the Earth's Magnetic Field and the Local Environment were Imperceptible.* While Chapter II detailed the level of expected change in the Earth's magnetic field over time, calibration in the vehicle platform did not yield this level of sensitivity (see Figure 3.15). Therefore the daily diurnal effect and the tiny changes over time were not factored into the magnetometer measurements. Additionally, no significant events in the Earth's magnetic field occurred during data collection. The investigation takes place at a fairly benign area of the Earth's magnetic field in the mid-latitudes. As mentioned in Chapter II, if the study were conducted closer to the poles, the increased effects of magnetic variation would have to be addressed.

*4.2 Magnetic Field Mapping*

At the foundation of this research is the ability to effectively and consistently map the magnetic field measurements to a position location. Although the IGRF and WMM provide excellent tools for determining the Earth's magnetic field with respect to position, they do not account for local perturbations or the effects on the magnetic field due to a vehicle. Attempting to use pure modeling to relate the predictive models and account for the local and vehicle perturbations is outside the scope of this research. Therefore, magnetic field mapping (i.e., using magnetic field measurements collected at known positions) provides the ability to relate a magnetometer measurement to a particular position.

*4.2.1 Time Delineated Magnetic Field Maps.* The three-axis magnetometer measurement observations were collected over three different road environments. The upper left map in Figure 4.1 shows the initial route used for comparison and consists of a fairly benign road environment to allow the best possibility for consistent measurement collection. The upper right map covers a suburban neighborhood and allows investigation of the ability to discern position on parallel roads in a similar environment. The bottom map covers a large area and shows the relative locations
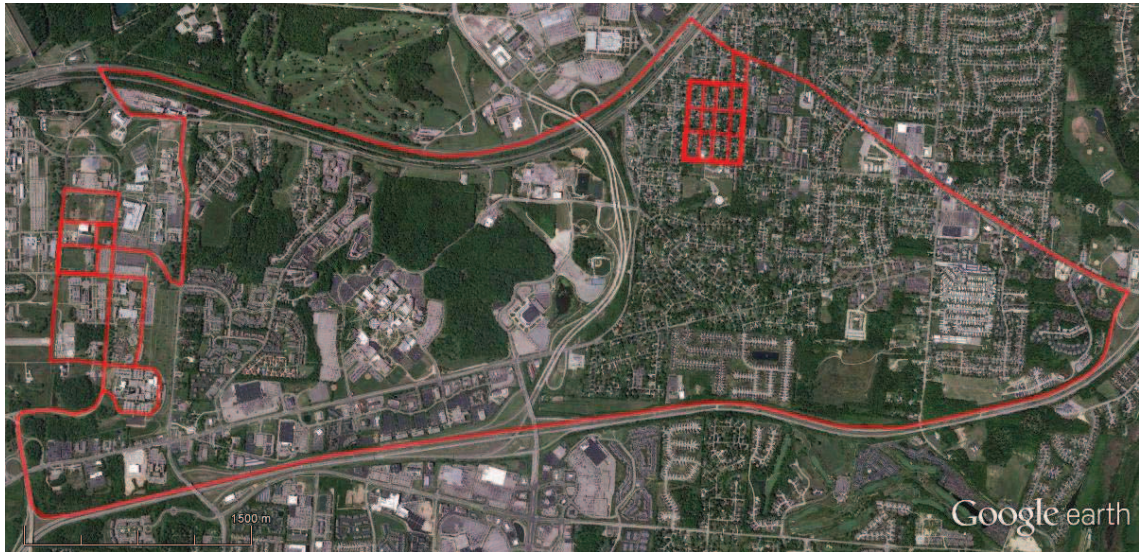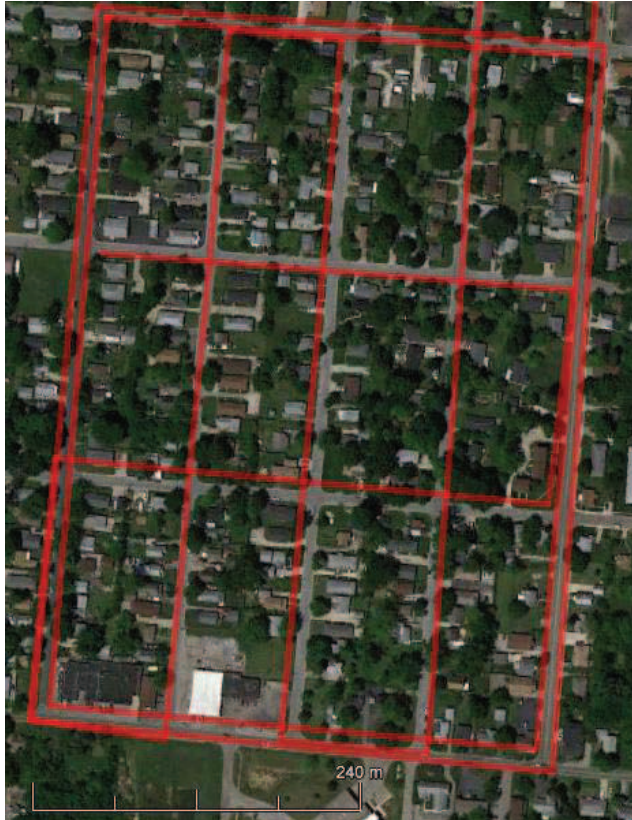
Figure 4.1:    Magnetic field map routes in red, courtesy of Google Earth.

of the suburban neighborhood and AFIT map areas. The colors were only used to highlight the route and possess no other meaning.

In order to map the magnetometer measurements, the collection platform must include both a magnetometer and position information (i.e. GPS or something similar). For this research, the HMR2300 [22] detailed in Chapter II provided the 50Hz magnetometer measurements. Although the HMR2300 is capable of providing measurements up to 150Hz, the increased measurement fidelity was not warranted due to the nature of the observable magnetic fields. For position information, the SPAN system delivered integrated GPS/inertial position, heading, roll, tilt, and pitch information. The SPAN system 3D position accuracy is 1.5 meters root-mean-squared (RMS), while the heading accuracy is 0.053 degrees RMS [39]. While the SPAN is overkill for this purpose, the additional information provided by the SPAN may be used with the magnetometer and position data for future research.

Figure 4.2 depicts a sample comparison of magnetometer measurements from the same vehicle in the $x$ axis ($B_x$) for three maps, with the magnetometer measurements plotted by position to show repeatability of the mapping process. The small inset shows the entire route with $B_x$ on the z-axis when plotted by position, as well as the vehicle position track for all three routes. The larger plot highlights a specific section of $B_x$ values along with the vehicle position. Clearly, driving variation during collection is conspicuous in both the vehicle positions and the magnetometer measurements. However, the magnetometer measurements do show consistency even with the translated position. The variation in maps expresses the same variation a vehicle attempting to navigate with only a magnetometer would experience. Therefore, determining the map variation provides insight for the level of position uncertainty a vehicle attempting to navigate using the magnetic field map will possess.

While the changes in the Earth's magnetic field mentioned in Chapter II affect the magnetometer measurements, the effects are an order of magnitude smaller

68
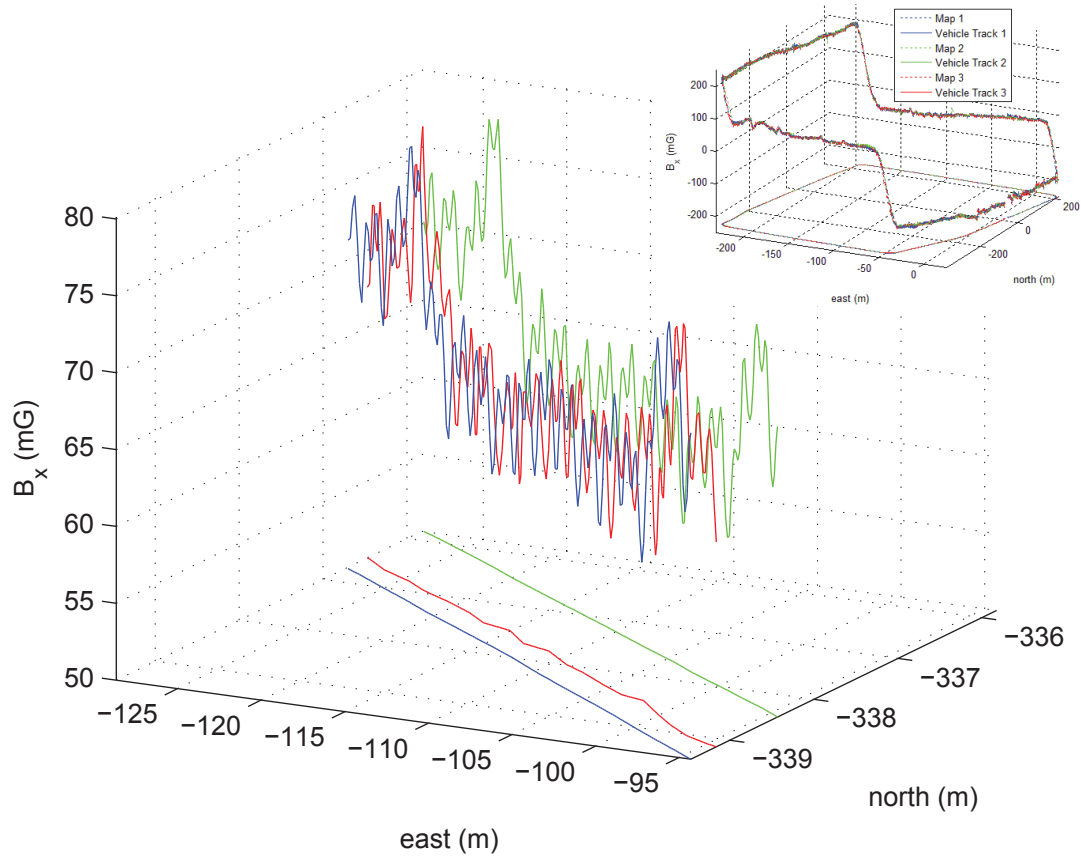
Figure 4.2:    Comparison of magnetometer measurements in the $x$ axis for three magnetic field maps. Each map represents one of three successive collections in the same vehicle repeating the same route. Results were similar in the $y$ and $z$ axes, respectively.

and not discernible due to the significantly larger errors of driving inconsistencies, magnetometer measurement variation, and uncertainty in the position information. These errors exist in each map and are interrelated as well as indistinguishable. The position variation is what could be expected when driving the same route based on typical vehicles, driving patterns, and the position information. In turn, the variation of the magnetometer measurements from map to map is dependent on the position variation as well as the vehicle calibration and magnetic field noise experienced by the magnetometer.

Since the magnetic field data is not always linear and predictable in this environment, simply interpolating by position to align the vehicle tracks and the corresponding magnetometer measurements is not suitable. In order to express the entire variation, a sufficient statistic must be determined. Using the data highlighted in Figure 4.3, each 50Hz position in Car Track 1 was aligned with the corresponding positions in Car Track 2 as well as two Truck and SUV tracks using the along track coordinates. The comparison tracks (all but Car Track 1) position and magnetometer measurements were interpolated to a higher rate so that the comparison would be between the closest position on each track. Hence, the minimum distance between each track is used as the comparison point for the set of six tracks. At each comparison point, the standard deviation of the magnetometer measurements in each axis is computed. The standard deviation of the distances between the comparison points is also computed, to provide an indication of the position variation amongst the tracks. The mean is computed from this collection of standard deviations at each comparison point to find the average standard deviation for all six tracks. Consequently, the overall magnetometer mapping variation estimate was derived from the empirical data of several maps traversing the same route and shown in Figure 4.3 as well as Table 4.1.

*4.2.2 Assumption of Gaussian Total Error.* After describing the details of errors due to magnetometers and the Earth's magnetic field in Chapter II, the
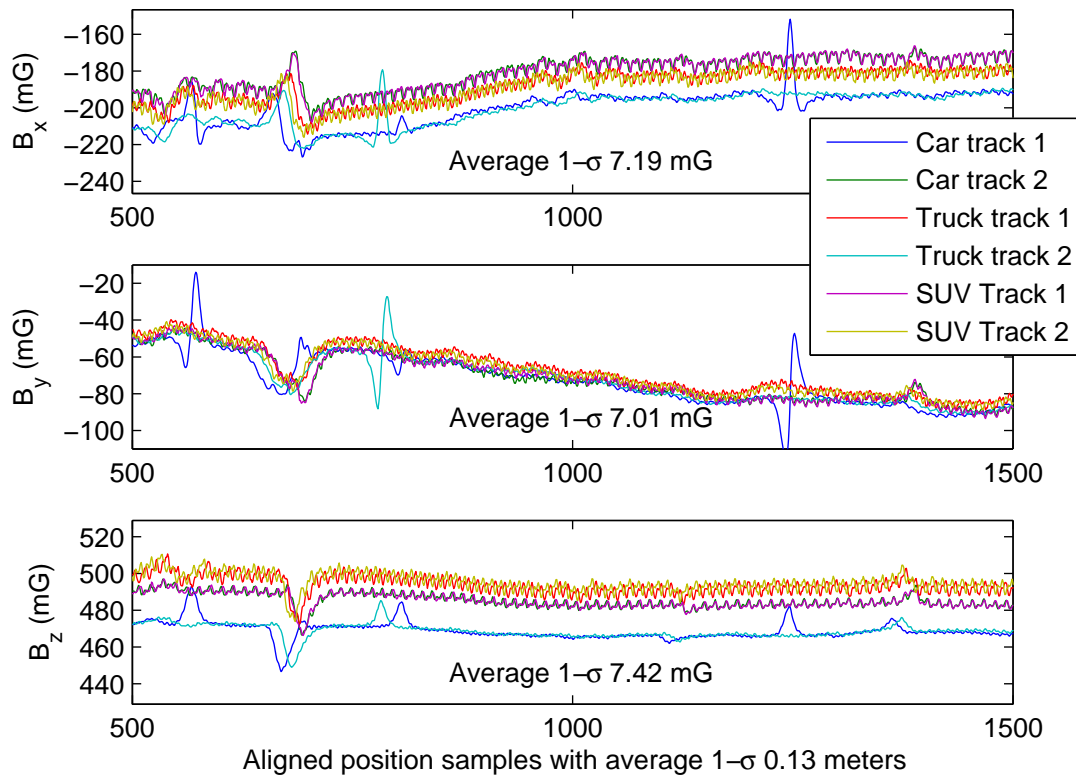
Figure 4.3: Comparison of magnetometer measurements in each axis. This sample section of the entire route highlights the typical variation in each axis among the vehicle tracks.

Table 4.1: Empirical mapping variation

| Platform | $B_x$ (mG) | $B_y$ (mG) | $B_z$ (mG) |
|---|---|---|---|
| Same-vehicle average 1-$\sigma$ | 2.66 | 2.51 | 2.77 |
| Cross-vehicle average 1-$\sigma$ | 7.19 | 7.01 | 7.42 |

addition of driving variation induces further error as evident in Chapter III. Recalling Figure 3.15 and Table 3.3, even when position variation was minimized, calibrated magnetometer measurements from different vehicles still contained unresolved error. In order to continue progress towards navigation, an assumption of Gaussian errors has been used in lieu of an exhaustive analysis of the combined contribution of each error source. The overall effect of the errors was modeled as zero-mean additive white-Gaussian noise using the statistics in Table 4.1.

*4.2.3 Magnetic Field Maps based on Distance.* The magnetic field map can also be constructed based on a fixed distance between magnetometer measurements. For example, the entire magnetic field map could consist of magnetometer measurements equally spaced in 1m intervals. There are several motivations for this type of map structure. By creating a fixed distance map, the velocity of the vehicle is no longer a factor. This allows investigation of combining multiple measurements into a measurement section. An incoming magnetometer measurement section could be compared to a magnetic field map section. Additionally, a significant reduction in magnetic field map storage size is realized. Magnetic field maps based on time samples often have several repetitive entries consuming storage space but contributing no additional information. Imagine stopping at a traffic signal for a long period of time. When the magnetic field map is small, the issue is trivial. However, as the magnetic field map grows to cover large regions, the storage space requirement will increase significantly. For example, the file size of the large area map with 50Hz entries shrank nearly 85% when converted to a distance map with entries every 0.5m. The size of a magnetic field map for an average city would be megabytes instead of gigabytes. The effects of using the distance-based magnetic field map will be analyzed in Section 4.4.

*4.2.4 Magnetic Perturbations and Velocity Determine the Sampling Rate/Distance.* Recalling information from Chapter II, magnetic variations describe grad-

ual changes in the magnetic field over large areas, such as a large deposit of ferrous material in the Earth. Perturbations, on the other hand, describe much smaller and more localized changes in the Earth's magnetic field due to nearby ferrous material or electromagnetic fields. Using the example of an underground feature composed of ferrous material, the magnetometer senses a distinct change in the Earth's magnetic field when driving over the feature even though it is buried beneath the road. Since these changes are recorded in the magnetic field map, the perturbations become features for navigation, as long as they are fixed.

Figure 4.4 depicts the same underground feature for two sample rates and a sample distance. A magnetometer measurement at 0 on the x-axis was used to match the magnetometer measurement to the magnetic field map, with several epochs of both the magnetometer measurement and the magnetic field map shown before and after to highlight the overall conformance. The underground feature is typical of a small feature which provides localized magnetic field change, clearly different than the magnetic field change associated with mere position change. Not only is the feature definable by change in each axis, but the feature is observable for approximately 10 meters. Perturbations play a critical role as unique magnetic field features. Understanding these features and the magnetometer limitations in sensing them is warranted.

The sampling rate (or distance) is dependent on the velocity during collection. For example, if the maximum speed of the vehicle will only be 10 meters per second (m/s), or about 22 miles per hour (mph), sampling at 5Hz yields five measurements over a 10m distance and will capture a small feature such as that shown in Figure 4.4. If speeds of 30m/s ($\approx$ 65mph) are possible, 10Hz sampling will yield a measurement about every 3m which would still detect the small feature. Clearly, the sampling rate/distance must be a function of the expected velocity of the vehicle. For the datasets in this research, which include some highway speeds up to 30m/s, 10Hz or
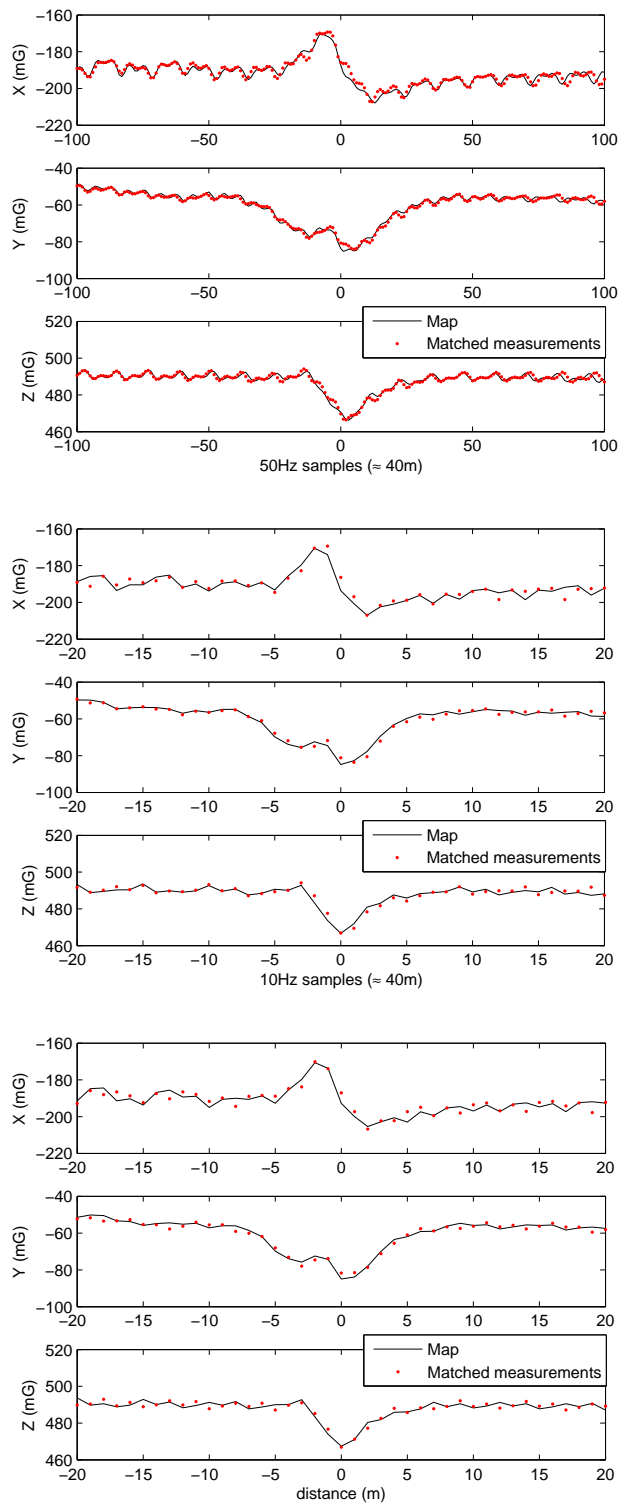
Figure 4.4: An underground feature at 50Hz (top), 10Hz (middle), and 1m (bottom) respectively.

3m would be the minimum sampling rate/distance viable in order to capture the available magnetic features.

## 4.3  Likelihood Techniques for Magnetic Field Map Matching

In order to determine the ability to successfully match magnetometer measurements with those contained in the magnetic field map, several Gaussian likelihood techniques were explored. The use of the Gaussian likelihood provides the foundation for each technique in order to include the uncertainty found in map variation. The magnetometer measurement was compared with measurements stored in the magnetic field map to determine a likelihood value for each potential magnetic field map location using the likelihood function given in Equation 2.51. If the magnetometer measurement matched a measurement contained in the magnetic field map perfectly, the likelihood would be very high. Similarly, a magnetometer measurement very different from those contained in the magnetic field map would have a likelihood approaching zero. Figure 4.5 depicts a sample set of likelihoods at a single epoch, where the $\beta$ term has been removed to normalize the plot. The sample set of likelihoods at a single epoch shows the relationship between a single measurement and the entire magnetic field map. The likelihood is near zero for a large portion of the map, but depicts several peaks which are possible locations based on the magnetometer measurement. The peaks are formed as the magnetometer measurement approaches a potential match in the magnetic field map.

The likelihood map in Figure 4.6 shows the likelihood of each point on the magnetic field map for each epoch. The color intensity shows the relative difference between low likelihoods (near zero) and high likelihoods (near the maximum). The information this graphic conveys is that there are definite areas with sufficient measurements to perform likelihood matching and obtain a position estimate. If the entire graphic were solid blue (low likelihood), none of the magnetometer measurements correlated well with the magnetic field map, or there was insufficient change

75
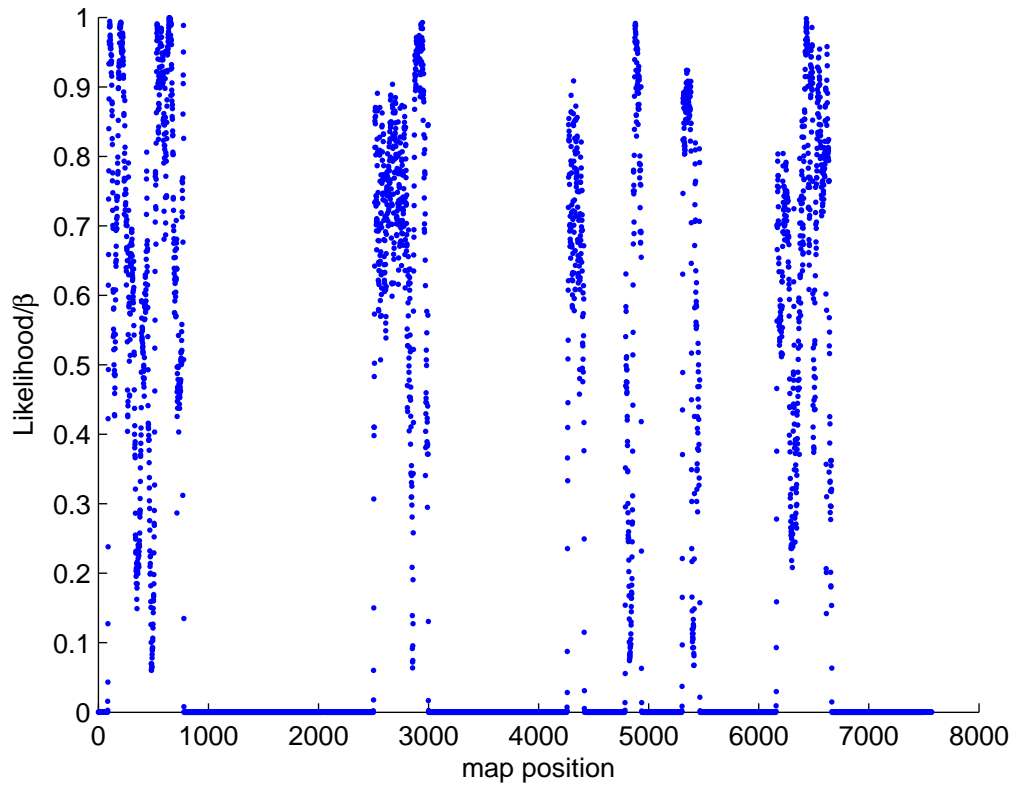
Figure 4.5: A sample set of likelihoods at a single epoch. The $\beta$ term has been removed to normalize the plot.
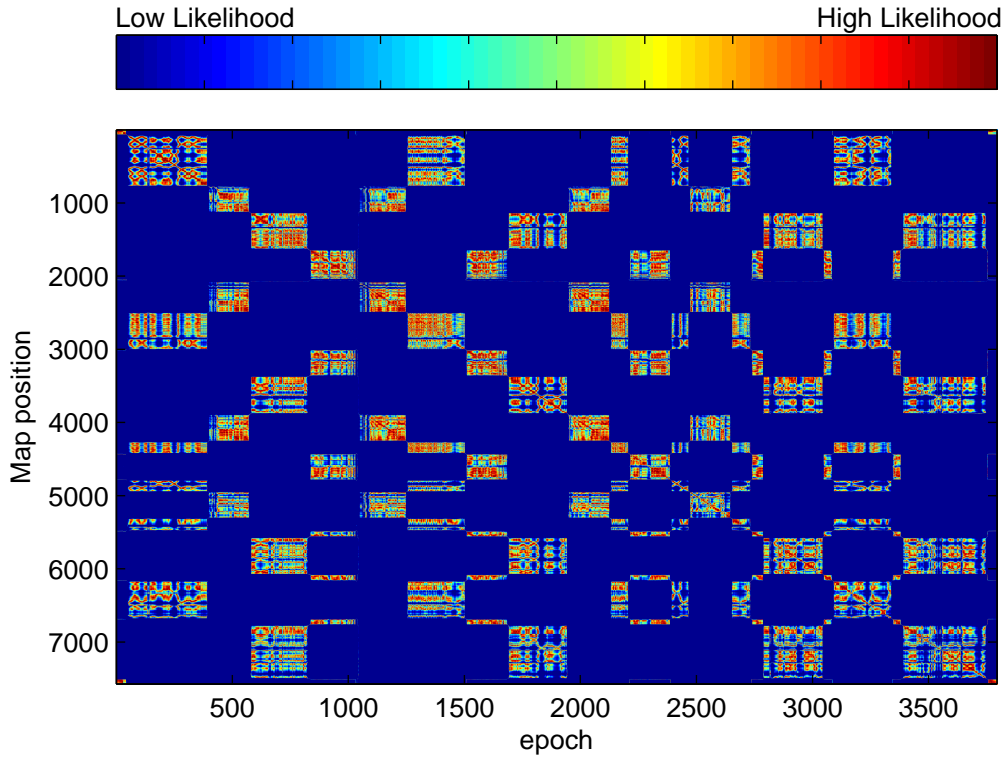
Figure 4.6:     The likelihood at each epoch plotted vertically with the color level indicating the relative likelihood.

in the magnetometer measurements and the magnetic field map to differentiate between positions. As previously discussed, features provide unique areas and the more unique the feature, fewer locations on the likelihood map will be highlighted. But by and large, the areas emphasized in the likelihood map are due to similar heading characteristics. Although not explicitly calculated, the horizontal axes of the magnetometer provide the information used for heading. As a result, the likelihood of similar headings will be higher than magnetometer measurements from slightly different headings. Perpendicular or opposite direction headings will yield likelihoods near zero.

The magnetic field map is composed of numerous positions defined by their fairly unique three-axis magnetometer measurements and restricted to roads. An

incoming magnetometer measurement can easily be compared to every magnetic field map measurement and the resulting set of likelihoods used to determine the most likely position on the map. While the direct approach of maximum likelihood (ML) is apparent, additional likelihood techniques were developed specifically to improve the ability to discern which magnetic field map location correlated to the incoming magnetometer measurements. The maximum likelihood ratio (MLR) and the aggregate bin likelihood (ABL) techniques, as well as the maximum likelihood, are detailed in the paragraphs that follow.

*4.3.1 Maximum Likelihood (ML).* Using the maximum of the likelihoods from Equation 2.51 provided a simple and effective way to determine the best magnetic field map location according to the magnetometer measurement. However, due to the nature of the magnetometer measurements, the maximum likelihood value is not always correct. Another look at the sample set of likelihoods for a single epoch depicted in Figure 4.5 easily casts doubt that simply picking the maximum likelihood will result in the correct magnetic field map location. The maximum likelihood also provides a straightforward baseline indicator for comparing other techniques.

*4.3.2 Maximum Likelihood Ratio (MLR).* Since using the maximum likelihood alone does not always produce the correct location via the magnetic field map, a technique to help determine if the maximum likelihood is correct proved useful. When multiple likelihood peaks are present, the maximum likelihood is divided by the second highest likelihood a specified minimum distance from the position of the maximum likelihood (e.g., 20m) to form the maximum likelihood ratio. If the ratio exceeds some value (e.g., 2) then the maximum likelihood is sufficiently unique to provide a location estimate. However if the ratio does not exceed the threshold, no location estimate is reported, meaning some epochs will be deemed insufficient to provide an estimate. To reflect the availability, the percentage of availability was calculated by dividing the number of reported position estimates returned by the

MLR by the total number magnetometer measurements. For example, a 35% availability rate conveys that if 1000 magnetometer measurements were compared to a magnetic field map, the MLR technique only reported that 350 of the magnetometer measurements were sufficiently unique to warrant a location estimate.

The motivation for this approach stems from observation of the set of likelihoods as magnetometer measurements are compared to the magnetic field map. As each incoming magnetometer measurement gets closer in position to a magnetic field map location that correlates well, the set of likelihoods form a peak. If the magnetometer measurement and magnetic field map correlation is truly unique, a single peak is formed. However, multiple peaks are often formed indicating other possible locations. The maximum likelihood ratio provides a method to determine if the second highest peak is sufficiently different in position and substantially lower in likelihood to assert that the maximum likelihood is correct.

Clearly, the ratio and minimum distance values play an important part in the results provided by the MLR. A very short minimum distance will only allow sharper peaks which express a close match between the magnetometer measurement and a particular magnetic field map location. This may eliminate areas where the peak is wide due to the magnetometer measurement being equally likely for several epochs (common on roadways). While a larger minimum distance would alleviate this symptom, it also may reduce the accuracy of the match, since the maximum likelihood may be at any location within the minimum distance due to several high likelihood values in succession. The ratio also affects the quality of the match. As the value of the ratio increases, the vertical distance between the maximum likelihood peak and the next peak increases and expresses the uniqueness of the peak. However, too high a ratio will reduce matches to only the very unique. On the other hand, a ratio that is too low will not allow sufficient distinction between peaks of nearly the same height, and reduce discernment that the maximum likelihood is the correct peak. Overall, a high ratio combined with a short minimum distance will identify

unique peaks higher than all other peaks. However, the cost for the increase in quality is the number of available matches between a magnetometer measurement and the magnetic field map. Conversely, a lower ratio and longer minimum distance will allow more matches, but with less accuracy. In order to continue advancement towards navigation, an exhaustive tradeoff value was not conducted. The ratio and minimum distance values for the MLR were selected from empirical analysis, with the effects conveyed in the accuracy analysis of Section 4.4. Refinement of these parameters is left for future work.

*4.3.3   Aggregate Bin Likelihood (ABL).*   Although the MLR seeks to discern when the maximum likelihood is correct, the aggregate bin likelihood is a method to choose the best measurement-map match even when the maximum likelihood is incorrect as evidenced in Figure 4.7. Since a quality match involves a likelihood peak, multiple peaks of nearly the same height may cause the maximum likelihood choice to be incorrect. In order to implement the ABL technique, the likelihood values are normalized by dividing the likelihood by the sum of the likelihood. The normalized likelihood is then compared to a threshold value to determine if the normalized peaks are of sufficient size to make an estimate on the correct peak. If peak size is insufficient, no location estimate is provided. Then, the ABL technique uses the normalized likelihood values within a narrow sliding window, or bin, and then sums the normalized likelihood within the bin. The bin with the highest value is chosen as the location estimate. Accordingly, the ABL rewards peaks with a close concentration of high likelihood values and devalues peaks with only a few likelihoods in the bin. This technique is well suited for magnetic field maps with contiguous data points based on typical road travel. Sparse magnetic field maps or magnetic field maps with indiscriminate relative positions would fair poorly.

Similar to the MLR, the values for the threshold and bin size play a critical role in the success of the ABL. The threshold determines the level required in the normalized likelihood to discern a magnetic field map location. Too low of a threshold

will allow too many possible peaks and lead to reduced matching quality. A threshold that is too high will only allow unique peaks that could easily be found using the MLR.

Since the estimate uses the sum of the normalized likelihood within the bin, a larger bin size rewards areas where the magnetometer measurement is equally likely over an area. Conversely, a very small bin size will eliminate good magnetometer measurements which create unique peaks. The choice for threshold and bin size were determined through empirical analysis of magnetometer measurement and magnetic field map matching. As with any parameter of this type, the choices of threshold and bin size change the quality of matching. As with the MLR, an exhaustive tradeoff value was not conducted. The bin size and threshold values for the ABL were selected from empirical analysis, with the effects conveyed in the accuracy analysis of Section 4.4.

An example of the likelihood techniques is shown in Figure 4.7 for illustration. The figure shows a case when multiple likelihood peaks are present, yet the ABL is able to discern the correct position even when the maximum likelihood (ML) is different. In this case the MLR also incorrectly confirms the ML. While this is not the typical case, it showcases the different likelihood techniques. Each technique uses the same fundamental likelihood information, but the MLR and ABL techniques attempt to verify the correct likelihood when many similar likelihood values are present.

## 4.4 Likelihood Technique and Measurement Composition Analysis

An analysis of the ability to determine how accurately a technique can match a magnetometer measurement to the magnetic field map and obtain the correct position is useful. From a fundamental perspective, knowing the profic

While studying the effectiveness of the likelihood techniques, a plethora of test cases investigating all the possible measurement compositions was developed, viewable in Appendix A. For magnetometer measurements, the parameters of com-
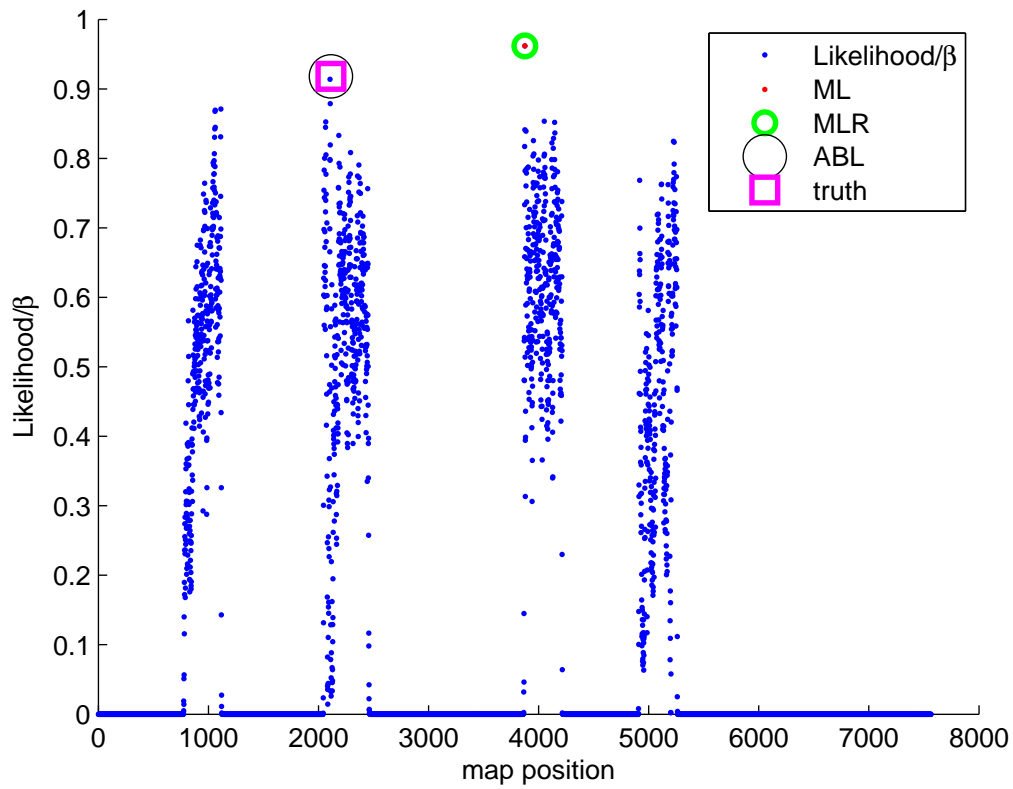
Figure 4.7:    Examples of the ML, MLR and ABL techniques. In this case the ML and MLR have chosen the incorrect position.

Table 4.2:    Baseline Test Cases.

| Test Case | Measurements | | | Map | |
|---|---|---|---|---|---|
| | Vehicle | Units | Type | Vehicle | Units |
| ABT001 | Truck | 50Hz | uncal | Truck | 50Hz |
| ABT002 | Truck | 50Hz | cal | Truck | 50Hz |
| ABT003 | SUV | 50Hz | uncal | SUV | 50Hz |
| ABT004 | SUV | 50Hz | cal | SUV | 50Hz |
| ABT005 | Car | 50Hz | uncal | Car | 50Hz |
| ABT006 | Car | 50Hz | cal | Car | 50Hz |
| ABT007 | Truck | 50Hz | cal | SUV | 50Hz |
| ABT008 | Truck | 50Hz | cal | Car | 50Hz |
| ABT009 | SUV | 50Hz | cal | Truck | 50Hz |
| ABT010 | SUV | 50Hz | cal | Car | 50Hz |
| ABT011 | Car | 50Hz | cal | Truck | 50Hz |
| ABT012 | Car | 50Hz | cal | SUV | 50Hz |

| Test Case Identifiers | |
|---|---|
| Character 1 (map) | A=AFIT, H=hood, L=large |
| Character 2 (measurement type) | B=baseline, D=distance, T=time |
| Character 3 (map type) | D=distance, T=time |
| Characters 4-6 (test case) | ###=test case # |

position include: time, distance, calibrated or uncalibrated, single or multiple epoch, demeaning, differencing, and/or by feature. Additionally, some or all of these compositions can be mingled to produce a different measurement composition. Conversely, some compositions are exclusive. For example, uncalibrated measurements of different vehicles can only be compared when using multiple epochs and either a demeaning or differencing technique. A full description of each measurement composition will be discussed before the results and analysis are presented.

A baseline set of 12 test cases (a subset of the entire test matrix found in Appendix A) initiates the examination of measurement composition and likelihood technique performance, shown in Table 4.2. The test case identifiers help distinguish the environments as well as the parameter variation. The first character identifies the map section as shown in Figure 4.1. The letter **A** stands for the rectangular road path around AFIT. The letter **H** signifies the crosshatched neighborhood, and **L** represents the large area map. The second character labels the measurement type by distance or time, but with a specific callout for baseline to allow comparison of the baseline data across all results. The third character denotes the map type in distance or time. Finally, characters four through six designate the specific case.

The highest resolution magnetometer measurements and magnetic field maps consisted of 50Hz data. For all test cases, the adjustable parameters of the MLR

and ABL techniques were held constant to reflect the changes due to the different measurement and map composition, rather than to maximize performance from a particular technique.

*4.4.1 Baseline: Same-Vehicle Cases.* Test cases ABT01-06 in Figure 4.8 involve calibrated and uncalibrated magnetometer measurements taken in the same vehicle platform, as well as the response from the three likelihood techniques discussed in Section 4.3.

The multiple bar graphs show the percentage of correct matches based on the 2D horizontal distance from the vehicle position. The right vertical axis details the likelihood technique used for each group of calibrated and uncalibrated magnetometer measurements. The left vertical axis displays the vehicle used for both the magnetometer measurements and the magnetic field map. The horizontal axes represent the percentage accuracy of magnetometer measurements to the magnetic field map by each likelihood technique. The red asterisk highlights the percent available.

As an example, the uncalibrated magnetometer measurements in the Truck were used to determine the position based on a magnetic field map from the Truck created at a different day/time. The ML ability to correctly determine position based solely on the magnetometer measurement at a single epoch and the magnetic field map was 44% for a 2D miss distance less than three meters. For a 2D miss distances of 3-10m and 10-20m, the ML accuracy was 14% and 10% respectively. The remaining 32% had 2D miss distances greater than 20m. To make the accuracy of available measurement percentages relevant, the percent available is also required. Since the ML provides a match for every available measurement, the percent available will always be 100%. But the MLR and ABL do not provide a match for every measurement, resulting in a much lower percent avaiable.

Immediately, the trade-off between the accuracy of available measurements and the percent available becomes clear when viewed across the three likelihood
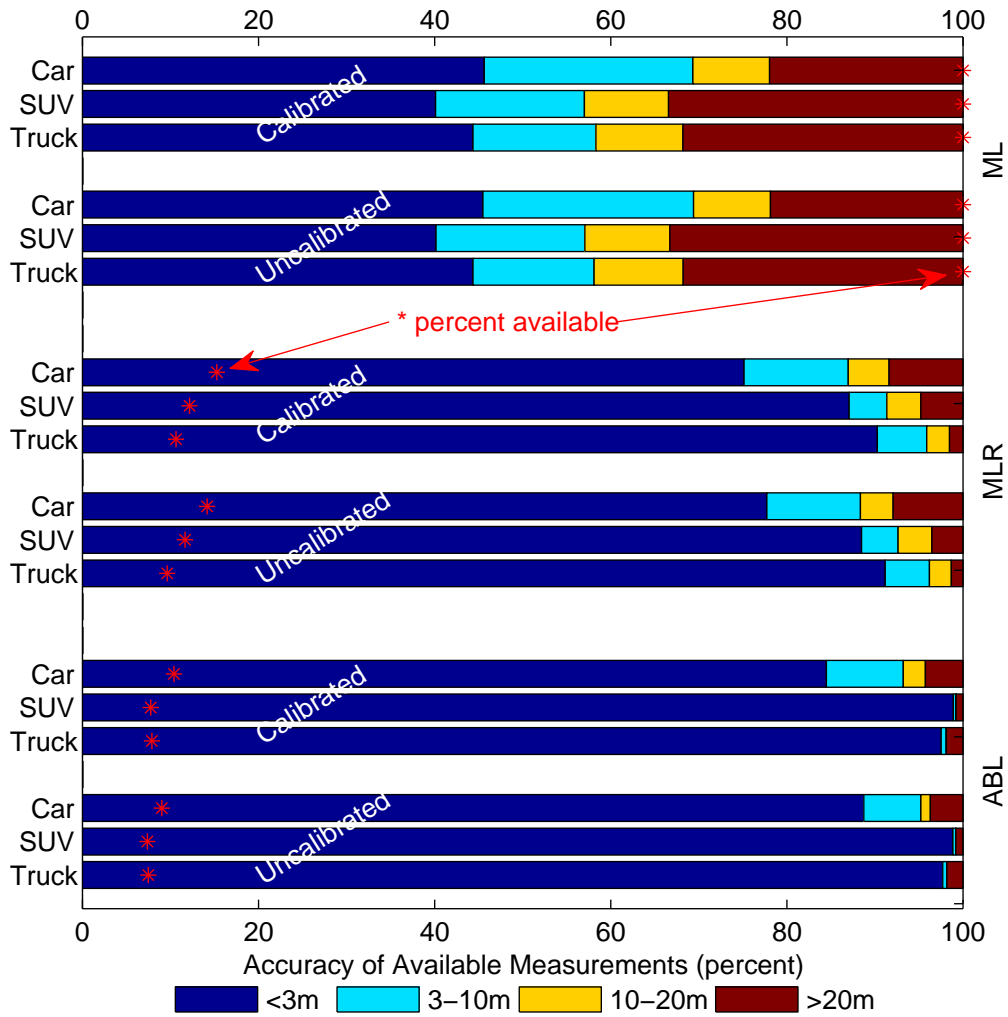
Figure 4.8: Results for test cases ABT01-06. This baseline compares the ability to correctly match 50Hz magnetometer measurements with 50Hz measurements contained in the magnetic field map previously taken in the same vehicle.

85

techniques. The ability to obtain quality matches comes at the cost of the number of matches reported as a result of the inability to distinguish the correct likelihood value. Recalling Figure 4.5, the sample likelihood shows the difficulty in choosing the correct likelihood when multiple peaks are present. Thus the MLR and ABL techniques seek ways to provide better quality matches by rejecting instances when the correct determination is unlikely.

The calibrated and uncalibrated results show consistency throughout Figure 4.8. This demonstrates two things. First, calibrated or uncalibrated measurements are equally valuable in the same-vehicle case. The magnetometer measurements maintained the same relationship with or without calibration. Second, the ability to match magnetometer measurements to the magnetic field map is independent of calibration. The results across all three likelihood techniques were relatively the same.

However, all three techniques displayed a slight improvement in all vehicle platforms when using uncalibrated measurements. Since these are all same-vehicle cases, uncalibrated measurements have reduced spread, or to put it another way, more consistency as evidenced in Table 4.1. The calibration parameters are the best estimate to transform magnetometer measurements with bias and distortion to corrected measurements representative of Earth's magnetic field at each position. In Chapter III, the average spread decreased significantly for the cross-vehicle cases after calibration. Since the calibration parameters are not perfect, the average spread of the measurements increases very slightly after calibration for the same-vehicle cases as compared to purely uncalibrated measurements. In turn, the ability to accurately match magnetometer measurements to the magnetic field map decreases slightly, causing the minor performance difference between calibrated and uncalibrated measurements from the same vehicle platform.

Of utmost importance concerning the likelihood techniques is the inverse relationship between the accuracy of available measurements and the percent available.

86

Since the ML returns a match for each magnetometer measurement available, 100% will always be available, although the overall accuracy suffers. In contrast, the MLR and ABL display a significantly lower percent available yet a higher percent of accurate matches. In the same-vehicle baseline cases, the ABL yields a modest performance improvement over the MLR.

*4.4.2 Baseline: Cross-Vehicle Cases.* Test cases ABT07-12 in Figure 4.9 compare the cross-vehicle case where the magnetometer measurements are compared to a magnetic field map from a different vehicle (e.g., Truck-SUV indicates measurements were used from the Truck and the magnetic field map was from the SUV). Direct comparison of cross-vehicle measurements requires the magnetometer measurements to be calibrated. Uncalibrated measurements include significant bias and distortion specific to the vehicle platform making direct comparison at a single epoch inappropriate.

Test cases ABT07-12 specifically look at the cross-vehicle case, when magnetometer measurements are compared to a magnetic field map created in a different vehicle platform. In the cross-vehicle cases, only calibrated measurements are compared since the distortions for different vehicle platforms prohibits direct comparison at a single epoch. The left vertical axis of Figure 4.9 conveys the measurement-map arrangement for each bar graph. A set of data from a vehicle used as measurements was different than the set of data used for the magnetic field map. Therefore SUV-Car is not simply a reversal in the use of the data from Car-SUV.

For the ML cases, the performance is fairly consistent and reflects the increased difficulty of matching magnetometer measurements to the magnetic field map of a different vehicle. The results are quite different from the same vehicle platform case. Although calibration attempts to resolve the magnetometer measurements by removing errors introduced by the vehicle platform, it is not perfect. The differences associated with using magnetometer measurements from a vehicle different than the
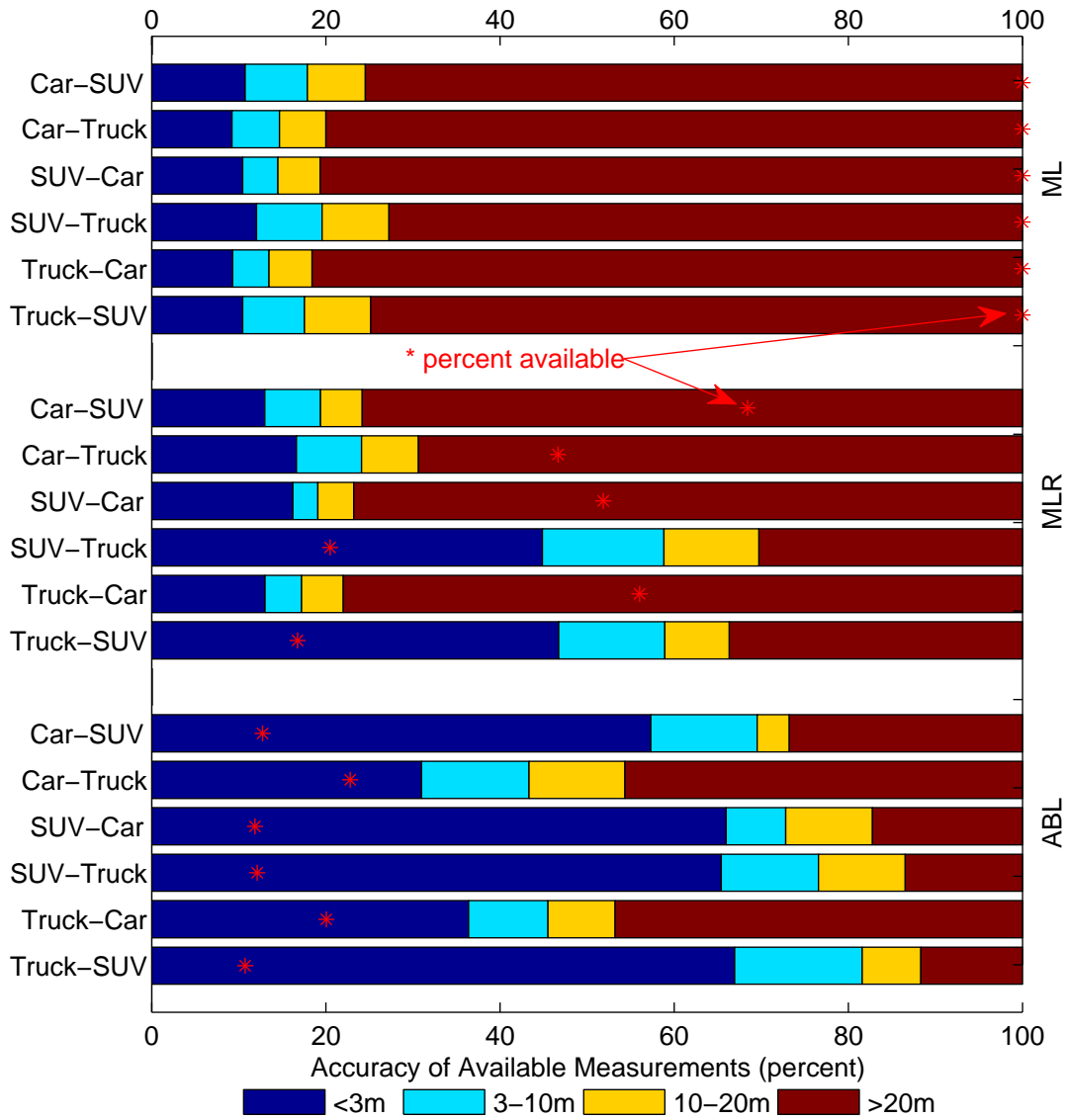
Figure 4.9: Results for test cases ABT07-12. This baseline compares the ability to correctly match 50Hz magnetometer measurements with 50Hz measurements contained in the magnetic field map taken in a different vehicle platform. The left vertical axis denotes the measurement-map arrangement of the vehicle platforms.

magnetic field map are realized in the decreased accuracy across all three likelihood techniques. The cross-vehicle platform cases highlight the challenges of effectively matching a magnetometer measurement to a magnetic field map. Several factors contribute to the diminished accuracy. First, the platform characteristics are not homogeneous, resulting in different levels of distortion in the magnetometer measurements. Second, the installation does not resolve the position of the magnetometer to an absolute position attainable in all three vehicles. Instead, magnetometer placement mitigates as much electro-magnetic interference as possible. While these factors were minimized as much as possible, they could not be eliminated through installation or calibration, as evidenced in Table 4.1, when viewing the same-vehicle versus the cross-vehicle statistics.

In most cases, the MLR shows a marginal increase in accuracy, with the exception of the SUV-Truck and Truck-SUV comparisons. While the ML showed a slight improvement for these cases, the MLR performance was significantly higher than the ML. A closer inspection of the calibrated magnetometer measurements and magnetic field maps revealed the Truck and SUV magnetometer data were overlapping for all of the data involved, while the Car had a significant portion of data approximately 10mG from the Truck and SUV data sets. While still in the expected spread range, this slight shift of the data could be contributed to a combination of factors such as driving variation, the specific distortion of the vehicle, and difference in installation. In addition, the overlapping Truck and SUV data could produce more likelihood peaks that were unique.

The ABL provided increased accuracy over the ML and MLR techniques in all cases. The Car-Truck and Truck-Car cases yielded lower accuracy, yet a higher percent available. Examining the likelihood for the Car-Truck cases versus the Truck-SUV cases showed that the Car-Truck cases often had distinct peaks that were closer together. This would be conveyed in the higher percent available, but also increase the possibility of reduced accuracy due to the closer proximity of the peaks.

*4.4.3 Baseline Summary.* Analysis of the baseline cases demonstrates the consistency of the calibration and likelihood techniques for both the same-vehicle and cross-vehicle cases. For the same-vehicle cases, calibration made a minimal difference in performance, leaving little reason to pursue cases focusing on comparison of calibrated and uncalibrated data. Although the cross-vehicle cases proved less accurate in these instances, the likelihood techniques maintained their relative performance difference when compared to each other. Since the cross-vehicle cases represent the most operationally feasible cases and require the most improvement, test cases from this point on will focus on the cross-vehicle cases with the understanding that the same-vehicle cases will exhibit better performance, whether calibrated or uncalibrated. As expected, the measurement-map arrangement (Truck-SUV vs. SUV-Truck) made little difference in performance and therefore the rest of the test cases will only use the Truck-SUV, Truck-Car, and Car-SUV arrangements to represent typical results.

## 4.5 Varying the Measurement Composition

While the baseline test cases present the initial approach for utilizing the magnetometer measurements, many other possibilities exist. This section will explore various methods of magnetometer measurement and magnetic field map composition in order to determine effective combinations and trade-offs. The initial analysis concentrates on the smaller data set around AFIT in order to glean the most proficient methods to use with the significantly larger and more difficult areas consisting of the neighborhood and large area map.

*4.5.1 Sampling Rate Variation.* First, a word of caution. Although the sampling rate is reduced here to analyze the effects of accuracy among the likelihood methods, it should not be reduced during the initial vehicle installation and noise mitigation. Sampling at 50Hz or above allowed observation of vehicle specific electromagnetic interference that was not observable at 10Hz and only recognizable at 25Hz

after being observed at 50Hz. The increased sampling rate provided the necessary feedback to mitigate extreme interference through repositioning of the magnetometer in the vehicle. Future work could include identification and mitigation of typical interference when repositioning is not possible and/or a study on the effects of interference on magnetometer measurements for navigation. For this initial exploration, mitigation of as much interference as possible was preferred.

To explore the sampling rate variation, the magnetometer measurements and magnetic field map sampling rates were varied from 50Hz to 10Hz to determine the effect fewer measurements would have on the accuracy of available measurements. As previously mentioned, 10Hz is the lowest sampling rate in time that would adequately detect magnetic field features at the highest possible velocity for these data sets. An intermediate sampling rate of 25Hz is not shown, but produced results in between the 50Hz and 10Hz sampling rates as expected. Figure 4.10 shows the results. For ease of comparison, the 50Hz-50Hz baseline cases from Figure 4.9 are included in Figure 4.10 for the Truck-SUV, Truck-Car, and Car-SUV test cases. For each likelihood technique, the results were consistent with the baseline cases.

Beginning with the maximum likelihood, there is negligible difference in performance. The MLR technique depicts mixed results, with Truck-SUV cases trending downward slightly as the sampling rate decreases, while the Truck-Car and Car-SUV cases trend upward slightly. The ABL technique trends upward slightly as the sampling rate decreases for the Truck-SUV and Car-SUV cases, but stays constant for the Truck-Car cases. What can be determined from all three techniques is that reducing the sampling rate has minor effects on performance.

4.5.2 *Distance Variation.* As mentioned previously, it is possible to construct magnetic field maps based on distance rather than time using the position information obtained when creating the map. Likewise, incoming magnetometer measurements can be arranged by distance if knowledge of velocity or distance trav-
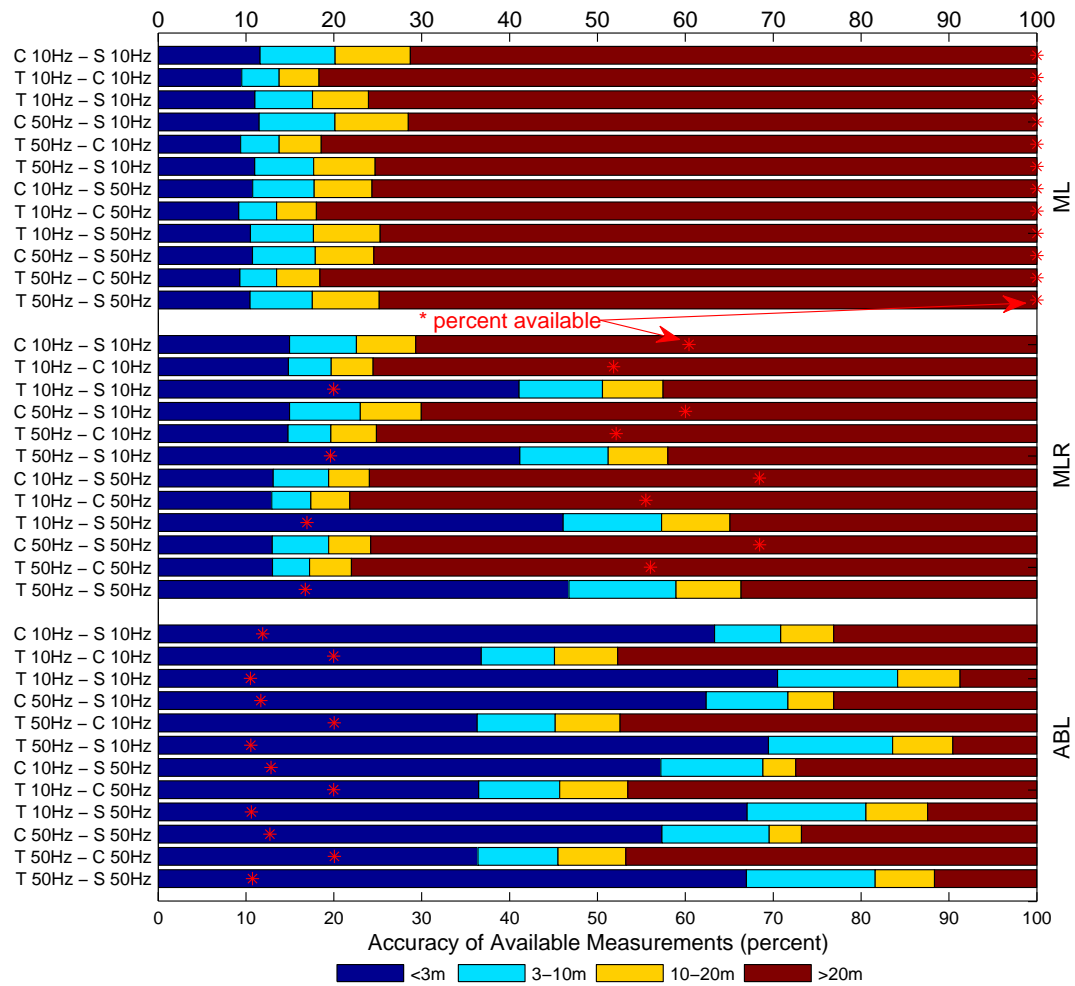
Figure 4.10: Samping rate variation results for the Truck-SUV, Truck-Car, and Car-SUV test cases. The vertical axis abbreviations are T=Truck, S=SUV, and C=Car.

eled is also obtained. Assuming this information is available, the incoming magnetometer measurements can be compared to the previously created magnetic field map based on distance. In order to compare the effects of distance based magnetic field maps and magnetometer measurements, the distance between points was varied and the results appear in Figure 4.11. Since 3m was deemed the maximum distance between samples in order to effectively capture features, the distance variation examined distances from 0.5m to 3m. Although the baseline cases were not included in Figure 4.11 to reduce the size, the 0.5m measurement coupled with 0.5m map cases are comparable to the baseline, albeit with slightly lower percentages in the MLR and ABL results.

While the overall performance is reduced compared to the results using time sampled measurements and maps, the consistency across the test cases remains. For all the techniques the impact is minimal. Interestingly, the typically more accurate Truck-SUV case worsens as the distance between measurements increases while the Car-SUV case improves slightly. The change in the Truck-Car case is neglig

*4.5.3 Mixed Variation.* For the single epoch case, it is also possible to use measurements sampled in time on maps arranged by distance and vice-versa. Figure 4.12 shows an example of mixed variation performance for 10Hz and 1m compositions, along with the baseline cases.

Not intended to be comprehensive, this example shows that utilizing magnetometer measurements with mixed variation is possible and provides results consistent with the baseline with significantly fewer measurements. Although the expected supposition would be magnetometer measurements and a magnetic field map of the same type, mixed variation expands the dimension of possibilities for potential collection systems. As for the results, they are mixed as well. While the ML, MLR, and ABL are comparable with the baseline, a clear choice of measurements in time and maps in distance (or vice-versa) is not obvious. The ML and MLR techniques

Figure 4.11:     Distance variation results

94
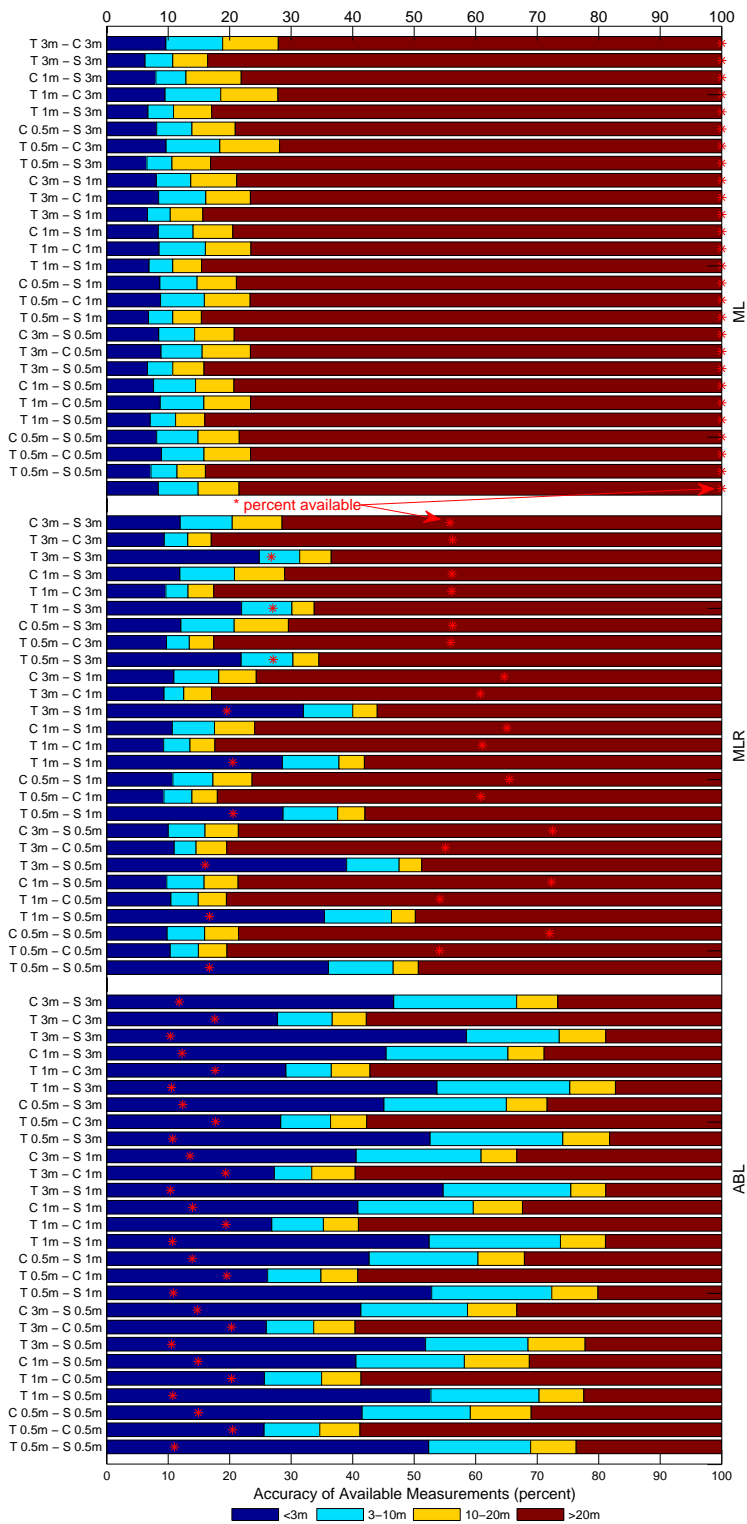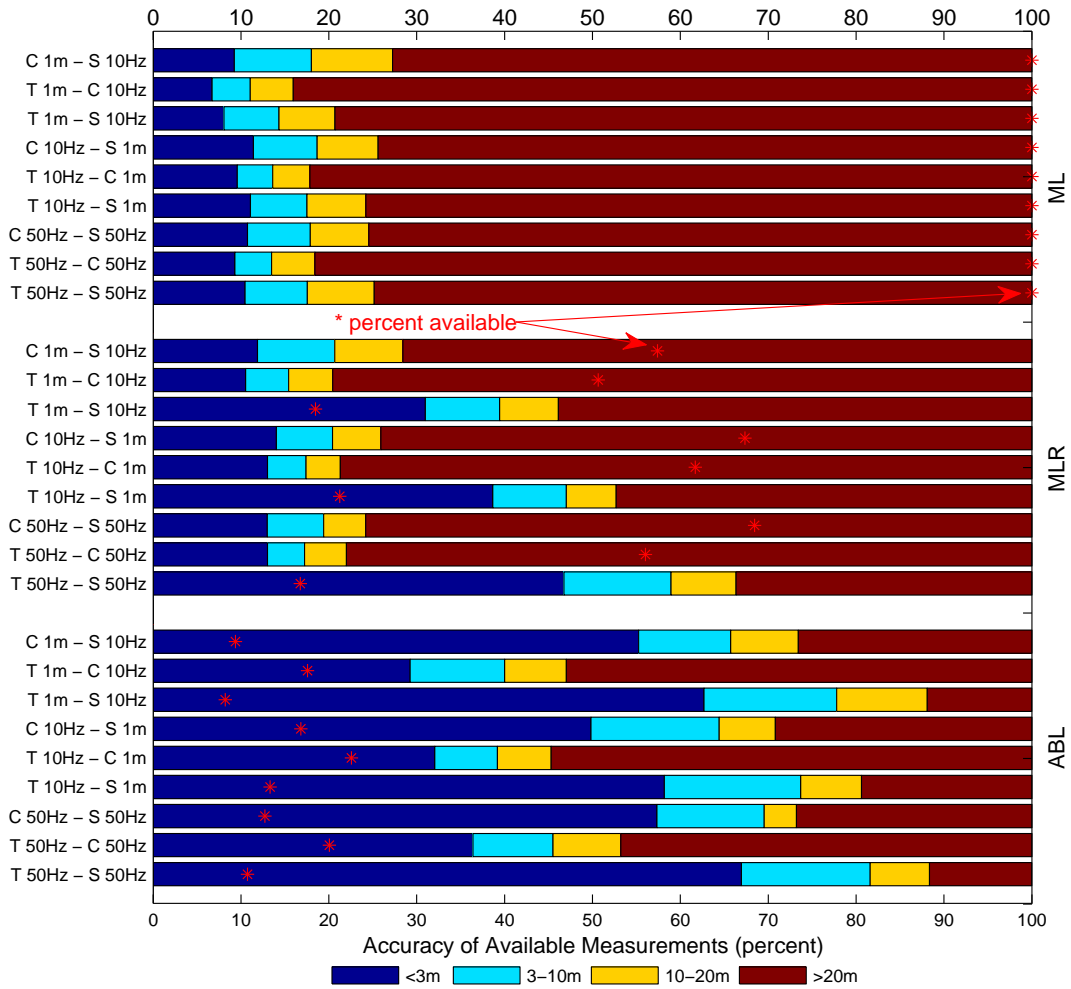
Figure 4.12:    Time/Distance variation results

show a very slight edge to measurements in time and maps in distance. In contrast, the ABL yielded a slight improvement in accuracy using measurements in distance and maps in time, albeit with a decrease in the percent available. For conclusive results a complete analysis is required and is recommended as follow-on work. For now, the acknowledgment that mixed variation is possible and produces acceptable results must suffice.

*4.5.4 Summary of Single Epoch Variation Results.* The analysis presented up until now covers the standard single epoch cases. Both in time and distance, the results conveyed the ability to match magnetometer measurements to the magnetic field map utilizing the various likelihood techniques. Not only were the effects of sampling rate explored, but the concept of using distance based maps and measurements yielded worthwhile results. This adequately prefaces the next section, probing the merits of multiple epoch measurement composition in order to improve matching accuracy.

*4.6 Multiple Magnetometer Measurement Composition*

Knowledge of velocity or distance traveled allows using magnetometer measurements based on distance for comparison with a distance based magnetic field map. This also allows investigation into different lengths and different measurement compositions. The composition of multiple successive magnetometer measurements separated by distance creates a measurement section. The measurement section can then be compared against sections in the magnetic field map. For example, if the measurements are separated by 1m and the map is composed of magnetic field measurements every 1m, a 3m measurement section could be formed for comparison. The impetus for comparing sections is the hypothesis that a particular section, especially if part of a feature, will be more unique than a single measurement, and therefore provide better accuracy when matching to the magnetic field map. The measure-

ment section also lends itself to other processing techniques such as demeaning and differencing.

Multiple magnetometer measurement composition is also possible using successive time samples and was explored, but had significantly lower results using calibrated or uncalibrated measurements. For instance, four 50Hz magnetometer measurements compared with four 50Hz magnetic field map measurements may or may not align in time, introducing another dimension of variability. Without velocity correction, the magnetometer measurement section may be expanded or compressed compared to the same measurement section in the magnetic field map due to velocity differences at the time of collection.

*4.6.1 Variation of Distance and Section Length.* In Figure 4.13, single epoch cases of the 1m measurement-map combination and the 3m measurement-map combination are compared against a 3m measurement section composed of 1m and 3m separation distances respectively. By definition, the single epoch cases use a single magnetometer measurement. The 3m section composed of 1m magnetometer measurements uses four measurements. The 3m section composed of 3m magnetometer measurements uses two measurements. Now instead of finding the best single epoch match, the comparison is a multipoint line of the measurement section.

Looking across all three likelihood techniques, the measurement sections composed of multiple magnetometer measurements outperformed the single epoch cases. In all but one case, the 3m section composed of 1m measurements surpassed the 3m section composed of 3m measurements. This seems intuitive, since a section composed of four points allows more distinction than a section composed of two points. Following this line of reasoning, a 3m section composed of 0.5m measurements was also explored but is not shown since the performance was nearly identical to the 1m measurement case. Conversely, the same was determined for measurement sections longer than 3m.

97
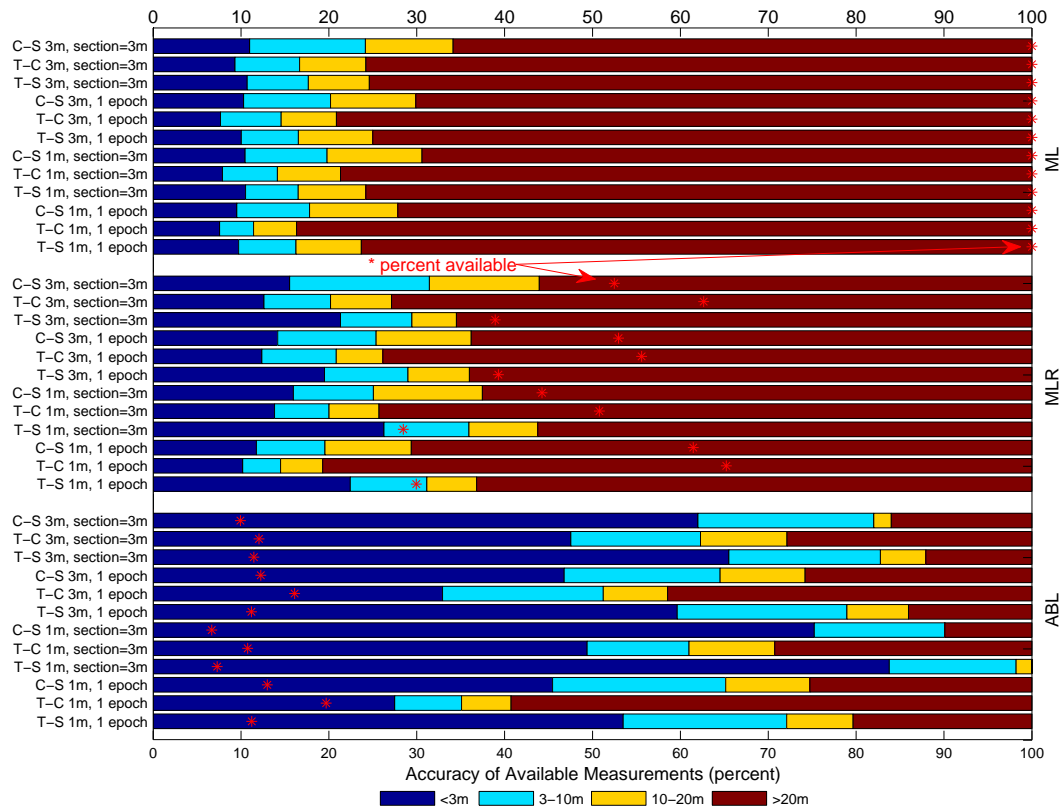
Figure 4.13:   Multiple measurement distance variation results.

Of notable importance, none of the maps or measurements start at exactly the same origin position. Therefore a 3m measurement section comprised of two 3m measurements could have a fundamental shift, such as 2m, which would cause less accuracy than the same 3m measurement section comprised of four 1m measurements. Also, this analysis is limited to the likelihood techniques developed as part of this research. A full expedition in multiple magnetometer measurement matching could be conducted to determine the most effective methods. This could include not only estimation techniques such as likelihood, but methods developed in the signal processing and/or image registration disciplines.

*4.6.2 Demeaning and Differencing.* Combining measurements into sections also provides the ability to examine the measurements in different ways. Two possibilities are demeaning and differencing. Demeaning subtracts the mean of the measurement section from the entire measurement section allowing comparison to a section of the magnetic field map that is also demeaned. Differencing uses the change between measurements or a section of measurements to identify the location on the map. For example, a section of four measurements is differenced to create a section of three measurements composed of the differences between the four section measurements. The likelihood is then conveying where the pattern of differenced measurements appears in the magnetic field map. Since these methods effectively eliminate the effects of bias, calibrated or uncalibrated measurements/maps can be used. Figure 4.14 displays the results of both demeaning and differencing using 3m sections composed of 1m measurements. Although not shown, results from sections composed of 0.5m and 3m measurements displayed similar results.

By and large, the demeaned cases yielded improved performance over the differenced cases. Although the baseline cases are not shown here, a quick glance at Figure 4.9 reveals that overall performance appears to decrease. However, for the Truck-Car cases, the accuracy improved dramatically using the MLR and ABL techniques.
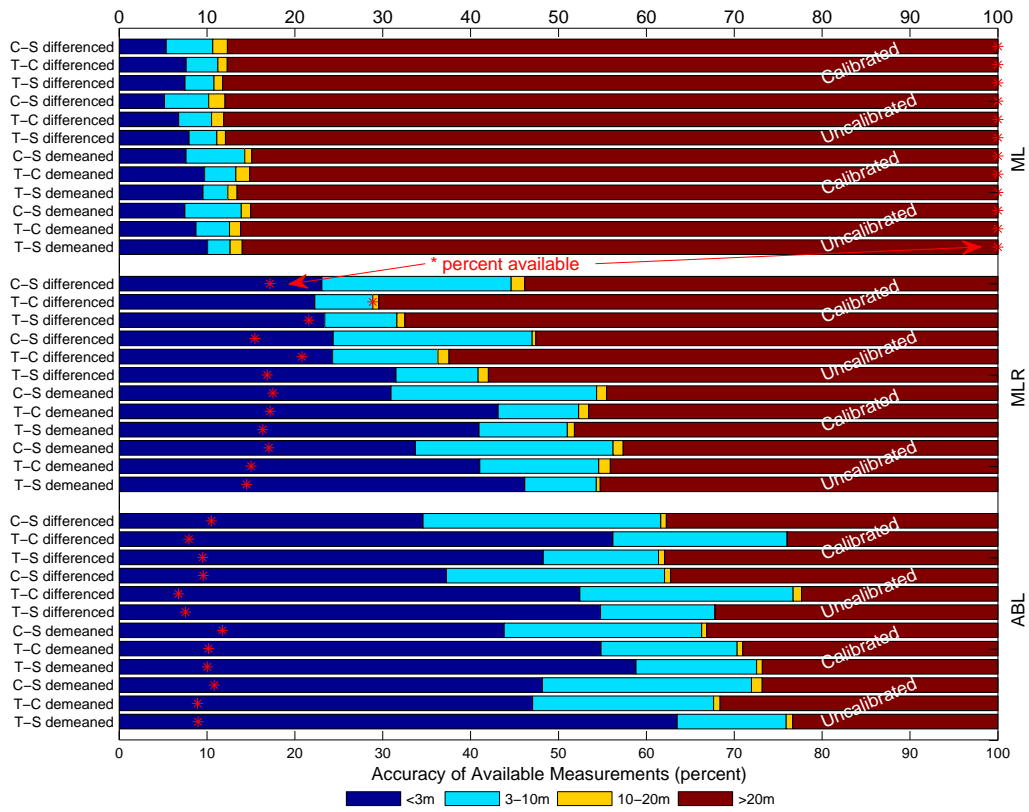
Figure 4.14: Demeaned and Differenced variation results using a 3m section composed of 1m measurements.

For the first time, calibrated and uncalibrated measurements can be compared for the cross-vehicle cases. Overall, the edge in performance is characteristic of the uncalibrated cases. This revelation elicits the potential of tremendously simplifying the map creation process. Instead of finding an empty parking lot with a fairly level surface and attempting to determine the possibility of hidden ferrous material underneath, the magnetic field map is effortlessly made "as-is" and the calibration process is eliminated. Although the decrease in performance is undesired, the simplification is certainly attractive.

*4.6.3 Magnetic Field Features.* Glancing back at the underground feature in Figure 4.4, it is easily seen that magnetic field features detail a deviation from the otherwise slowly changing magnetic field environment. Navigation by features seems like a logical extension from the multi-epoch cases already shown. However, there are a few distinctions.

Foremost, the features must be detected for both the incoming magnetometer measurements and in the magnetic field map. Not only must the feature be detected, but it must be determined to be fixed, or unchanging. While this research uses the advantage of multiple map tracks to identify fixed features, future work would explore aspects such as feature identification and false feature mitigation to ensure the magnetic field map only contained viable features for navigation.

Secondly, feature based maps are sparse when compared to the magnetic field maps thus far. The sparseness makes using the MLR and the ABL unsuitable, since both techniques often yield the same result as the maximum likelihood, or no result at all by determining the feature is not unique enough. Another comparison method is to use a "best-fit" method such as the root-sum-squared (RSS) to compare the magnetometer measurement feature with the features in the magnetic field map.

Comparing features also requires some adjustment in terms of feature alignment and length. The initial observation point of the magnetometer feature may

101

be slightly different than the feature in the magnetic field map, resulting in misalignment before comparison. While this is very easily done using the human eye, it is quite difficult for the magnetometer measurements which are similar in nature to signals, but in the feature sense also to images. The method employed here was simply to determine the defining peak (high or low) of the magnetometer feature and align it with the defining peak of the magnetic field map feature. The next issue is that features may be of differing lengths. Since the observed magnetometer feature may be slightly different in length than the magnetic field map feature, a minor alteration is necessary to make the feature comparisons of equal length. After aligning the magnetic field map feature to align with the magnetometer feature, the shorter of the two becomes the length for comparison. This is done for each feature in the magnetic field map, allowing the likelihood and RSS to be computed.

The RSS can be thresholded to determine the quality of fit which serves two purposes. First, it provides a way to discount a magnetometer feature which does not match any of the features in the magnetic field map well. A feature may be observed that may not be in the magnetic field map. Secondly, it allows the ability to adjust the quality of fit so that the observed magnetometer feature will match the correct feature in the magnetic field map. Again, the cost is the number of positions reported. An increase in the accuracy results in fewer reported matches. The maximum likelihood does not lend itself to thresholding since a feature can be equally poor when compared with the features in the magnetic field map, producing similar likelihood values. A comparison of how well an observed magnetometer feature can be determined from the features in the magnetic field map is shown in Figure 4.15. The results include features from calibrated data, as well as features using the demeaned and differencing techniques for both calibrated and uncalibrated data.

The familiar Truck-SUV, Truck-Car, and Car-SUV cases consist of calibrated features composed of 1m measurements. Although not shown, results from features
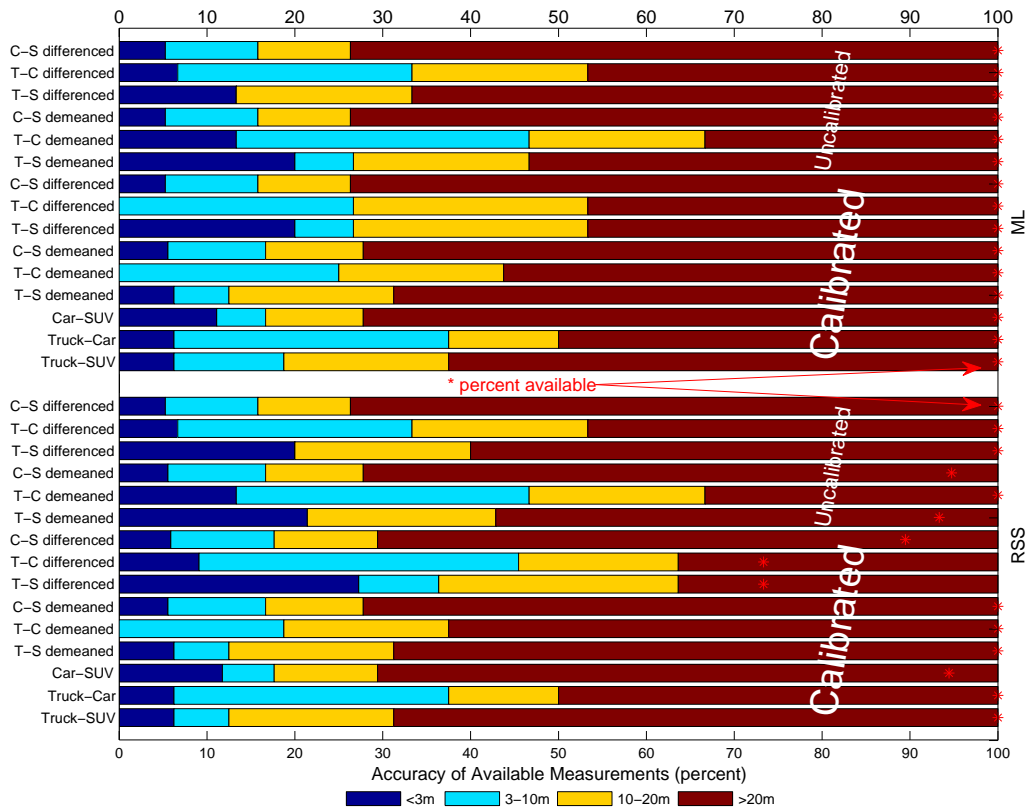
Figure 4.15: Results using features composed of 1m measurements, including the additional techniques of demeaning and differencing.

composed of 0.5m and 3m measurements displayed similar results. In most cases, the RSS provided similar results to the maximum likelihood.

Of particular interest is the lack of improvement for the calibrated demeaned cases while the calibrated differenced cases show improvement using either the maximum likelihood or the RSS. The opposite is revealed for the uncalibrated cases. Since the bias has already been removed during the calibration process, attempting to further demean simply reduces the differences in the observed magnetometer feature and the features in the magnetic field map such that the RSS becomes arbitrarily lower due to demeaning, not due a better fit. Imagine a small feature, large enough to be detected but with only a small peak and short in length (e.g. 20mG and 1m) in a single axis. When compared with the features in the magnetic field map the RSS will be nearly equal due to the demeaning of both the observed magnetometer feature and the features in the magnetic field map.

While the RSS is adjustable, it is not always better than the maximum likelihood. However, this analysis does show the results comparing the two very straightforward methods. Future work in this area would include better methods to feature match using tools from both the signal and image recognition skillsets.

4.7    *Targeted Investigation of the Neighborhood and Large Area Maps*

The analysis thus far helped determine the techniques and magnetometer measurement compositions demonstrating the most success. This is necessary, since the significant increase in map area discourages the use of 50Hz data due to the volume of measurements and processing time. In addition, over a large area the effects of driving variability are increased due to traffic, parked vehicles, and other uncontrollable circumstances. The remaining analysis will focus on how these techniques fare in the significantly larger suburban neighborhood and large area map environments from Figure 4.1. Although the rightmost map in Figure 4.1 shows all three maps, the
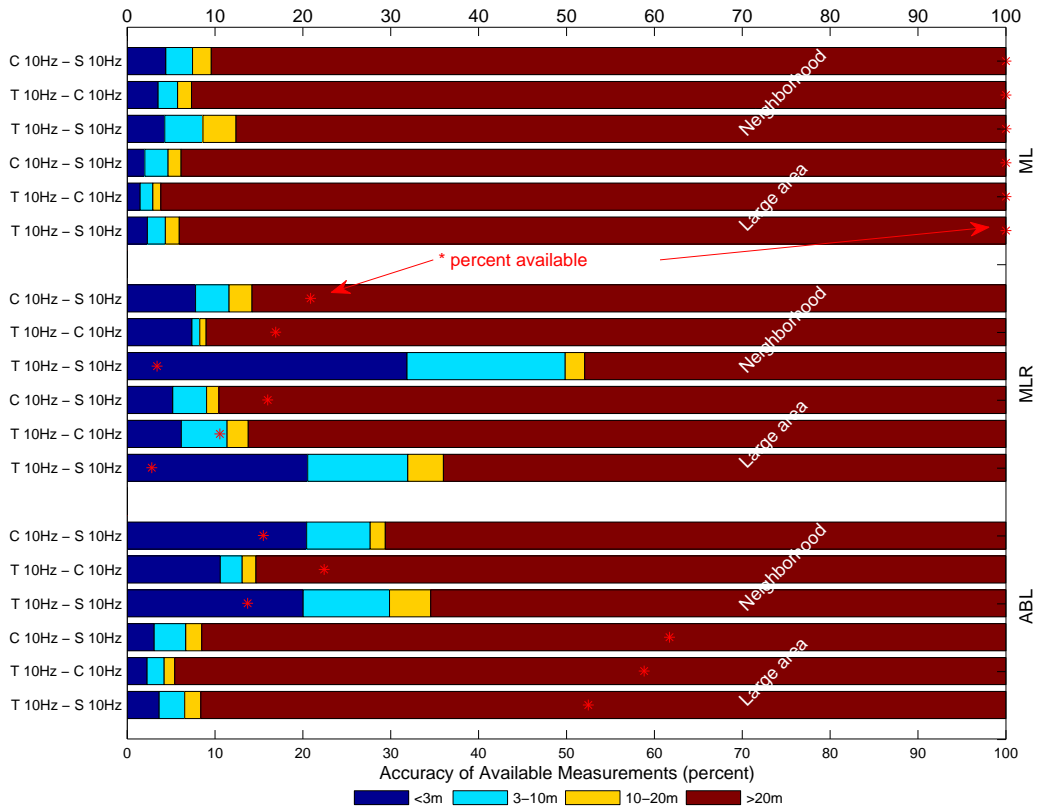
Figure 4.16:    Results for test cases which use single epoch 10Hz magnetometer measurements with 10Hz neighborhood and large area time-based magnetic field maps.

large area map investigation excluded the AFIT map and suburban neighborhood map portions to prevent duplication of effort.

*4.7.1   Magnetometer Measurements Based on Time.*    Recalling that the 10Hz-10Hz cases from Figure 4.10 performed nearly as well as the 50Hz-50Hz cases, Figure 4.16 conveys the cross-vehicle cases for the neighborhood and large area maps using 10Hz magnetometer measurements and a 10Hz magnetic field map. A brief comparison with the baseline cases in Figure 4.9 reveals a definite drop in the ability to accurately match the incoming magnetometer measurements to the magnetic

field map. This is expected, since the neighborhood map area and layout also decrease the amount of truly unique magnetometer measurements across the magnetic field map. Or said another way, the increased number of measurements with similar characteristics makes discerning a particular position from the magnetic field map more difficult. These circumstances provide the motivation for using the neighborhood, since parallel roads and similar environments tend to yield very similar magnetometer measurements. This also emphasizes the expectation that as the map area increases, there will be fewer truly unique magnetometer measurements in the magnetic field map.

The maximum likelihood is consistent across both maps, but realizes nearly a 40% reduction in accuracy compared to the baseline 50Hz data in the AFIT magnetic field map. The MLR technique shows mixed results. Although the Truck-SUV cases continue to have higher accuracy, the percent available is uncharacteristically low. Adding another oddity, the ABL technique suffers from reduced accuracy using the large area map yet also displayed an increase in the percent available. This indicates the configurable threshold for the ABL technique is too low for such a large area and volume of measurements. However, changing the threshold at this juncture would complicate the unbiased review of each technique across all measurement compositions and map areas. Both the MLR and ABL techniques have configurable parameters which can obtain improved accuracy at the expense of the percent available. Since the focus is not the optimum configuration of a particular technique, holding the configurable parameters constant seems prudent.

*4.7.2  Magnetometer Measurements Based on Distance.*    Switching to distance based magnetometer measurements and magnetic field maps yielded a slight improvement a shown in Figure 4.17. Compared to Figure 4.16 the results are very similar, conveying that using single epoch 1m or 3m separated magnetometer measurements is as effective as using 10Hz measurements for the neighborhood and large area maps. This was also supported in the smaller AFIT map cases.
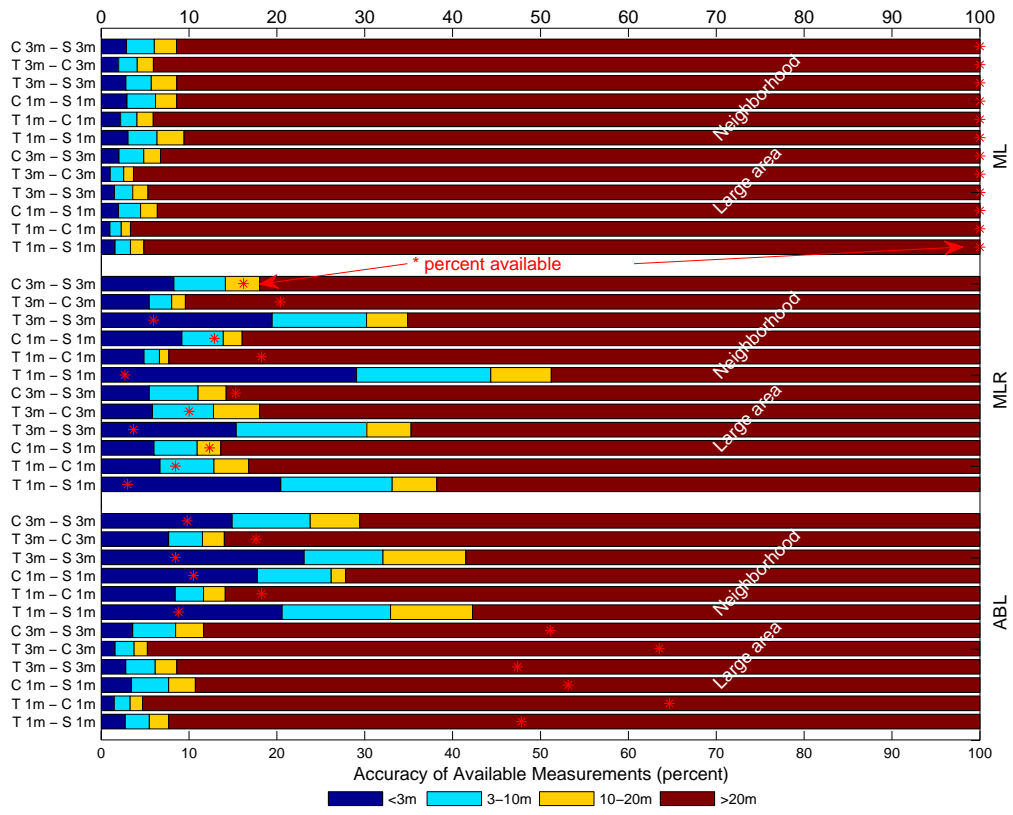
Figure 4.17: Results for test cases which use the neighborhood and large area distance based maps.
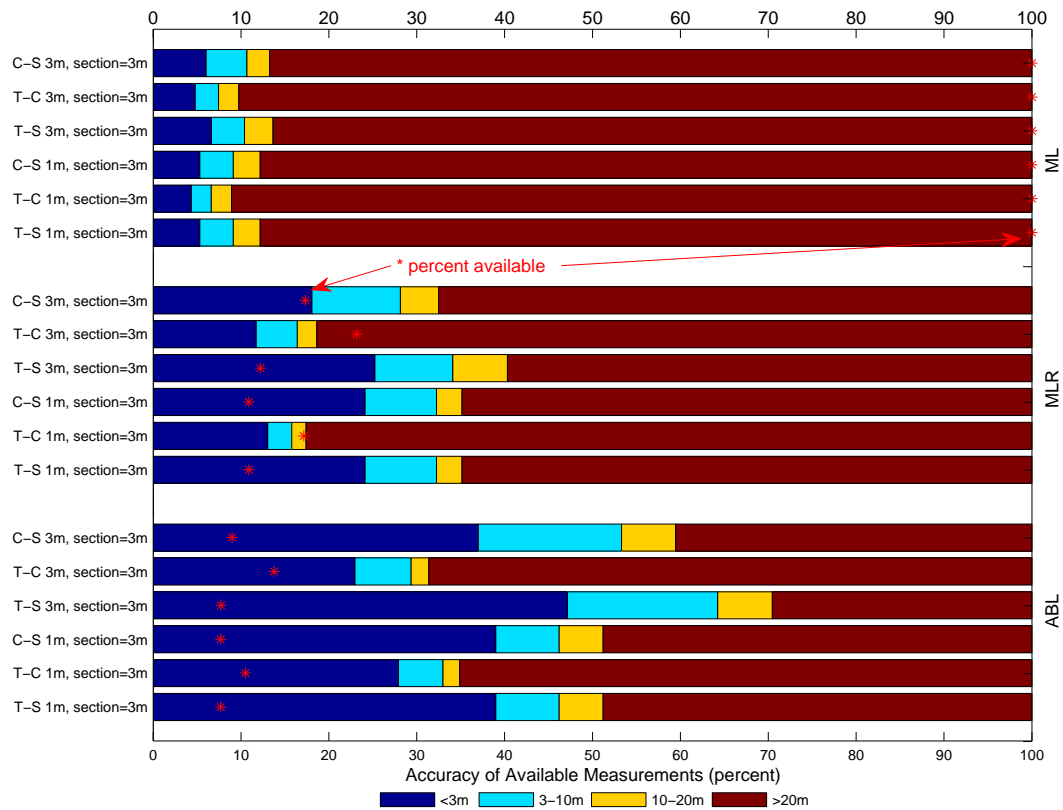
Figure 4.18:    Results for test cases which use the neighborhood section based maps.

*4.7.3   Multiple Magnetometer Measurement Sections.*    The measurement sections formed from successive multiple magnetometer measurements attempt to exploit the distinctiveness of each measurement such that the section emphasizes only similar sequences found in the magnetic field map. Figures 4.18 and 4.19 show the improvement across all techniques is evident, which uses 3m measurement sections composed of 1m and 3m separation distances, respectively.

While the maximum likelihood is nearly the same, the results of the neighborhood and large area maps are separated here to show the differing results for the MLR and ABL techniques. For the neighborhood map in Figure 4.18, the MLR technique results were comparable using either separation distance. The ABL technique

108
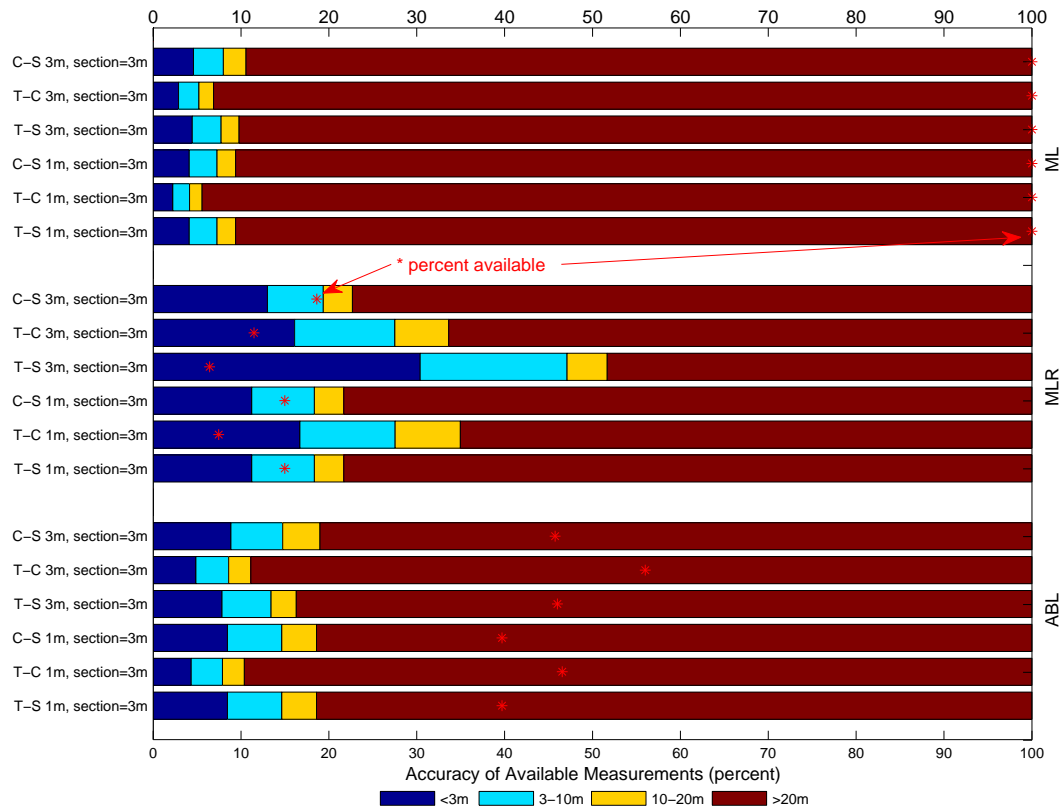
Figure 4.19:    Results for test cases which use the large area section based maps.

offered further improvement, without a significant drop in the percent available. On the other hand, the large area map in Figure 4.19 displays varying results for the MLR technique, with a slight edge to the 3m section composed of 3m measurements. However, the ABL technique reverted back to the lower accuracy with higher percent available results seen in the single epoch cases.

*4.7.4   Demeaning and Differencing.*     Again, the techniques of demeaning and differencing were applied and shown in Figures 4.20 and 4.21. While the overall results are lower compared to the smaller AFIT map, the performance is improved compared to the 10Hz-10Hz cases initially shown for the neighborhood and large area map cases. The uncalibrated measurements continue to edge the calibrated measurements in most cases. Additionally, the majority of demeaned cases continue to outperform the differenced cases. Regarding the neighborhood map results in Figure 4.20, the ABL technique shows a slight improvement versus the MLR technique. However, in the large area map, performance was comparable.

*4.7.5   Features.*     The neighborhood and large area maps shown in Figures 4.22 and 4.23 show reduced accuracy compared to the results from the AFIT map in Figure 4.15, as expected. Again, the three cross-vehicle cases are compared in Figure 4.22 for calibrated data as well as the demeaned and differenced techniques for both calibrated and uncalibrated data. Although some variation in results is evident, the performance is comparable between the maximum likelihood and the RSS. The results from the large area map in Figure 4.23 depict a further reduction in the overall accuracy, but slightly different performance from the individual techniques. For both the maximum likelihood and the RSS, the uncalibrated demeaned data showed a slight edge in most cases.

The ability to accurately determine position based on the magnetometer feature and the magnetic field map is affected by reduction in unique features as map size increases. To combat this problem, limiting the magnetic field map features
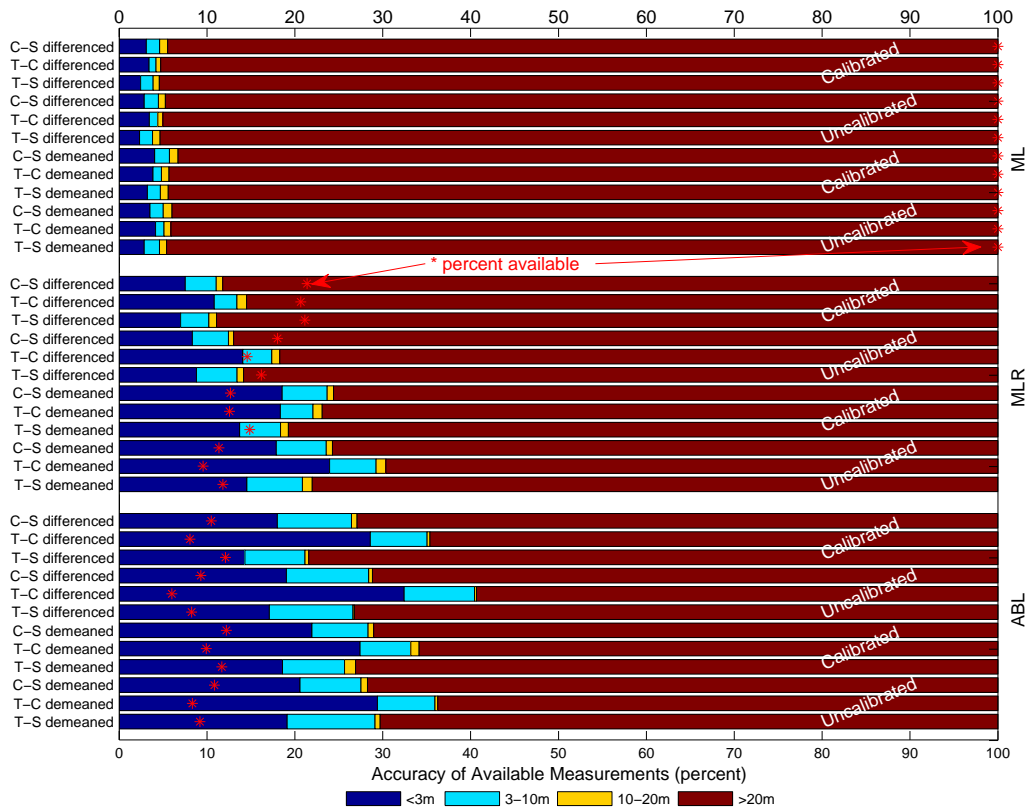
Figure 4.20: Demeaned and Differenced variation results using a 3m section composed of 1m measurements using the neighborhood map.
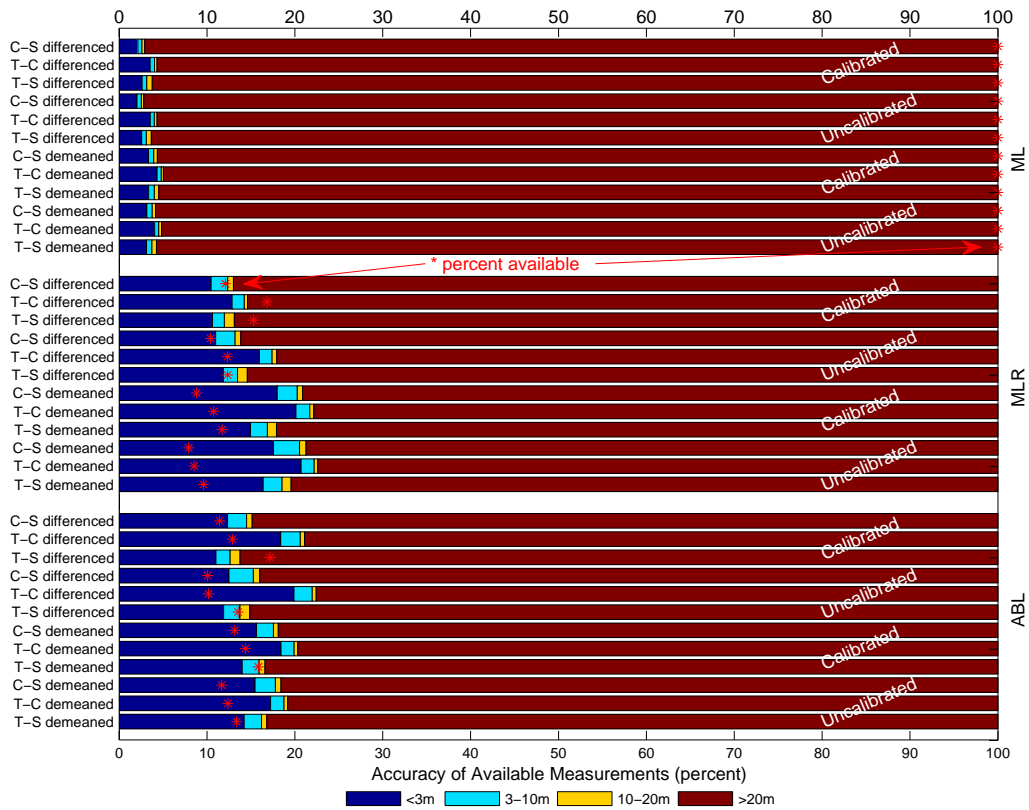
Figure 4.21: Demeaned and Differenced variation results using a 3m section composed of 1m measurements using the large area map.
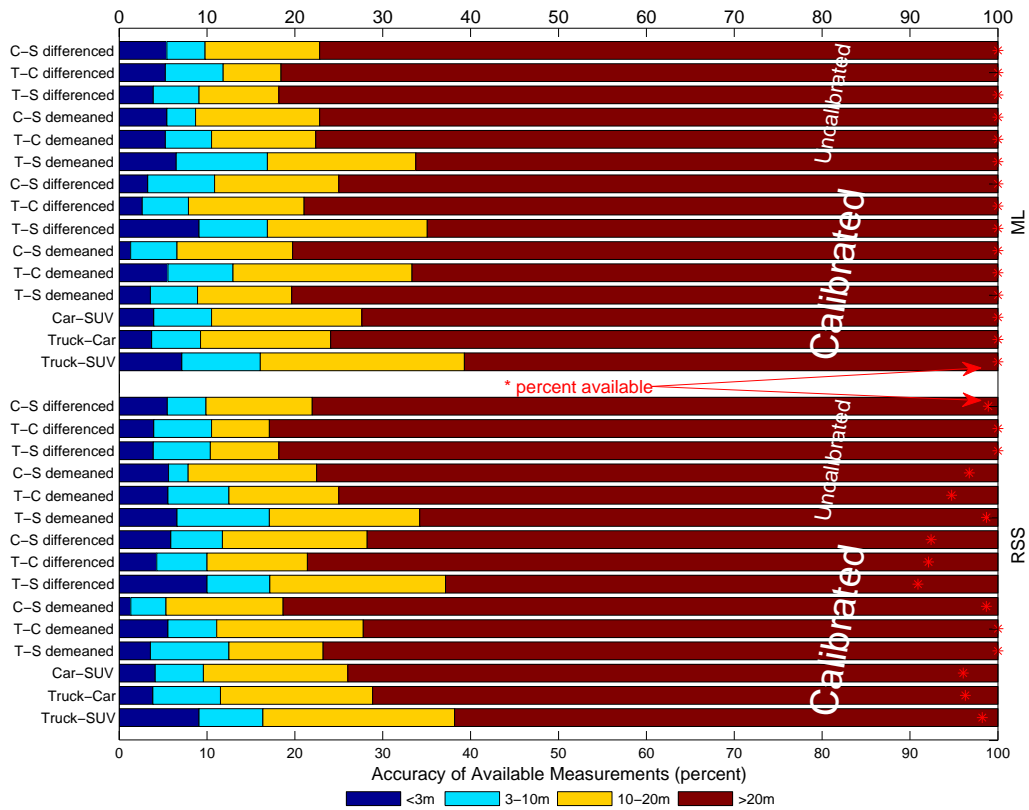
Figure 4.22: Results using features composed of 1m measurements, including the additional techniques of demeaning and differencing for the neighborhood map.
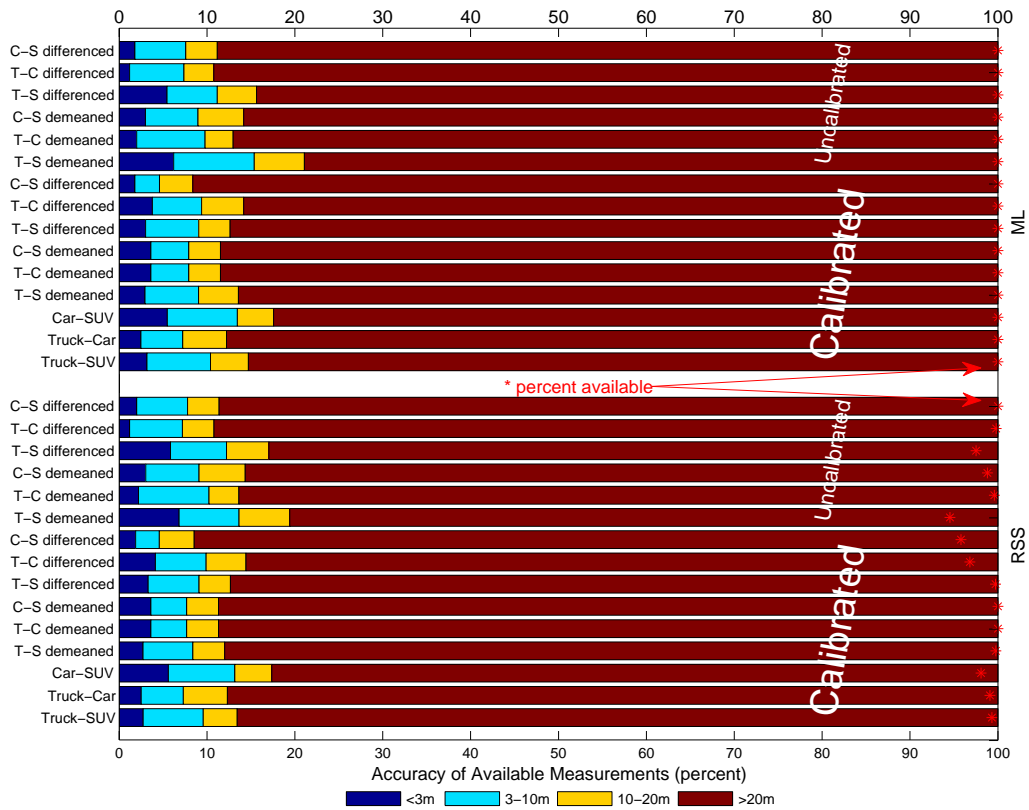
Figure 4.23:    Results using features composed of 1m measurements, including the additional techniques of demeaning and differencing for the large area map.

to only those within a specified distance of the last known position would greatly increase the ability to identify the matching feature and determine the next position with greater accuracy.

## 4.8   Summary of Chapter Results

Overall, the results presented here guide the optimal measurement composition based on the type of available measurements, the environment, the ground vehicle characteristics, and the processing capability. For example, if only uncalibrated measurements can be used for a cross-vehicle scenario, the demeaning technique using distance separated measurement sections is the most suitable. Another example might include an attempt at real-time response with minimal processing power in the same vehicle, which would suggest using the maximum likelihood with either calibrated or uncalibrated magnetometer measurements. Standalone, these techniques provide straightforward estimates of position based solely on magnetometer measurements and the magnetic field map. The MLR and ABL techniques deliver configurable levels of accuracy at the expense of the availability of measurements. The primary factor in accuracy is the ability to distinguish unique magnetic field measurements and the reduction in that ability as larger map sizes expose more areas with similar magnetic field environments. Finally, this chapter offers many detailed results. A few of the key points are expressed here.

- The ability to align the magnetometer measurement to the same position over multiple runs is crucial to the mapping process. Multiple passes over the same route include measurement error as well as position error due to normal driving variation.

- Increased sampling is important for interference mitigation during installation/setup. Reduced sampling during position estimation provided nearly the same results as long as the sampling rate effectively captured the changes in the observable magnetic field.

- Measurements/maps based on time contain extra measurements which do not necessarily provide additional information (such as while stopped for extended periods). Distance-based measurements/maps help rectify this problem, but require knowledge of distance-traveled to be used in this way.

- The high degree of repeatability between magnetometer measurements and position in the same-vehicle cases translated into significantly better position estimates over the cross-vehicle cases. Although calibration was improved in Chapter III, substantial work remains in reducing the differences between magnetometer measurements from different vehicles.

- For single epoch cases, the 10Hz measurement/map combination provided the best position estimation capability. However, the 3m section composed of 1m measurements provided similar performance using the ML and MLR techniques, but nearly a 15% increase in accuracy using the ABL technique. The use of the measurement sections also allowed uncalibrated magnetometer measurements to be used for cross-vehicle cases using the demeaning and differencing techniques.

  .

## V.  Ground Vehicle Magnetic Field Navigation

$\mathrm{T}$HIS research has determined that magnetic field maps are repeatable, even between dissimilar vehicles. The research has also shown the level of accuracy in determining a position based on a magnetometer measurement and the magnetic field map, dependent on the measurement composition. What remains is how well this information can be used for navigation. The next logical step is to generate a navigation solution and evaluate the level of performance dependent on the measurement used in the navigation filter. A particle filter as described in Section 2.7 is used to compare the performance when using various measurements.

### 5.1   The MagNavigate Particle Filter

Since the particle filter is not the focus of the development, the navigation solution comparison will use the same particle filter and modify the measurement composition. This allows an evaluation of the potential navigation accuracy of the different measurement compositions as they apply to the navigation solution. This also allows comparison using a position estimate as the measurement, capitalizing on the techniques demonstrated in Chapter IV. However, a few details on the particle filter should be explained. Recalling the particle filter information from Chapter II, the collection of particles and weights is expressed as

$$\mathbf{X} = \left[ \begin{array}{cccc} \mathbf{x_1} & \mathbf{x_2} & \ldots & \mathbf{x}_{NP} \end{array} \right]^{\mathbf{T}} \qquad NP = \text{number of particles} \qquad (5.1)$$

$$\mathbf{W} = \left[ \begin{array}{cccc} w_1 & w_2 & \ldots & w_{NP} \end{array} \right]^{\mathbf{T}} \qquad\qquad\qquad\qquad (5.2)$$

$$1 = \sum_{i=1}^{NP} w_i \qquad\qquad\qquad\qquad (5.3)$$

with the state vector of each particle represented as

$$\mathbf{x} = [\mathbf{p} \ \mathbf{v} \ \mathbf{a}] \qquad\qquad\qquad\qquad (5.4)$$

117

where $\mathbf{p}$, $\mathbf{v}$, and $\mathbf{a}$ are the 2D position, velocity, and acceleration vectors. The filter is initialized by randomly placing the particles within 50m of the true position, with zero velocity and acceleration. The navigation solutions presented here are the weighted particle mean at each epoch. The number of particles used is 500, which is sufficient to prevent divergence, but not overly burdensome for processing on a typical 2.66 gigahertz 32-bit laptop with 4 gigabytes of random access memory. To gain a sense of processing time, a 20 minute collection of measurements separated by a distance of 1m could be processed in approximately four minutes using the particle filter implemented in `Matlab`$^{®}$ .

Particle propagation is performed using a first-order Gauss-Markov acceleration model [32], with a time constant of 2 seconds and a standard deviation of 5 m/s$^2$, reasonable for a ground vehicle including starting and stopping. Particles propagated freely based on the dynamics model, but are penalized based on their distance from the closest known map location. This is accomplished by including an additional Gaussian likelihood function (Equation 2.51) based on the distance of each particle from the closest known map location, with a mean of zero and a standard deviation of six meters.

Figure 5.1 gives an illustration of the propagation cycle. The upper left of Figure 5.1 shows the initial random particle collection (red dots) before any distance based restriction is applied using the suburban neighborhood map (thin black line). The weighted particle mean (blue asterisk, which overlays the black dot) conveys the current position estimate. The uncertainty (dashed blue line) is calculated as in Van der Merwe [36]. After the map-matching likelihood update is applied to the particle weights and resampled [40], the particles near the road have been kept as well new particles spawned near the same locations, seen in the upper right of Figure 5.1. As propagation continues, if no measurement updates were applied the particles will continue along the map. The lower left depicts propagation after 100 cycles when no measurement updates were applied. The vehicle track via the vehicle (thick black

118
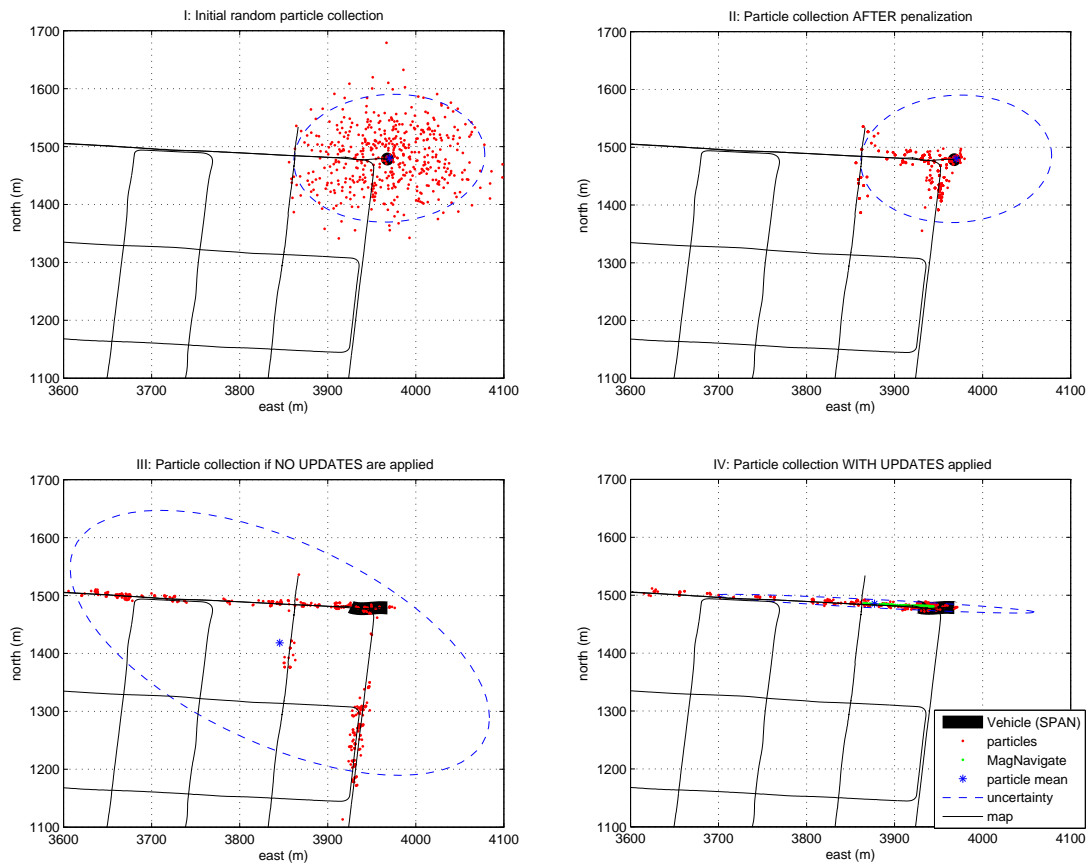
Figure 5.1:    Examples of particle filter propagation in the suburban neighborhood map.

line) conveys how far the position should have moved. In contrast, the lower right shows the particle collection after 100 propagation cycles when regular measurement updates were applied, conveying movement along the road. The navigation solution (MagNavigate green dots) highlight the weighted particle mean, slightly ahead of the vehicle track. Particle resampling occurs after each update to eliminate particles which are no longer viable and introduce new particles [40]. The outcome is a navigation solution detailing the position of the vehicle based solely on the magnetometer measurements and magnetic field map.

In order to compare the two different measurement inputs ($\mathbf{z}$ in Equation 2.51) to the particle filter, the measurement update in the particle filter consists of either a position update or a magnetometer update. The position update refers to obtaining a position estimate based on the likelihood techniques in Chapter IV (maximum likelihood, MLR, or ABL). The position update is expressed as

$$\mathbf{z} = [p_E \; p_N] \tag{5.5}$$

where the east position $p_E$ and north position $p_N$ are in the local level frame. Similarly, the magnetometer update using the three-axis measurements directly from the magnetometer is expressed as

$$\mathbf{z} = [\hat{B}_x \; \hat{B}_y \; \hat{B}_z] \tag{5.6}$$

where $\hat{B}_x$, $\hat{B}_y$, and $\hat{B}_z$ are the observed three-axis magnetometer measurements in the $x, y$, and $z$-axis, respectively. The magnetometer axes were aligned with the body frame of the vehicle.

The position coordinates were converted to a local level frame of east, north and up (ENU) using a coordinate transformation. All roadways were traversed under normal conditions (i.e., speed limits, stop signs, traffic lights, passing vehicles, pedestrians). Appendix B contains navigation solutions for different measurement compositions as well as the navigation solution test matrix for all of the comparisons.

For the navigation results presented in this chapter, an overview of the navigation track for each map area compares the navigation solution to the actual vehicle track. Additionally, the corresponding error plot provides detailed error information as well as insight into filter performance. The errors in each axis as well as the overall position error are prefixed by $\delta$ (e.g., the error between the navigation solution and the actual vehicle position in the east axis is $\delta$E). These figures as well as

performance statistics for several navigation solutions are used to provide a deeper understanding of navigation using magnetic field variations.

## 5.2  Navigation Solutions

The smaller map around AFIT offers an excellent introduction to navigation solutions using magnetic field variations, as seen in Figure 5.2. The AFIT map area served as a fairly benign environment for initial investigation and is representative of the navigation solution tracks around AFIT. The SPAN provided the vehicle track (thick black line) for comparison to evaluate the typical accuracy of the navigation solution. The navigation solution (MagNavigate dotted green line) represents the weighted particle mean. While the system appears to track quite well, Figure 5.2 does not convey the "along-track"' error in the system. The corresponding position error plot in Figure 5.3 displays the position errors versus time for east, north, and horizontal position.

At first glance, the error information in Figure 5.3 does not seem to correlate with the nearly perfectly overlapping tracks in Figure 5.2. Even at the depicted scale, a 44m position error should be noticeable. Recalling that the magnetic field changes slowly when features or heading changes are not present, the navigation solution suffers from propagation error. On the straight portions of Figure 5.2 good measurement updates may not be available due to the lack of change in the magnetic field which in turn causes the large propagation error. Secondly, a magnetic field map location further along the road may match up well with the recent incoming magnetometer measurement, causing the navigation solution to surge ahead. The filter must be agile enough to catch up when the measurements cause the particle velocities to slow down significantly, which in turn enables the possibility of surging ahead.

Focusing on Figure 5.3 also provides key insight into the performance of the navigation filter. The along-track error previously mentioned can easily be seen in
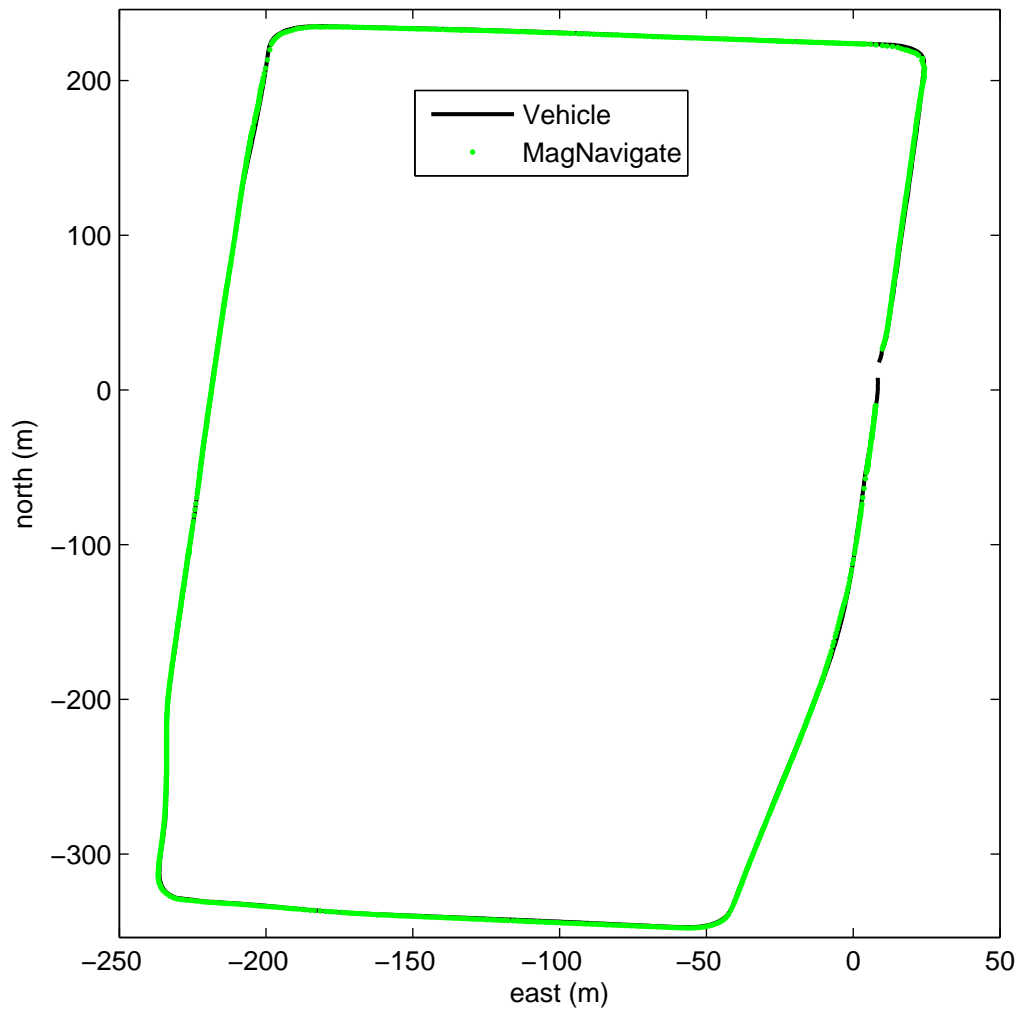
Figure 5.2:    AFIT map navigation using 1m distance separated magnetometer measurements in the navigation filter. The Vehicle track (thick black line) and MagNavigate track (dotted green line) are shown.
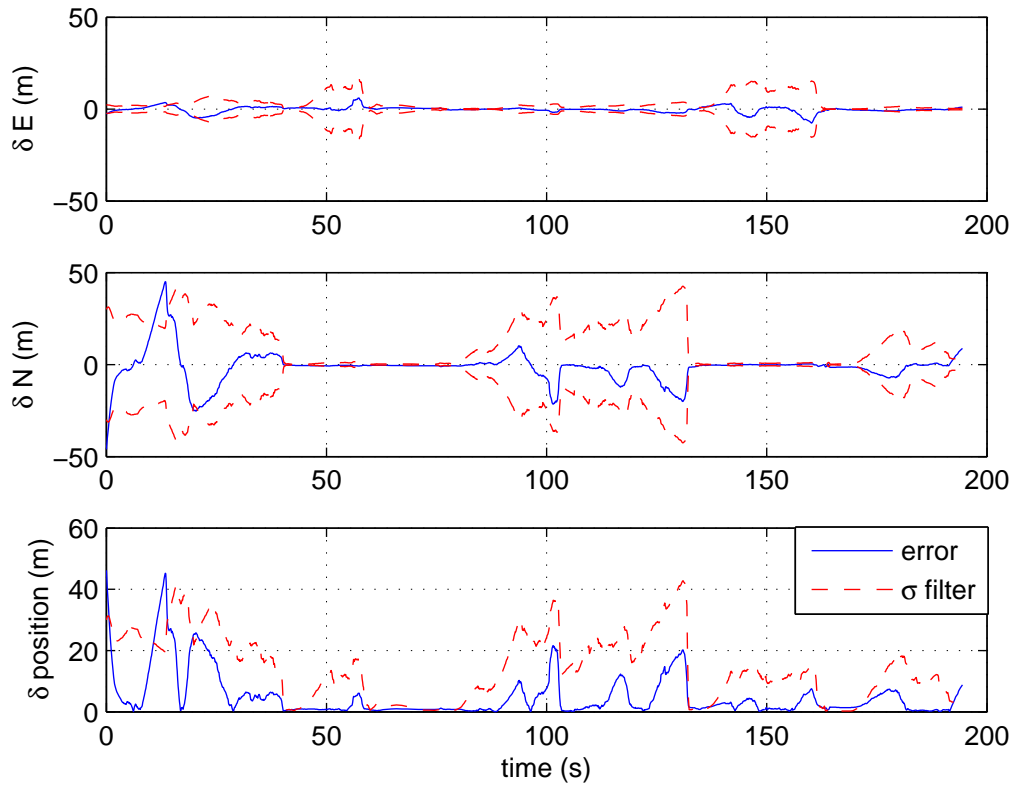
Figure 5.3: MagNavigate position errors (solid blue line) as compared with the actual vehicle position using the AFIT map. The dotted red line represents the standard deviation of the particle collection. The max position error is 44m, and the RMS position error is 8m.

each axis as well as the overall position error. In each axis, a positive error highlights when the navigation solution is slightly behind the vehicle track. Conversely, a negative error in each axis reveals the navigation solution has surged ahead of the vehicle track. This explains the sudden shift from 45m to -25m of error in the north (N) axis in just six seconds. The bulk of the particles are traveling slower than the actual vehicle, causing the gradual increase in error. Suddenly, a measurement update (or several measurement updates) with very good measurements cause the weighted particle mean to surge forward, ahead of the actual vehicle track. As additional good measurement updates are processed, the particle filter converges on the correct solution and reduces the position error. The transition from large uncertainty to convergence is indicated by the standard deviation $(1\text{-}\sigma)$ of the particle collection, highlighted by red dashes. The filter $1\text{-}\sigma$ provides an indication of how well the filter is performing as well as the general spread or uncertainty in the particles.

Overall, Figures 5.2 and 5.3 represent the characteristics of the navigation filter for all navigation solutions presented in this chapter. However, performance will be affected by different measurement compositions and more challenging environments. Now that the concept of the particle filter has been developed along with a sample navigation solution and errors, the focus can shift to performance depending on the measurement update applied.

*5.2.1  Navigation Performance Using A Position Update.*    As previously mentioned, the particle filter can use a position update ($\mathbf{z} = [p_E \; p_N]$ from Equation 5.5) as the incoming measurement based on the likelihood techniques in Chapter IV. While the position update is certainly useful for applications such as updating an inertial system, standalone navigation performance can be compared with the magnetometer update in the next section to determine the advantages/disadvantages of each update method.

First, the most promising position update methods were chosen based on results in Chapter IV. The cross-vehicle cases were examined using calibrated measurements consisting of a) a single epoch, b) a 3m section composed of multiple 1m epochs, and c) a 3m uncalibrated demeaned section composed of multiple 1m epochs. Examining repeated plots such as Figures 5.2 and 5.3 for every combination of navigation solution would be cumbersome. Instead, the results have been grouped to show performance statistics for comparison of the overall position errors by using the maximum position error and the horizontal RMS position error. Figure 5.4 provides the results of navigation solutions using a position estimate as the measurement in the navigation filter.

Using the same nomenclature from Chapter IV (e.g. T-S 1m conveys the Truck-SUV case using 1m separated magnetometer measurements and magnetic field map), three cases using the three likelihood techniques are shown in Figure 5.4. For each case the maximum horizontal position error is displayed in red along with the horizontal root-mean-square (RMS) position error in blue. Across all results, single epoch measurement updates were nearly as effective as the 3m section of multiple epoch measurements. Also, the 3m uncalibrated demeaned section of multiple epoch measurements did not deliver stellar navigation performance. However, the ability to use uncalibrated measurements from different vehicles for navigation is verified.

Since the MLR and ABL only provide position updates when the magnetometer measurements uniquely match the magnetic field map, these techniques often result in a better quality position estimate, yet reduced availability. In contrast, the maximum likelihood provides a position estimate at each epoch, but the results in Chapter IV conveyed the match is often incorrect. Yet the navigation filter is able to use the more frequent, but less accurate, maximum likelihood nearly as effectively as the less frequent, but more accurate, MLR updates. Figure 5.5 depicts the significant propagation error for the ABL as a result of the much lower availability. While the ABL is often more accurate in obtaining the position estimate in Chapter

125
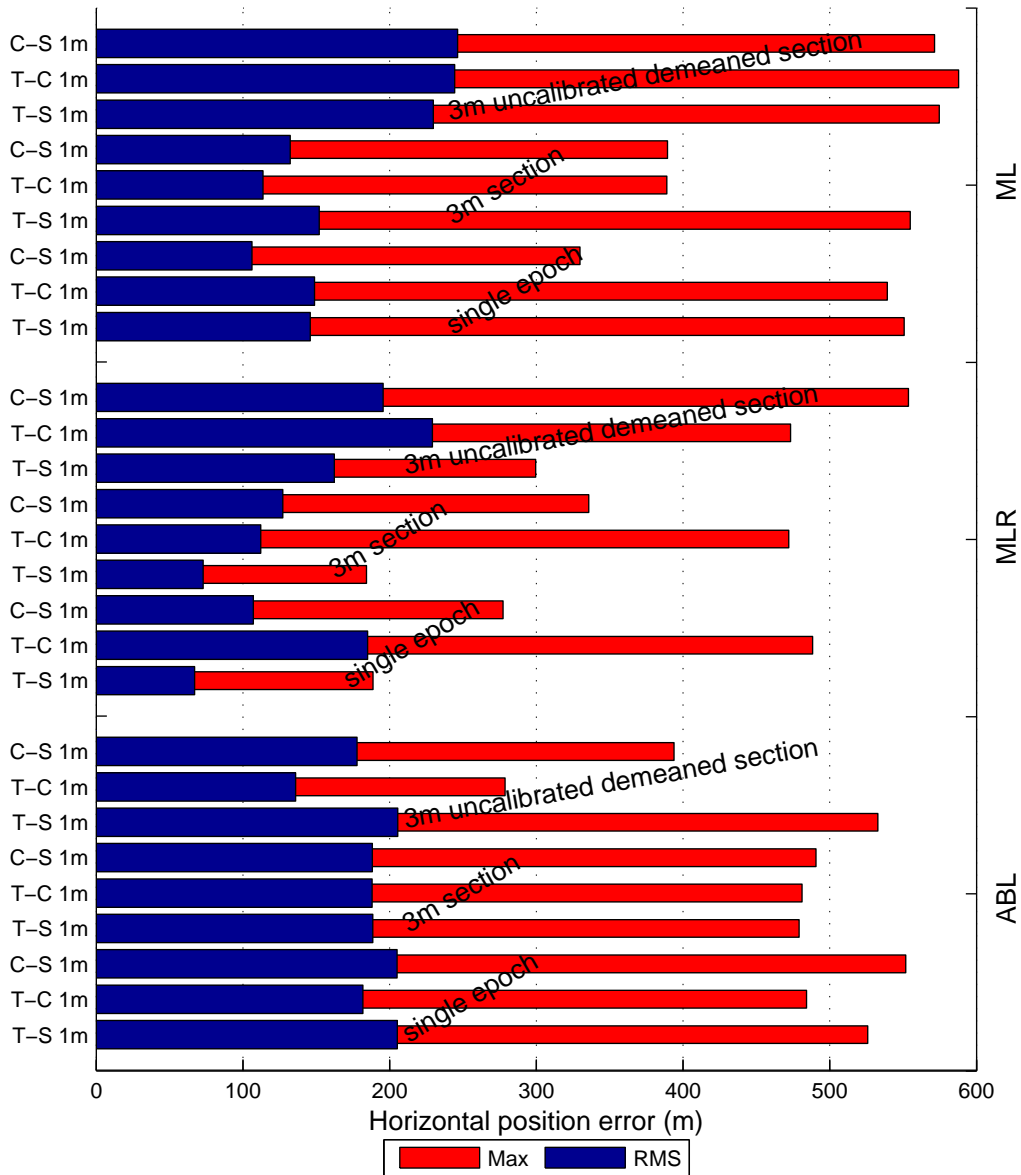
Figure 5.4: Navigation performance comparing measurement composition methods when used as a position update in the navigation filter.

126
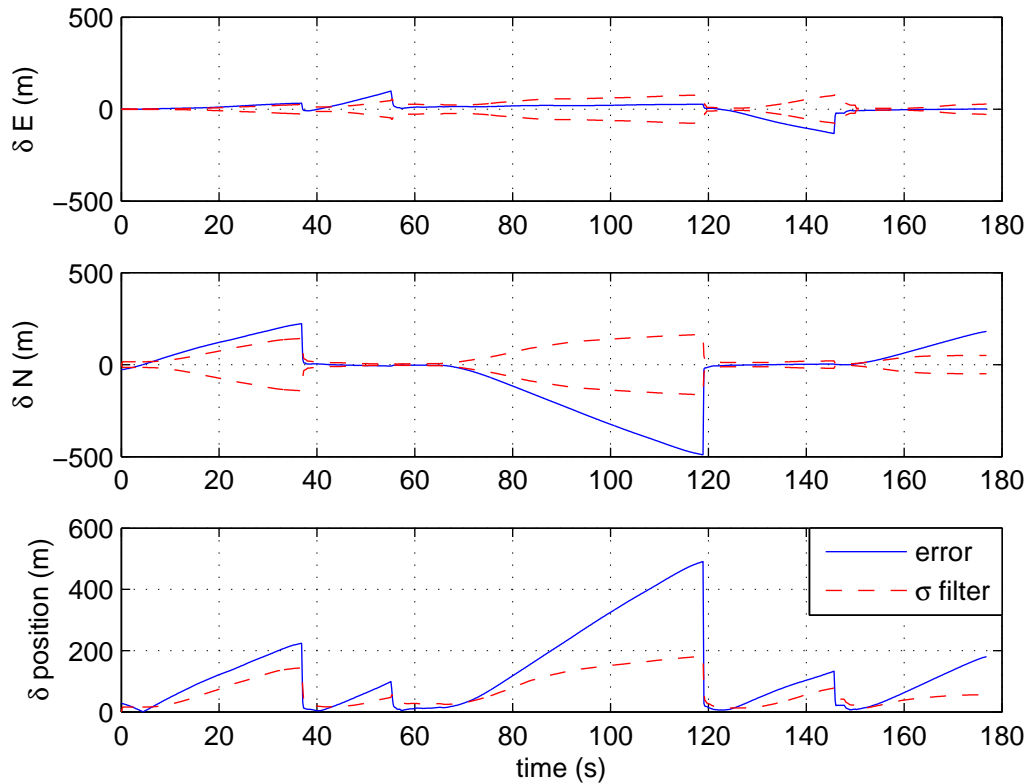
Figure 5.5: AFIT map errors using the ABL technique to select the position estimate for the navigation filter.

IV, the much lower availability allows the navigation solution position error to grow significantly before a measurement update is applied, yielding large max and RMS position errors. However, the navigation solutions immediately following the update have less than 20m of error, with some updates providing solutions with less than 3m of error.

While not exhaustive, these results highlight the typical navigation performance utilizing a position update in the navigation filter based on the techniques from Chapter IV. The MLR provided the best mixture of accuracy and availability resulting in the best performance from this particle based navigation filter. The next step is to use the actual magnetometer measurements as the measurement update to the navigation filter.

127

*5.2.2 Navigation Performance Using A Magnetometer Update.* The goal for this research from the outset has been to use the measurements received from the magnetometer as direct input to the navigation filter. The magnetometer update ($\mathbf{z} = [\hat{B}_x \ \hat{B}_y \ \hat{B}_z]$ from Equation 5.6) utilizes the three-axis magnetometer measurements as direct input to the particle filter. The initial results in Figure 5.6 examine magnetometer measurements and magnetic field maps separated by distance, including a case for comparing the effects of calibration.

For the same-vehicle cases, calibrated or uncalibrated measurements can be used and provide side-by-side comparison with nearly identical navigation solutions. Furthermore, the cross-vehicle cases were investigated using both the modified ellipsoid calibration method and the simple calibration method used for comparison in Chapter III. For the cases shown here and other cases not shown, the modified ellipsoid calibration yielded improved navigation results over the simple calibration method every time. Therefore the modified ellipsoid calibration has been used for all results that will be presented.

The navigation results labeled "Feature" explored the concept of feature-based maps and measurements from Chapter IV, but incorporated the magnetometer measurements directly, instead of using a likelihood or RSS technique. In these cases, magnetic field maps were only composed of 1m separated sections of measurements identified as features. In turn, 1m separated sections of magnetometer measurements were only used as a measurement update after being identified as a feature. Propagation error is still prevalent, but has lower impact since features are found fairly frequently. For the T-S and C-S feature cases, the results are nearly as good as the same cases using single epoch 1m separated distance measurements. However, in the T-C case, the navigation solution suffers due to the poor matching of features from the Truck to similar features in the Car.

As expected, the same-vehicle cases provided the best navigation results due to the minimal difference in magnetometer measurements based on position. While

128
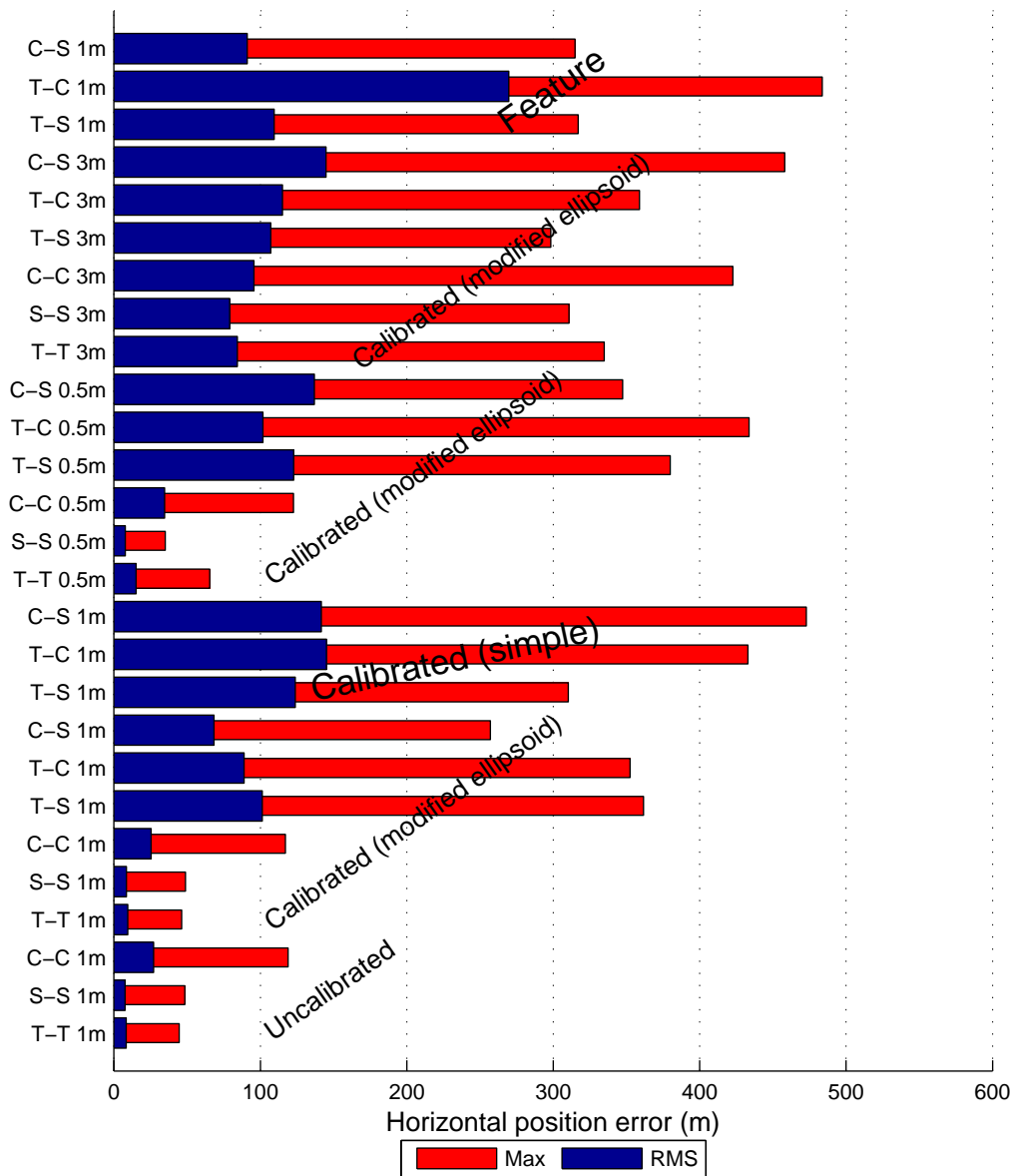
Figure 5.6:    Navigation performance comparing distance based measurements.

the Car-Car cases had higher RMS values between 25-34m, there is clear division between the same-vehicle and cross-vehicle cases in terms of navigation performance for 0.5m and 1m separated magnetometer measurements. However, for 3m separated magnetometer measurements, the cross-vehicle cases were only slightly higher than the same-vehicle cases. In turn, the increased frequency of the 0.5m distance separated magnetometer measurements did not translate to improved navigation performance for the cross-vehicle cases. Ultimately, the 1m separated magnetometer measurements displayed the best overall performance for the same-vehicle and cross-vehicle cases.

*5.2.3 Comparison/Contrast of Update Methods.* While Figures 5.4 and 5.6 show separate performance statistics as well as measurement composition comparison, an examination of the best results from both the position update and the direct magnetometer update promotes discussion on the merits of each. Figure 5.7 provides a side-by-side comparison of the maximum likelihood and MLR used as a position update versus the direct magnetometer update. All of these results use 1m distance-based measurements.

The maximum likelihood displays the largest max error, yet delivers RMS errors slightly higher than the MLR and magnetometer update. Although Chapter IV highlighted the poor accuracy of the maximum likelihood, when used in the particle filter a fairly consistent level of navigation is achieved. By comparison, the MLR delivers one case of improved performance (T-S), along with a similar performance for the C-S and worse performance for the T-C case. The results are inconsistent due to factors such as measurement availability and propagation error. Lastly, the direct incorporation of measurements for the magnetometer update appeared fairly consistent while delivering some of the best RMS values. Given this assessment, the magnetometer update is used in the remaining results in this research. However, this does not discount the value of the position update. While this particle filter implementation yields a slight edge in performance using the magnetometer update,

130
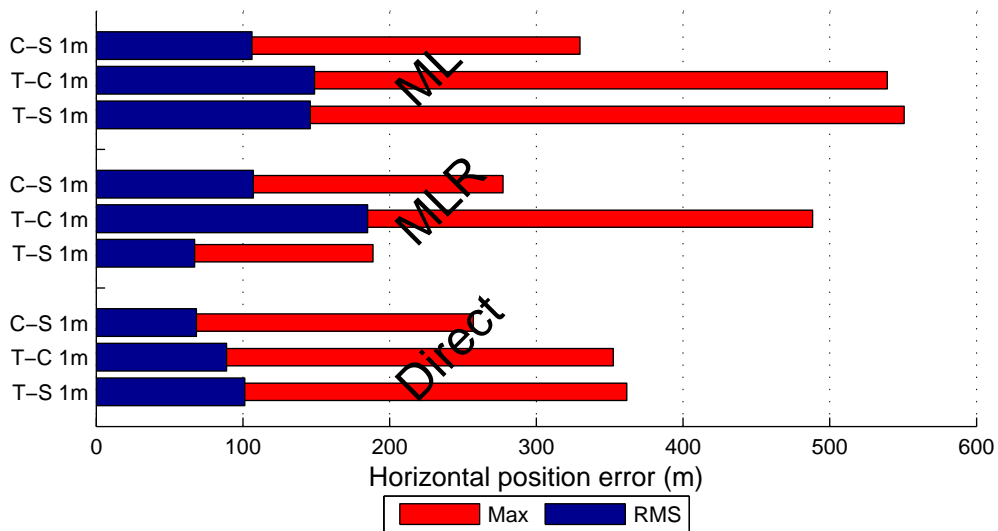
Figure 5.7:   Side-by-side comparison of the best results from the position update (ML and MLR) and the direct magnetometer update in terms of navigation performance.

the same cannot be assumed for every filter implementation. Additionally, multiple sensor implementations may benefit from the adjustable performance allowed by the MLR and ABL as position updates rather than attempting incorporation of the magnetometer update. These examples are recommended as future work.

With the knowledge gained exploring measurement composition, position or magnetometer updates, and anticipated errors, navigation in larger, more challenging environments is explored.

## 5.3   Navigation Solutions using the Large Area and Suburban Neighborhood Maps

The large area and suburban neighborhood maps offer two diverse challenges to ground vehicle navigation using only magnetic fields, evident in the performance results in Figure 5.8. Looking back at Figure 4.1, the large map contains stretches of highway and roads without significant structure to create magnetic features. This creates an environment with fewer features over long periods, conducive to propagation error. Conversely, the suburban neighborhood is riddled with similar features
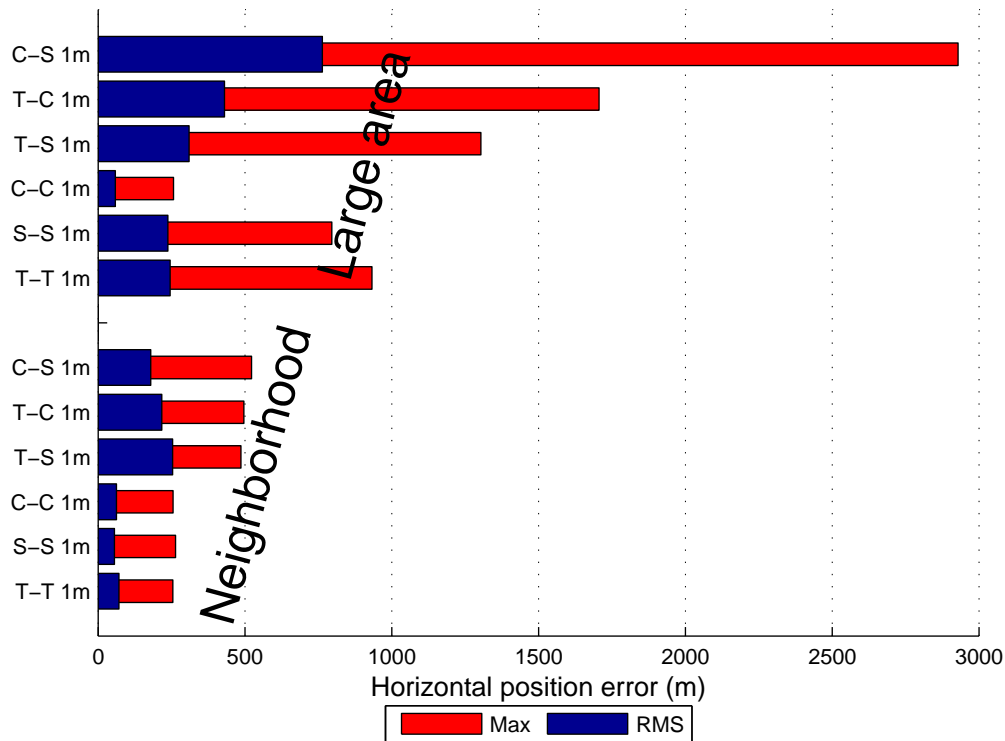
Figure 5.8: Navigation performance of the suburban neighborhood and large area maps for same-vehicle and cross-vehicle cases.

and roadways, which will dilute the uniqueness of magnetometer measurements in the magnetic field map. This will increase the possibility of selecting the wrong road during navigation. A review of the overall results in Figure 5.8 imparts the general performance, with further inspection of a few specific cases immediately following in order to describe interesting navigation solutions.

Attention is immediately drawn to the large area cases with significant max and RMS errors. While the same-vehicle cases had RMS values near 240m and max values near 850m, the Car-Car case exhibited surprising results of 58m/257m RMS/-max. An inspection of the raw measurements revealed that the Car-Car case shown here exhibited nearly identical magnetometer measurements in all three axes between the magnetometer measurements and the magnetic field map. While salient, driving

variation and other interference make this an exception rather than the norm. A look at the Truck and SUV cases saw similar agreement in the $x$ and $y$ axes, but a lower level of repeatability in the $z$ axes. While not apparent during calibration, the $z$ axis magnetometer measurements did experience more interference during certain sections of the road in the Truck and SUV. While seemingly minor, the effects are seen in the navigation performance. A study of interference based on vehicle response over a multitude of roads could improve this type of error and is recommended as follow on work. The suburban neighborhood navigation performance is consistent for the same-vehicle ($\approx$ 60m/255m RMS/max) and cross-vehicle ($\approx$ 215m/500m RMS/max) cases. The decrease in performance can be attributed to the challenging environment, where discerning a particular position is difficult with so many similar areas. The following figures and error plots for the large area and suburban neighborhood environments provide a more detailed analysis on specific cases, at the same time explaining the increased max and RMS errors.

Figure 5.9 and 5.10 depict the navigation solution and corresponding error plot for the large area map. The large area map contains a few problem areas, which is to be expected. The portions that do not track well are largely the result of propagation error, stemming from the lack of significant change in the magnetometer measurements. In the case of the lower left corner, near 0m east and -1300m north, the navigation solution has surged ahead. However, the recent incoming magnetometer measurements were of sufficient quality that existing particles behind the heavily weighted particles that surged continue to garner enough weighting that the navigation solution changes direction momentarily. Continuing incoming magnetometer measurements convey the inappropriate change in direction and the navigation filter regains the proper direction of travel and navigation solution. Although not common, this error tended to occur during the highway stretches. The highly noticeable track error on the northern portion of the map actually shows the navigation solution is no longer on the road. In this particular case, the particles have propagated

133
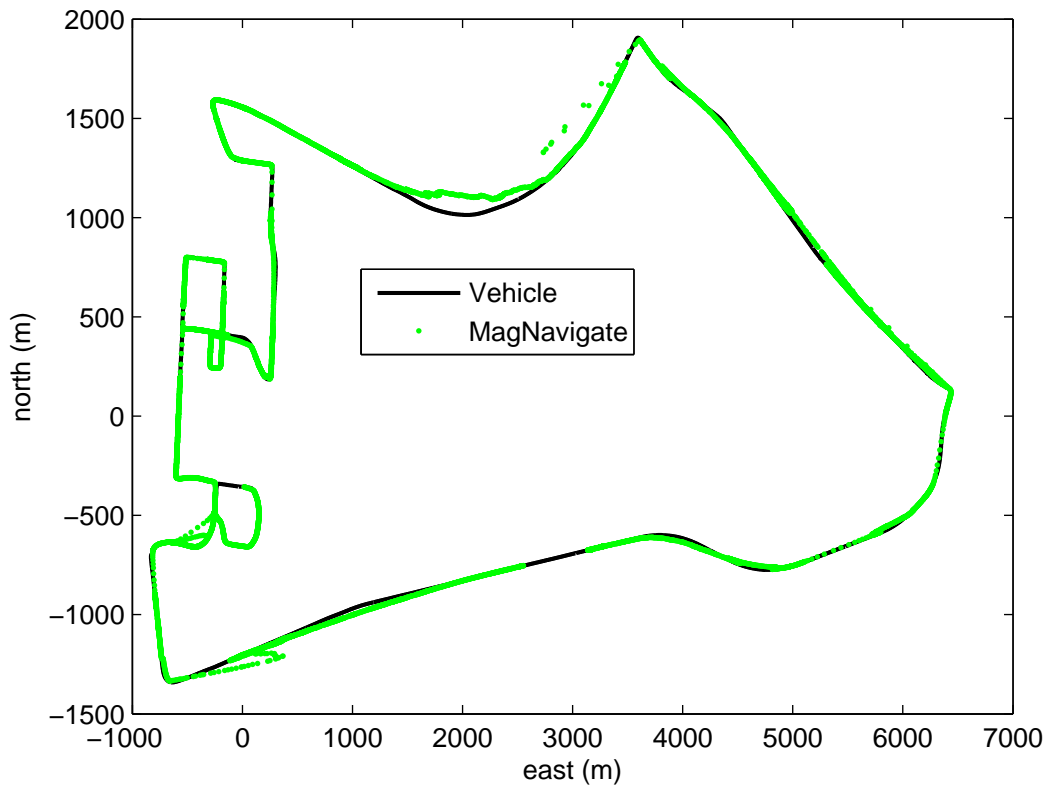
Figure 5.9: Large area map navigation solution using 1m separated magnetometer measurements in the navigation filter.

all along this stretch of road. The navigation solution (the weighted particle mean) lies just north of the true trajectory since particles to the east and west contained enough weighting to cause the weighted particle mean to be off the road, even though all the particles are on the road.

Further to the right near 4000m east and 1900m north the particles have largely split into two groups, with the first group maintaining the correct navigation solution. However, examining the error plot in Figure 5.10 near epoch 11000 highlights a spike in all three error plots. For this short series of epochs the incorrect group of particles momentarily gains enough weight to shift the navigation solution. Within a few measurement updates, the correct group of particles regains the weight to shift the navigation solution back where it should be and continue on the correct path.

For those few epochs, the magnetometer measurement update matched the wrong location in the magnetic field map so well that the navigation solution is actually shifted approximately 1 kilometer (km). This update error is quite different than the typical propagation errors which are experienced the majority of the time.

Moving on to Figures 5.11 and 5.12, the suburban neighborhood map exemplifies how propagation error can pose challenges in the navigation filter. In this case, a roadworker caused an abrupt vehicle stop. Without a distance measurement update conveying the stop, the particles continue to propagate rapidly, both north and east. The resulting lag causes the weighted particle mean to be off the road, and the incoming magnetometer measurements have little impact due to the separation of the particles from the estimated location. Ultimately the navigation filter diverges and selects the wrong road on the last leg of the route. In the AFIT and large area maps, the penalization of off-road particles meant that the navigation solution (i.e. the weighted particle mean) is often on the road. As shown in the large area map, there are a few instances where the navigation solution could be away from the road. However, the suburban neighborhood map showcases the example when particles have propagated to roads parallel or perpendicular to the current location and the resulting navigation solution may be centered around these particles if the particles have fairly even weights. This would be especially hazardous with a mismatched dynamics model, or in this case where there is a large time difference between the distance based magnetometer measurements.

Figures 5.13 and 5.14 provide an example of better navigation filter performance using the Truck-SUV measurement-map combination. The typical navigation solutions for the suburban neighborhood maps using 1m distance separated magnetometer measurements did well. Most, importantly, the navigation solution is able to properly determine the correct road, without inadvertently skipping over to a parallel road which would have similar heading characteristics.
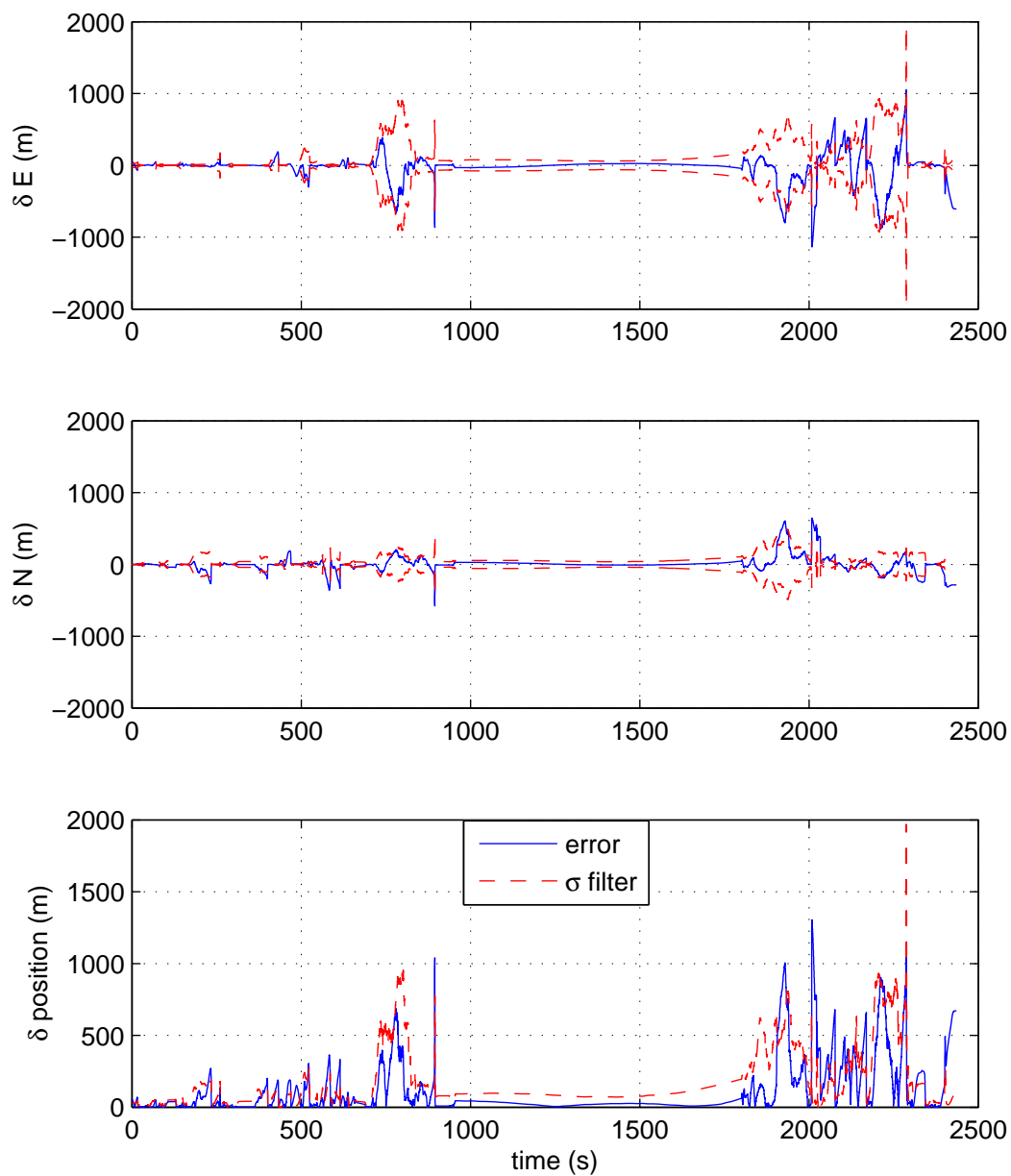
Figure 5.10: Large area map errors (solid blue line) as compared with the actual vehicle position. The max position error is 1335m, while the RMS position error is 309m.
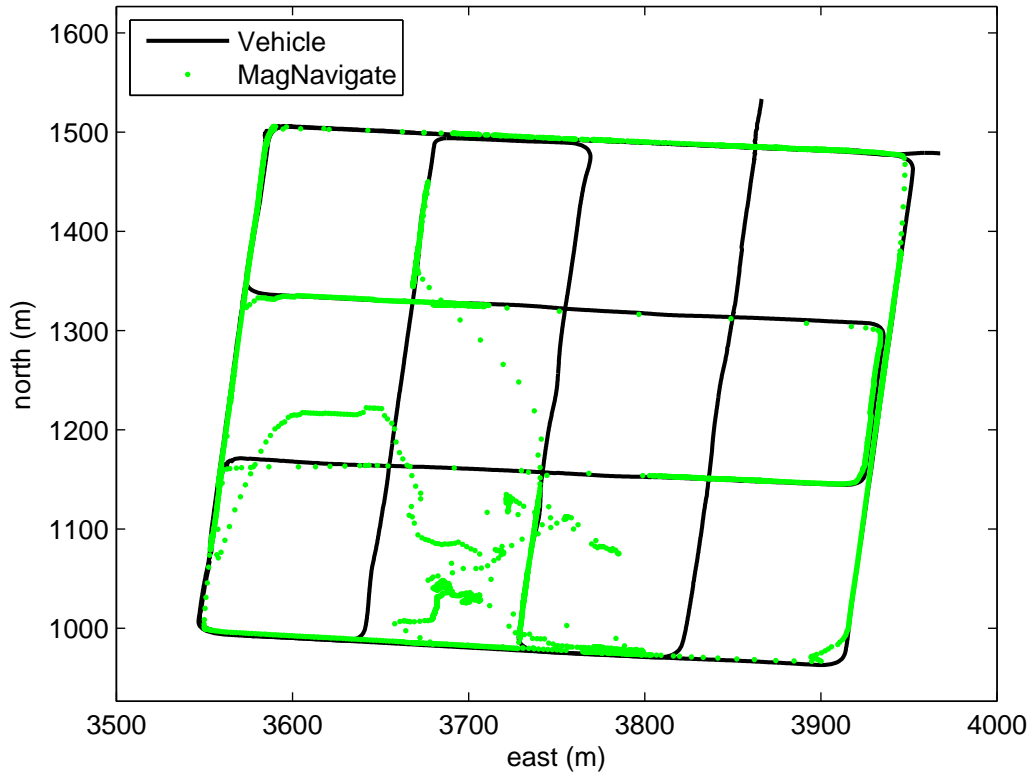
Figure 5.11:    Suburban neighborhood map illustrating the navigation solution diverges due to rapid propagation of particles after an abrupt stop.
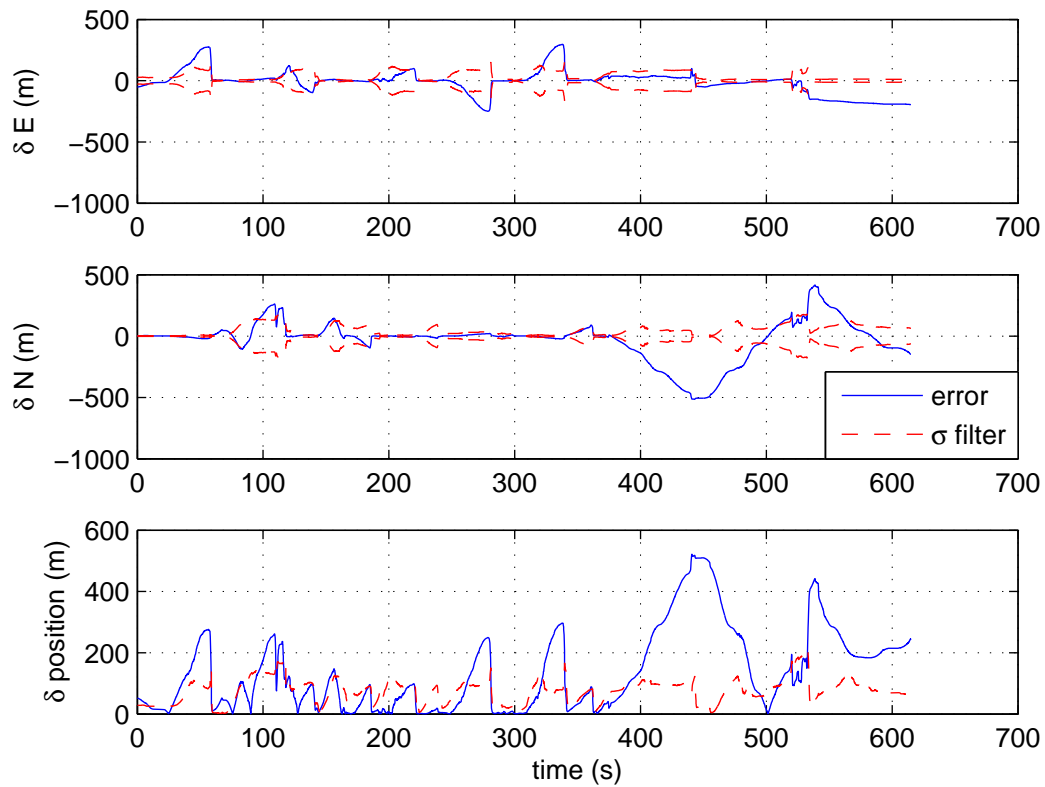
Figure 5.12: Suburban neighborhood map errors (solid blue line) as compared with the actual vehicle position. The max position error is 503m, while the RMS position error is 182m.
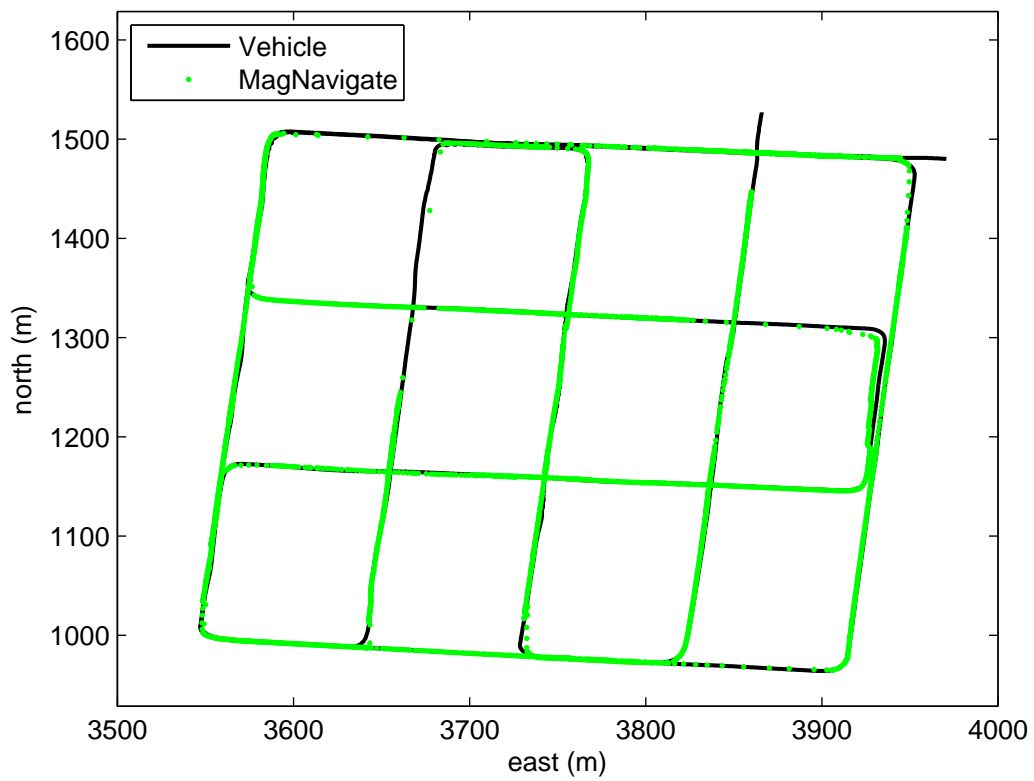
Figure 5.13:    Suburban neighborhood map navigation solution using the Truck-SUV measurement combination in the navigation filter.
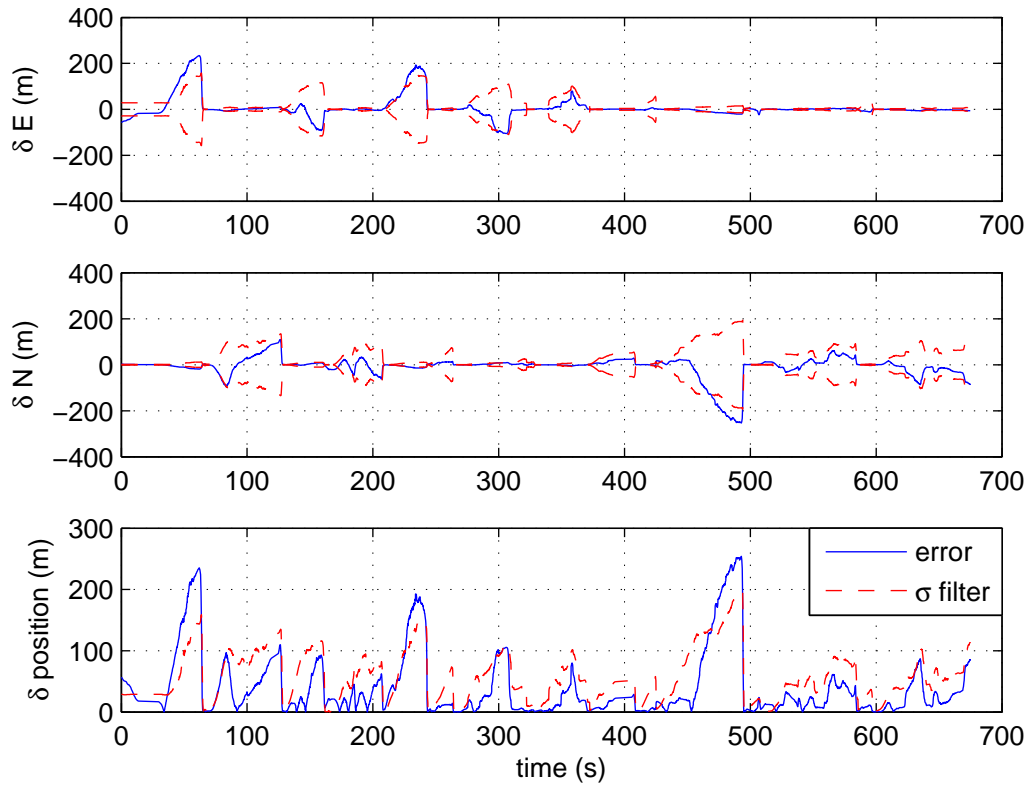
Figure 5.14:    Suburban neighborhood map errors (solid blue line) as compared with the actual vehicle position. The max position error is 263m, while the RMS position error is 55m.

## 5.4 Chapter Summary

This chapter presents navigation performance statistics as well as insight into the principles of magnetic field navigation. This chapter summary allows the opportunity to stress a few key points. Most notably, ground vehicle navigation using only magnetic field variations delivers a self-contained navigation system capable of road-level navigation in differing environments. Furthermore, the modified ellipsoid calibration from Chapter III improved navigation performance in all cases. In terms of the position update versus the magnetometer update, the magnetometer update showed a slight edge in performance due to better consistency and lower RMS errors. However, the position update using the maximum likelihood and MLR techniques delivered similar performance, and would be especially useful as an update to another sensor or navigation system. In all cases, propagation error is attributed to the majority of large navigation errors. In the next chapter, conclusions are given concerning results presented in this dissertation as well as the contributions to magnetometry and navigation.

.

# VI. Conclusions

NAVIGATION using magnetic field information is viable. This dissertation presents an approach for mapping, calibrating, and navigating using only magnetic field information. This chapter presents conclusions regarding this research, followed by potential areas for future research.

## 6.1  Conclusions

The most significant conclusion for this research is the demonstration of viable navigation solutions using only magnetometer measurements and magnetic field maps for ground vehicles. Navigation solutions are presented using position estimate methods from Chapter IV, as well as direct incorporation of the magnetometer measurement in the navigation filter in Chapter V.

*Calibration* In order to successfully compare different vehicle cases, the magnetic field data was calibrated. The need for accurate calibration spurred the development of a new calibration method. The modified ellipsoid calibration bridged the current state of the art in two and three-dimensional calibration methods. Existing three-dimensional ellipsoid calibrations require sufficient rotation in multiple axes to define the ellipsoid, which is not possible for a strapdown magnetometer mounted in a ground vehicle. Existing two-dimensional methods do not accurately calibrate the measurements in each horizontal axis, relegating their usefulness to accurate heading applications. The modified ellipsoid calibration method developed in this research provides accurate calibration in each horizontal axis with only rotation about a single axis.

*Position Measurement Generation* The measurement analysis provided key information on the best utilization of magnetometer measurements and the ability to determine a position estimate with this information. A multitude of compositions were explored to determine the most promising techniques, as well as their potential

accuracy in different map areas. Specifically, the maximum likelihood ratio (MLR) and aggregate bin likelihood (ABL) methods were developed to increase the accuracy of the position estimate, albeit at the cost of availability. Although performance in the navigation filter was eroded by propagation error when there are no available measurements, these techniques would make excellent sources for a position update to existing navigation systems.

*Filter-Based Solutions* Perturbations in the magnetic field are largely unknown, and unpredictable. Therefore the measurement model does not exist, and attempting to match a single filter estimate with a single position in the magnetic field map would most likely lead to disparity between the incoming magnetometer measurement and the estimated measurement from the magnetic field map. The particle filter allows for simultaneous multiple estimates, using the likelihoods of all the map points rather than attempting to determine a single position solution. When combined with the propagated state estimate, the adjusted weights and the weighted particle mean provide a navigation solution based on the multiple estimates. Additionally, even though some particles may not contain significant weight, as long as they remain viable they possess the potential to be in the right location at the right time to gain importance in the navigation solution.

In summary, this research capitalizes on the rich information and global prevalence of the Earth's magnetic field to provide a self-contained navigation solution. The research demonstrates the ability to navigate in various environments with a single magnetometer and the magnetic field map. While the approach demonstrates an initial capability, there are areas which merit additional research, addressed in the next section.

## 6.2 Future Work

While this research analyzed several aspects of magnetic field navigation in ground vehicles, many more exist. A portion of these opportunities are expanded

here, ranging from the magnetometer measurements themselves to different approaches for finding the navigation solution.

Although several measurement compositions were explored, the basic magnetometer measurement always consisted of the three-axis magnetometer measurement $\hat{\mathbf{B}} = [\hat{B}_x \ \hat{B}_y \ \hat{B}_z]$. However, the magnetometer measurement could consist of horizontal magnitude $\left\|\hat{\mathbf{B}}_\mathbf{h}\right\|$ and the vertical axis $\hat{B}_z$ or even the overall magnitude $\left\|\hat{\mathbf{B}}\right\|$. While initial investigations indicated these were less advantageous than the full three-axis measurement, a level of navigation could be realized. Furthermore, there may be situations when a horizontal or 3D approach would be valuable (such as when the attitude is not known for a given map position).

Magnetic field mapping also presents several opportunities for future work in various ways. An analysis of the navigation potential for magnetic field maps would yield the potential accuracy that could be expected, possibly determining whether a map or map section is useful at all. The topic of decorrelation distance is also highly intriguing, since knowing the effective distance a magnetometer measurement is valid could be used to further refine position estimates. Additionally, to be used on a large scale the magnetic field maps would need to be shared in some fashion. The issues of commonality, measurement quality, and how to effectively resolve measurements of the same position while ensuring the best measurements are kept represent a few of the challenges. Map amalgamation would allow information from multiple maps to be shared and proliferated, while maintaining the most current magnetic field information.

Mapping also provides an interesting subject in terms of the World Magnetic Model (WMM). A study on the differences between collected and predicted magnetic field information could lead to improved position estimates and navigation performance when localized features are further apart. This may help to resolve local variation, find features, and navigate over large distances without first mapping

144

them. This may also lead to other implementations, such as outdoor pedestrian navigation using Earth's magnetic field.

Investigation of a few time and distance (mixed variation) combinations were presented in Chapter IV. A study on the optimality of maps based on distance using magnetometer measurements based on time would be useful for the leader-follower case presented by Storms [42]. Since the follower has the most simplistic sensor suite, using only the time-based magnetometer measurements requires no knowledge of distance traveled (i.e., no other sensors). This is the most likely case for simple implementations, since an end-user is probably also not a map generator, but merely using the magnetic field map from another source.

Localized feature identification, false feature mitigation, and improved feature matching embody a large area of possible advancement. In this research, localized features were simply observed, but not categorized or specifically identified based on their characteristics. This would not only help in determining the uniqueness of a feature, but would aid in false feature mitigation. For instance, if a passing vehicle produces the same characteristics in a set of magnetometer measurements, once identified they could be removed from the magnetic field and incoming magnetometer measurements. This will also require an improvement in feature matching, which could benefit from tools developed in the signal and/or image recognition fields of study.

Interference is also a significant source of error in several aspects. Installation in the ground vehicles provided enough open space to mitigate severe interference, but still affected the magnetometer measurements. Identification and mitigation of typical interference from the environment would improve the observed magnetometer measurements, and may allow elimination of severe interference when repositioning is not possible. Furthermore, a study on the effects of interference in terms of position estimates or navigation solutions would highlight their overall effect.

While Chapter II demonstrated that the HMR2300 was more than adequate to detect small changes in the Earth's magnetic field for the ground vehicle application, a determination on the magnetometer sensitivity required for navigation would be useful. The study would explore tradeoffs in sensitivity versus:

- The ability to effectively calibrate the magnetometer on a platform

- Localized feature detection

- Position estimate and/or navigation solution performance

- Magnetic field maps created from magnetometers with different sensitivities

The sensitivity analysis, combined with other recommended future work, could lead to a cost-benefit analysis for dispatched items such as weapons, micro air vehicles, or ordnance disposal robots.

The MLR and ABL techniques developed in Chapter IV proved effective tools to improve position estimates compared to the maximum likelihood. However, a full tradeoff study of accuracy versus availability in terms of map size and composition would provide confidence intervals to determine when and if the magnetometer measurement position estimate should be used.

Ultimately the performance disparity between the same-vehicle cases and the cross-vehicle cases point to the importance of calibration in reducing the difference between magnetometer measurements from different vehicles. Although not the only factor (e.g., installation, vehicle characteristics), more accurate calibration is key. Although several authors have tackled this problem, few have displayed significant gains in eliminating the errors for strapdown implementations in large vehicles. Further research might suggest augmentation during calibration, such as gimballing or inertial aiding. Pairing the magnetometer with a very small inertial measurement unit could provide significant gains in calibration and navigation.

A study in magnetic navigation covering different vehicle types would be beneficial. For the ground vehicles in this research, each vehicle affected the magne-

146

tometer measurements differently, as evidenced in Chapter III. Smaller autonomous air/land/water vehicles should see increased benefit from a full 3D ellipsoid calibration, but may exhibit more magnetometer measurement error due to the relative proximity of on-board systems. The introduction of air vehicles also leads to investigation of how height above the surface of the Earth factors into the magnetometer measurements.

There are also many possibilities for improving the navigation solution. The foremost would be limiting the searchable magnetic field map by the last known position. In this research, magnetometer measurements were compared against the entire magnetic field map, even though many of the magnetic field map locations may not have been viable for the vehicle. Limiting the searchable area would improve the uniqueness of potential matches. Another possible navigation improvement would be exploring different filter implementations, such as the Rao-Blackwellized particle filter [45] or the unscented Kalman filter [36]. Multi-sensor and dissimilar sensor pairings are currently being investigated, with the magnetometer as the secondary information source. Switching the paradigm to have the magnetometer information corrected based on information from a secondary sensor could also yield significant gains in measurement quality. Synergizing the information obtained from the magnetometer with other sensors (e.g. inertial, visual) would also improve navigation solutions.

## *Appendix A. Measurement Analysis Test Cases*

THE following spreadsheets detail the entire matrix of measurement analysis test cases. Cases highlighted in green were specifically used for results presented in Chapters IV and V. Non-highlighted cases were explored, but did not yield results substantially different than those reported in the main body of the document.

The test case identifiers help distinguish the environments as well as the parameter variation. The first character identifies the map section as shown in Figure 4.1. The letter **A** stands for the rectangular road path around AFIT. **H** signifies the suburban neighborhood, and **L** represents the large area map. The second character labels the measurement type by distance or time, but with a specific callout for baseline to allow comparison of the baseline data across all results. The third character denotes the map type in distance or time. Finally, characters four through six designate the specific case. Breaks in the test case numbers represent the start of a different test case series and are not to be perceived as missing test cases. The column heading **Measurements** defines the test case parameters used for the incoming magnetometer measurements, while **Map** defines the parameters of the map used. The **ComparisonMethod** heading denotes whether an additional technique such as demeaning (**Demean**), differencing (**Diff**) or feature (**Feature**) composition was used. For all test cases, the vehicle (**Veh**) descriptors of **T**, **S**, and **C** stand for the Truck, SUV, or Car, respectively. The units (**Units**) are in time or distance. The calibration type (**Type**) conveys uncalibrated (uncal), calibrated (cal), or simple (sf1). The number of measurements (#**Meas**) would be one for single epoch, four for a 3m section of 1m measurements, and so forth. Since a single epoch only uses a single measurement, the comparison methods of demeaning, differencing, or feature are marked not applicable (N/A). Once multiple measurements are explored, these change to a yes (y) or no (n).

| Test Case | Veh | Description | Units | Type | #Meas | | Veh | Description | Units | Demean | Diff | Feature |
|---|---|---|---|---|---|---|---|---|---|---|---|---|
| | | **Measurements** | | | | | | **Map** | | **Comparison Method** | | |
| Baseline | | | | | | | | | | | | |
| ABT01 | T | AFIT run2 | 50Hz | uncal | 1 | | T | AFIT map3 | 50Hz | N/A | N/A | N/A |
| ABT02 | T | AFIT run2 | 50Hz | cal | 1 | | T | AFIT map3 | 50Hz | N/A | N/A | N/A |
| ABT03 | S | AFIT run1 | 50Hz | uncal | 1 | | S | AFIT map2 | 50Hz | N/A | N/A | N/A |
| ABT04 | S | AFIT run1 | 50Hz | cal | 1 | | S | AFIT map2 | 50Hz | N/A | N/A | N/A |
| ABT05 | C | AFIT run1 | 50Hz | uncal | 1 | | C | AFIT map3 | 50Hz | N/A | N/A | N/A |
| ABT06 | C | AFIT run1 | 50Hz | cal | 1 | | C | AFIT map3 | 50Hz | N/A | N/A | N/A |
| ABT07 | T | AFIT run2 | 50Hz | cal | 1 | | S | AFIT map2 | 50Hz | N/A | N/A | N/A |
| ABT08 | T | AFIT run2 | 50Hz | cal | 1 | | C | AFIT map3 | 50Hz | N/A | N/A | N/A |
| ABT09 | S | AFIT run1 | 50Hz | cal | 1 | | T | AFIT map3 | 50Hz | N/A | N/A | N/A |
| ABT10 | S | AFIT run1 | 50Hz | cal | 1 | | C | AFIT map3 | 50Hz | N/A | N/A | N/A |
| ABT11 | C | AFIT run1 | 50Hz | cal | 1 | | T | AFIT map3 | 50Hz | N/A | N/A | N/A |
| ABT12 | C | AFIT run1 | 50Hz | cal | 1 | | S | AFIT map2 | 50Hz | N/A | N/A | N/A |
| | | | | | | | | | | | | |
| Vary measurement and map time | | | | | | | | | | | | |
| ATT01 | T | AFIT run2 | 10Hz | uncal | 1 | | T | AFIT map3 | 50Hz | N/A | N/A | N/A |
| ATT02 | T | AFIT run2 | 10Hz | cal | 1 | | T | AFIT map3 | 50Hz | N/A | N/A | N/A |
| ATT03 | S | AFIT run1 | 10Hz | uncal | 1 | | S | AFIT map2 | 50Hz | N/A | N/A | N/A |
| ATT04 | S | AFIT run1 | 10Hz | cal | 1 | | S | AFIT map2 | 50Hz | N/A | N/A | N/A |
| ATT05 | C | AFIT run1 | 10Hz | uncal | 1 | | C | AFIT map3 | 50Hz | N/A | N/A | N/A |
| ATT06 | C | AFIT run1 | 10Hz | cal | 1 | | C | AFIT map3 | 50Hz | N/A | N/A | N/A |
| ATT07 | T | AFIT run2 | 10Hz | cal | 1 | | S | AFIT map2 | 50Hz | N/A | N/A | N/A |
| ATT08 | T | AFIT run2 | 10Hz | cal | 1 | | C | AFIT map3 | 50Hz | N/A | N/A | N/A |
| ATT09 | S | AFIT run1 | 10Hz | cal | 1 | | T | AFIT map3 | 50Hz | N/A | N/A | N/A |
| ATT10 | S | AFIT run1 | 10Hz | cal | 1 | | C | AFIT map3 | 50Hz | N/A | N/A | N/A |
| ATT11 | C | AFIT run1 | 10Hz | cal | 1 | | T | AFIT map3 | 50Hz | N/A | N/A | N/A |
| ATT12 | C | AFIT run1 | 10Hz | cal | 1 | | S | AFIT map2 | 50Hz | N/A | N/A | N/A |
| ATT13 | T | AFIT run2 | 50Hz | uncal | 1 | | T | AFIT map3 | 10Hz | N/A | N/A | N/A |
| ATT14 | T | AFIT run2 | 50Hz | cal | 1 | | T | AFIT map3 | 10Hz | N/A | N/A | N/A |
| ATT15 | S | AFIT run1 | 50Hz | uncal | 1 | | S | AFIT map2 | 10Hz | N/A | N/A | N/A |
| ATT16 | S | AFIT run1 | 50Hz | cal | 1 | | S | AFIT map2 | 10Hz | N/A | N/A | N/A |
| ATT17 | C | AFIT run1 | 50Hz | uncal | 1 | | C | AFIT map3 | 10Hz | N/A | N/A | N/A |
| ATT18 | C | AFIT run1 | 50Hz | cal | 1 | | C | AFIT map3 | 10Hz | N/A | N/A | N/A |
| ATT19 | T | AFIT run2 | 50Hz | cal | 1 | | S | AFIT map2 | 10Hz | N/A | N/A | N/A |
| ATT20 | T | AFIT run2 | 50Hz | cal | 1 | | C | AFIT map3 | 10Hz | N/A | N/A | N/A |
| ATT21 | S | AFIT run1 | 50Hz | cal | 1 | | T | AFIT map3 | 10Hz | N/A | N/A | N/A |
| ATT22 | S | AFIT run1 | 50Hz | cal | 1 | | C | AFIT map3 | 10Hz | N/A | N/A | N/A |
| ATT23 | C | AFIT run1 | 50Hz | cal | 1 | | T | AFIT map3 | 10Hz | Demean | Diff | Feature |
| ATT24 | C | AFIT run1 | 50Hz | cal | 1 | | S | AFIT map2 | 10Hz | N/A | N/A | N/A |
| ATT25 | T | AFIT run2 | 10Hz | uncal | 1 | | T | AFIT map3 | 10Hz | N/A | N/A | N/A |
| ATT26 | T | AFIT run2 | 10Hz | cal | 1 | | T | AFIT map3 | 10Hz | N/A | N/A | N/A |
| ATT27 | S | AFIT run1 | 10Hz | uncal | 1 | | S | AFIT map2 | 10Hz | N/A | N/A | N/A |
| ATT28 | S | AFIT run1 | 10Hz | cal | 1 | | S | AFIT map2 | 10Hz | N/A | N/A | N/A |
| ATT29 | C | AFIT run1 | 10Hz | uncal | 1 | | C | AFIT map3 | 10Hz | N/A | N/A | N/A |
| ATT30 | C | AFIT run1 | 10Hz | cal | 1 | | C | AFIT map3 | 10Hz | N/A | N/A | N/A |

| | | | | | | | | | | | | |
|---|---|---|---|---|---|---|---|---|---|---|---|---|
| ATT31 | T | AFIT run2 | 10Hz | cal | 1 | | S | AFIT map2 | 10Hz | N/A | N/A | N/A |
| ATT32 | T | AFIT run2 | 10Hz | cal | 1 | | C | AFIT map3 | 10Hz | N/A | N/A | N/A |
| ATT33 | S | AFIT run1 | 10Hz | cal | 1 | | T | AFIT map3 | 10Hz | N/A | N/A | N/A |
| ATT34 | S | AFIT run1 | 10Hz | cal | 1 | | C | AFIT map3 | 10Hz | N/A | N/A | N/A |
| ATT35 | C | AFIT run1 | 10Hz | cal | 1 | | T | AFIT map3 | 10Hz | N/A | N/A | N/A |
| ATT36 | C | AFIT run1 | 10Hz | cal | 1 | | S | AFIT map2 | 10Hz | N/A | N/A | N/A |
| | | | | | | | | | | | | |
| Compare sensor measurements in time, to a map based on distance | | | | | | | | | | | | |
| ATD01 | T | AFIT run2 | 10Hz | uncal | 1 | | T | AFIT map3 | 0.5m | N/A | N/A | N/A |
| ATD02 | T | AFIT run2 | 10Hz | cal | 1 | | T | AFIT map3 | 0.5m | N/A | N/A | N/A |
| ATD03 | S | AFIT run1 | 10Hz | uncal | 1 | | S | AFIT map2 | 0.5m | N/A | N/A | N/A |
| ATD04 | S | AFIT run1 | 10Hz | cal | 1 | | S | AFIT map2 | 0.5m | N/A | N/A | N/A |
| ATD05 | C | AFIT run1 | 10Hz | uncal | 1 | | C | AFIT map3 | 0.5m | N/A | N/A | N/A |
| ATD06 | C | AFIT run1 | 10Hz | cal | 1 | | C | AFIT map3 | 0.5m | N/A | N/A | N/A |
| ATD07 | T | AFIT run2 | 10Hz | cal | 1 | | S | AFIT map2 | 0.5m | N/A | N/A | N/A |
| ATD08 | T | AFIT run2 | 10Hz | cal | 1 | | C | AFIT map3 | 0.5m | N/A | N/A | N/A |
| ATD09 | S | AFIT run1 | 10Hz | cal | 1 | | T | AFIT map3 | 0.5m | N/A | N/A | N/A |
| ATD10 | S | AFIT run1 | 10Hz | cal | 1 | | C | AFIT map3 | 0.5m | N/A | N/A | N/A |
| ATD11 | C | AFIT run1 | 10Hz | cal | 1 | | T | AFIT map3 | 0.5m | N/A | N/A | N/A |
| ATD12 | C | AFIT run1 | 10Hz | cal | 1 | | S | AFIT map2 | 0.5m | N/A | N/A | N/A |
| ATD13 | T | AFIT run2 | 10Hz | uncal | 1 | | T | AFIT map3 | 1m | N/A | N/A | N/A |
| ATD14 | T | AFIT run2 | 10Hz | cal | 1 | | T | AFIT map3 | 1m | N/A | N/A | N/A |
| ATD15 | S | AFIT run1 | 10Hz | uncal | 1 | | S | AFIT map2 | 1m | N/A | N/A | N/A |
| ATD16 | S | AFIT run1 | 10Hz | cal | 1 | | S | AFIT map2 | 1m | N/A | N/A | N/A |
| ATD17 | C | AFIT run1 | 10Hz | uncal | 1 | | C | AFIT map3 | 1m | N/A | N/A | N/A |
| ATD18 | C | AFIT run1 | 10Hz | cal | 1 | | C | AFIT map3 | 1m | N/A | N/A | N/A |
| ATD19 | T | AFIT run2 | 10Hz | cal | 1 | | S | AFIT map2 | 1m | N/A | N/A | N/A |
| ATD20 | T | AFIT run2 | 10Hz | cal | 1 | | C | AFIT map3 | 1m | N/A | N/A | N/A |
| ATD21 | S | AFIT run1 | 10Hz | cal | 1 | | T | AFIT map3 | 1m | N/A | N/A | N/A |
| ATD22 | S | AFIT run1 | 10Hz | cal | 1 | | C | AFIT map3 | 1m | N/A | N/A | N/A |
| ATD23 | C | AFIT run1 | 10Hz | cal | 1 | | T | AFIT map3 | 1m | N/A | N/A | N/A |
| ATD24 | C | AFIT run1 | 10Hz | cal | 1 | | S | AFIT map2 | 1m | N/A | N/A | N/A |
| ATD25 | T | AFIT run2 | 10Hz | uncal | 1 | | T | AFIT map3 | 3m | N/A | N/A | N/A |
| ATD26 | T | AFIT run2 | 10Hz | cal | 1 | | T | AFIT map3 | 3m | N/A | N/A | N/A |
| ATD27 | S | AFIT run1 | 10Hz | uncal | 1 | | S | AFIT map2 | 3m | N/A | N/A | N/A |
| ATD28 | S | AFIT run1 | 10Hz | cal | 1 | | S | AFIT map2 | 3m | N/A | N/A | N/A |
| ATD29 | C | AFIT run1 | 10Hz | uncal | 1 | | C | AFIT map3 | 3m | N/A | N/A | N/A |
| ATD30 | C | AFIT run1 | 10Hz | cal | 1 | | C | AFIT map3 | 3m | N/A | N/A | N/A |
| ATD31 | T | AFIT run2 | 10Hz | cal | 1 | | S | AFIT map2 | 3m | N/A | N/A | N/A |
| ATD32 | T | AFIT run2 | 10Hz | cal | 1 | | C | AFIT map2 | 3m | N/A | N/A | N/A |
| ATD33 | S | AFIT run1 | 10Hz | cal | 1 | | T | AFIT map3 | 3m | N/A | N/A | N/A |
| ATD34 | S | AFIT run1 | 10Hz | cal | 1 | | C | AFIT map3 | 3m | N/A | N/A | N/A |
| ATD35 | C | AFIT run1 | 10Hz | cal | 1 | | T | AFIT map3 | 3m | N/A | N/A | N/A |
| ATD36 | C | AFIT run1 | 10Hz | cal | 1 | | S | AFIT map2 | 3m | N/A | N/A | N/A |
| ADT37 | T | AFIT run2 | 0.5m | uncal | 1 | | T | AFIT map3 | 10Hz | N/A | N/A | N/A |
| ADT38 | T | AFIT run2 | 0.5m | cal | 1 | | T | AFIT map3 | 10Hz | N/A | N/A | N/A |
| ADT39 | S | AFIT run1 | 0.5m | uncal | 1 | | S | AFIT map2 | 10Hz | N/A | N/A | N/A |

| | | | | | | | | | | | | |
|---|---|---|---|---|---|---|---|---|---|---|---|---|
| ADT40 | S | AFIT run1 | 0.5m | cal | 1 | | S | AFIT map2 | 10Hz | N/A | N/A | N/A |
| ADT41 | C | AFIT run1 | 0.5m | uncal | 1 | | C | AFIT map3 | 10Hz | N/A | N/A | N/A |
| ADT42 | C | AFIT run1 | 0.5m | cal | 1 | | C | AFIT map3 | 10Hz | N/A | N/A | N/A |
| ADT43 | T | AFIT run2 | 0.5m | cal | 1 | | S | AFIT map2 | 10Hz | N/A | N/A | N/A |
| ADT44 | T | AFIT run2 | 0.5m | cal | 1 | | C | AFIT map3 | 10Hz | N/A | N/A | N/A |
| ADT45 | S | AFIT run1 | 0.5m | cal | 1 | | T | AFIT map3 | 10Hz | N/A | N/A | N/A |
| ADT46 | S | AFIT run1 | 0.5m | cal | 1 | | C | AFIT map3 | 10Hz | N/A | N/A | N/A |
| ADT47 | C | AFIT run1 | 0.5m | cal | 1 | | T | AFIT map3 | 10Hz | N/A | N/A | N/A |
| ADT48 | C | AFIT run1 | 0.5m | cal | 1 | | S | AFIT map2 | 10Hz | N/A | N/A | N/A |
| ADT49 | T | AFIT run2 | 1m | uncal | 1 | | T | AFIT map3 | 10Hz | N/A | N/A | N/A |
| ADT50 | T | AFIT run2 | 1m | cal | 1 | | T | AFIT map3 | 10Hz | N/A | N/A | N/A |
| ADT51 | S | AFIT run1 | 1m | uncal | 1 | | S | AFIT map2 | 10Hz | N/A | N/A | N/A |
| ADT52 | S | AFIT run1 | 1m | cal | 1 | | S | AFIT map2 | 10Hz | N/A | N/A | N/A |
| ADT53 | C | AFIT run1 | 1m | uncal | 1 | | C | AFIT map2 | 10Hz | N/A | N/A | N/A |
| ADT54 | C | AFIT run1 | 1m | cal | 1 | | C | AFIT map3 | 10Hz | N/A | N/A | N/A |
| ADT55 | T | AFIT run2 | 1m | cal | 1 | | S | AFIT map2 | 10Hz | N/A | N/A | N/A |
| ADT56 | T | AFIT run2 | 1m | cal | 1 | | C | AFIT map3 | 10Hz | N/A | N/A | N/A |
| ADT57 | S | AFIT run1 | 1m | cal | 1 | | T | AFIT map3 | 10Hz | N/A | N/A | N/A |
| ADT58 | S | AFIT run1 | 1m | cal | 1 | | C | AFIT map3 | 10Hz | N/A | N/A | N/A |
| ADT59 | C | AFIT run1 | 1m | cal | 1 | | T | AFIT map3 | 10Hz | N/A | N/A | N/A |
| ADT60 | C | AFIT run1 | 1m | cal | 1 | | S | AFIT map2 | 10Hz | N/A | N/A | N/A |
| ADT61 | T | AFIT run2 | 3m | uncal | 1 | | T | AFIT map3 | 10Hz | N/A | N/A | N/A |
| ADT62 | T | AFIT run2 | 3m | cal | 1 | | T | AFIT map3 | 10Hz | N/A | N/A | N/A |
| ADT63 | S | AFIT run1 | 3m | uncal | 1 | | S | AFIT map2 | 10Hz | N/A | N/A | N/A |
| ADT64 | S | AFIT run1 | 3m | cal | 1 | | S | AFIT map2 | 10Hz | N/A | N/A | N/A |
| ADT65 | C | AFIT run1 | 3m | uncal | 1 | | C | AFIT map3 | 10Hz | N/A | N/A | N/A |
| ADT66 | C | AFIT run1 | 3m | cal | 1 | | C | AFIT map3 | 10Hz | N/A | N/A | N/A |
| ADT67 | T | AFIT run2 | 3m | cal | 1 | | S | AFIT map2 | 10Hz | N/A | N/A | N/A |
| ADT68 | T | AFIT run2 | 3m | cal | 1 | | C | AFIT map3 | 10Hz | N/A | N/A | N/A |
| ADT69 | S | AFIT run1 | 3m | cal | 1 | | T | AFIT map3 | 10Hz | N/A | N/A | N/A |
| ADT70 | S | AFIT run1 | 3m | cal | 1 | | C | AFIT map3 | 10Hz | N/A | N/A | N/A |
| ADT71 | C | AFIT run1 | 3m | cal | 1 | | T | AFIT map3 | 10Hz | N/A | N/A | N/A |
| ADT72 | C | AFIT run1 | 3m | cal | 1 | | S | AFIT map2 | 10Hz | N/A | N/A | N/A |
| | | | | | | | | | | | | |
| Compare sensor measurements in distance to a map based on distance | | | | | | | | | | | | |
| ABD01 | T | AFIT run2 | 1m | uncal | 1 | | T | AFIT map3 | 1m | N/A | N/A | N/A |
| ABD02 | T | AFIT run2 | 1m | cal | 1 | | T | AFIT map3 | 1m | N/A | N/A | N/A |
| ABD03 | S | AFIT run1 | 1m | uncal | 1 | | S | AFIT map2 | 1m | N/A | N/A | N/A |
| ABD04 | S | AFIT run1 | 1m | cal | 1 | | S | AFIT map2 | 1m | N/A | N/A | N/A |
| ABD05 | C | AFIT run1 | 1m | uncal | 1 | | C | AFIT map2 | 1m | N/A | N/A | N/A |
| ABD06 | C | AFIT run1 | 1m | cal | 1 | | C | AFIT map3 | 1m | N/A | N/A | N/A |
| ABD07 | T | AFIT run2 | 1m | cal | 1 | | S | AFIT map2 | 1m | N/A | N/A | N/A |
| ABD08 | T | AFIT run2 | 1m | cal | 1 | | C | AFIT map3 | 1m | N/A | N/A | N/A |
| ABD09 | S | AFIT run1 | 1m | cal | 1 | | T | AFIT map3 | 1m | N/A | N/A | N/A |
| ABD10 | S | AFIT run1 | 1m | cal | 1 | | C | AFIT map3 | 1m | N/A | N/A | N/A |
| ABD11 | C | AFIT run1 | 1m | cal | 1 | | T | AFIT map3 | 1m | N/A | N/A | N/A |
| ABD12 | C | AFIT run1 | 1m | cal | 1 | | S | AFIT map2 | 1m | N/A | N/A | N/A |

| | | | | | | | | | | | | |
|---|---|---|---|---|---|---|---|---|---|---|---|---|
| Compare sensor measurements in distance to a map based on distance | | | | | | | | | | | | |
| ADD01 | T | AFIT run2 | 0.5m | uncal | 1 | | T | AFIT map3 | 0.5m | N/A | N/A | N/A |
| ADD02 | T | AFIT run2 | 0.5m | cal | 1 | | T | AFIT map3 | 0.5m | N/A | N/A | N/A |
| ADD03 | S | AFIT run1 | 0.5m | uncal | 1 | | S | AFIT map2 | 0.5m | N/A | N/A | N/A |
| ADD04 | S | AFIT run1 | 0.5m | cal | 1 | | S | AFIT map2 | 0.5m | N/A | N/A | N/A |
| ADD05 | C | AFIT run1 | 0.5m | uncal | 1 | | C | AFIT map3 | 0.5m | N/A | N/A | N/A |
| ADD06 | C | AFIT run1 | 0.5m | cal | 1 | | C | AFIT map3 | 0.5m | N/A | N/A | N/A |
| ADD07 | T | AFIT run2 | 0.5m | cal | 1 | | S | AFIT map2 | 0.5m | N/A | N/A | N/A |
| ADD08 | T | AFIT run2 | 0.5m | cal | 1 | | C | AFIT map3 | 0.5m | N/A | N/A | N/A |
| ADD09 | S | AFIT run1 | 0.5m | cal | 1 | | T | AFIT map3 | 0.5m | N/A | N/A | N/A |
| ADD10 | S | AFIT run1 | 0.5m | cal | 1 | | C | AFIT map3 | 0.5m | N/A | N/A | N/A |
| ADD11 | C | AFIT run1 | 0.5m | cal | 1 | | T | AFIT map3 | 0.5m | N/A | N/A | N/A |
| ADD12 | C | AFIT run1 | 0.5m | cal | 1 | | S | AFIT map2 | 0.5m | N/A | N/A | N/A |
| ADD13 | T | AFIT run2 | 1m | uncal | 1 | | T | AFIT map3 | 0.5m | N/A | N/A | N/A |
| ADD14 | T | AFIT run2 | 1m | cal | 1 | | T | AFIT map3 | 0.5m | N/A | N/A | N/A |
| ADD15 | S | AFIT run1 | 1m | uncal | 1 | | S | AFIT map2 | 0.5m | N/A | N/A | N/A |
| ADD16 | S | AFIT run1 | 1m | cal | 1 | | S | AFIT map2 | 0.5m | N/A | N/A | N/A |
| ADD17 | C | AFIT run1 | 1m | uncal | 1 | | C | AFIT map3 | 0.5m | N/A | N/A | N/A |
| ADD18 | C | AFIT run1 | 1m | cal | 1 | | C | AFIT map3 | 0.5m | N/A | N/A | N/A |
| ADD19 | T | AFIT run2 | 1m | cal | 1 | | S | AFIT map2 | 0.5m | N/A | N/A | N/A |
| ADD20 | T | AFIT run2 | 1m | cal | 1 | | C | AFIT map3 | 0.5m | N/A | N/A | N/A |
| ADD21 | S | AFIT run1 | 1m | cal | 1 | | T | AFIT map3 | 0.5m | N/A | N/A | N/A |
| ADD22 | S | AFIT run1 | 1m | cal | 1 | | C | AFIT map3 | 0.5m | N/A | N/A | N/A |
| ADD23 | C | AFIT run1 | 1m | cal | 1 | | T | AFIT map3 | 0.5m | N/A | N/A | N/A |
| ADD24 | C | AFIT run1 | 1m | cal | 1 | | S | AFIT map2 | 0.5m | N/A | N/A | N/A |
| ADD25 | T | AFIT run2 | 3m | uncal | 1 | | T | AFIT map3 | 0.5m | N/A | N/A | N/A |
| ADD26 | T | AFIT run2 | 3m | cal | 1 | | T | AFIT map3 | 0.5m | N/A | N/A | N/A |
| ADD27 | S | AFIT run1 | 3m | uncal | 1 | | S | AFIT map2 | 0.5m | N/A | N/A | N/A |
| ADD28 | S | AFIT run1 | 3m | cal | 1 | | S | AFIT map2 | 0.5m | N/A | N/A | N/A |
| ADD29 | C | AFIT run1 | 3m | uncal | 1 | | C | AFIT map3 | 0.5m | N/A | N/A | N/A |
| ADD30 | C | AFIT run1 | 3m | cal | 1 | | C | AFIT map3 | 0.5m | N/A | N/A | N/A |
| ADD31 | T | AFIT run2 | 3m | cal | 1 | | S | AFIT map2 | 0.5m | N/A | N/A | N/A |
| ADD32 | T | AFIT run2 | 3m | cal | 1 | | C | AFIT map3 | 0.5m | N/A | N/A | N/A |
| ADD33 | S | AFIT run1 | 3m | cal | 1 | | T | AFIT map3 | 0.5m | N/A | N/A | N/A |
| ADD34 | S | AFIT run1 | 3m | cal | 1 | | C | AFIT map3 | 0.5m | N/A | N/A | N/A |
| ADD35 | C | AFIT run1 | 3m | cal | 1 | | T | AFIT map3 | 0.5m | N/A | N/A | N/A |
| ADD36 | C | AFIT run1 | 3m | cal | 1 | | S | AFIT map2 | 0.5m | N/A | N/A | N/A |
| ADD37 | T | AFIT run2 | 0.5m | uncal | 1 | | T | AFIT map3 | 1m | N/A | N/A | N/A |
| ADD38 | T | AFIT run2 | 0.5m | cal | 1 | | T | AFIT map3 | 1m | N/A | N/A | N/A |
| ADD39 | S | AFIT run1 | 0.5m | uncal | 1 | | S | AFIT map2 | 1m | N/A | N/A | N/A |
| ADD40 | S | AFIT run1 | 0.5m | cal | 1 | | S | AFIT map2 | 1m | N/A | N/A | N/A |
| ADD41 | C | AFIT run1 | 0.5m | uncal | 1 | | C | AFIT map3 | 1m | N/A | N/A | N/A |
| ADD42 | C | AFIT run1 | 0.5m | cal | 1 | | C | AFIT map3 | 1m | N/A | N/A | N/A |
| ADD43 | T | AFIT run2 | 0.5m | cal | 1 | | S | AFIT map2 | 1m | N/A | N/A | N/A |
| ADD44 | T | AFIT run2 | 0.5m | cal | 1 | | C | AFIT map3 | 1m | N/A | N/A | N/A |
| ADD45 | S | AFIT run1 | 0.5m | cal | 1 | | T | AFIT map3 | 1m | N/A | N/A | N/A |

| | | | | | | | | | | | | |
|---|---|---|---|---|---|---|---|---|---|---|---|---|
| ADD46 | S | AFIT run1 | 0.5m | cal | 1 | | C | AFIT map3 | 1m | N/A | N/A | N/A |
| ADD47 | C | AFIT run1 | 0.5m | cal | 1 | | T | AFIT map3 | 1m | N/A | N/A | N/A |
| ADD48 | C | AFIT run1 | 0.5m | cal | 1 | | S | AFIT map2 | 1m | N/A | N/A | N/A |
| ADD49 | T | AFIT run2 | 1m | uncal | 1 | | T | AFIT map3 | 1m | N/A | N/A | N/A |
| ADD50 | T | AFIT run2 | 1m | cal | 1 | | T | AFIT map3 | 1m | N/A | N/A | N/A |
| ADD51 | S | AFIT run1 | 1m | uncal | 1 | | S | AFIT map2 | 1m | N/A | N/A | N/A |
| ADD52 | S | AFIT run1 | 1m | cal | 1 | | S | AFIT map2 | 1m | N/A | N/A | N/A |
| ADD53 | C | AFIT run1 | 1m | uncal | 1 | | C | AFIT map3 | 1m | N/A | N/A | N/A |
| ADD54 | C | AFIT run1 | 1m | cal | 1 | | C | AFIT map3 | 1m | N/A | N/A | N/A |
| ADD55 | T | AFIT run2 | 1m | cal | 1 | | S | AFIT map2 | 1m | N/A | N/A | N/A |
| ADD56 | T | AFIT run2 | 1m | cal | 1 | | C | AFIT map3 | 1m | N/A | N/A | N/A |
| ADD57 | S | AFIT run1 | 1m | cal | 1 | | T | AFIT map3 | 1m | N/A | N/A | N/A |
| ADD58 | S | AFIT run1 | 1m | cal | 1 | | C | AFIT map3 | 1m | N/A | N/A | N/A |
| ADD59 | C | AFIT run1 | 1m | cal | 1 | | T | AFIT map3 | 1m | N/A | N/A | N/A |
| ADD60 | C | AFIT run1 | 1m | cal | 1 | | S | AFIT map2 | 1m | N/A | N/A | N/A |
| ADD61 | T | AFIT run2 | 3m | uncal | 1 | | T | AFIT map3 | 1m | N/A | N/A | N/A |
| ADD62 | T | AFIT run2 | 3m | cal | 1 | | T | AFIT map3 | 1m | N/A | N/A | N/A |
| ADD63 | S | AFIT run1 | 3m | uncal | 1 | | S | AFIT map2 | 1m | N/A | N/A | N/A |
| ADD64 | S | AFIT run1 | 3m | cal | 1 | | S | AFIT map2 | 1m | N/A | N/A | N/A |
| ADD65 | C | AFIT run1 | 3m | uncal | 1 | | C | AFIT map3 | 1m | N/A | N/A | N/A |
| ADD66 | C | AFIT run1 | 3m | cal | 1 | | C | AFIT map3 | 1m | N/A | N/A | N/A |
| ADD67 | T | AFIT run2 | 3m | cal | 1 | | S | AFIT map2 | 1m | N/A | N/A | N/A |
| ADD68 | T | AFIT run2 | 3m | cal | 1 | | C | AFIT map3 | 1m | N/A | N/A | N/A |
| ADD69 | S | AFIT run1 | 3m | cal | 1 | | T | AFIT map3 | 1m | N/A | N/A | N/A |
| ADD70 | S | AFIT run1 | 3m | cal | 1 | | C | AFIT map3 | 1m | N/A | N/A | N/A |
| ADD71 | C | AFIT run1 | 3m | cal | 1 | | T | AFIT map3 | 1m | N/A | N/A | N/A |
| ADD72 | C | AFIT run1 | 3m | cal | 1 | | S | AFIT map2 | 1m | N/A | N/A | N/A |
| ADD73 | T | AFIT run2 | 0.5m | uncal | 1 | | T | AFIT map3 | 3m | N/A | N/A | N/A |
| ADD74 | T | AFIT run2 | 0.5m | cal | 1 | | T | AFIT map3 | 3m | N/A | N/A | N/A |
| ADD75 | S | AFIT run1 | 0.5m | uncal | 1 | | S | AFIT map2 | 3m | N/A | N/A | N/A |
| ADD76 | S | AFIT run1 | 0.5m | cal | 1 | | S | AFIT map2 | 3m | N/A | N/A | N/A |
| ADD77 | C | AFIT run1 | 0.5m | uncal | 1 | | C | AFIT map3 | 3m | N/A | N/A | N/A |
| ADD78 | C | AFIT run1 | 0.5m | cal | 1 | | C | AFIT map3 | 3m | N/A | N/A | N/A |
| ADD79 | T | AFIT run2 | 0.5m | cal | 1 | | S | AFIT map2 | 3m | N/A | N/A | N/A |
| ADD80 | T | AFIT run2 | 0.5m | cal | 1 | | C | AFIT map3 | 3m | N/A | N/A | N/A |
| ADD81 | S | AFIT run1 | 0.5m | cal | 1 | | T | AFIT map3 | 3m | N/A | N/A | N/A |
| ADD82 | S | AFIT run1 | 0.5m | cal | 1 | | C | AFIT map3 | 3m | N/A | N/A | N/A |
| ADD83 | C | AFIT run1 | 0.5m | cal | 1 | | T | AFIT map3 | 3m | N/A | N/A | N/A |
| ADD84 | C | AFIT run1 | 0.5m | cal | 1 | | S | AFIT map2 | 3m | N/A | N/A | N/A |
| ADD85 | T | AFIT run2 | 1m | uncal | 1 | | T | AFIT map3 | 3m | N/A | N/A | N/A |
| ADD86 | T | AFIT run2 | 1m | cal | 1 | | T | AFIT map3 | 3m | N/A | N/A | N/A |
| ADD87 | S | AFIT run1 | 1m | uncal | 1 | | S | AFIT map2 | 3m | N/A | N/A | N/A |
| ADD88 | S | AFIT run1 | 1m | cal | 1 | | S | AFIT map2 | 3m | N/A | N/A | N/A |
| ADD89 | C | AFIT run1 | 1m | uncal | 1 | | C | AFIT map3 | 3m | N/A | N/A | N/A |
| ADD90 | C | AFIT run1 | 1m | cal | 1 | | C | AFIT map3 | 3m | N/A | N/A | N/A |
| ADD91 | T | AFIT run2 | 1m | cal | 1 | | S | AFIT map2 | 3m | N/A | N/A | N/A |
| ADD92 | T | AFIT run2 | 1m | cal | 1 | | C | AFIT map3 | 3m | N/A | N/A | N/A |

| | | | | | | | | | | | | |
|---|---|---|---|---|---|---|---|---|---|---|---|---|
| ADD93 | S | AFIT run1 | 1m | cal | 1 | | T | AFIT map3 | 3m | N/A | N/A | N/A |
| ADD94 | S | AFIT run1 | 1m | cal | 1 | | C | AFIT map3 | 3m | N/A | N/A | N/A |
| ADD95 | C | AFIT run1 | 1m | cal | 1 | | T | AFIT map3 | 3m | N/A | N/A | N/A |
| ADD96 | C | AFIT run1 | 1m | cal | 1 | | S | AFIT map2 | 3m | N/A | N/A | N/A |
| ADD97 | T | AFIT run2 | 3m | uncal | 1 | | T | AFIT map3 | 3m | N/A | N/A | N/A |
| ADD98 | T | AFIT run2 | 3m | cal | 1 | | T | AFIT map3 | 3m | N/A | N/A | N/A |
| ADD99 | S | AFIT run1 | 3m | uncal | 1 | | S | AFIT map2 | 3m | N/A | N/A | N/A |
| ADD100 | S | AFIT run1 | 3m | cal | 1 | | S | AFIT map2 | 3m | N/A | N/A | N/A |
| ADD101 | C | AFIT run1 | 3m | uncal | 1 | | C | AFIT map3 | 3m | N/A | N/A | N/A |
| ADD102 | C | AFIT run1 | 3m | cal | 1 | | C | AFIT map3 | 3m | N/A | N/A | N/A |
| ADD103 | T | AFIT run2 | 3m | cal | 1 | | S | AFIT map2 | 3m | N/A | N/A | N/A |
| ADD104 | T | AFIT run2 | 3m | cal | 1 | | C | AFIT map3 | 3m | N/A | N/A | N/A |
| ADD105 | S | AFIT run1 | 3m | cal | 1 | | T | AFIT map3 | 3m | N/A | N/A | N/A |
| ADD106 | S | AFIT run1 | 3m | cal | 1 | | C | AFIT map3 | 3m | N/A | N/A | N/A |
| ADD107 | C | AFIT run1 | 3m | cal | 1 | | T | AFIT map3 | 3m | N/A | N/A | N/A |
| ADD108 | C | AFIT run1 | 3m | cal | 1 | | S | AFIT map2 | 3m | N/A | N/A | N/A |
| | | | | | | | | | | | | |
| Comparison using multiple measurements | | | | | | | | | | | | |
| ADD200 | T | AFIT run2 | 0.5 | cal | 1 | | S | AFIT map2 | 0.5 | n | n | n |
| ADD201 | T | AFIT run2 | 0.5 | cal | 1 | | C | AFIT map3 | 0.5 | n | n | n |
| ADD202 | C | AFIT run1 | 0.5 | cal | 1 | | S | AFIT map2 | 0.5 | n | n | n |
| ADD203 | T | AFIT run2 | 0.5 | cal | 3 | | S | AFIT map2 | 0.5 | n | n | n |
| ADD204 | T | AFIT run2 | 0.5 | cal | 3 | | C | AFIT map3 | 0.5 | n | n | n |
| ADD205 | C | AFIT run1 | 0.5 | cal | 3 | | S | AFIT map2 | 0.5 | n | n | n |
| ADD206 | T | AFIT run2 | 0.5 | cal | 7 | | S | AFIT map2 | 0.5 | n | n | n |
| ADD207 | T | AFIT run2 | 0.5 | cal | 7 | | C | AFIT map3 | 0.5 | n | n | n |
| ADD208 | C | AFIT run1 | 0.5 | cal | 7 | | S | AFIT map2 | 0.5 | n | n | n |
| ADD209 | T | AFIT run2 | 1m | cal | 1 | | S | AFIT map2 | 1m | n | n | n |
| ADD210 | T | AFIT run2 | 1m | cal | 1 | | C | AFIT map3 | 1m | n | n | n |
| ADD211 | C | AFIT run1 | 1m | cal | 1 | | S | AFIT map2 | 1m | n | n | n |
| ADD212 | T | AFIT run2 | 1m | cal | 2 | | S | AFIT map2 | 1m | n | n | n |
| ADD213 | T | AFIT run2 | 1m | cal | 2 | | C | AFIT map3 | 1m | n | n | n |
| ADD214 | C | AFIT run1 | 1m | cal | 2 | | S | AFIT map2 | 1m | n | n | n |
| ADD215 | T | AFIT run2 | 1m | cal | 4 | | S | AFIT map2 | 1m | n | n | n |
| ADD216 | T | AFIT run2 | 1m | cal | 4 | | C | AFIT map3 | 1m | n | n | n |
| ADD217 | C | AFIT run1 | 1m | cal | 4 | | S | AFIT map2 | 1m | n | n | n |
| ADD218 | T | AFIT run2 | 3m | cal | 1 | | S | AFIT map2 | 3m | n | n | n |
| ADD219 | T | AFIT run2 | 3m | cal | 1 | | C | AFIT map3 | 3m | n | n | n |
| ADD220 | C | AFIT run1 | 3m | cal | 1 | | S | AFIT map2 | 3m | n | n | n |
| ADD221 | T | AFIT run2 | 3m | cal | 2 | | S | AFIT map2 | 3m | n | n | n |
| ADD222 | T | AFIT run2 | 3m | cal | 2 | | C | AFIT map3 | 3m | n | n | n |
| ADD223 | C | AFIT run1 | 3m | cal | 2 | | S | AFIT map2 | 3m | n | n | n |
| ADD224 | T | AFIT run2 | 3m | cal | 3 | | S | AFIT map2 | 3m | n | n | n |
| ADD225 | T | AFIT run2 | 3m | cal | 3 | | C | AFIT map3 | 3m | n | n | n |
| ADD226 | C | AFIT run1 | 3m | cal | 3 | | S | AFIT map2 | 3m | n | n | n |
| | | | | | | | | | | | | |
| Comparison of multiple measurements exploring demeaning and differencing | | | | | | | | | | | | |

| | | | | | | | | | | | | |
|---|---|---|---|---|---|---|---|---|---|---|---|---|
| ADD300 | T | AFIT run2 | 1m | uncal | 4 | | S | AFIT map2 | 1m | y | n | n |
| ADD301 | T | AFIT run2 | 1m | cal | 4 | | S | AFIT map2 | 1m | y | n | n |
| ADD302 | T | AFIT run2 | 1m | uncal | 4 | | C | AFIT map3 | 1m | y | n | n |
| ADD303 | T | AFIT run2 | 1m | cal | 4 | | C | AFIT map2 | 1m | y | n | n |
| ADD304 | C | AFIT run1 | 1m | uncal | 4 | | S | AFIT map2 | 1m | y | n | n |
| ADD305 | C | AFIT run1 | 1m | cal | 4 | | S | AFIT map2 | 1m | y | n | n |
| ADD306 | T | AFIT run2 | 1m | uncal | 4 | | S | AFIT map2 | 1m | n | y | n |
| ADD307 | T | AFIT run2 | 1m | cal | 4 | | S | AFIT map2 | 1m | n | y | n |
| ADD308 | T | AFIT run2 | 1m | uncal | 4 | | C | AFIT map3 | 1m | n | y | n |
| ADD309 | T | AFIT run2 | 1m | cal | 4 | | C | AFIT map2 | 1m | n | y | n |
| ADD310 | C | AFIT run1 | 1m | uncal | 4 | | S | AFIT map2 | 1m | n | y | n |
| ADD311 | C | AFIT run1 | 1m | cal | 4 | | S | AFIT map2 | 1m | n | y | n |
| ADD312 | T | AFIT run2 | 0.5m | uncal | 4 | | S | AFIT map2 | 0.5m | y | n | n |
| ADD313 | T | AFIT run2 | 0.5m | cal | 4 | | S | AFIT map2 | 0.5m | y | n | n |
| ADD314 | T | AFIT run2 | 0.5m | uncal | 4 | | C | AFIT map3 | 0.5m | y | n | n |
| ADD315 | T | AFIT run2 | 0.5m | cal | 4 | | C | AFIT map2 | 0.5m | y | n | n |
| ADD316 | C | AFIT run1 | 0.5m | uncal | 4 | | S | AFIT map2 | 0.5m | y | n | n |
| ADD317 | C | AFIT run1 | 0.5m | cal | 4 | | S | AFIT map2 | 0.5m | y | n | n |
| ADD318 | T | AFIT run2 | 0.5m | uncal | 4 | | S | AFIT map2 | 0.5m | n | y | n |
| ADD319 | T | AFIT run2 | 0.5m | cal | 4 | | S | AFIT map2 | 0.5m | n | y | n |
| ADD320 | T | AFIT run2 | 0.5m | uncal | 4 | | C | AFIT map3 | 0.5m | n | y | n |
| ADD321 | T | AFIT run2 | 0.5m | cal | 4 | | C | AFIT map2 | 0.5m | n | y | n |
| ADD322 | C | AFIT run1 | 0.5m | uncal | 4 | | S | AFIT map2 | 0.5m | n | y | n |
| ADD323 | C | AFIT run1 | 0.5m | cal | 4 | | S | AFIT map2 | 0.5m | n | y | n |
| ADD324 | T | AFIT run2 | 3m | uncal | 4 | | S | AFIT map2 | 3m | y | n | n |
| ADD325 | T | AFIT run2 | 3m | cal | 4 | | S | AFIT map2 | 3m | y | n | n |
| ADD326 | T | AFIT run2 | 3m | uncal | 4 | | C | AFIT map3 | 3m | y | n | n |
| ADD327 | T | AFIT run2 | 3m | cal | 4 | | C | AFIT map2 | 3m | y | n | n |
| ADD328 | C | AFIT run1 | 3m | uncal | 4 | | S | AFIT map2 | 3m | y | n | n |
| ADD329 | C | AFIT run1 | 3m | cal | 4 | | S | AFIT map2 | 3m | y | n | n |
| ADD330 | T | AFIT run2 | 3m | uncal | 4 | | S | AFIT map2 | 3m | n | y | n |
| ADD331 | T | AFIT run2 | 3m | cal | 4 | | S | AFIT map2 | 3m | n | y | n |
| ADD332 | T | AFIT run2 | 3m | uncal | 4 | | C | AFIT map3 | 3m | n | y | n |
| ADD333 | T | AFIT run2 | 3m | cal | 4 | | C | AFIT map2 | 3m | n | y | n |
| ADD334 | C | AFIT run1 | 3m | uncal | 4 | | S | AFIT map2 | 3m | n | y | n |
| ADD335 | C | AFIT run1 | 3m | cal | 4 | | S | AFIT map2 | 3m | n | y | n |
| | | | | | | | | | | | | |
| Comparison using features | | | | | | | | | | | | |
| ADD400 | T | AFIT run2 | 1m | cal | 4 | | S | AFIT map2 | 1m | n | n | y |
| ADD401 | T | AFIT run2 | 1m | cal | 4 | | C | AFIT map2 | 1m | n | n | y |
| ADD402 | C | AFIT run1 | 1m | cal | 4 | | S | AFIT map2 | 1m | n | n | y |
| ADD403 | T | AFIT run2 | 1m | uncal | 4 | | S | AFIT map2 | 1m | y | n | y |
| ADD404 | T | AFIT run2 | 1m | cal | 4 | | S | AFIT map2 | 1m | y | n | y |
| ADD405 | T | AFIT run2 | 1m | uncal | 4 | | C | AFIT map3 | 1m | y | n | y |
| ADD406 | T | AFIT run2 | 1m | cal | 4 | | C | AFIT map2 | 1m | y | n | y |
| ADD407 | C | AFIT run1 | 1m | uncal | 4 | | S | AFIT map2 | 1m | y | n | y |
| ADD408 | C | AFIT run1 | 1m | cal | 4 | | S | AFIT map2 | 1m | y | n | y |

| | | | | | | | | | | | | |
|---|---|---|---|---|---|---|---|---|---|---|---|---|
| ADD409 | T | AFIT run2 | 1m | uncal | 4 | | S | AFIT map2 | 1m | n | y | y |
| ADD410 | T | AFIT run2 | 1m | cal | 4 | | S | AFIT map2 | 1m | n | y | y |
| ADD411 | T | AFIT run2 | 1m | uncal | 4 | | C | AFIT map3 | 1m | n | y | y |
| ADD412 | T | AFIT run2 | 1m | cal | 4 | | C | AFIT map2 | 1m | n | y | y |
| ADD413 | C | AFIT run1 | 1m | uncal | 4 | | S | AFIT map2 | 1m | n | y | y |
| ADD414 | C | AFIT run1 | 1m | cal | 4 | | S | AFIT map2 | 1m | n | y | y |
| ADD415 | T | AFIT run2 | 0.5m | cal | 4 | | S | AFIT map2 | 0.5m | n | n | y |
| ADD416 | T | AFIT run2 | 0.5m | cal | 4 | | C | AFIT map2 | 0.5m | n | n | y |
| ADD417 | C | AFIT run1 | 0.5m | cal | 4 | | S | AFIT map2 | 0.5m | n | n | y |
| ADD418 | T | AFIT run2 | 0.5m | uncal | 4 | | S | AFIT map2 | 0.5m | y | n | y |
| ADD419 | T | AFIT run2 | 0.5m | cal | 4 | | S | AFIT map2 | 0.5m | y | n | y |
| ADD420 | T | AFIT run2 | 0.5m | uncal | 4 | | C | AFIT map3 | 0.5m | y | n | y |
| ADD421 | T | AFIT run2 | 0.5m | cal | 4 | | C | AFIT map2 | 0.5m | y | n | y |
| ADD422 | C | AFIT run1 | 0.5m | uncal | 4 | | S | AFIT map2 | 0.5m | y | n | y |
| ADD423 | C | AFIT run1 | 0.5m | cal | 4 | | S | AFIT map2 | 0.5m | y | n | y |
| ADD424 | T | AFIT run2 | 0.5m | uncal | 4 | | S | AFIT map2 | 0.5m | n | y | y |
| ADD425 | T | AFIT run2 | 0.5m | cal | 4 | | S | AFIT map2 | 0.5m | n | y | y |
| ADD426 | T | AFIT run2 | 0.5m | uncal | 4 | | C | AFIT map3 | 0.5m | n | y | y |
| ADD427 | T | AFIT run2 | 0.5m | cal | 4 | | C | AFIT map2 | 0.5m | n | y | y |
| ADD428 | C | AFIT run1 | 0.5m | uncal | 4 | | S | AFIT map2 | 0.5m | n | y | y |
| ADD429 | C | AFIT run1 | 3m | cal | 4 | | S | AFIT map2 | 3m | n | y | y |
| ADD430 | T | AFIT run2 | 3m | cal | 4 | | S | AFIT map2 | 3m | n | n | y |
| ADD431 | T | AFIT run2 | 3m | cal | 4 | | C | AFIT map2 | 3m | n | n | y |
| ADD432 | C | AFIT run1 | 3m | cal | 4 | | S | AFIT map2 | 3m | n | n | y |
| ADD433 | T | AFIT run2 | 3m | uncal | 4 | | S | AFIT map2 | 3m | y | n | y |
| ADD434 | T | AFIT run2 | 3m | cal | 4 | | S | AFIT map2 | 3m | y | n | y |
| ADD435 | T | AFIT run2 | 3m | uncal | 4 | | C | AFIT map3 | 3m | y | n | y |
| ADD436 | T | AFIT run2 | 3m | cal | 4 | | C | AFIT map2 | 3m | y | n | y |
| ADD437 | C | AFIT run1 | 3m | uncal | 4 | | S | AFIT map2 | 3m | y | n | y |
| ADD438 | C | AFIT run1 | 3m | cal | 4 | | S | AFIT map2 | 3m | y | n | y |
| ADD439 | T | AFIT run2 | 3m | uncal | 4 | | S | AFIT map2 | 3m | n | y | y |
| ADD440 | T | AFIT run2 | 3m | cal | 4 | | S | AFIT map2 | 3m | n | y | y |
| ADD441 | T | AFIT run2 | 3m | uncal | 4 | | C | AFIT map3 | 3m | n | y | y |
| ADD442 | T | AFIT run2 | 3m | cal | 4 | | C | AFIT map2 | 3m | n | y | y |
| ADD443 | C | AFIT run1 | 3m | uncal | 4 | | S | AFIT map2 | 3m | n | y | y |
| ADD444 | C | AFIT run1 | 3m | cal | 4 | | S | AFIT map2 | 3m | n | y | y |

| Test Case | Measurements | | | | | | Map | | | Comparison Method | | |
|---|---|---|---|---|---|---|---|---|---|---|---|---|
| | Veh | Description | Units | Type | #Meas | | Veh | Description | Units | Demean | Diff | Feature |
| HBT01 | T | sub run2 | 50Hz | uncal | 1 | | T | sub map3 | 50Hz | N/A | N/A | N/A |
| HBT02 | T | sub run2 | 50Hz | cal | 1 | | T | sub map3 | 50Hz | N/A | N/A | N/A |
| HBT03 | S | sub run1 | 50Hz | uncal | 1 | | S | sub map2 | 50Hz | N/A | N/A | N/A |
| HBT04 | S | sub run1 | 50Hz | cal | 1 | | S | sub map2 | 50Hz | N/A | N/A | N/A |
| HBT05 | C | sub run1 | 50Hz | uncal | 1 | | C | sub map2 | 50Hz | N/A | N/A | N/A |
| HBT06 | C | sub run1 | 50Hz | cal | 1 | | C | sub map2 | 50Hz | N/A | N/A | N/A |
| HBT07 | T | sub run2 | 50Hz | cal | 1 | | S | sub map2 | 50Hz | N/A | N/A | N/A |
| HBT08 | T | sub run2 | 50Hz | cal | 1 | | C | sub map2 | 50Hz | N/A | N/A | N/A |
| HBT09 | S | sub run1 | 50Hz | cal | 1 | | T | sub map3 | 50Hz | N/A | N/A | N/A |
| HBT10 | S | sub run1 | 50Hz | cal | 1 | | C | sub map2 | 50Hz | N/A | N/A | N/A |
| HBT11 | C | sub run1 | 50Hz | cal | 1 | | T | sub map3 | 50Hz | N/A | N/A | N/A |
| HBT12 | C | sub run1 | 50Hz | cal | 1 | | S | sub map2 | 50Hz | N/A | N/A | N/A |
| | | | | | | | | | | | | |
| Comparison based on time | | | | | | | | | | | | |
| HTT01 | T | sub run2 | 10Hz | uncal | 1 | | T | sub map3 | 10Hz | N/A | N/A | N/A |
| HTT02 | T | sub run2 | 10Hz | cal | 1 | | T | sub map3 | 10Hz | N/A | N/A | N/A |
| HTT03 | S | sub run1 | 10Hz | uncal | 1 | | S | sub map2 | 10Hz | N/A | N/A | N/A |
| HTT04 | S | sub run1 | 10Hz | cal | 1 | | S | sub map2 | 10Hz | N/A | N/A | N/A |
| HTT05 | C | sub run1 | 10Hz | uncal | 1 | | C | sub map2 | 10Hz | N/A | N/A | N/A |
| HTT06 | C | sub run1 | 10Hz | cal | 1 | | C | sub map2 | 10Hz | N/A | N/A | N/A |
| HTT07 | T | sub run2 | 10Hz | cal | 1 | | S | sub map2 | 10Hz | N/A | N/A | N/A |
| HTT08 | T | sub run2 | 10Hz | cal | 1 | | C | sub map2 | 10Hz | N/A | N/A | N/A |
| HTT09 | S | sub run1 | 10Hz | cal | 1 | | T | sub map3 | 10Hz | N/A | N/A | N/A |
| HTT10 | S | sub run1 | 10Hz | cal | 1 | | C | sub map2 | 10Hz | N/A | N/A | N/A |
| HTT11 | C | sub run1 | 10Hz | cal | 1 | | T | sub map3 | 10Hz | N/A | N/A | N/A |
| HTT12 | C | sub run1 | 10Hz | cal | 1 | | S | sub map2 | 10Hz | N/A | N/A | N/A |
| | | | | | | | | | | | | |
| Compare sensor measurements in distance to a map based on distance | | | | | | | | | | | | |
| HDD01 | T | sub run2 | 1m | uncal | 1 | | T | sub map3 | 1m | N/A | N/A | N/A |
| HDD02 | T | sub run2 | 1m | cal | 1 | | T | sub map3 | 1m | N/A | N/A | N/A |
| HDD03 | S | sub run1 | 1m | uncal | 1 | | S | sub map2 | 1m | N/A | N/A | N/A |
| HDD04 | S | sub run1 | 1m | cal | 1 | | S | sub map2 | 1m | N/A | N/A | N/A |
| HDD05 | C | sub run1 | 1m | uncal | 1 | | C | sub map2 | 1m | N/A | N/A | N/A |
| HDD06 | C | sub run1 | 1m | cal | 1 | | C | sub map2 | 1m | N/A | N/A | N/A |
| HDD07 | T | sub run2 | 1m | cal | 1 | | S | sub map2 | 1m | N/A | N/A | N/A |
| HDD08 | T | sub run2 | 1m | cal | 1 | | C | sub map2 | 1m | N/A | N/A | N/A |
| HDD09 | S | sub run1 | 1m | cal | 1 | | T | sub map3 | 1m | N/A | N/A | N/A |
| HDD10 | S | sub run1 | 1m | cal | 1 | | C | sub map2 | 1m | Demean | N/A | Feature |
| HDD11 | C | sub run1 | 1m | cal | 1 | | T | sub map3 | 1m | N/A | N/A | N/A |
| HDD12 | C | sub run1 | 1m | cal | 1 | | S | sub map2 | 1m | N/A | N/A | N/A |
| HDD13 | T | sub run2 | 3m | uncal | 1 | | T | sub map3 | 3m | N/A | N/A | N/A |
| HDD14 | T | sub run2 | 3m | cal | 1 | | T | sub map3 | 3m | N/A | N/A | N/A |
| HDD15 | S | sub run1 | 3m | uncal | 1 | | S | sub map2 | 3m | N/A | N/A | N/A |
| HDD16 | S | sub run1 | 3m | cal | 1 | | S | sub map2 | 3m | N/A | N/A | N/A |
| HDD17 | C | sub run1 | 3m | uncal | 1 | | C | sub map2 | 3m | N/A | N/A | N/A |

| | | | | | | | | | | | |
|---|---|---|---|---|---|---|---|---|---|---|---|
| HDD18 | C | sub run1 | 3m | cal | 1 | | C | sub map2 | 3m | N/A | N/A | N/A |
| HDD19 | T | sub run2 | 3m | cal | 1 | | S | sub map2 | 3m | N/A | N/A | N/A |
| HDD20 | T | sub run2 | 3m | cal | 1 | | C | sub map2 | 3m | N/A | N/A | N/A |
| HDD21 | S | sub run1 | 3m | cal | 1 | | T | sub map3 | 3m | N/A | N/A | N/A |
| HDD22 | S | sub run1 | 3m | cal | 1 | | C | sub map2 | 3m | N/A | N/A | N/A |
| HDD23 | C | sub run1 | 3m | cal | 1 | | T | sub map3 | 3m | N/A | N/A | N/A |
| HDD24 | C | sub run1 | 3m | cal | 1 | | S | sub map2 | 3m | N/A | N/A | N/A |
| | | | | | | | | | | | |
| Comparison using multiple measurements | | | | | | | | | | | |
| HDD200 | T | sub run2 | 1m | cal | 4 | | S | sub map2 | 1m | n | n | n |
| HDD201 | T | sub run2 | 1m | cal | 4 | | C | sub map2 | 1m | n | n | n |
| HDD202 | C | sub run1 | 1m | cal | 4 | | S | sub map2 | 1m | n | n | n |
| HDD203 | T | sub run1 | 3m | cal | 2 | | S | sub map2 | 3m | n | n | n |
| HDD204 | T | sub run1 | 3m | cal | 2 | | C | sub map2 | 3m | n | n | n |
| HDD205 | C | sub run1 | 3m | cal | 2 | | S | sub map2 | 3m | n | n | n |
| | | | | | | | | | | | |
| Comparison of multiple measurements exploring demeaning and differencing | | | | | | | | | | | |
| HDD300 | T | sub run2 | 1m | uncal | 4 | | S | sub map2 | 1m | y | n | n |
| HDD301 | T | sub run2 | 1m | cal | 4 | | S | sub map2 | 1m | y | n | n |
| HDD302 | T | sub run2 | 1m | uncal | 4 | | C | sub map2 | 1m | y | n | n |
| HDD303 | T | sub run2 | 1m | cal | 4 | | C | sub map2 | 1m | y | n | n |
| HDD304 | C | sub run1 | 1m | uncal | 4 | | S | sub map2 | 1m | y | n | n |
| HDD305 | C | sub run1 | 1m | cal | 4 | | S | sub map2 | 1m | y | n | n |
| HDD306 | T | sub run2 | 1m | uncal | 4 | | S | sub map2 | 1m | n | y | n |
| HDD307 | T | sub run2 | 1m | cal | 4 | | S | sub map2 | 1m | n | y | n |
| HDD308 | T | sub run2 | 1m | uncal | 4 | | C | sub map2 | 1m | n | y | n |
| HDD309 | T | sub run2 | 1m | cal | 4 | | C | sub map2 | 1m | n | y | n |
| HDD310 | C | sub run1 | 1m | uncal | 4 | | S | sub map2 | 1m | n | y | n |
| HDD311 | C | sub run1 | 1m | cal | 4 | | S | sub map2 | 1m | n | y | n |
| HDD312 | T | sub run2 | 0.5m | uncal | 4 | | S | sub map2 | 0.5m | y | n | n |
| HDD313 | T | sub run2 | 0.5m | cal | 4 | | S | sub map2 | 0.5m | y | n | n |
| HDD314 | T | sub run2 | 0.5m | uncal | 4 | | C | sub map2 | 0.5m | y | n | n |
| HDD315 | T | sub run2 | 0.5m | cal | 4 | | C | sub map2 | 0.5m | y | n | n |
| HDD316 | C | sub run1 | 0.5m | uncal | 4 | | S | sub map2 | 0.5m | y | n | n |
| HDD317 | C | sub run1 | 0.5m | cal | 4 | | S | sub map2 | 0.5m | y | n | n |
| HDD318 | T | sub run2 | 0.5m | uncal | 4 | | S | sub map2 | 0.5m | n | y | n |
| HDD319 | T | sub run2 | 0.5m | cal | 4 | | S | sub map2 | 0.5m | n | y | n |
| HDD320 | T | sub run2 | 0.5m | uncal | 4 | | C | sub map2 | 0.5m | n | y | n |
| HDD321 | T | sub run2 | 0.5m | cal | 4 | | C | sub map2 | 0.5m | n | y | n |
| HDD322 | C | sub run1 | 0.5m | uncal | 4 | | S | sub map2 | 0.5m | n | y | n |
| HDD323 | C | sub run1 | 0.5m | cal | 4 | | S | sub map2 | 0.5m | n | y | n |
| HDD324 | T | sub run2 | 3m | uncal | 4 | | S | sub map2 | 3m | y | n | n |
| HDD325 | T | sub run2 | 3m | cal | 4 | | S | sub map2 | 3m | y | n | n |
| HDD326 | T | sub run2 | 3m | uncal | 4 | | C | sub map2 | 3m | y | n | n |
| HDD327 | T | sub run2 | 3m | cal | 4 | | C | sub map2 | 3m | y | n | n |
| HDD328 | C | sub run1 | 3m | uncal | 4 | | S | sub map2 | 3m | y | n | n |
| HDD329 | C | sub run1 | 3m | cal | 4 | | S | sub map2 | 3m | y | n | n |

| | | | | | | | | | | | | |
|---|---|---|---|---|---|---|---|---|---|---|---|---|
| HDD330 | T | sub run2 | 3m | uncal | 4 | | S | sub map2 | 3m | n | y | n |
| HDD331 | T | sub run2 | 3m | cal | 4 | | S | sub map2 | 3m | n | y | n |
| HDD332 | T | sub run2 | 3m | uncal | 4 | | C | sub map2 | 3m | n | y | n |
| HDD333 | T | sub run2 | 3m | cal | 4 | | C | sub map2 | 3m | n | y | n |
| HDD334 | C | sub run1 | 3m | uncal | 4 | | S | sub map2 | 3m | n | y | n |
| HDD335 | C | sub run1 | 3m | cal | 4 | | S | sub map2 | 3m | n | y | n |
| | | | | | | | | | | | | |
| Comparison using features | | | | | | | | | | | | |
| HDD400 | T | sub run2 | 1m | cal | 4 | | S | sub map2 | 1m | n | n | y |
| HDD401 | T | sub run2 | 1m | cal | 4 | | C | sub map2 | 1m | n | n | y |
| HDD402 | C | sub run1 | 1m | cal | 4 | | S | sub map2 | 1m | n | n | y |
| HDD403 | T | sub run2 | 1m | uncal | 4 | | S | sub map2 | 1m | y | n | y |
| HDD404 | T | sub run2 | 1m | cal | 4 | | S | sub map2 | 1m | y | n | y |
| HDD405 | T | sub run2 | 1m | uncal | 4 | | C | sub map2 | 1m | y | n | y |
| HDD406 | T | sub run2 | 1m | cal | 4 | | C | sub map2 | 1m | y | n | y |
| HDD407 | C | sub run1 | 1m | uncal | 4 | | S | sub map2 | 1m | y | n | y |
| HDD408 | C | sub run1 | 1m | cal | 4 | | S | sub map2 | 1m | y | n | y |
| HDD409 | T | sub run2 | 1m | uncal | 4 | | S | sub map2 | 1m | n | y | y |
| HDD410 | T | sub run2 | 1m | cal | 4 | | S | sub map2 | 1m | n | y | y |
| HDD411 | T | sub run2 | 1m | uncal | 4 | | C | sub map2 | 1m | n | y | y |
| HDD412 | T | sub run2 | 1m | cal | 4 | | C | sub map2 | 1m | n | y | y |
| HDD413 | C | sub run1 | 1m | uncal | 4 | | S | sub map2 | 1m | n | y | y |
| HDD414 | C | sub run1 | 1m | cal | 4 | | S | sub map2 | 1m | n | y | y |
| HDD415 | T | sub run2 | 0.5m | cal | 4 | | S | sub map2 | 0.5m | n | n | y |
| HDD416 | T | sub run2 | 0.5m | cal | 4 | | C | sub map2 | 0.5m | n | n | y |
| HDD417 | C | sub run1 | 0.5m | cal | 4 | | S | sub map2 | 0.5m | n | n | y |
| HDD418 | T | sub run2 | 0.5m | uncal | 4 | | S | sub map2 | 0.5m | y | n | y |
| HDD419 | T | sub run2 | 0.5m | cal | 4 | | S | sub map2 | 0.5m | y | n | y |
| HDD420 | T | sub run2 | 0.5m | uncal | 4 | | C | sub map2 | 0.5m | y | n | y |
| HDD421 | T | sub run2 | 0.5m | cal | 4 | | C | sub map2 | 0.5m | y | n | y |
| HDD422 | C | sub run1 | 0.5m | uncal | 4 | | S | sub map2 | 0.5m | y | n | y |
| HDD423 | C | sub run1 | 0.5m | cal | 4 | | S | sub map2 | 0.5m | y | n | y |
| HDD424 | T | sub run2 | 0.5m | uncal | 4 | | S | sub map2 | 0.5m | n | y | y |
| HDD425 | T | sub run2 | 0.5m | cal | 4 | | S | sub map2 | 0.5m | n | y | y |
| HDD426 | T | sub run2 | 0.5m | uncal | 4 | | C | sub map2 | 0.5m | n | y | y |
| HDD427 | T | sub run2 | 0.5m | cal | 4 | | C | sub map2 | 0.5m | n | y | y |
| HDD428 | C | sub run1 | 0.5m | uncal | 4 | | S | sub map2 | 0.5m | n | y | y |
| HDD429 | C | sub run1 | 0.5m | cal | 4 | | S | sub map2 | 0.5m | n | y | y |
| HDD430 | T | sub run2 | 3m | cal | 4 | | S | sub map2 | 3m | n | n | y |
| HDD431 | T | sub run2 | 3m | cal | 4 | | C | sub map2 | 3m | n | n | y |
| HDD432 | C | sub run1 | 3m | cal | 4 | | S | sub map2 | 3m | n | n | y |
| HDD433 | T | sub run2 | 3m | uncal | 4 | | S | sub map2 | 3m | y | n | y |
| HDD434 | T | sub run2 | 3m | cal | 4 | | S | sub map2 | 3m | y | n | y |
| HDD435 | T | sub run2 | 3m | uncal | 4 | | C | sub map2 | 3m | y | n | y |
| HDD436 | T | sub run2 | 3m | cal | 4 | | C | sub map2 | 3m | y | n | y |
| HDD437 | C | sub run1 | 3m | uncal | 4 | | S | sub map2 | 3m | y | n | y |
| HDD438 | C | sub run1 | 3m | cal | 4 | | S | sub map2 | 3m | y | n | y |

| HDD439 | T | sub run2 | 3m | uncal | 4 | | S | sub map2 | 3m | n | y | y |
|--------|---|----------|----|-------|---|---|---|----------|----|---|---|---|
| HDD440 | T | sub run2 | 3m | cal | 4 | | S | sub map2 | 3m | n | y | y |
| HDD441 | T | sub run2 | 3m | uncal | 4 | | C | sub map2 | 3m | n | y | y |
| HDD442 | T | sub run2 | 3m | cal | 4 | | C | sub map2 | 3m | n | y | y |
| HDD443 | C | sub run1 | 3m | uncal | 4 | | S | sub map2 | 3m | n | y | y |
| HDD444 | C | sub run1 | 3m | cal | 4 | | S | sub map2 | 3m | n | y | y |

| Test Case | Veh | Measurements Description | Units | Type | #Meas | | Veh | Map Description | Units | Comparison Method Demean | Diff | Feature |
|---|---|---|---|---|---|---|---|---|---|---|---|---|
| LBT01 | T | large run2 | 50Hz | uncal | 1 | | T | large map3 | 50Hz | N/A | N/A | N/A |
| LBT02 | T | large run2 | 50Hz | cal | 1 | | T | large map3 | 50Hz | N/A | N/A | N/A |
| LBT03 | S | large run1 | 50Hz | uncal | 1 | | S | large map2 | 50Hz | N/A | N/A | N/A |
| LBT04 | S | large run1 | 50Hz | cal | 1 | | S | large map2 | 50Hz | N/A | N/A | N/A |
| LBT05 | C | large run1 | 50Hz | uncal | 1 | | C | large map2 | 50Hz | N/A | N/A | N/A |
| LBT06 | C | large run1 | 50Hz | cal | 1 | | C | large map2 | 50Hz | N/A | N/A | N/A |
| LBT07 | T | large run2 | 50Hz | cal | 1 | | S | large map2 | 50Hz | N/A | N/A | N/A |
| LBT08 | T | large run2 | 50Hz | cal | 1 | | C | large map2 | 50Hz | N/A | N/A | N/A |
| LBT09 | S | large run1 | 50Hz | cal | 1 | | T | large map3 | 50Hz | N/A | N/A | N/A |
| LBT10 | S | large run1 | 50Hz | cal | 1 | | C | large map2 | 50Hz | N/A | N/A | N/A |
| LBT11 | C | large run1 | 50Hz | cal | 1 | | T | large map3 | 50Hz | N/A | N/A | N/A |
| LBT12 | C | large run1 | 50Hz | cal | 1 | | S | large map2 | 50Hz | N/A | N/A | N/A |
| | | | | | | | | | | | | |
| Comparison based on time | | | | | | | | | | | | |
| LTT01 | T | large run2 | 10Hz | uncal | 1 | | T | large map3 | 10Hz | N/A | N/A | N/A |
| LTT02 | T | large run2 | 10Hz | cal | 1 | | T | large map3 | 10Hz | N/A | N/A | N/A |
| LTT03 | S | large run1 | 10Hz | uncal | 1 | | S | large map2 | 10Hz | N/A | N/A | N/A |
| LTT04 | S | large run1 | 10Hz | cal | 1 | | S | large map2 | 10Hz | N/A | N/A | N/A |
| LTT05 | C | large run1 | 10Hz | uncal | 1 | | C | large map2 | 10Hz | N/A | N/A | N/A |
| LTT06 | C | large run1 | 10Hz | cal | 1 | | C | large map2 | 10Hz | N/A | N/A | N/A |
| LTT07 | T | large run2 | 10Hz | cal | 1 | | S | large map2 | 10Hz | N/A | N/A | N/A |
| LTT08 | T | large run2 | 10Hz | cal | 1 | | C | large map2 | 10Hz | N/A | N/A | N/A |
| LTT09 | S | large run1 | 10Hz | cal | 1 | | T | large map3 | 10Hz | N/A | N/A | N/A |
| LTT10 | S | large run1 | 10Hz | cal | 1 | | C | large map2 | 10Hz | N/A | N/A | N/A |
| LTT11 | C | large run1 | 10Hz | cal | 1 | | T | large map3 | 10Hz | N/A | N/A | N/A |
| LTT12 | C | large run1 | 10Hz | cal | 1 | | S | large map2 | 10Hz | N/A | N/A | N/A |

## *Appendix B.   Navigation Solution Cases*

THE following spreadsheets detail the entire matrix of navigation solution cases. Cases highlighted in green were specifically used for results presented in Chapter V and Appendix B. Non-highlighted cases were explored, but did not yield results substantially different than those reported in the main body of the document.

The test case identifiers help distinguish the environments as well as the parameter variation. The first character identifies the map section as shown in Figure 4.1. The letter **A** stands for the rectangular road path around AFIT. **H** signifies the suburban neighborhood, and **L** represents the large area map. The second character labels the measurement type by distance or time. The third character denotes the map type in distance or time. Finally, characters four through six designate the specific case. Breaks in the test case numbers represent the start of a different test case series and are not to be perceived as missing test cases. The column heading "Measurements" defines the test case parameters used for the incoming magnetometer measurements, while "Map" defines the parameters of the map used. The "Comparison Method" heading denotes whether an additional technique such as demeaning (Demean), differencing (Diff) or feature (Feature) composition was used. For all test cases, the vehicle (**Veh**) descriptors of **T**, **S**, and **C** stand for the Truck, SUV, or Car, respectively. The units (**Units**) are in time or distance. The calibration type (**Type**) conveys uncalibrated (uncal), calibrated (cal), or simple (sf1). The number of measurements (#**Meas**) would be one for single epoch, four for a 3m section of 1m measurements, and so forth. Since a single epoch only uses a single measurement, the comparison methods of demeaning, differencing, or feature are marked not applicable (N/A). Once multiple measurements are explored, these change to a yes (y) or no (n).

| | Measurements | | | | | | Map | | | Comparison Method | | |
|---|---|---|---|---|---|---|---|---|---|---|---|---|
| Test Case | Veh | Description | Units | Type | #Meas | | Veh | Description | Units | Demean | Diff | Feature |
| ANT01 | T | AFIT run2 | 50Hz | uncal | 1 | | T | AFIT map3 | 50Hz | N/A | N/A | N/A |
| ANT02 | T | AFIT run2 | 50Hz | cal | 1 | | T | AFIT map3 | 50Hz | N/A | N/A | N/A |
| ANT03 | S | AFIT run1 | 50Hz | uncal | 1 | | S | AFIT map2 | 50Hz | N/A | N/A | N/A |
| ANT04 | S | AFIT run1 | 50Hz | cal | 1 | | S | AFIT map2 | 50Hz | N/A | N/A | N/A |
| ANT05 | C | AFIT run1 | 50Hz | uncal | 1 | | C | AFIT map3 | 50Hz | N/A | N/A | N/A |
| ANT06 | C | AFIT run1 | 50Hz | cal | 1 | | C | AFIT map3 | 50Hz | N/A | N/A | N/A |
| ANT07 | T | AFIT run2 | 50Hz | cal | 1 | | S | AFIT map2 | 50Hz | N/A | N/A | N/A |
| ANT08 | T | AFIT run2 | 50Hz | cal | 1 | | C | AFIT map3 | 50Hz | N/A | N/A | N/A |
| ANT09 | C | AFIT run1 | 50Hz | cal | 1 | | S | AFIT map2 | 50Hz | N/A | N/A | N/A |
| ANT10 | T | AFIT run2 | 10Hz | cal | 1 | | T | AFIT map3 | 10Hz | N/A | N/A | N/A |
| ANT11 | S | AFIT run1 | 10Hz | cal | 1 | | S | AFIT map2 | 10Hz | N/A | N/A | N/A |
| ANT12 | C | AFIT run1 | 10Hz | cal | 1 | | C | AFIT map3 | 10Hz | N/A | N/A | N/A |
| ANT13 | T | AFIT run2 | 10Hz | cal | 1 | | S | AFIT map2 | 10Hz | N/A | N/A | N/A |
| ANT14 | T | AFIT run2 | 10Hz | cal | 1 | | C | AFIT map3 | 10Hz | N/A | N/A | N/A |
| ANT15 | C | AFIT run1 | 10Hz | cal | 1 | | S | AFIT map2 | 10Hz | N/A | N/A | N/A |
| | | | | | | | | | | | | |
| Compare sensor measurements in distance to a map based on distance | | | | | | | | | | | | |
| AND01 | T | AFIT run2 | 1m | uncal | 1 | | T | AFIT map3 | 1m | N/A | N/A | N/A |
| AND02 | T | AFIT run2 | 1m | cal | 1 | | T | AFIT map3 | 1m | N/A | N/A | N/A |
| AND03 | S | AFIT run1 | 1m | uncal | 1 | | S | AFIT map2 | 1m | N/A | N/A | N/A |
| AND04 | S | AFIT run1 | 1m | cal | 1 | | S | AFIT map2 | 1m | N/A | N/A | N/A |
| AND05 | C | AFIT run1 | 1m | uncal | 1 | | C | AFIT map2 | 1m | N/A | N/A | N/A |
| AND06 | C | AFIT run1 | 1m | cal | 1 | | C | AFIT map3 | 1m | N/A | N/A | N/A |
| AND07 | T | AFIT run2 | 1m | cal | 1 | | S | AFIT map2 | 1m | N/A | N/A | N/A |
| AND08 | T | AFIT run2 | 1m | cal | 1 | | C | AFIT map3 | 1m | N/A | N/A | N/A |
| AND09 | C | AFIT run1 | 1m | cal | 1 | | S | AFIT map2 | 1m | N/A | N/A | N/A |
| AND10 | T | AFIT run2 | 0.5m | cal | 1 | | T | AFIT map3 | 0.5m | N/A | N/A | N/A |
| AND11 | S | AFIT run1 | 0.5m | cal | 1 | | S | AFIT map2 | 0.5m | N/A | N/A | N/A |
| AND12 | C | AFIT run1 | 0.5m | cal | 1 | | C | AFIT map3 | 0.5m | N/A | N/A | N/A |
| AND13 | T | AFIT run2 | 0.5m | cal | 1 | | S | AFIT map2 | 0.5m | N/A | N/A | N/A |
| AND14 | T | AFIT run2 | 0.5m | cal | 1 | | C | AFIT map3 | 0.5m | N/A | N/A | N/A |
| AND15 | C | AFIT run1 | 0.5m | cal | 1 | | S | AFIT map2 | 0.5m | N/A | N/A | N/A |
| AND16 | T | AFIT run2 | 3m | cal | 1 | | T | AFIT map3 | 3m | N/A | N/A | N/A |
| AND17 | S | AFIT run1 | 3m | cal | 1 | | S | AFIT map2 | 3m | N/A | N/A | N/A |
| AND18 | C | AFIT run1 | 3m | cal | 1 | | C | AFIT map3 | 3m | N/A | N/A | N/A |
| AND19 | T | AFIT run2 | 3m | cal | 1 | | S | AFIT map2 | 3m | N/A | N/A | N/A |
| AND20 | T | AFIT run2 | 3m | cal | 1 | | C | AFIT map3 | 3m | N/A | N/A | N/A |
| AND21 | C | AFIT run1 | 3m | cal | 1 | | S | AFIT map2 | 3m | N/A | N/A | Feature |
| AND22 | T | AFIT run2 | 1m | simple | 1 | | S | AFIT map2 | 1m | N/A | N/A | N/A |
| AND23 | T | AFIT run2 | 1m | simple | 1 | | C | AFIT map3 | 1m | N/A | N/A | N/A |
| AND24 | C | AFIT run1 | 1m | simple | 1 | | S | AFIT map2 | 1m | N/A | N/A | N/A |
| | | | | | | | | | | | | |
| Position estimate used as a measurement | | | | | | | | | | | | |
| AND30 | T | AFIT run2 | 1m | ML | 1 | | T | AFIT map3 | 1m | N/A | N/A | N/A |
| AND31 | S | AFIT run1 | 1m | ML | 1 | | S | AFIT map2 | 1m | N/A | N/A | N/A |

| AND32 | C | AFIT run1 | 1m | ML | 1 | C | AFIT map3 | 1m | N/A | N/A | N/A |
|---|---|---|---|---|---|---|---|---|---|---|---|
| AND33 | T | AFIT run2 | 1m | ML | 1 | S | AFIT map2 | 1m | N/A | N/A | N/A |
| AND34 | T | AFIT run2 | 1m | ML | 1 | C | AFIT map3 | 1m | N/A | N/A | N/A |
| AND35 | C | AFIT run1 | 1m | ML | 1 | S | AFIT map2 | 1m | N/A | N/A | N/A |
| AND36 | T | AFIT run2 | 1m | MLR | 1 | S | AFIT map2 | 1m | N/A | N/A | N/A |
| AND37 | T | AFIT run2 | 1m | MLR | 1 | C | AFIT map3 | 1m | N/A | N/A | N/A |
| AND38 | C | AFIT run1 | 1m | MLR | 1 | S | AFIT map2 | 1m | N/A | N/A | N/A |
| AND39 | T | AFIT run2 | 1m | ABL | 1 | S | AFIT map2 | 1m | N/A | N/A | N/A |
| AND40 | T | AFIT run2 | 1m | ABL | 1 | C | AFIT map3 | 1m | N/A | N/A | N/A |
| AND41 | C | AFIT run1 | 1m | ABL | 1 | S | AFIT map2 | 1m | N/A | N/A | N/A |
| AND42 | T | AFIT run2 | 1m | ML | 4 | S | AFIT map2 | 1m | n | n | n |
| AND43 | T | AFIT run2 | 1m | ML | 4 | C | AFIT map3 | 1m | n | n | n |
| AND44 | C | AFIT run1 | 1m | ML | 4 | S | AFIT map2 | 1m | n | n | n |
| AND45 | T | AFIT run2 | 1m | MLR | 4 | S | AFIT map2 | 1m | n | n | n |
| AND46 | T | AFIT run2 | 1m | MLR | 4 | C | AFIT map3 | 1m | n | n | n |
| AND47 | C | AFIT run1 | 1m | MLR | 4 | S | AFIT map2 | 1m | n | n | n |
| AND48 | T | AFIT run2 | 1m | ABL | 4 | S | AFIT map2 | 1m | n | n | n |
| AND49 | T | AFIT run2 | 1m | ABL | 4 | C | AFIT map3 | 1m | n | n | n |
| AND50 | C | AFIT run1 | 1m | ABL | 4 | S | AFIT map2 | 1m | n | n | n |
| | | | | | | | | | | | |
| Demeaned comparison | | | | | | | | | | | |
| AND60 | T | AFIT run2 | 1m | ML/un | 4 | S | AFIT map2 | 1m | y | n | n |
| AND61 | T | AFIT run2 | 1m | ML/un | 4 | C | AFIT map3 | 1m | y | n | n |
| AND62 | C | AFIT run1 | 1m | ML/un | 4 | S | AFIT map2 | 1m | y | n | n |
| AND63 | T | AFIT run2 | 1m | ML | 4 | S | AFIT map2 | 1m | y | n | n |
| AND64 | T | AFIT run2 | 1m | ML | 4 | C | AFIT map3 | 1m | y | n | n |
| AND65 | C | AFIT run1 | 1m | ML | 4 | S | AFIT map2 | 1m | y | n | n |
| AND66 | T | AFIT run2 | 1m | MLR/un | 4 | S | AFIT map2 | 1m | y | n | n |
| AND67 | T | AFIT run2 | 1m | MLR/un | 4 | C | AFIT map3 | 1m | y | n | n |
| AND68 | C | AFIT run1 | 1m | MLR/un | 4 | S | AFIT map2 | 1m | y | n | n |
| AND69 | T | AFIT run2 | 1m | MLR | 4 | S | AFIT map2 | 1m | y | n | n |
| AND70 | T | AFIT run2 | 1m | MLR | 4 | C | AFIT map3 | 1m | y | n | n |
| AND71 | C | AFIT run1 | 1m | MLR | 4 | S | AFIT map2 | 1m | y | n | n |
| AND72 | T | AFIT run2 | 1m | ABL/un | 4 | S | AFIT map2 | 1m | y | n | n |
| AND73 | T | AFIT run2 | 1m | ABL/un | 4 | C | AFIT map3 | 1m | y | n | n |
| AND74 | C | AFIT run1 | 1m | ABL/un | 4 | S | AFIT map2 | 1m | y | n | n |
| AND75 | T | AFIT run2 | 1m | ABL | 4 | S | AFIT map2 | 1m | y | n | n |
| AND76 | T | AFIT run2 | 1m | ABL | 4 | C | AFIT map3 | 1m | y | n | n |
| AND77 | C | AFIT run1 | 1m | ABL | 4 | S | AFIT map2 | 1m | y | n | n |
| | | | | | | | | | | | |
| Comparison using features | | | | | | | | | | | |
| AND80 | T | AFIT run2 | 1m | cal | varies | S | AFIT map2 | 1m | n | n | y |
| AND81 | T | AFIT run2 | 1m | cal | varies | C | AFIT map3 | 1m | n | n | y |
| AND82 | C | AFIT run1 | 1m | cal | varies | S | AFIT map2 | 1m | n | n | y |

| Test Case | | Measurements | | | | | Map | | | Comparison Method | | |
|-----------|-----|-------------|-------|-------|-------|-----|-------------|-------|--------|------|---------|
| | Veh | Description | Units | Type | #Meas | Veh | Description | Units | Demean | Diff | Feature |
| HNT01 | T | sub run2 | 50Hz | uncal | 1 | T | sub map3 | 50Hz | N/A | N/A | N/A |
| HNT02 | T | sub run2 | 50Hz | cal | 1 | T | sub map3 | 50Hz | N/A | N/A | N/A |
| HNT03 | S | sub run1 | 50Hz | uncal | 1 | S | sub map2 | 50Hz | N/A | N/A | N/A |
| HNT04 | S | sub run1 | 50Hz | cal | 1 | S | sub map2 | 50Hz | N/A | N/A | N/A |
| HNT05 | C | sub run1 | 50Hz | uncal | 1 | C | sub map3 | 50Hz | N/A | N/A | N/A |
| HNT06 | C | sub run1 | 50Hz | cal | 1 | C | sub map3 | 50Hz | N/A | N/A | N/A |
| HNT07 | T | sub run2 | 50Hz | cal | 1 | S | sub map2 | 50Hz | N/A | N/A | N/A |
| HNT08 | T | sub run2 | 50Hz | cal | 1 | C | sub map3 | 50Hz | N/A | N/A | N/A |
| HNT09 | C | sub run1 | 50Hz | cal | 1 | S | sub map2 | 50Hz | N/A | N/A | N/A |
| HNT10 | T | sub run2 | 10Hz | cal | 1 | T | sub map3 | 10Hz | N/A | N/A | N/A |
| HNT11 | S | sub run1 | 10Hz | cal | 1 | S | sub map2 | 10Hz | N/A | N/A | N/A |
| HNT12 | C | sub run1 | 10Hz | cal | 1 | C | sub map3 | 10Hz | N/A | N/A | N/A |
| HNT13 | T | sub run2 | 10Hz | cal | 1 | S | sub map2 | 10Hz | N/A | N/A | N/A |
| HNT14 | T | sub run2 | 10Hz | cal | 1 | C | sub map3 | 10Hz | N/A | N/A | N/A |
| HNT15 | C | sub run1 | 10Hz | cal | 1 | S | sub map2 | 10Hz | N/A | N/A | N/A |
| | | | | | | | | | | | |
| Compare sensor measurements in distance to a map based on distance | | | | | | | | | | | |
| HND01 | T | sub run2 | 1m | uncal | 1 | T | sub map3 | 1m | N/A | N/A | N/A |
| HND02 | T | sub run2 | 1m | cal | 1 | T | sub map3 | 1m | N/A | N/A | N/A |
| HND03 | S | sub run1 | 1m | uncal | 1 | S | sub map2 | 1m | N/A | N/A | N/A |
| HND04 | S | sub run1 | 1m | cal | 1 | S | sub map2 | 1m | N/A | N/A | N/A |
| HND05 | C | sub run1 | 1m | uncal | 1 | C | sub map2 | 1m | N/A | N/A | N/A |
| HND06 | C | sub run1 | 1m | cal | 1 | C | sub map3 | 1m | N/A | N/A | N/A |
| HND07 | T | sub run2 | 1m | cal | 1 | S | sub map2 | 1m | N/A | N/A | N/A |
| HND08 | T | sub run2 | 1m | cal | 1 | C | sub map3 | 1m | N/A | N/A | N/A |
| HND09 | C | sub run1 | 1m | cal | 1 | S | sub map2 | 1m | N/A | N/A | N/A |
| HND10 | T | sub run2 | 0.5m | cal | 1 | T | sub map3 | 0.5m | N/A | N/A | N/A |
| HND11 | S | sub run1 | 0.5m | cal | 1 | S | sub map2 | 0.5m | N/A | N/A | N/A |
| HND12 | C | sub run1 | 0.5m | cal | 1 | C | sub map3 | 0.5m | N/A | N/A | N/A |
| HND13 | T | sub run2 | 0.5m | cal | 1 | S | sub map2 | 0.5m | N/A | N/A | N/A |
| HND14 | T | sub run2 | 0.5m | cal | 1 | C | sub map3 | 0.5m | N/A | N/A | N/A |
| HND15 | C | sub run1 | 0.5m | cal | 1 | S | sub map2 | 0.5m | N/A | N/A | N/A |
| HND16 | T | sub run2 | 3m | cal | 1 | T | sub map3 | 3m | N/A | N/A | N/A |
| HND17 | S | sub run1 | 3m | cal | 1 | S | sub map2 | 3m | N/A | N/A | N/A |
| HND18 | C | sub run1 | 3m | cal | 1 | C | sub map3 | 3m | N/A | N/A | N/A |
| HND19 | T | sub run2 | 3m | cal | 1 | S | sub map2 | 3m | N/A | N/A | N/A |
| HND20 | T | sub run2 | 3m | cal | 1 | C | sub map3 | 3m | N/A | N/A | N/A |
| HND21 | C | sub run1 | 3m | cal | 1 | S | sub map2 | 3m | N/A | N/A | N/A |
| | | | | | | | | | | | |
| Comparison using features | | | | | | | | | | | |
| HND30 | T | sub run2 | 3m | cal | varies | S | sub map2 | 3m | n | n | y |
| HND31 | T | sub run2 | 3m | cal | varies | C | sub map3 | 3m | n | n | y |
| HND32 | C | sub run1 | 3m | cal | varies | S | sub map2 | 3m | n | n | y |

| Test Case | | Measurements | | | | | Map | | | Comparison Method | | |
|---|---|---|---|---|---|---|---|---|---|---|---|---|
| | Veh | Description | Units | Type | #Meas | Veh | Description | Units | Demean | Diff | Feature |
| LNT01 | T | large run1 | 50Hz | uncal | 1 | T | large map2 | 50Hz | N/A | N/A | N/A |
| LNT02 | T | large run1 | 50Hz | cal | 1 | T | large map2 | 50Hz | N/A | N/A | N/A |
| LNT03 | S | large run1 | 50Hz | uncal | 1 | S | large map2 | 50Hz | N/A | N/A | N/A |
| LNT04 | S | large run1 | 50Hz | cal | 1 | S | large map2 | 50Hz | N/A | N/A | N/A |
| LNT05 | C | large run1 | 50Hz | uncal | 1 | C | large map2 | 50Hz | N/A | N/A | N/A |
| LNT06 | C | large run1 | 50Hz | cal | 1 | C | large map2 | 50Hz | N/A | N/A | N/A |
| LNT07 | T | large run1 | 50Hz | cal | 1 | S | large map2 | 50Hz | N/A | N/A | N/A |
| LNT08 | T | large run1 | 50Hz | cal | 1 | C | large map2 | 50Hz | N/A | N/A | N/A |
| LNT09 | C | large run1 | 50Hz | cal | 1 | S | large map2 | 50Hz | N/A | N/A | N/A |
| LNT10 | T | large run1 | 10Hz | cal | 1 | T | large map2 | 10Hz | N/A | N/A | N/A |
| LNT11 | S | large run1 | 10Hz | cal | 1 | S | large map2 | 10Hz | N/A | N/A | N/A |
| LNT12 | C | large run1 | 10Hz | cal | 1 | C | large map2 | 10Hz | N/A | N/A | N/A |
| LNT13 | T | large run1 | 10Hz | cal | 1 | S | large map2 | 10Hz | N/A | N/A | N/A |
| LNT14 | T | large run1 | 10Hz | cal | 1 | C | large map2 | 10Hz | N/A | N/A | N/A |
| LNT15 | C | large run1 | 10Hz | cal | 1 | S | large map2 | 10Hz | N/A | N/A | N/A |
| | | | | | | | | | | | |
| Compare sensor measurements in distance to a map based on distance | | | | | | | | | | | |
| LND01 | T | large run1 | 1m | uncal | 1 | T | large map2 | 1m | N/A | N/A | N/A |
| LND02 | T | large run1 | 1m | cal | 1 | T | large map2 | 1m | N/A | N/A | N/A |
| LND03 | S | large run1 | 1m | uncal | 1 | S | large map2 | 1m | N/A | N/A | N/A |
| LND04 | S | large run1 | 1m | cal | 1 | S | large map2 | 1m | N/A | N/A | N/A |
| LND05 | C | large run1 | 1m | uncal | 1 | C | large map2 | 1m | N/A | N/A | N/A |
| LND06 | C | large run1 | 1m | cal | 1 | C | large map2 | 1m | N/A | N/A | N/A |
| LND07 | T | large run1 | 1m | cal | 1 | S | large map2 | 1m | N/A | N/A | N/A |
| LND08 | T | large run1 | 1m | cal | 1 | C | large map2 | 1m | N/A | N/A | N/A |
| LND09 | C | large run1 | 1m | cal | 1 | S | large map2 | 1m | N/A | N/A | N/A |
| LND10 | T | large run1 | 0.5m | cal | 1 | T | large map2 | 0.5m | N/A | N/A | N/A |
| LND11 | S | large run1 | 0.5m | cal | 1 | S | large map2 | 0.5m | N/A | N/A | N/A |
| LND12 | C | large run1 | 0.5m | cal | 1 | C | large map2 | 0.5m | N/A | N/A | N/A |
| LND13 | T | large run1 | 0.5m | cal | 1 | S | large map2 | 0.5m | N/A | N/A | N/A |
| LND14 | T | large run1 | 0.5m | cal | 1 | C | large map2 | 0.5m | N/A | N/A | N/A |
| LND15 | C | large run1 | 0.5m | cal | 1 | S | large map2 | 0.5m | N/A | N/A | N/A |
| LND16 | T | large run1 | 3m | cal | 1 | T | large map2 | 3m | N/A | N/A | N/A |
| LND17 | S | large run1 | 3m | cal | 1 | S | large map2 | 3m | N/A | N/A | N/A |
| LND18 | C | large run1 | 3m | cal | 1 | C | large map2 | 3m | N/A | N/A | N/A |
| LND19 | T | large run1 | 3m | cal | 1 | S | large map2 | 3m | N/A | N/A | N/A |
| LND20 | T | large run1 | 3m | cal | 1 | C | large map2 | 3m | N/A | N/A | N/A |
| LND21 | C | large run1 | 3m | cal | 1 | S | large map2 | 3m | N/A | N/A | N/A |
| | | | | | | | | | | | |
| Comparison using features | | | | | | | | | | | |
| LND30 | T | large run1 | 3m | cal | 1 | S | large map2 | 3m | N/A | N/A | N/A |
| LND31 | T | large run1 | 3m | cal | 1 | C | large map2 | 3m | N/A | N/A | N/A |
| LND32 | C | large run1 | 3m | cal | 1 | S | large map2 | 3m | N/A | N/A | N/A |

## Bibliography

1. Agency, Defense Mapping. *Handbook of Magnetic Compass Adjustment*. Defense Mapping Agency, Washington D.C., USA, 1980.

2. Alonso, R. and M. D. Shuster. "Complete Linear Attitude-Independent Magnetometer Calibration". *Journal of Astronautical Sciences*, 50(4):477–490, 2002.

3. Arulampalam, S., S. Maskell, N. Gordon, and T. Clapp. "A Tutorial on Particle Filters for Online Nonlinear/Non-Gaussian Bayesian Tracking". *Signal Processing, IEEE Transactions on*, vol. 50, 174–188. 2002.

4. Ascher, C., C. Kessler, M. Wankerl, and G.F. Trommer. "Using OrthoSLAM and Aiding Techniques for Precise Pedestrian Indoor Navigation". *Proceedings of the 22nd International Technical Meeting of the Satellite Division of the Institute of Navigation*, 743–749. Savannah, GA, 2009.

5. Boteler, D.H., R.J. Pirjola, and H. Nevanlinna. "The effects of geomagnetic disturbances on electrical systems at the Earth's surface". *Advances in Space Research*, 22(1):17 – 27, 1998. ISSN 0273-1177. Solar-Terrestrial Relations: Predicting the Effects on the Near-Earth Environment.

6. Brauer, P., J.M.G. Merayo, T. Risbo, and F. Primdahl. "Magnetic Calibration Of Vector Magnetometers: Linearity, Thermal Effects And Stability", unknown.

7. Cai, J., N.L. Andersen, and C. Malureanu. "In-Field Practical Calibration of Three-Axis Magnetometers". *Proceedings of the 2010 International Technical Meeting of The Institute of Navigation*, 67–73. San Diego, CA, 2010.

8. Campbell, W.H. *Earth Magnetism: A Guided Tour through Magnetic Fields*. Complementary Science Series. Harcourt/Academic Press, San Diego, CA, 2001.

9. Camps, F., S. Harasse, and A. Monin. "Numerical Calibration for 3-axis Accelerometers and Magnetometers". *Proceedings of the IEEE International Conference on Electro-Information Technology*, 217–221. Ontario, Canada, 2009.

10. Caruso, M.J. "Applications of Magnetoresistive Sensors in Navigation Systems". *Sensors and Actuators*, SP-1220:159–168, February 1997. URL http://www.ssec.honeywell.com/position-sensors/datasheets/sae.pdf.

11. Castagnetti, C., L. Biagi, and A. Capra. "Design of a Low-Cost GPS/Magnetometer System for Land-Based Navigation: Integration and Autocalibration Algorithms". *Proceedings of the International Federation of Surveyors Working Week 2011*, 73–88. Marrakech, Morocco, 2011.

12. Clark, C.S. *Multiple Model Adaptive Estimation and Control Redistribution Performance on the Vista F-16 During Partial Actuator Impairments*. Master's thesis, Air Force Institute of Technology, March 1997.

13. Crassidis, J.L., K. Lai, and R.R. Harman. "Real-time Attitude-Independent Three-Axis Magnetometer Calibration". *Journal of Guidance, Control, and Dynamics*, 28(1):115–120, 2005.

14. Foster, C.C. and G.H. Elkaim. "Extension of a Two-Step Calibration Methodology to Include Nonorthogonal Sensor Axes". *IEEE Transactions on Aerospace and Electronic Systems*, 51(1):70–80, 2003.

15. Gebre-Egziabher, D., G.H. Elkaim, J.D. Powell, and B.W. Parkinson. "A Gyro-Free Quaternion-Based Attitude Determination System Suitable for Implementation Using Low Cost Sensors". *Proceedings of IEEE 2000 Position Location and Navigation Symposium*, 185–192. San Diego, CA, 2000.

16. Gebre-Egziabher, D., G.H. Elkaim, J.D. Powell, and B.W. Parkinson. "A nonlinear, two-step estimation algorithm for calibrating solid-state strapdown magnetometers". *Proceedings of the 8th International St. Petersburg Conference on Integrated Navigation Systems*, 28–30. St. Petersburg, Russia, May 2001.

17. Gebre-Egziabher, D., G.H. Elkaim, J.D. Powell, and B.W. Parkinson. "Calibration of Strapdown Magnetometers in Magnetic Field Domain". *Journal of Aerospace Engineering*, 19(2):87–102, 2006. URL `http://link.aip.org/link/?QAS/19/87/1`.

18. Goldenberg, Felix (Goodrich Corporation Advanced Sensors Technical Center). "Geomagnetic navigation beyond the magnetic compass". *Record - IEEE PLANS, Position Location and Navigation Symposium, IEEE/ION Position, Location, and Navigation Symposium*, 2006:684–694, 2006.

19. Von der Hardt, H.J. "An Automatic Calibration Method for a Multisensor System: Application to a Mobile Robot Localization System". *Proceedings of the 1998 IEEE International Conference on Robotics and Autonomation*, 3141–3146. Leuven, Belgium, May 1998.

20. Haverinen, J. and A. Kemppainen. "A Global Self-Localization Technique Utilizing Local Anomalies of the Ambient Magnetic Field". *Robotics and Automation, 2009. ICRA '09. IEEE International Conference on*, 3142 –3147. may 2009. ISSN 1050-4729.

21. Haverinen, J. and A. Kemppainen. "A Geomagnetic Field Based Positioning Technique for Underground Mines". *Robotic and Sensors Environments (ROSE), 2011 IEEE International Symposium on*, 7–12. sept. 2011.

22. Honeywell, Solid State Electronics Center. "HMR2300 Smart Digital Magnetometer Datasheet". 12001 Highway 55, Plymouth, MN, 55441, September 2006. `http://www.ssec.honeywell.com/magnetic/datasheets/hmr2300.pdf`.

23. Johnson, D.W. and W.J. Johnson. "Comparison of Total Magnetic Field to Vertical Magnetic Gradient Data from Effigy Mounds National Park, Iowa", 2005. URL `http://www.archaeology-geophysics.com/Publications.html`.

24. Judd, T. and T. Vu. "Use of a New Pedometric Dead Reckoning Module in GPS Denied Environments". *Position, Location and Navigation Symposium*, 120–128. Monterey, CA, May 2008.

25. Kao, W. and C. Tsai. "Adaptive and Learning Calibration of a Magnetic Compass". *Measurement and Science Technology*, 17(11):3073–3082, 2006.

26. Kemppi, P., J. Pajunen, and T. Rautiainen. "Use of Artificial Magnetic Anomalies in Indoor Pedestrian Navigation". *Vehicular Technology Conference Fall (VTC 2010-Fall), 2010 IEEE 72nd*, 1 –5. sept. 2010. ISSN 1090-3038.

27. Ladetto, Q., V. Gabaglio, and B. Merminod. "Two Different Approaches for Augmented GPS Pedestrian Navigation". *International Symposium on Location Based Services for Cellular Users*. 2001.

28. Langley, R.B. "The Magnetic Compass and GPS". *GPS World*, 44(3):1070–1078, 2008.

29. Li, Q. and J.G. Griffiths. "Least Squares Ellipsoid Specific Fitting". *Geometric Modeling and Processing 2004 Proceedings*, 335–340. IEEE Computer Society, Los Alamitos, CA, USA, 2004.

30. Lohmann, K.J., C.M.F. Lohmann, and N.F. Putman. "Magnetic maps in animals: nature's GPS". *The Journal of Experimental Biology*, 210(21):3697–3705, November 2007.

31. Maus, S., C. Manoj, J. Rauberg, I. Michaelis, and H. Luhr. "NOAA/NGDC candidate models for the 11th generation International Geomagnetic Reference Field and the concurrent release of the 6th generation Pomme magnetic model". *Earth, Planets and Space*, 62(1):729–735, 2006.

32. Maybeck, P.S. *Stochastic Models, Estimation, and Control*, volume 1. Academic Press, Inc., Orlando, Florida, 1979.

33. Maybeck, P.S. *Stochastic Models, Estimation, and Control*, volume 2. Academic Press, Inc., Orlando, Florida, 1982.

34. Merayo, J.M.G., P. Brauer, F. Primdahl, and J.R. Petersen. "Absolute Magnetic Calibration And Alignment Of Vector Magnetometers In The Earth's Magnetic Field". *Workshop on Calibration of Space-Borne Magnetometers in Ground and In-Flight Space Magnetometer Calibration Techniques*, ESA SP–490. Braunschweig, Germany, 1999.

35. Merayo, J.M.G., P. Brauer, F. Primdahl, J.R. Petersen, and O.V. Nielsen. "Scalar calibration of vector magnetometers". *Measurement Science and Technology*, 11(2):120, 2000. URL http://stacks.iop.org/0957-0233/11/i=2/a=304.

36. Van der Merwe, R., A. Doucet, N. de Frietas, and E. Wan. *Unscented Particle Filter.* Technical Report CUED/F-INFENG/TR 380, Cambridge University Engineering Department, Cambridge CB2 1PZ, England, 2000.

37. Moafipoor, S., D.A. Grejner-Brzezinska, and C. Toth. "Adaptive Calibration of a Magnetometer Compass for a Personal Navigation System". *Proceedings of the International Global Navigation Satellite Systems Society IGNSS Symposium.* Sydney, Australia, 2007. CDROM.

38. Nelson, James H., Loius Hurwitz, and David G. Knapp. *Magnetism of the Earth.* Publication 40-1, United States Department of Commerce: Coast and Geodetic Survey, Washington D.C., 1962.

39. NovAtel. "SPAN Technology for OEMV User Manual Rev 8". 1120-68 Avenue NE, Calgary, AB, Canada, T2E 8S5, August 2010. `http://www.novatel.com`.

40. Rekleitis, I. "A Particle Filter Tutorial for Mobile Robot Localization TR-CIM-0402", 2003.

41. Renaudin, V., M.H. Afzal, and G. Lachapelle. "New Method for Magnetometers Based Orientation Estimation". *Proceedings of the IEEE/ION PLANS Conference*, 348–356. Palm Springs, CA, May 2010.

42. Storms, W.F. *Magnetic Field Aided Indoor Navigation.* Master's thesis, Air Force Institute of Technology, March 2009.

43. Strangway, David W. *History of the Earth's Magnetic Field.* McGraw-Hill, Inc., New York, NY, 1970.

44. Vasconcelos, J.F., G. Elkaim, C. Silvestre, P. Oliveira, and B. Cardeira. "A Geometric Approach to Strapdown Magnetometer Calibration in the Sensor Frame". *IEEE Transactions on Aerospace and Electronic Systems*, 47(2):1293–1306, 2011.

45. Vernaza, P. and D. Lee. "Rao-Blackwellized Particle Filtering for 6-DOF Estimation of Attitude and Position via GPS and Inertial Sensors". *IEEE Conference on Robotics and Automation*, 1571–1578. Orlando, FL, May 2006.

46. Veth, M.J. "EENG 766 2010 Section06 Introduction to Particle Filtering", 2010.

47. Wang, J.H. and Y. Gao. "A New Magnetic Compass Calibration Algorithm Using Neural Networks". *Measurement and Science Technology*, 17(1):153, 2006.

48. Wilson, John M., Robert J. Kline-Schoder, Marc A. Kenton, Paul H. Sorensen, and Odile H. Clavier. "Passive Navigation Using Local Magnetic Field Variations". *Institute of Navigation International Technical Meeting*, 770–779. Institute of Navigation, Monterey, CA, January 2006.

| 1. REPORT DATE *(DD-MM-YYYY)* | 2. REPORT TYPE | 3. DATES COVERED *(From - To)* |
|---|---|---|
| 13 Sep 2012 | Dissertation | Aug 2009 - 13 Sep 2012 |

| 4. TITLE AND SUBTITLE | 5a. CONTRACT NUMBER |
|---|---|
| Ground Vehicle Navigation Using Magnetic Field Variation | |
| | 5b. GRANT NUMBER |
| | 5c. PROGRAM ELEMENT NUMBER |

| 6. AUTHOR(S) | 5d. PROJECT NUMBER |
|---|---|
| Shockley, Jeremiah A, Maj | |
| | 5e. TASK NUMBER |
| | 5f. WORK UNIT NUMBER |

| 7. PERFORMING ORGANIZATION NAME(S) AND ADDRESS(ES) | 8. PERFORMING ORGANIZATION REPORT NUMBER |
|---|---|
| Air Force Institute of Technology<br>Graduate School of Engineering and Management (AFIT/EN)<br>2950 Hobson Way<br>Wright-Patterson AFB OH 45433-7765 | AFIT/DEE/ENG/12-17 |

| 9. SPONSORING/MONITORING AGENCY NAME(S) AND ADDRESS(ES) | 10. SPONSOR/MONITOR'S ACRONYM(S) |
|---|---|
| Intentionally Left Blank | |
| | 11. SPONSOR/MONITOR'S REPORT NUMBER(S) |

**12. DISTRIBUTION/AVAILABILITY STATEMENT**

Distribution A. Approved for Public Release; Distribution Unlimited

**13. SUPPLEMENTARY NOTES**

This material is declared a work of the U.S. Government and is not subject to copyright protection in the United States.

**14. ABSTRACT**

The Earth's magnetic field has been the bedrock of navigation for centuries. The latest research highlights the uniqueness of magnetic field measurements based on position due to large scale variations as well as localized perturbations. These observable changes in the Earth's magnetic field as a function of position provide distinct information which can be used for navigation. This dissertation describes ground vehicle navigation exploiting variation in Earth's magnetic field using a self-contained navigation system consisting of only a magnetometer and magnetic field maps. In order to achieve navigation, effective calibration enables repeatable magnetic field measurements from different vehicles and facilitates mapping of the observable magnetic field as a function of position. A new modified ellipsoid calibration technique for strapdown magnetometers in large vehicles is described, as well as analysis of position measurement generation comparing a multitude of measurement compositions using existing and newly developed likelihood techniques. Finally, navigation solutions are presented.

**15. SUBJECT TERMS**

^navigation, magnetic field, vehicle, particle filter

| 16. SECURITY CLASSIFICATION OF: | | | 17. LIMITATION OF ABSTRACT | 18. NUMBER OF PAGES | 19a. NAME OF RESPONSIBLE PERSON |
|---|---|---|---|---|---|
| a. REPORT | b. ABSTRACT | c. THIS PAGE | | | Dr. John F. Raquet |
| U | U | U | UU | 186 | 19b. TELEPHONE NUMBER *(Include area code)*<br>(937) 255-3636 x4580   john.raquet@afit.edu |

Reset